INTERFACIAL BIOORTHOGONAL CROSSLINKING FOR THE FABRICATION OF FUNCTIONAL HYDROGELS

by

Kevin Thomas Dicker

A dissertation submitted to the Faculty of the University of Delaware in partial fulfillment of the requirements for the degree of Doctor of Philosophy in Materials Science and Engineering

Winter 2018

INTERFACIAL BIOORTHOGONAL CROSSLINKING FOR THE FABRICATION OF FUNCTIONAL HYDROGELS

by

Kevin Thomas Dicker

Approved: _____
Darrin J. Pochan, Ph.D.
Chair of the Department of Materials Science and Engineering

Approved: _____
Babatunde A. Ogunnaike, Ph.D.
Dean of the College of Engineering

Approved: _____
Ann L. Ardis, Ph.D.
Senior Vice Provost for Graduate and Professional Education

I certify that I have read this dissertation and that in my opinion it meets the academic and professional standard required by the University as a dissertation for the degree of Doctor of Philosophy.

Signed: _____

Xinqiao Jia, Ph.D.
Professor in charge of dissertation

I certify that I have read this dissertation and that in my opinion it meets the academic and professional standard required by the University as a dissertation for the degree of Doctor of Philosophy.

Signed: _____

Joseph M. Fox, Ph.D.
Member of dissertation committee

I certify that I have read this dissertation and that in my opinion it meets the academic and professional standard required by the University as a dissertation for the degree of Doctor of Philosophy.

Signed: _____

April M. Kloxin, Ph.D.
Member of dissertation committee

I certify that I have read this dissertation and that in my opinion it meets the academic and professional standard required by the University as a dissertation for the degree of Doctor of Philosophy.

Signed: _____

Christopher J. Kloxin, Ph.D.
Member of dissertation committee

ACKNOWLEDGMENTS

My Ph.D. journey has been a rollercoaster with many ups and downs throughout the 6.5 years I have spent here at the University of Delaware. I started with working on several different projects before ultimately landing on my thesis project and experienced many successes and failures along the way. I would not have been able to achieve those successes and overcome the failures with the help and collaborations of many people.

First and foremost I would like to thank my advisor, Dr. Xinqiao Jia. Dr. Jia has always pushed me to be a better scientist and researcher. She has instilled valuable lessons in me, to be a critical thinker and to always remember to keep the "so what" question in mind. I would also like to thank my collaborator Dr. Joseph Fox. I started collaborating with Dr. Fox in 2012 when we first attempted to apply tetrazine ligation to our hydrogels. I really value Dr. Fox's insight and problem solving skills. If I had a synthetic issue, he was there to provide a potential solution. Dr. Fox is also always able to put a positive spin on the project, even when things looked grim which was often the needed morale boost. I would also like to thank my other committee members: Dr. April Kloxin and Dr. Christopher Kloxin. Both have provided valuable discussion and suggestions on how to improve and advance my dissertation work.

I would like to thank all of my collaborators. I have to acknowledge the Fox Group for without them I really would not have a thesis project, at least not the one described herein. Dr. Han Zhang first started this project with me back in 2012 and it blossomed into a very fruitful project for both of us. Dr. Yi (George) Li joined the

project in 2014 and helped a lot with the synthesis of TCO conjugated molecules, specifically the MMP degradable crosslinker. I would also like to thank Dr. Axel Moore, Nikolay Garabedian and their advisor Dr. David Burris. All of the mechanical studies done in Chapters 3 and 4 were done in collaboration with Axel, Nick and the Burris Group's micromaterial tester. Axel also helped to design and analysis for the Hoop Stress study for the hydrogel channels. I would like to thank Dr. Robert Akins and his group, specifically Dr. Rebecca Scott and Karyn Robinson. The *in vitro* vascular work was done with cells acquired from his lab and they also provided me with a lot of useful insight with the project.

I would like to thank the Bioimaging Facility at Delaware Biotechnical Institute, specifically Dr. Jeff Kaplan and Michael Moore. A vast amount of my dissertation work was done shown in chapters 2-4 used one of the many confocal microscopes in the Bioimaging Facility. Jeff and Mike helped with laser tuning, training and suggestions on how to acquire better quality images.

I am thankful for Team Jia, all past and present members, for their encouragement, collaboration and suggestions throughout my UD career. Specifically I would like to thank Dr. Xian Xu for his help with the prostate cancer cell study in Chapter 2, Jiyeon Song for her collaboration with the hydrogel sphere patterning project in Chapter 3, Aidan Zerdoum for his collaboration and discussions on the biological side of my projects, Dr. Shuang Liu for her helpful discussions and suggestions and He Zhang whom provided several of the small Tetrazine and TCO molecules needed for my project.

Additionally, I would like to thank the Materials Science and Engineering Staff: Charlie Garbini, Christine Williamson, Kathy Forwood, Naima Hall, Robin

Buccos, and Judy Allarey. Without their help in scheduling, taking care of paperwork, and all of the other behind the scenes work they do, it would have been much more difficult to finish this work. In addition, Charlie maintained a safe working environment for all of us graduate students in lab.

I would like to thank my parents, David and Mary Alice, for there love and support through this long process. I would like to thank my brother Stephen who went through this ludicrous PhD journey before me and was able to provide me lots of useful advice. Finally I would like to thank my beautiful and patient wife Donna for all of her love, support and encouragement throughout my graduate studies at UD.

TABLE OF CONTENTS

LIST OF TABLES xi
LIST OF FIGURES xii
ABSTRACT xxii

Chapter

1 INTRODUCTION 1

1.1 Overview 1
1.2 Modular and Orthogonal Synthesis of Hybrid Polymers and Networks 2

1.2.1 Synthetic Strategies 4
1.2.2 Modular synthesis of hybrid hydrogel networks 10

1.2.2.1 Hydrogels synthesized by oxime/hydrazone chemistry. 12
1.2.2.2 Hydrogels synthesized by Michael addition or thiol-ene chemistry. 14
1.2.2.3 Hydrogels synthesized by cycloaddition reactions 17
1.2.2.4 Hydrogels synthesized by other orthogonal reactions 19
1.2.2.5 Manipulation of hydrogel properties using multiple reactions 20

1.2.3 Conclusion and perspective 22

1.3 Hyaluronic Acid 23

1.3.1 Introduction 23
1.3.2 Biosynthesis and Degradation 26
1.3.3 HA-protein interactions 32
1.3.4 HA in morphogenesis and wound healing 38
1.3.5 HA in cancer 42
1.3.6 HA in biomedical applications 48
1.3.7 Summary and outlook 54

1.4 Dissertation Summary 56

REFERENCES 58

2 INTERFACIAL BIOORTHOGONAL CROSSLINKING 80

2.1 Introduction 80
2.2 Materials and Methods 82

2.2.1 Materials 82
2.2.2 Synthesis of Hydrogel Precursors 83

2.2.2.1 sTCO-OH 83
2.2.2.2 sTCO-carbonate(2) 84
2.2.2.3 sTCO-PEG18-sTCO 85
2.2.2.4 sTCO-PEG11-Boc(6) 86
2.2.2.5 sTCO-Alexa Fluor® 647(5) 87
2.2.2.6 Diphenyl-Tetrazine-OH(2) 88
2.2.2.7 Diphenyl-Tetrazine-carbonate(3) 89
2.2.2.8 Diphenyl-Tetrazine-PEG18-Amine(4) 90
2.2.2.9 Diphenyl-Tetrazine Modified Hyaluronic Acid 91

2.2.3 Kinetic analysis of the reaction between TCO (4) and 3,6-diphenyl-s-tetrazine (6) in H_2O 92
2.2.4 Determination of molecular weight and solution viscosity. 92
2.2.5 Interfacial bioorthogonal crosslinking. 93
2.2.6 Rheological characterization. 94
2.2.7 Selective interfacial tagging. 94
2.2.8 Interfacial cell encapsulation and 3D culture. 95

2.3 Results and Discussion 96

2.3.1 Hydrogel Preparation 96
2.3.2 Liquid-Filled Hydrogel Channel Formation 101
2.3.3 Interfacial Hydrogel Microsphere Patterning 104
2.3.4 3D Encapsulation of Prostate Cancer Cells 109

2.4 Conclusions 111
2.5 Spectral Data for Chapter 2 113

REFERENCES 130

3 3D PATTERNING OF SYNTHETIC HYDROGELS VIA INTERFACIAL BIOORTHOGONAL CHEMISTRY FOR SPATIAL CONTROL OF STEM CELL BEHAVIOR 133

3.1 Introduction 133
3.2 Materials and Methods 135
3.2.1 Materials 135
3.2.2 Synthesis of Hydrogel Precursors 136
3.2.2.1 Synthesis of 2-(4-(6-methyl-1,2,4,5-tetrazin-3-yl)phenyl)acetohydrazide (Tz-hydrazide) 136
3.2.2.2 Synthesis of tetrazine functionalized hyaluronic Acid (HA-Tz) 137
3.2.2.3 Synthesis of PEG-based TCO crosslinker (PEG-bisTCO) 138
3.2.2.4 Synthesis of MMP-degradable TCO crosslinker (GIW-bisTCO) 139
3.2.2.5 Synthesis of RGD-TCO 141
3.2.2.6 Synthesis of PEG-TCO 141
3.2.2.7 PEG-dTCO 142
3.2.3 Analysis of reaction kinetics. 144
3.2.4 Hydrogel Synthesis. 145
3.2.5 Hydrogel Swelling and Degradation 145
3.2.6 Fluorescent Tagging 146
3.2.7 Mechanical Properties 146
3.2.8 Cell Maintenance and 3D Culture 147
3.2.9 Cell Viability Study 147
3.2.10 Cell Morphology 148
3.2.11 Statistical Analysis 148
3.3 Results and Discussion 148
3.4 Conclusions 166
3.5 Spectral Data for Chapter 3 167
REFERENCES 192
4 FORMATION OF LIQUID FILLED HYDROGEL CHANNELS 195
4.1 Introduction 195
4.2 Materials and Methods 197
4.2.1 Materials 197
4.2.2 Synthesis of Hydrogel Precursors 198
4.2.2.1 Synthesis of VPM-bisTCO 198

4.2.3 Chamber Fabrication 199
4.2.4 Hydrogel Channel Formation 200
4.2.5 Pressure Dilation Assay 200
4.2.6 Covalent Patterning of Fluorophores 202
4.2.7 Cell Maintenance and 3D culture 202
4.2.8 Three dimensional (3D) matrix patterning 203
4.2.9 Three dimensional (3D) cell patterning 204
4.2.10 Cell Viability 204
4.2.11 Vascular Cell Patterning 208

4.3 Results and Discussion 209
4.4 Conclusions 223
4.5 Spectral Data for Chapter 4 223

REFERENCES 228

5 CONCLUSIONS AND FUTURE DIRECTIONS 231

5.1 Conclusions and Significance 231
5.2 Future Directions 233

5.2.1 Incorporation of Triggerable Dihydrotetrazine (DHT) 234
5.2.2 Gradient Patterning 235
5.2.3 Hydrogel Channels for In Vitro Models 237

REFERENCES 240

Appendix

A COPYRIGHT PERMISSION FOR REPRINT OF PUBLISHED ARTICLES 242

LIST OF TABLES

Table 1.1 Classic orthogonal reactions used in synthesis of biomaterials. Reproduced by permission of The Royal Society of Chemistry. 5

Table 3.1 Preparation of HA-based hydrogels with varying stiffness, degradability and adhesivity. 157

LIST OF FIGURES

Figure 1.1 Schematic summary of biomaterials synthesized using modular approaches employing orthogonal chemistry. Reproduced by permission of The Royal Society of Chemistry. 4

Figure 1.2 (A) Chemical structure of HA and schematic illustration of (B) HA biosynthesis and (C) biodegradation. (A) HA is a linear polysaccharide with disaccharide repeats of $_{D}$-glucuronic acid and *N*-acetyl-$_{D}$-glucosamine. (B) HA is synthesized by transmembrane proteins HAS1, 2 and 3 and is extruded into the extracellular space as the polymerization proceeds. Reproduced with permission, Copyright 2008, The Japanese Biochemical Society.[177] 25

Figure 1.3 Tapping mode AFM images of HA deposited on freshly cleaved mica. HA with (A, B) moderate or (C, D) high molecular weight, (A–C) produced in bacteria or (D) extracted from rooster comb, was deposited from 10 μg ml^{-1}s olution in H2O (A, B), 5 μg ml^{-1} solution in 10 mM MgCl2 or 500 μg ml^{-1} solution in 0.15 M NaCl (D). Scale bar: 250 nm, Z range: 2.5–6 nm. Reproduced with permission,[199] Copyright 2005, Elsevier. 29

Figure 1.4 HA organizes the cartilage ECM via non-covalent binding with aggrecan. Reproduced with permission,[249] Copyright 1996, Orthopaedic Research Society. Electron micrograph of an aggrecan/HA aggregate (from fetal bovine cartilage) shadowed with platinum. Each aggregate consists of ~100 aggrecan monomers bound to HA. With a molecular weight >10^8, such a complex occupies a volume equivalent to that of a bacterium. 36

Figure 1.5 HA organized as (A) monocyte-adhesive cables or (B, C) pericellular coat. (A) Monocyte-adhesive HA cable, produced by treating human colon smooth muscle cells with poly I:C for 17 h:green, HA; red, CD44; and blue, nuclei. Scale bar, 50 lm. Arrowheads point to areas without any leukocytes. (B, C) HA coat around a MCF-7 cell, as revealed by confocal imaging a probe made of aggrecan G1 domain and link protein tagged with Alexa Fluor 594®(red). Green staining represents green fluorescent protein tagged HAS3 (GFP-HAS3). The HA coat was visualized by particle exclusion using red blood cells (green). Scale bar, 10 μm. (A) Reproduced with permission,[254] Copyright 2003, Elsevier. (B, C): Reproduced with permission,[260] Copyright 2008, Elsevier. 38

Figure 2.1 **a**) Instantaneous crosslinking via tetrazine-TCO ligation. **b**) Gel interface forms when a droplet of tetrazine modified hyaluronic acid (HA-Tz) contacts a solution of bis-trans cyclooctene crosslinker (bis-TCO). Crosslinking at the gel/liquid interface is faster than the rate of diffusion through the gel interface. 98

Figure 2.2 Interfacial crosslinking of HA-Tz droplets. **a**. HA-Tz droplet (pink) dropped into a bath of bis-TCO. Upon contact with the bath, an instantaneous crosslinked shell forms on the outside of the droplet. As the crosslinking is allowed to proceed, bis-TCO will diffuse across the crosslinked shell, reacting with HA-Tz at the gel-liquid interface until completely crosslinked (2 Hr). **b**. The crosslinked wall thickness of the microsphere over the two hour crosslinking period monitors by the disappearance of the pink chromophore. 100

Figure 2.3 Rheological properties of the crosslinked hydrogel microspheres. Elastic (G') and loss modulus (G") as a function of time (**a**) and frequency (**b**). 101

Figure 2.4 Hydrogel channels via interfacial bioorthogonal crosslinking. Channel structures were pulled by injecting while withdrawing an aqeous solution of bis-TCO (2 mM) and Alexa-TCO (2 μM) into a vessel containing HA-Tz (2 wt%). A crosslinked channel wall forms at the interface between the two liquids and the channel wall continues to grow with diffusion of the bis-TCO crosslinker until fully depleted. ... 102

Figure 2.5 Visualization of hydrogel channel formation. **a–c**, Top and side views of Z-stack confocal images show the formation of a 3-D channel structure. **a**. Confocal imaging 1 minute after creating the channel showed distinct walls (153 ± 13 μM) had formed at the interface. The interior of the channel still contained unreacted dye. **b**. After 60 min, the same channel structure was reimaged. The dye from the interior of the channel had almost completely migrated to the walls, which had thickened to 254 ± 18 μM , consistent with an interfacial polymerization at the exterior of the structures. **c**. Imaging of the same channel after 60 min shown from a side view. **d**. Plot of channel wall thickness over time. 104

Figure 2.6 Fluorescent tagging with 3D spatial resolution. **a**, Schematic depiction of a small molecule-TCO conjugate being covalently introduced at the gel-solution interface during crosslinking of HA-Tz by bis-TCO. Alternating the presence/absence of Alexa-TCO leads to gels with distinct tagged and untagged gel layers. **b–g,** Confocal microscopy images of microspheres with spatially resolved 3-D tagging by Alexa-TCO. Displayed beneath images **b** and **c** are image density profile plots. **b,** Interfacial crosslinking the presence of Alexa-TCO for 30 min, and then in the absence of Alexa-TCO for 90 min gave microspheres that were labeled on the exterior. **c**, Confocal microscopy image of a microsphere with a radial gradient of 3-D tagging by Alexa-TCO, with increasing concentration of Alexa-TCO toward the center of the capsule. Interfacial crosslinking was carried out with 0.5 mL of a 400 μM bis-TCO solution. Initially, no Alexa-TCO was present. Once crosslinking was initiated, a syringe pump was used to add 200 μL of a 2.8 μM Alexa-TCO/400 μM bis-TCO solution over the course of 90 min, and crosslinking was continued for an additional 30 min without further addition of Alexa-TCO. **d,** Crosslinking in the absence and then presence of Alexa-TCO gave capsules that were labeled at the core. **e-g** Onion-like structures could be created by alternating the presence and absence of Alexa-TCO during the crosslinking procedure. Images of three, five and seven layered gels are displayed..... 107

Figure 2.7 Use of interfacial bioorthogonal crosslinking to encapsulate LNCaP cells in HA microspheres. **a**. Live/dead staining of cells cultured in HA microspheres at day 1 and day 5. Live cells were stained green by Syto 13 and dead cells were stained red by propidium iodide. **b**. Cell proliferation analyzed by Trypan Blue exclusion showed a steady increase in cell number over 14 days of culture. *$p < 0.05$. **c**. Confocal image of an entire microsphere after live/dead staining showing individually dispersed LNCaP cells at day 2. **d**. Confocal image of an entire microsphere after live/dead staining showing the presence of dispersed tumoroids with aggregated cells at day 14. The insert shows a ~100 μm tumoroid strained for F-actin (green) and nuceli (blue) at day 14. All confocal images shown are maximum intensity projections of z-stacks. 110

Figure 2.8 A representative stopped-flow kinetic run for determining the second order rate constant for the reaction between **4** and **6** in H_2O. Linear correlation was found between time(s) and ln (A/A_0). 113

Figure 2.9 UV-vis spectra of aqueous solutions of (a) compound **4** at a concentration of 27.5 μM and (b) HA-Tz at a concentration of 0.153 g/L. In both measurements, a UV cuvette with a pathlength of 1 cm was used. 114

Figure 2.10 ^{1}H NMR spectrum of HA-Tz in D_2O. 115

Figure 2.11 Viscosity profile of 2 wt% HA (black) and HA-Tz (red) in PBS. 116

Figure 2.12 a-e) Color intensity plots of Figure 2.4b-f, respectively. 116

Figure 2.13 ^{1}H NMR spectrum of bis-TCO in $CDCl_3$. 117

Figure 2.14 ^{13}C NMR spectrum of bis-TCO in $CDCl_3$. 118

Figure 2.15 ^{1}H NMR spectrum of (4-(6-phenyl-1,2,4,5-tetrazin-3-yl)phenyl)methanol in DMSO-d_6. 119

Figure 2.16 ^{13}C NMR spectrum of (4-(6-phenyl-1,2,4,5-tetrazin-3-yl)phenyl)methanol in DMSO-d_6. 120

Figure 2.17 ^{1}H NMR spectrum of 4-nitrophenyl 4-(6-phenyl-1,2,4,5-tetrazin-3-yl)benzyl carbonate in $CDCl_3$ 121

Figure 2.18 ^{13}C NMR spectrum of 4-nitrophenyl 4-(6-phenyl-1,2,4,5-tetrazin-3-yl)benzyl carbonate in $CDCl_3$ 122

Figure 2.19 ^{1}H NMR spectrum of tetrazine-OEG-amine in $CDCl_3$. 123

Figure 2.20 ^{13}C NMR spectrum of tetrazine-OEG-amine in $CDCl_3$. 124

Figure 2.21 ^{1}H NMR spectrum of TCO-OEG-NHBoc in MeOD. 125

Figure 2.22 ^{13}C NMR spectrum of TCO-OEG-NHBoc in MeOD. 126

Figure 2.23 High resolution magic angle spinning (HR MAS) ^{1}H NMR spectrum of crosslinked HA-Tz/bis-TCO gels..... 127

Figure 2.24 LC-MS analysis of Alexa-TCO with Shimadzu LCMS-2020. (ESI negative mode, 60% ACN/H_2O) 128

Figure 2.25 HPLC analysis of Alexa-TCO with Shimadzu prominence HPLC with SPD-M20A diode array detector (5 min: 5% ACN/H_2O; 22 min: 100% ACN; 24 min: 100% ACN)..... 128

Figure 3.1 Fabrication of biomimetic hydrogels with a 3D core-shell pattern to provide spatial guidance cues to encapsulated hMSCs. (**A**) TCO-conjugated molecules diffuse across the crosslinked shell to react at the gel-liquid interface. (**B**) hMSCs adopt different morphologies depending their spatial localization within the matrix. 150

Figure 3.2 Synthetic toolbox for core-shell patterning. (**A**) Tetrazine-TCO ligation mechanism. (**B**) Hydrogel building blocks include tetrazine-modified HA (HA-Tz), non-degradable and MMP-degradable TCO crosslinkers (PEG-bisTCO and GIW-bisTCO) and monofunctional molecules (PEG-TCO, and RGD-TCO)..... 152

Figure 3.3 Covalent tagging of fluorescent dyes in a spatial core-shell pattern. (**A**) Confocal microscopy images of the hydrogel showing a distinct core-shell structure (central slice). (**B**) Intensity plot across the gel showing the presence of a sharp interface between the core and the shell regions..... 153

Figure 3.4 Characterization of hydrogel mechanical properties using a custom-built, micro-materials tester. (A) Schematic of the micro-materials tester used in this study. The hydrogel rested on the lower glass flat was compressed by a borosilicate plate. (B) Representative force-displacement curve demonstrating the top plate approach, contact with and compress the hydrogel. (C) Young's modulus of hydrogels prepared using different and mono- and bis-TCO derivatives. Hertzian model of parallel plate compression was used and Young's modulus was calculated assuming a Poisson ratio of 0.5. The crosslinking reservoir contained 0% or 25% monofunctional TCO capper. (D) Young's modulus of hydrogels formulated according to Table 1 and used for subsequent cell culture studies. * $p < 0.05$ 156

Figure 3.5 3D culture of hMSCs in homogeneous hydrogels prepared using either PEG-bisTCO (Gel A) or GIW- and RGD-TCO (Gel B). (A) Confocal images of 3D cultures stained by calcein AM (green) and ethidium homodimer (red) for live and dead cells, respectively, after 1, 4 and 7 days of culture. (B) Quantification of cell viability based on live/dead assay using ImageJ. (C) Confocal images of 3D cultures stained by F-actin (red) and DAPI (blue) after 1 and 7 days of culture. (D-G) Characterization of cell morphology by Feret diameter (D-E) and circularity (F-G) using ImageJ. (H) Higher magnification (40×) confocal images of hMSCs stained for DAPI (blue), F-actin (Red) and integrin β1 (green) after 7 days of culture. * $p < 0.05$. Scale bar = 100 μm. 158

Figure 3.6 (A) Force deformation curves for hydrogels crosslinked with either PEG-bisTCO or GIW-bisTCO. Modulus was altered by tuning the relative concentration of mono-functional capper, PEG-TCO. (B) Young's modulus of hydrogels crosslinked with either PEG-bisTCO or GIW-bisTCO. Modulus was altered by tuning the relative concentration of mono-functional capper, PEG-TCO. * $p < 0.05$. (C) Hydrogel degradation. HA-Tz was crosslinked by either PEG-bisTCO or GIW-bisTCO. Hydrogels were incubated with or without of collagenase type IV and the gel mass was measured every 30 min for 4 h. 160

Figure 3.7 3D culture of hMSCs in hydrogels with bioactive core-shell patterning. Cells grown in homogeneous gels (**A-B**), prepared using (**A**) PEG-bisTCO or (**B**) GIW-bisTCO and RGD-TCO (0.17 mM), were included for comparison purposes. Hydrogels with a core-shell pattern (**C, D, E**) were created following conditions outlined in Table 1. Construct in **C**, prepared using PEG-bisTCO and GIW-bisTCO/RGD-TCO had a blank shell (red) and a bioactive core (light blue). Construct in **D**, prepared using GIW-bisTCO/RGD-TCO with or without the PEG-TCO capper had a stiff shell (light blue) and a softer core (dark blue). Construct in **E**, prepared using GIW-bisTCO with low and high concentrations of RGD-TCO, had a stiffer, less adhesive shell and a softer, more adhesive core. Cultures were maintained for 7 days before staining and confocal imaging. Live and dead cells were stained green and red, respectively, F-actin and nuclei were stained red and blue, respectively. Scale bar = 200 μm. 161

Figure 3.8 UV-Vis spectra of aqueous solutions of Tz-hydrazide (A, 4.7 mM to 0.47 mM) and HA-Tz (C, 0.27mM). The extinction coefficient was determined from the standard curve with a linear regression (B). A UV cuvette with a pathlength of 1 cm was used. 167

Figure 3.9 Stopped flow results for reactions of Tz-hydrazide with PEG-TCO (**A**) or with PEG-dTCO (**B**). Red circles: raw data; Blue line: fitted curve. 168

Figure 3.10 ^{1}H NMR spectrum of Tz-hydrazide in methanol-d_4. 168

Figure 3.11 ^{13}C NMR spectrum of Tz-hydrazide in $CDCl_3$. 169

Figure 3.12 ^{1}H NMR spectrum of HA-Tz in D_2O. 170

Figure 3.13 ^{1}H NMR spectrum of PEG-bisTCO in $CDCl_3$. 171

Figure 3.14 ^{13}C NMR spectrum of PEG-bisTCO in $CDCl_3$ 172

Figure 3.15 UPLC-MS trace of PEG-bisTCO. 173

Figure 3.16 UPLC-MS spectrum of PEG-bisTCO. 174

Figure 3.17 HRMS spectrum of PEG-bisTCO. 175

Figure 3.18 UPLC-MS trace of the GIW peptide. 176

Figure 3.19 UPLC-MS spectrum of the GIW peptide. 177

Figure 3.20 HRMS of the GIW peptide. 178

Figure 3.21 UPLC-MS trace of GIW-bisTCO. 179

Figure 3.22 UPLC-MS spectrum of GIW-bisTCO. 180

Figure 3.23 HRMS spectrum of GIW-bisTCO. 181

Figure 3.24 ^{1}H NMR spectrum of PEG-TCO in $CDCl_3$ 182

Figure 3.25 ^{13}C NMR spectrum of PEG-TCO in $CDCl_3$ 183

Figure 3.26 UPLC-MS spectrum of PEG-TCO. 184

Figure 3.27 UPLC-MS spectrum of PEG-TCO. 185

Figure 3.28 HRMS spectrum of PEG-TCO. 186

Figure 3.29 ^{1}H NMR spectrum of PEG-dTCO in $CDCl_3$ 187

Figure 3.30 ^{13}C NMR spectrum of PEG-dTCO in $CDCl_3$ 188

Figure 3.31 UPLC-MS trace of PEG-dTCO. 189

Figure 3.32 UPLC-MS spectrum of PEG-dTCO. 190

Figure 3.33 HRMS spectrum of PEG-dTCO. 191

Figure 4.1 Light microscope images of encapsulated vascular cells within the hydrogel channels over 5 days of culture. (A-C) HAAE cells were injected into the lumen of the channel and attach to the inner surface while (D-F) vSMCs and (G-I) AoAFs are encapsulated within the hydrogel. Scale bar = 200 μm. 206

Figure 4.2 Confocal microscope images of encapsulated vascular cells within the hydrogel channels after 7 days of culture. (A-C) HAAE cells were injected into the lumen of the channel and attach to the inner surface while (D-F) vSMCs and (G-I) AoAFs are encapsulated within the hydrogel. Cells were Live/Dead stained with calcein AM (green) and ethidium homodimer (red). Scale bar = 200 μm. 207

Figure 4.3 Synthetic toolbox used for hydrogel channel formation and patterning. (A) Tetrazine-TCO ligation mechanism. Hydrogel building blocks including (B) Tetrazine-modified Hyaluronic Acid (HA-Tz), bisTCO crosslinkers either (C) non-degradable (PEG-bisTCO) or (D) MMP-degradable (GIW-bisTCO and VPM-bisTCO) and (E) cell adhesive peptide conjugate (RGD-TCO). (F) Spatially patterned hydrogel channels are prepared via interfacial crosslinking by perfusion of TCO conjugated molecules into the lumen of the channel with subsequent diffusion through the channel wall to create further crosslinking at the gel-liquid interface. 209

Figure 4.4 Mechanical properties of hydrogel channels. (A) Schematic for pressure-dilation experiments on hydrogel channels. The head tank is driven by a linear actuator in 2.54 mm increments. FEP tubing connects the head tank to one end of the PDMS chamber while the outlet is plugged. The chamber well is filled with HA-Tz and topped with a glass slide to prevent distortion effects from the fluid meniscus. A calibrated Dino-Lite camera is positioned over top of the channel to capture images of channel dilation during step changes in head pressure. (B) Images of hydrogel channels captured before and after applied pressure and thresholded areas of central 30% of channels used to quantify Young's modulus. (C) Average channel diameter and Young's modulus as a function of relative pressure over the range of 0-150 Pa. Young's modulus was calculated via best fit ($R^2 > 0.99$) of a stress-strain model for cylindrical pressure vessels with variable modulus and thickness to experimental data. The error bars represent standard deviation (n = 6)..... 213

Figure 4.5 Covalent patterning of TCO conjugated fluorophores. (A) The initial wall layer is formed with a crosslinking solution containing Clover-TCO (Green) followed by solutions of (B) Cy3-TCO (red) and (C) Cy5-TCO (blue). The formed channel is presented as a (D) end profile, (E) side profile and (F) tilted profile based on confocal z-stacks. (G) The gray value of the three layers. Scale bar = 200 μm..... 215

Figure 4.6 NIH3T3 fibroblast response to bioactive and blank patterened regions after (A) 7 days and (B) 28 days of culture. (C) The hydrogel channel was formed with inner and outer layers (blue) of PEG-bisTCO and Alexa-TCO while the middle (black) region is crosslinked with GIW-bisTCO and RGD-TCO. NIH3T3 were transfected with green fluorescent protein (Green) and stained with ethidium homodimer (Red). Scale bar = 200 μm..... 217

Figure 4.7 Cell Patterning. (A) NIH3T3 fibroblasts stained with Cell Tracker Red (Red) or Cell Tracker Green (Green) were patterned into the hydrogel channel. Sequentially altering of HA-Tz baths containing cell tracker red cells or green cells led to a red-green-red sandwich pattern shown as a confocal z-stack of (B) the channel and (C) the channel wall. Scale bar = 100 μm. 218

Figure 4.8 Vascular cell encapsulation and patterning. Vascular (A-D) endothelial (HAAE) were cultured on the inner lumen while (E-H) smooth muscle (vSMC) and (I-L) fibroblast (AoAF) cells were 3D encapsulated within the channel wall for 7 days. Cells were stained with (A-C,E-G,I-K) calcein AM (green) and ethidium homodimer (red) or (D,H,L) fixed and stained with DAPI (blue) and phalloidin (red). (M-P) The three cell types were stained with cell trackers and patterned into the channel with (M) the endothelial cells (blue) attached to the inner wall, (N) the smooth muscle cells (green) in the first layer of the wall and (O) the fibroblasts (red) in the outer layer of the wall. (P) The cells are shown in an end profile in their anatomical order. (A-C,E-G,I-K,M-P) Scale bar = 200 μm. (E,H,L) Scale bar = 50 μm. 221

Figure 4.9 UPLC-MS spectrum of VPM peptide. 224

Figure 4.10 UPLC-MS spectrum of VPM peptide. 225

Figure 4.11 UPLC-MS spectrum of VPM-bisTCO. 226

Figure 4.12 UPLC-MS spectrum of VPM-bisTCO. 227

ABSTRACT

Tetrazine ligation, the cycloaddition of *s*-tetrazine (Tz) with *trans*-cyclooctene (TCO) derivatives, is particularly attractive for the synthesis of cell-instructive hydrogel matrices. This reaction is high yielding, does not require a catalyst, does not produce any toxic side products, and is the fastest bioorthogonal reaction ($>10^6$ $M^{-1}s^{-1}$ faster). Using tetrazine-modified hyaluronic acid (HA-Tz) and polyethylene glycol (PEG) flanked with TCO (bisTCO), the formation of hydrogel spheres via a diffusion-controlled process at the gel-liquid interface was demonstrated. Syringe delivery of HA-Tz into a reservoir of bisTCO resulted in the instantaneous formation of a crosslinked shell, through which bisTCO diffused inwards to introduce further crosslinking. Prostate cancer LNCaP cells were encapsulated in the hydrogel spheres with high viability, proliferated readily in the HA matrix and formed 3D, tissue-like cell aggregates.

The interfacial diffusion-controlled process has also permitted the creation of hydrogel spheres with pre-determined spatial distribution of TCO-tagged biomolecules. Through temporally controlled introduction of TCO conjugates during the crosslinking process, the enzymatic degradability, cell adhesivity, and mechanical properties of the synthetic microenvironment was tuned with spatial precision. Using human mesenchymal stem cells (hMSCs) and hydrogels with a core-shell structure, the ability of the synthetic ECM with spatially defined guidance cues to modulate cell morphology in a biomimetic fashion was demonstrated.

Introduction of aqueous solutions of bisTCO to a reservoir of HA-Tz led to the fabrication of liquid-filled hydrogel channels of desired lengths. An instantaneous covalently-crosslinked channel wall formed at the interface between the two aqueous solutions. bisTCO molecules diffuse through the crosslinked wall, reacting with the HA-Tz at the gel-liquid interface and subsequently growing the channel wall outward until fully exhausted. This interfacial, diffusion controlled crosslinking enabled the creation of 3D spatial patterns of ligands and other biomolecules to modulate the biochemical environment within the hydrogel channel walls via perfusion of TCO conjugates into the lumen of the channel at predetermined times. This chemistry also permitted the 3D spatial patterning of different cell populations by systematically alternating cell laden HA-Tz reservoirs during crosslinking. Vascular endothelial cells, smooth muscle cells and adventitial fibroblasts were spatially patterned into the hydrogel channels in anatomical order with high viability.

Tetrazine ligation is suitable for the construction of crosslinked tissue-mimetic hydrogel networks with 3D spatial patterns without the necessity of external triggers or templates. The novel bioorthogonal, interfacial, diffusion-driven crosslinking was utilized to fabricate hydrogels with 3D spatial patterns of biochemical and biomechanical signals which can be employed to study tissue with layered structures or interfaces between tissue. Liquid-filled hydrogel channels with spatial patterns of biomolecules and different cell populations will enable the construction of complex, physiologically relevant *in vitro* vasculature models.

Chapter 1

INTRODUCTION

1.1 Overview

Considerable research efforts have been made over the past decades in the fields of Biomaterials and Tissue engineering for tissue repair and regeneration. When designing a biomaterial for damaged tissue repair, material properties, including matrix stiffness and composition, must be considered. Hydrogels or fibrous scaffolds are an attractive option to serve as tissue-mimetic biomaterials due to their tunability. Hydrogels can be made of synthetic materials, such as poly(ethylene glycol) (PEG), or of naturally occurring materials such as Hyaluronic Acid (HA). While PEG provides a 'blank slate' for facile engineering of the material properties, it is not native to cells. In comparion, HA, which is found ubiquitously throughout the extracellular matrix, is recognized by cells through cell surface receptors, CD44 and RHAMM.

In order to make a viable biomaterial, crosslinking chemistry must be cytocompatible. One promising set of reactions for crosslinking are bioorthogonal reactions. Bioorthogonal is the coupling of two biomolecules in a covalent linkage which can occur inside living systems without interfering with native biochemical processes. These reactions proceed with fast kinetics, are compatible in aqueous conditions at ambient temperatures, and do not have toxic reagents, catalysts or byproducts. These rapid and bioorthogonal reactions, which are desirable for the construction of complex, three-dimensional (3D) tissue models, are reviewed below.

1.2 Modular and Orthogonal Synthesis of Hybrid Polymers and Networks

Nature combined relatively simple building blocks in a modular and repetitive fashion to construct biological materials with complex organizations and diverse functions.[1] Many types of cells present multiple copies of glycans in branched structures on the cell surface that contribute to the concerted interactions with the binding partners in cell signaling.[2,3] Many proteins in the natural extracellular matrix (ECM) contain repetitive motifs linked together in a modular and tandem fashion with spatial periodicity, conferring structural and biological roles and maintaining intimate interactions with cell surface receptors.[1,4–7] The ECM of different types of tissues has variable composition and compliance depending on how the modular components are combined and integrated.[1] In order to foster desired cellular behaviors for tissue growth and morphogenesis, tissue specific microenvironments must be recreated *in vitro*. However, a complete replication and reconstitution of the natural proteins and ECMs is technically daunting and economically unrealistic. An attractive alternative is the hybridization of synthetic polymers with molecules of biological origin that are synthetically tractable and can be readily manipulated. Overall, rational combination of judiciously selected synthetic and biological building blocks has resulted in hybrid systems with enhanced biological functions and improved materials properties. The hybrid materials can be engineered to mimic the natural proteins[8] in terms of their molecular architectures, dynamic responsiveness and cell-instructive properties, with the added attributes of tunability and processibility provided by the synthetic polymer constituents.[9–11]

Over the past decade, significant advancement has been made in the development of customized and biomimetic materials using modular building blocks and employing bioorthogonal reactions.[12] Covalent integration of modular building

blocks with distinct chemical compositions and diverse functionality has resulted in advanced materials with synergistically enhanced properties.[13] These developments, originally inspired by biological design principles, have been fueled by recent advances in polymer chemistry and biomaterials science,[14] and most significantly by repurposing of efficient organic reactions.[15] Bioorthogonal chemistry[16] refers to chemical transformations that occur between a pair of molecules with mutually reactive functional groups without significant interference from co-existing functionalities in physiological biological milieu. Additional features of bioorthogonal chemistry include biocompatibility, specificity, high yield and fast reaction kinetics.[17,18] Examples include (Table 1.1) the hydrazone/oxime chemistry.[19,20] Michael addition,[21] radical mediated thiol-ene (or thiol-yne) chemistry,[22,23] Diels–Alder reactions,[24,25] copper-catalyzed alkyne-azide cycloaddition (CuAAC, popularly known as the "click" reaction),[26] strain-promoted azide-alkyne cycloaddition (SPAAC)[27,28] and inverse electron demand Diels-Alder reaction (sometimes referred to as the tetrazine ligation).[29–31] The reaction rate can be tuned through changes in structure.

Bioorthogonal chemistry is being exploited by the biomaterials community for efficient and modular fabrication of bioactive and cell-instructive materials. Summarized in this section is recent progress in the development of hybrid and biomimetic materials constructed by covalent coupling of discrete modular building blocks. The building blocks include synthetic polymer, peptide, protein, carbohydrate or polysaccharide. I discuss the materials properties, in the context of their interactions with mammalian cells, as a consequence of the modular coupling of diverse building blocks. I will offer some examples of biomedical application of the modular

constructs. Topics covered in this review are summarized in Figure 1.1. Overall, the modular approaches, enabled by powerful reactions, aid in the efficient fabrication of materials with controlled complexity from the bottom up in a plug-and-play fashion. The resultant materials exhibit collective properties that exceed the simple sum of the individual constituents and are readily adaptable to the individual pathology.

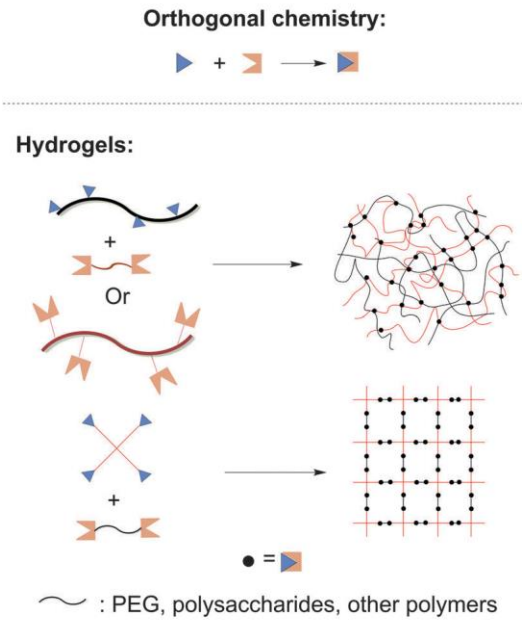

Figure 1.1 Schematic summary of biomaterials synthesized using modular approaches employing orthogonal chemistry. Reproduced by permission of The Royal Society of Chemistry.

1.2.1 Synthetic Strategies

Table 1.1 Classic orthogonal reactions used in synthesis of biomaterials. Reproduced by permission of The Royal Society of Chemistry.

Orthogonal reactions
Hydrazone ligation: 
Oxime ligation: 
Thiol–Michael addition: 
Thiol–ene chemistry: 
Diels–Alder reaction: 
Copper-catalyzed alyne–azide cycloaddition (CuAAC): 
Strain-promoted azide–alkyne cycloaddition (SPAAC): 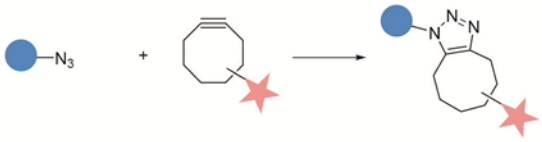
Tetrazine ligation: 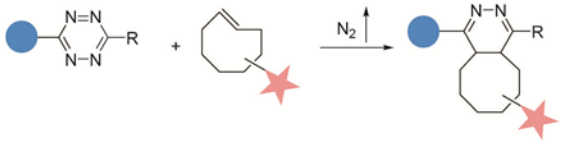
Staudinger ligation: 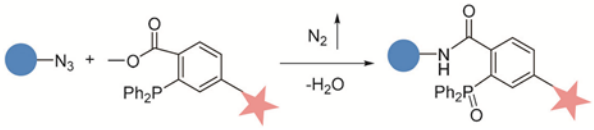

Popular bioorthogonal reactions utilized for biomaterials synthesis can be roughly divided into three categories (Table 1.1): (1) carbonyl-based condensation

reactions; (2) addition reactions through alkenes/ynes and (3) cycloaddition reactions. The reaction of aldehyde or ketone with hydrazine or aminooxy derivatives results in hydrazone or oxime bonds with water being the only by-product.[32] This reaction is chemoselective and can be carried out under aqueous conditions without interference from functionalities found in biomolecules and cells, thus widely exploited for bioconjugation purposes. Oxime/hydrazone condensations are relatively slow at low substrate concentrations. The reaction can be accelerated by lowering the pH or by nucleophilic catalysis using aniline through rapid transimination.[33] Using carefully chosen carbonyl and hydrazine substrates, hydrazone formation can be rapid at biological pH even in the absence of a catalyst.[34] Rate constants for the fastest carbonyl/hydrazine combinations are 2−20 $M^{-1}s^{-1}$. Alternatively, dialdehydes can react with O-alkylhydroxylamines at rates of 500 $M^{-1}s^{-1}$ at neutral pH values in the absence of catalysts through an unusually stable cyclic intermediate, which ultimately undergoes dehydration to yield an oxime.[35] Although hydrolytically more stable than the imine counterparts, hydrazone/oxime linkages are still susceptible to hydrolysis, especially under acidic conditions, reversing back to the starting hydrazide or hydroxyamines. Of note, the rate constant for the acid-catalyzed hydrolysis of the oxime was nearly 10^3-fold lower than those for simple hydrazones.[36]

Molecules containing alkene functionality can participate in multiple types of bioconjugation reactions, including Michael addition with heteroatomic donors and radical-based thiol-ene reaction. Although Michael addition involves the addition of a nucleophile, such as enolates, amines and thiols, to an activated electrophilic olefin,[21] the reaction is fastest when thiols are used as Michael donors. Acrylates, vinyl sulfones, or maleimides are frequently used as Michael acceptors and under these

conditions, thiolate anion is the active species,[37] thus the reaction rates increase with pH.[17,32] Although thiol/maleimide reaction is fast, the resultant adduct can be labile or exchangeable under physiologically relevant conditions.[38]

In the presence of thiol-containing molecules, alkenes can also react with thiyl radicals, frequently generated under light irradiation in the presence of photoinitiators, to form thio-ether linkage.[22,39,40] The physicochemical nature of the reaction enables the direct manipulation of materials properties in both space and time through the controlled application of light. Generally speaking, the conversion rate of the thiol–alkene reaction is directly related to the electron density on the alkene, with electron-rich alkenes being consumed much more quickly than electron-poor alkenes. Electron-rich alkenes, such as (meth)acrylates undergo rapid homopolymerization under thiol-ene conditions. Highly substituted alkenes are less reactive than singly substituted alkenes and for rapid reactions involving multifunctional alkenes as alkene groups must be located at terminal positions. In addition, thiols based on mercaptopropionate esters and glycolate esters react more quickly than simple alkyl thiols. [22,39,41] Thiyl radicals can also add to triple bonds and a single alkyne unit can accommodate the addition of two thiol species in the single "two-step" conjugation reaction.[42] Unlike radical polymerization, thiol-ene photocoupling reaction is insensitive to O_2 inhibition and can tolerate other functional groups. Native cysteine and amine residues can complete with the desired thiols.

The [4+2] cycloaddition between an electron-rich diene and an electron-deficient dienophile, known as the Diels-Alder (DA) reaction,[24] is highly selective and proceeds at high yield without any catalyst.[43] Electron-withdrawing substituents on the alkene and the electron-donating groups on the diene are important for

increasing reaction rates. The reaction can be greatly accelerated in water due to increased hydrophobic effects. Retro-DA reaction occurs at an elevated temperature, producing the original diene and dienophile.[44,45]

The CuAAC reaction generally proceeds with quantitative yield and complete specificity in the presence of a wide variety of other functional groups.[17,26] The reaction rate is dependent on the concentration of Cu^{I} and can be accelerated by heat,[46] tailored ligands,[47] and microwave irradiation.[48] In the presence of 20–500 μM Cu^{I}, the second-order rate constants were found in the range of 10-200 $M^{-1}s^{-1}$.[49] Various ligands have been designed to stabilize Cu^{I} and to increase its catalytic efficiency.[50–52] Work from the Ting group shows that[53] copper-chelating azides undergo much faster reactions than non-chelating azides under a variety of biocompatible conditions. This kinetic enhancement increased CuAAC detection of alkyne-modified proteins allowed for site-specific protein labeling to be performed on the surface of living cells with only 10–40 μM Cu^{I}/Cu^{II}.[53,54] The toxicity concerns of CuAAC arise from Cu^{I}-promoted generation of reactive oxygen species[55] and the electrophilic properties of oxidized ascorbate (when used as reducing agent).[56]

Bertozzi and coworkers developed a Cu-free variant of CuAAC chemistry by promoting ring strain using cyclooctynes.[27,57] The reactivity of the cyclooctyne can be modulated by appending electron withdrawing groups at the propargylic position or by augmentation of strain energy through aryl ring or cyclopropyl ring fusion[28,58] Nitrones, nitrile oxides, diazoalkanes and syndones have been used as alternative 1,3-dipoles. Limitations of SPAAC include modest kinetics, hydrophobicity of the cyclooctyne component and instability of fast reacting cyclooctynes under physiological conditions.[47,58]

The tetrazine ligation is an inverse electron demand D-A reaction that proceeds with unusually fast rates.[59] This reaction involves the cycloaddition of *s*-tetrazine with *trans*-cyclooctene (TCO) derivatives, with N_2 being the only by-product.[60] Such reactions are high yielding, do not require a catalyst, do not produce any toxic side products, and are more than three orders of magnitude faster than pre-existing methods for bioorthogonal ligation. Increasing the strain in TCO by cycloproyl fusion led to the discovery of the fastest bioorthogonal reaction reported to date (second-order rate constant up to $3.3 \times 10^6\ M^{-1}s^{-1}$ in H_2O at room temperature). Various TCO derivatives exhibit reactivity towards tetrazine spanning 8 orders of magnitude.[31,61,62] Other complementary dienophiles (e.g. norbornene,[63] cyclopropenes,[18,64–69] cyclooctynes[62,70,71] and terminal alkenes[72]) have been utilized for tetrazine ligation, but at a significantly lower rates than TCO derivatives. Owing to its ability to create bonds rapidly in high yield and at low concentrations, tetrazine ligation has become an enabling tool for a host of biomedical applications,[29–31,68,73,74] as well as biomaterials synthesis and fabrication.[30,75–78]

Other reactions, such as Staudinger ligation[79,80] and native chemical ligation,[81] are useful in bioconjugation, but have not been widely employed in biomaterials synthesis. Staudinger ligation refers to the amide bond formation between an azide and a phosphine derivative containing a neighboring electrophilic group. In native chemical ligation, a peptide having a C-terminal thioester reacts with an N-terminal cysteine residue in another peptide to undergo a transthioesterification reaction, resulting in the formation of the neighboring α-amine group on cysteine. A subsequent nucleophilic attack of the electron-rich nitrogen in the ester carbonyl

results in an S-N shift, forming a native amide bond. Both reactions proceed at physiological pH under mild conditions without any additional additives.

Reactions described above require two components. Century-old multicomponent reactions, such as the Biginelli reaction and the Ugi reaction,[82,83] have also been explored for biomaterials synthesis where three or more building blocks are rapidly and almost quantitatively combined.[84] Although these reactions are useful in recombinatorial chemistry and polymer synthesis, the abundance of amines and carboxylic acids in the biological environment limits their utility in 3D cell cultures. Enzyme-catalyzed reactions require very specific substrates and proceed with high efficiency and minimal toxicity, thus it is orthogonal and specific.[85] For example, transglutaminase (also known as Factor XIII), when activated by thrombin and Ca^{2+} to factor XIIIa during the blood coagulation cascade, is capable of catalyzing covalent crosslinks between the ε-amine group of lysine side chains and the γ-glutamyl side chain of glutamine residues.

1.2.2 Modular synthesis of hybrid hydrogel networks

Orthogonal coupling of multifunctional building blocks with complementary reactivity in a step-wise fashion beyond the gel point gives rise to crosslinked networks with tissue-like properties. Compared to networks synthesized by convention reactions, bioorthogonally constructed hydrogels are theoretically more homogeneous, exhibit less interference from other functionalities and are more biocompatible to cells and biomacromolecules. Because the reaction rate can be readily adjusted, gelation kinetics and consequently network properties can be easily manipulated. Using biocompatible polymers and bioactive peptides/proteins as the modular building blocks and employing bioorthogonal reactions, various groups are working on the

development of cell-instructive synthetic ECM to interrogate complex processes of tissue formation and regeneration.[86]

Covalent hydrogel networks are not necessarily static.[87] Overtime, the soluble polymers entrapped in the network can slowly diffuse out. If chemically or enzymatically degradable linkages are present in the network, hydrogels will erode and become softer as a result of matrix degradation.[88–90] Certain reactions are reversible; thus hydrogels prepared with these reactions can be dynamic or erodible.[91] If responsive signals or motifs are incorporated, hydrogel properties can be altered in response to a specific signal input.[86,92–96] Bioorthogonal reactions are uniquely suitable for time-dependent modulation of hydrogel properties.[97] For example, hydrogels could become stiffened or softened overtime, or could present or erase a biological signal post-gelation in the presence of cells. A cytocompatible covalent adaptable hydrogel capable of mimicking the modulus and stress relaxation properties of many complex biological tissues might be conducive to cell growth.

In this section, we highlight the synthesis of hydrogels using modular building blocks and employing step growth orthogonal coupling. Owing to its cytocompatible and bio-inert nature, PEG is widely employed for the preparation of hydrogel networks, thereby serving as a blank slate for the incorporation of bioactive signals. Because PEG does not contain abundant functional groups along the polymer backbone, frequently 4 and 8-armed PEG are used. To overcome these limitations, anionic copolymerization of ethylene oxide with glycidyl ether derivatives afforded PEG based copolymers with diverse backbone functionality.[98–100] Alternatively, hyperbranched poly(glycerol) (hPG) was used in place of PEG.[101] Hyaluronic acid (HA) is a linear polysaccharide with disaccharide repeats of D-glucuronic acid and N-

acetyl-D-glucosamine. Unlike PEG, HA is abundantly expressed in the natural ECM, interacting with various proteins or proteoglycans to organize the ECM, to activate various signaling pathways, to maintain tissue homeostasis and to facilitate tumor metastasis.[102,103] Biomimetic synthetic extracellular matrices have been produced using HA derivatives carrying orthogonal functional groups in combination with synthetic polymers or peptides.[104,105] Finally, a new class of de novo saccharide-peptide copolymers has been used in the synthesis of hybrid hydrogels.[106–111]

1.2.2.1 Hydrogels synthesized by oxime/hydrazone chemistry.

We have synthesized HA-based hydrogels[112] employing hydrazone ligation using hydrazide-modified HA (HA-ADH) and an HA derivative carrying aldehyde groups (HA-ALD). The orthogonal nature of the hydrazone chemistry, combined with the rapid gelation kinetics, permits in situ cell encapsulation and subsequent 3D culture for the creation of physiologically relevant prostate cancer models.[113–115] The hydrazone ligation permits facile incorporation of therapeutic molecules for local release purposes.[112] Structural proteins can also be integrated in the network without compromising their assembly properties and bioactivities.[116] The same hydrazone chemistry, when restricted in the inverse emulsion droplets resulted in nanoporous HA microgels.[117] The resultant microgels contain reactive handles that can be used for bioconjugation[118] or crosslinking purposes.[117,119] Simple mixing of these functional microgels with an aqeuous solution of HA-ADH, HA-ALD or PEG-dialdehyde results in a hierachically structured, elastic hydrogel within 5 minutes. This type of network contains highly crosslinked HA microgels in a loosely crosslinked secondary HA network. The viscoelastic properties of the matrix can be readily modulated by varying the particle size, surface functional group, inter-particle and intra-particle

crosslinking.[120] When appropriately functionalized with collagen like polypeptide[121] or gelatin,[122] the HA doubly crosslinked networks(DXNs) facilitate integrin mediated attachment of MSCs and matrix mediated osteogenic differentiation. Separately, Patenaude and Hoare applied the same chemistry to the preparation of injectable HA/poly(N-isopropylacrylamide) hydrogels.[123]

The reversible nature of the hydrazone chemistry, combined with the tunability of the reaction kinetics, has led to the discovery of novel hydrogel properties. Hydrolysis of the hydrazone linkage recreates the respective hydrazide and aldehyde groups. If respective partners are located in close proximity, local network integrity can be restored via the reformation of new hydrazone bonds.[124] Hydrazone-based hydrogel networks are reported to be dynamically adaptable and self-healing. McKinnon et al.[125] described PEG hydrogels formed through the ligation of an aliphatic hydrazine-terminated multiarm PEG macromer with aldehyde-terminated multi-arm PEG macromer. Rapid gelation occurred under physiological conditions via the formation of bis-aliphatic hydrazone bond without the need for analine catalysis and not surprisingly, the hydrolysis rate is pH-dependent. The modular nature of hydrogel construction and the large number of easily tuned variables provide access to gels with a wide range of modulus and stress relaxation characteristics. These covalently adaptable hydrogels, when incorporated with RGD, also through hydrazone bonds, allow for the development of physiologically relevant morphologies for mouse myoblasts, whereas static, non-adaptable gels prevent cytoskeletal rearrangement and extension. Taken together, these studies show that hydrazone linked hydrogels offer unique advantages in terms of dynamic tunability and should serve as a valuable complement to existing hydrogel technologies.[126]

1.2.2.2 Hydrogels synthesized by Michael addition or thiol-ene chemistry.

Michael-type additions are versatile reactions for the formation of hydrogel networks. Frequently, acrylate, maleimide or acrylamide-based double bonds are used. Cross-reaction with native proteins is not an issue since most cysteine thiols in proteins exist in the oxidized S-S form and lysine amines react with these alkenes at a much lower rate. Using thiolated HA (HA-SH), prepared using a dihydrazide reagent containing an internal disulfide bond[127–129] synthetic ECM have been developed using PEG diacrylate (PEGDA) as the Michael donor.[104,130] When thiol is used in a stoichiometic excess to acrylate, the fast Michael addition reaction contributes to the initial network formation and the slow disulfide bond formation gradually increases gel stiffness.[131,132] Depending on the molecular weight of HA and PEG, percent functional group incorporation in HA, concentrations of HA and PEG and thiol/acrylate ratio, hydrogels with elastic modulus varying from 11 Pa to 3500 Pa have been prepared.[133] Co-crosslinking thiolated HA with other thiolated biomacromolecules (heparin or gelatin) creates a more complex network containing immobilized biological cues for growth factor sequestration or for integrin engagement.[134] This type of hydrogel system has been commercialized and widely used in cell therapy, growth factor delivery and the regeneration of healthy bladder, bone, cartilage, sinus, spinal cord and vocal fold tissues and the creation of disease models.[104]

Although the incorporation of thiolated gelatin in HA gels facilitates the attachment and spreading of fibroblasts on the hydrogel surface, cells remain circular inside the gel in 3D.[135] In order for cells of mesenchymal origin to spread in 3D hydrogel networks, both matrix metalloproteinase (MMP) degradable crosslinker and RGD signals must be incorporated and cell spreading is more significant in gels with

higher RGD density.[136] These observations reconfirm the early observations from the Hubbell group on vinyl sulfone-terminated multiarm PEG macromers and a cysteine-terminated MMP substrate as the crosslinkers that both RGD and MMP signals for 3D attachment and migration of cells of mesenchymal origin.

The hydrolysis of the ester linkages at the crosslinking points in the above HA/PEG gels may compromise the overall gel stability and complicate the interpretation of cellular enzymatic processes. To improve the hydrolytic stability of HA gels, acrylate groups were introduced to HA via an amide linkage (HA-AM). Thus, HA gels are formed within 30 minutes of mixing of HA-SH and HA-AM and slow gel stiffening occurs overnight, reaching a plateau modulus of 234±30 Pa.

The reaction permits direct encapsulation of prostate cancer cells as well as HA microgels containing sequestered growth factors.[137] Prostate cancer cells entrapped in HA matrices formed distinct multicellular aggregates which grew and merged to form spherical aggregates, expressing E-cadherin, and showing cortical organization of F-actin. Compared to 2D-cultured cells, the engineered tumoroids increased the expression of pro-angiogenic factors and multidrug resistant proteins. The engineered models were utilized to assess the treatment efficacy of nanoparticle-based drug delivery systems.[115,137,138]

Guan and coworkers synthesized copolymers containing peptide-saccharide along the backbone.[111] Chemically crosslinked hydrogels were prepared via Michael addition by mixing hybrid polymers with cysteine or vinyl sulfone groups. Intriguingly, variation of a single amino acid (valine (V), cysteine (C), tyrosine (Y)) in the polymer backbone has profound effects on the gel properties and the behaviors of

encapsulated chondrocytes.[106] The synthetic saccharide/peptide hydrogels have also proven useful for islet transplantation.[108]

Micrometer-sized hydrogel particles containing living cells were fabricated with an exquisite control through the use of droplet-based microfluidics and PEG and hyperbranched polyglycerol (hPG). Gelation was achieved via the nucleophilic Michael addition of dithiolated PEG macro-cross-linkers to acrylated hPG building blocks. Microgel properties were varied through the use of PEG linkers with different molecular weights along with different concentrations of macromonomers. Fibroblasts and lymphoblasts were successfully encapsulated in the microgel with high viability.[139]

Thiol-ene photochemistry has been extensively explored for hydrogel synthesis because this photoinitiated polymerization occurs at neutral pH and can be controlled both spatially and temporally.[140] Proteins and cells have been entrapped in these gels for the controlled release of protein therapeutics and 3D culture purposes. For example, the bioactivity of lysozyme was maintained above 90% following the exposure to thiol-ene photopolymerization conditions.[141] Bovine chondrocytes were encapsulated in a similar gel with high viability and synthesized ECM resembling that of a hylain cartilage. Contrarily, when encapsulated in a radically crosslinked gel, lysozyme exhibit a compromised activity (50%) and chondrocytes adopt a hypertrophic phenotype, thus pointing to the advantages of step growth mechanism for hydrogen preparation.[142]

Cell-adhesive, MMP-degradable PEG hydrogels were prepared using thiol-ene photopolymerization. MSCs entrapped in the resultant matrices undergo classical trilineage differentiation in the presence of differentiation media. Pancreatic ductal

epithelial cells (transformed cell line) formed ductal cyst-like structures in 3D and cellular aggregation was dependent on the immobilized laminin-derived peptide signals as well as MMP-mediated matrix degradation.[143,144] Similarly, norbornene-functionalized HA (HA-Norb) was combined with di-thiols to create non-toxic hydrogels with a wide range of mechanical properties. By limiting the initial extent of crosslinking, HA-Norb gels were synthesized with remaining pendent norbornene groups that could be reacted with thiol containing molecules in the presence of light and an initiator, including with spatial control. Secondary reactions with a di-thiol crosslinker changed mechanical properties, whereas reaction with mono-thiol peptides had no influence on the gel elastic modulus. This orthogonal chemistry was used sequentially to pattern multiple peptides into a single hydrogel, demonstrating the robustness of this system for the formation of complex hydrogels.[145]

Application of thiol-ene chemistry in a confined space or at an interface has resulted in the production of microgels or multilayered hydrogels. For example, taking advantages of the ability of eosin-Y to generate radicals upon visible light exposure and its high diffusivity, hydrogels with multilayer structures were prepared by step growth thiol-ene photochemical reactions. The initial light exposure resulted in the formation of the core hydrogels, through which the residual eosin-Y diffuses outwards to initiate further crosslinking. The thickness of the thiol-ene gel coating could be easily controlled by adjusting visible light exposure time, eosin-Y concentration initially loaded in the core gel, or macromer concentration in the coating solution.[146]

1.2.2.3 Hydrogels synthesized by cycloaddition reactions

Diels–Alder click reaction was applied to the synthesis of HA hydrogels by reacting furan-modified HA with bis-maleimide-PEG. Biomolecules were

photopatterned into the hydrogel by two-photon laser processing, resulting in spatially defined growth factor gradients. The Young's modulus was controlled by either changing the hydrogel concentration or the furan substitution on the HA backbone, thereby decoupling the hydrogel concentration from mechanical properties. Porosity was prepared by cryogelation, and the addition of galactose further influenced the porosity, pore size, and Young's modulus of the cryogels. These HA-based hydrogels offer a tunable platform with a diversity of properties for directing cell function, with applications in tissue engineering and regenerative medicine.[147]

CuAAC has been applied to hydrogel synthesis as early as 2006.[148] The goal was to make a more perfect hydrogel network with robust mechanical properties. However, an efficient chemistry does not guarantee perfect networks. In fact, carbon black additive has to be incorporated in the gel to improve the mechanical properties. CuAAC of tetrakis(2-propynyloxymethyl)-methane (TMOP), diazide end-functionalized triblock copolymers of poly(β-caprolactone) with PEG (N_3-PCL-PEG-PCL-N_3) afforded amphiphilic co-networks whose properties can be tuned by varying the hydrophilic/hydrophobic ratio. Both hydrophilic and hydrophobic drugs can be encapsulated in the resultant networks and the drug release is attributable to the well-defined molecular structure and tunable hydrophobic/hydrophilic composition of the hydrogels.[149]

The toxicity issues associated with Cu motivated researchers to explore the utility of other orthogonal reactions for hydrogel synthesis. For example, the inverse-electron-demand D-A reaction between norbornene and tetrazine has been utilized for gelation purposes. Mixing of multifunctional PEG-tetrazine macromer with a dinorbornene peptide resulted in hydrogel formation within minutes. MSCs were

encapsulated in such gels with high post-encapsulation viability. The specificity of the tetrazine norbornene reaction allows for sequential modification of the network via thiol-ene photochemistry.[76] pH-Cleavable cell-laden microgels were fabricated in microfluidic channels by SPAAC employing PEG dicyclooctyne and dendritic poly(glycerol) displaying azide groups through an acid-labile benzacetal linker. Cells were encapsulated in the microgel with a high viability and were subsequently selectively released by varying the pH without compromising the overall cell viability and cell spreading. The capture and release microgel platform allows cells to be studied and manipulated during the encapsulation and then be isolated and harvested by decomposition of the microgel scaffolds.[150]

1.2.2.4 Hydrogels synthesized by other orthogonal reactions

Other orthogonal reactions are less explored for hydrogel synthesis due to the complication in synthesis and/or slow kinetics. Staudinger ligation has been explored for the covalent stablization of ionically crosslinked alginate hydrogels using azide functionalized alginate and 1-methyl-2-diphenylphosphinoterephthalate-terminated, telechelic PEG.[151] Native chemical ligation has been explored to create covalently crosslinked hydrogels using macromonomers of four-armed PEG with either thioester or N-terminal cysteine peptides[152] A similar strategy has been applied to prepare anti-inflammatory hydrogels supporting islet cell survival in the presence of diffusible pro-inflammatory cytokines[153,154]

Enzyme-catalyzed reactions, although highly specific and naturally biocompatible, are underexplored for the synthesis of bioactive hydrogels. Ehrbar et al. used activated coagulation transglutaminase factor XIIIa (FXIIIa) for gelation and site-specific coupling of cell adhesion ligands and engineered growth factor proteins to

PEG-based proteolytically degradable hydrogels. Primary stromal cells can invade and proteolytically remodel these networks both in an *in vitro* and *in vivo* setting. These hybrid networks can potentially serve as alternatives for fibrin as provisional drug delivery platforms in tissue engineering.[155] Using a photocaged FXIIIa substrate, Mosiewicz et al. created PEG-based hydrogels with masked peptide. Subsequent laser-scanning lithography afforded highly localized biomolecule tethering. This approach for the 3D manipulation of cells within gels should open up avenues for the study and manipulation of cell signaling.[156]

Mosiewicz et al.[157] employed phosphopantetheinyl transferase (PPTase) to catalyze covalent cross-linking of PEG-based hydrogels. Gels were formed within minutes under physiological conditions by mixing two aqueous precursors containing multiarm PEG macromers end-functionalized with the PPTase substrate Coenzyme A (CoA) and a genetically engineered dimer of a carrier protein. Bioactive hydrogels were produced by covalent incorporation of a CoA-functionalized cell adhesion peptide (RGDS), resulting in specific adhesion of primary fibroblasts on the hydrogel surfaces. 3D encapsulation of cells resulted in high cell viability (ca. 95%) and single cell migration over long distances within RGDS-modified gels. In general, enzyme-catalyzed gelation reactions usually result in heterogeneous hydrogels with low mechanical strength due to the low conversion imposed by the inability of enzymes to diffuse readily during the gelation process.[158]

1.2.2.5 Manipulation of hydrogel properties using multiple reactions

Bioorthogonal reactions are frequently combined to generate complex hydrogels with dynamic properties. In some cases, certain functional groups participate in multiple types of reactions, some of which may not necessarily be

orthogonal in nature. In other cases, two independent reactions are used to sculpt the hydrogels. Burdick and coworkers devised a step-wise approach to fabricate hydrogels that stiffen over time in the presence of cells. The initial network was established by Michael addition between thiol and methacrylate or maleimide and the additional crosslinking was achieved by radical chain polymerization. Time dependent gel stiffening was found to selectively differentiate MSCs,[159] which is directed by the generation of degradation-mediated cellular traction independently of cell morphology or matrix mechanics. Moreover, switching the permissive hydrogel to a restrictive state through delayed secondary crosslinking reduced further hydrogel degradation, suppressed traction, and caused a switch from osteogenesis to adipogenesis in the absence of changes to the extended cellular morphology.[160]

Photoinitiated thiol-ene chemistry is frequently combined with other orthogonal reactions for light-directed spatial patterning purposes in the presence or absence of cells. For example, thiol-ene photochemistry was combined with aniline-catalyzed oxime ligation or CuAAC for 3D patterning of peptides in PEG gels post gelation.[161] Using copper-free click chemistry, DeForest et al. directly encapsulated cells in PEG-based hydrogels. Subsequently, thiol–ene photocoupling chemistry is introduced that enables patterning of biological functionalities within the gel in real time and with micrometer-scale resolution. This material system enables us to tailor independently the biophysical and biochemical properties of the cell culture microenvironments *in situ*.[97] This synthetic approach uniquely allows for the direct fabrication of biologically functionalized gels with ideal structures that can be photopatterned, and all in the presence of cells.

1.2.3 Conclusion and perspective

Discussed in this section is modular approaches for the synthesis of hybrid polymeric biomaterials using diverse building blocks and employing orthogonal reactions. These highly efficient and selective reactions have enabled facile control over the composition, structure and properties of polymeric biomaterials, considerably expanding the design options. Bioorthogonal chemistry is particularly attractive for the fabrication of hydrogels in the presence of living cells to produce biologically relevant 3D constructs with desired mechanical properties and spatial presentation of biological signals. Proteins can also be entrapped in the matrix with high bioactivity and be released in a controlled manner. Light-triggerable reactions and diffusion controlled ligation mechanism are particularly attractive for spatial patterning purposes.

Although orthogonal reactions have become an enabling technology for the synthesis of hybrid biomaterials, it is important to note that a "good chemistry" does not necessarily lead to a "good material". Polymers and networks synthesized by modular coupling inevitably follow the characteristics of step growth polymerization in that the molecular weight of the polymers or the average molecular weight between crosslinks exhibit high polydispersity. Orthogonal reactions when inappropriately applied defeat the purpose of the modular design. For example, ultrafast tetrazine/TCO ligation, when applied to solution polymerization or crosslinking, results in oligomeric cyclic product or highly heterogeneous, ill-defined hydrogels. The application of this chemistry at the interface enabled the diffusion controlled process that opens up a wide range of biomaterials applications. Furthermore, hydrogel properties are not solely dependent on the crosslinking chemistry. Phase separation and network defects[162] may negatively affect network properties. Multiarm PEGs are frequently used for hydrogel synthesis. The high functionality facilitates rapid gelation, but

inevitably, leads to more network defects. An attractive approach is the combination or orthogonal chemistry with orthogonal supramolecular assembly.[163]

Overall, orthogonal reactions have provided researchers with the unprecedented ability to link two entities in high yield without interference from other functional groups. These reactions have become powerful and enabling tools for polymer and materials synthesis. As organic chemists continue to expand the chemistry toolbox, further advancement in biomaterials synthesis and fabrication is anticipated. With improved biological understanding of biological design principles, more sophisticated and biologically relevant materials with controlled spatial and temporal properties will lead to further advance in the biomedical field.

1.3 Hyaluronic Acid

1.3.1 Introduction

Hyaluronan(HA) was first purified from the vitreous humor of bovine eyes by Karl Meyer in 1934.[164] He named the molecule ‘‘hyaluronic acid’’ because of the hyaloid appearance of the substance when swollen in water and the probable presence of hexuronic acid as one of the components. In the 1950s, Meyer and colleagues determined that HA was a linear polysaccharide composed of repeating β -1,4-linked $_D$-glucuronic acid (GlcA) and β-1,3-linked *N*-acetyl-$_D$-glucosamine (GlcNAc) disaccharide units (Figure 1.2a).[165] The various names of HA reflect the properties of the molecule under various conditions. When first isolated, HA behaved like a mild acid; therefore, Meyer named it ‘‘hyaluronic acid’’[1].[164] Under physiological conditions, HA exists as a polyelectrolyte with associated cations, frequently as a sodium salt; therefore, the name sodium hyaluronate. The name was later amended to

‘‘hyaluronate’’ in reference to its salt form or ‘‘hyaluronan,’’ a term used to encompass all forms of the molecule.[166]

HA is found ubiquitously in the extracellular matrix (ECM) of all vertebrate tissues, although its concentration and binding partners vary. In bodily fluids, the concentration of HA ranges from 0.01– 0.1 μg g^{-1} in blood serum to 1400–3600 μg g^{-1} in synovial fluid; HA content in soft connective tissues ranges from 8.5–18 μg g^{-1} in the thoracic lymph to 140–338 μg g^{-1} in the vitreous body.[167] HA is also present on some cell surfaces as a pericellular sugary coat, a feature thought to be involved in cell differentiation and morphogenesis. In the cumulus cell–oocyte complex, the HA concentration can be as high as 0.5–1.0 mg ml^{-1}.[168,169] Classically considered an extracellular molecule, the presence of HA in the cytoplasm and the nucleus was suggested as early as the 1970s[170,171] and was convincingly confirmed in the 1990s.[172–175] Although intracellular HA has been suggested to play important roles in inflammation, its intracellular functions remain largely unknown.[176]

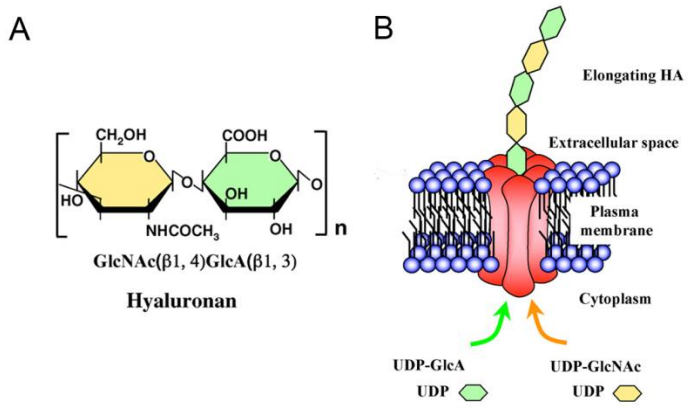

Figure 1.2 (A) Chemical structure of HA and schematic illustration of (B) HA biosynthesis and (C) biodegradation. (A) HA is a linear polysaccharide with disaccharide repeats of D-glucuronic acid and *N*-acetyl-D-glucosamine. (B) HA is synthesized by transmembrane proteins HAS1, 2 and 3 and is extruded into the extracellular space as the polymerization proceeds. Reproduced with permission, Copyright 2008, The Japanese Biochemical Society.[177]

HA is not branched, nor does it contain any sulfate groups.[178] Despite its simple chemical composition, HA fulfills several distinct molecular functions that contribute not only to the structural and physiological characteristics of tissues, but also to the mediation of cell behaviors during morphogenesis, tissue remodeling, inflammation and diseases. Owing to its unique biophysical properties, HA contributes directly to the maintenance of tissue homeostasis and biomechanics. Through its interactions with proteoglycans and link proteins, HA organizes and maintains the structural integrity of extracellular and pericellular matrices. As a signaling molecule, HA interacts with a variety of cell surface receptors and HA-binding proteins to activate intracellular events to mediate cell functions.[179]

After more than two decades of intense study, the molecular details of the role of HA in normal and pathophysiological processes are finally emerging. The

fascinating characteristics of HA have motivated two distinct groups of scientists to investigate HA-related phenomena and applications. While biologists continue to unravel the complex biological functions of HA and its receptors in various cell signaling processes, biomedical engineers are creating a range of HA-based hydrogel materials with increasing complexity and diverse functions for tissue regeneration purposes.[180,104,181] This paper highlights the essential biological functions of HA, with the goal of motivating the biomaterials community to investigate HA as both a synthetic building block and a biological signaling motif. This is not an all-inclusive review, and readers are referred to in-depth reviews in an edited book for further reading.[179]

1.3.2 Biosynthesis and Degradation

Unlike other glycosaminoglycan (GAG) molecules that are synthesized in the Golgi apparatus, HA is synthesized at the plasma membrane by a group of highly specialized membrane proteins, HA synthases (HASs).[182] There are three well-conserved HAS isozymes present in mammalian species: HAS1, HAS2 and HAS3[183] each possessing two distinct binding domains for UDP-sugars (Figure 1.2B). Polymerization of HA occurs at the inner face of the plasma membrane, where HAS alternatively adds UDP-GlcA and UDP-GlcNAc monomers to the reducing end of the growing polymer. As the polymerization is occurring, the non-reducing end of the sugar chain is translocated into the extracellular space through a pore in the HAS structure.[184] An intriguing question is why nature uses three different isozymes for the synthesis of HA with such a simple repeating unit. Although these three enzymes share a structural identity of ~55–70%, they differ in terms of their ability to synthesize HA. HAS1 has a significantly higher Michaelis constant (K_m) value, the

substrate concentration where the reaction rate is half of its maximum, for both UDP-GlcA and UDP-GlcNAc compared with HAS2 and HAS3, suggesting that HAS1 has a slower rate of HA synthesis compared with the other synthases.[185,186] As discussed below, HA of different sizes exhibits distinctly different, sometimes conflicting biological functions. Therefore, the expression of various HAS isozymes is likely to be a fine control system critical for the effective mediation of diverse cell behaviors. While HAS1 and HAS2 are able to produce large-sized HA (up to 2000 kDa), HA produced by HAS3 is of a lower molecular mass (100–1000 kDa).[185,187] McDonald and coworkers were the first to recognize the isoform specificity for HA production in embryogenesis; they discovered that HAS2 (but not HAS1 or HAS3) knock-out mice died at day 9.5 from incomplete atrioventricular septum formation.[188]

The expression levels of HAS isozymes differ during morphogenesis and in disease states.[189] Thus, the differential distribution of HA in tissues varies at individual developmental stages and in pathological conditions, and is controlled by the spatio-temporally regulated transcription of the three different synthases. HA is abundant in fetal tissues, but is partially replaced by collagen fibers and proteoglycans during development, so that the mature tissues can fulfill more stringent mechanical tasks.[190] For example, the newborn vocal fold is composed of a loose connective tissue rich in HA. As the vocal fold develops and matures, HA content is reduced, and the fibrous proteins are deposited across the lamina propria in a gradient fashion. Overall, HA is indispensable for vocal fold development and maturation,[191] and its presence in vocal fold is evolutionarily beneficial for the tissue to cope with constant trauma.[192] As discussed below, HA is enriched in tumors and tumor- associated

stromal tissues, possibly as a result of increased expression or activity of HAS isozymes.

The diverse functions of HA originate from its primary and secondary structures.[193,194] Connected by glycosidic links, individual saccharide units in HA are relatively rigid, adopting a $^4C_1$ chair with the bulky substituents located in sterically favorable equatorial positions. X-ray diffraction[195] and nuclear magnetic resonance[196] characterizations suggest that HA can adopt stiff helical structures in the solid state, possibly as a result of the chemical structure of the disaccharide, extensive hydrophobic patch and internal hydrogen bonds. The presence of multiple dynamically formed and broken hydrogen bonds between adjacent saccharides is thought to contribute to the semi-flexibility of the polymer chain in solution.[196–198] Using tapping mode AFM, Cowman and coworkers observed extended, relaxed and condensed conformations of HA (Figure 1.3) that had been deposited on mica surfaces under various conditions.[199] The researchers suggested that, in connective tissue ECM, HA may adopt a relaxed coil or partially condensed conformation, whereas HA tethered to the cell surface or in cytosol may exist as fully condensed rods. When subjected to shear flow in tight intercellular spaces or in protein–HA complexes, tissue HA may become fibrous.

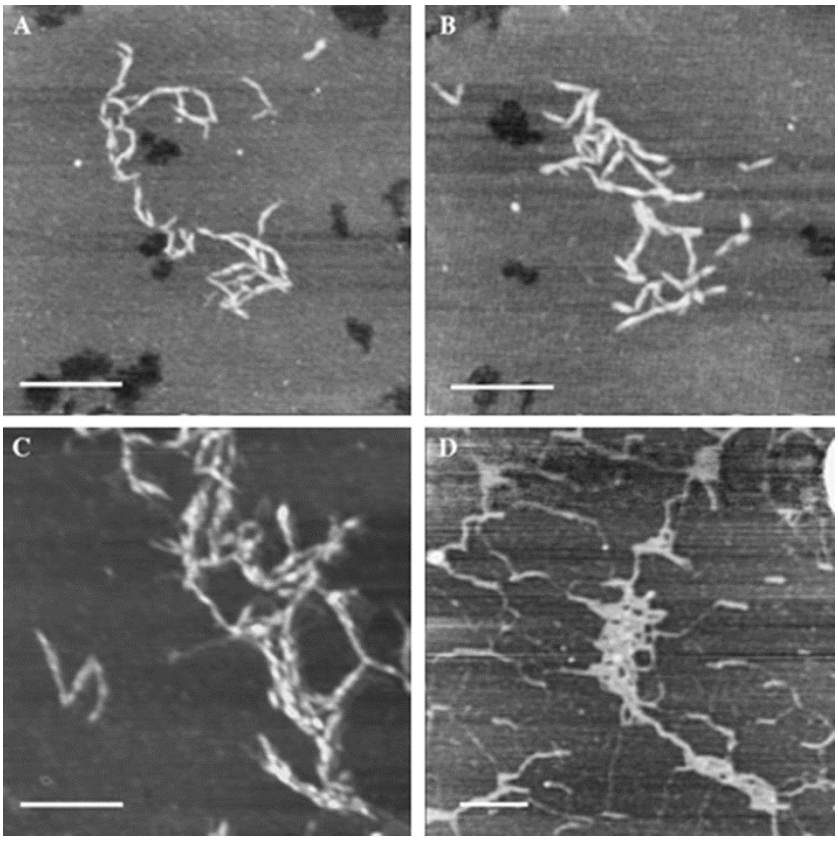

Figure 1.3 Tapping mode AFM images of HA deposited on freshly cleaved mica. HA with (A, B) moderate or (C, D) high molecular weight, (A–C) produced in bacteria or (D) extracted from rooster comb, was deposited from 10 μg ml^{-1}s olution in H_2O (A, B), 5 μg ml^{-1} solution in 10 mM $MgCl_2$ or 500 μg ml^{-1} solution in 0.15 M NaCl (D). Scale bar: 250 nm, Z range: 2.5–6 nm. Reproduced with permission,[199] Copyright 2005, Elsevier.

At physiological pH, HA is a highly charged molecule containing associated counter ions, such as Na^+, K^+, Ca^{2+} and Mg^{2+}. Solutions of high molecular mass HA are highly viscous because of polymer chain entanglement.[200] Such entangled networks display time dependent viscoelasticity, exhibiting elastic properties when subjected to rapid and transient fluid flow, and behaving as viscous liquid when

exposed to slow fluid flow of a longer duration. Again, take the vocal fold as an example, HA is a major modulator of the tissue viscosity, providing shock-absorbing properties to the tissue.[201,202] Moreover, the shear-thinning properties of HA create optimum conditions for phonation by decreasing the tissue stiffness while vibrating.[203] The entangled HA network in the extracellular space also effectively controls the solute/protein diffusion. Obviously, the viscoelastic properties of HA and its hydration capacity depend on the molecular weight of HA. During rapid growth and tissue remodeling, HA fulfills the requirements to fill the vacant space, to undergo deformation, to maintain tissue hydration and to buffer the local environment. Such an HA-rich environment can keep cells partially localized or provide cells with a substrate on which to migrate.[204,205]

HA synthesis and degradation is tightly regulated during embryonic development and homeostatic processes. The half-life of HA varies from less than a day in rapidly turning over skin and serum to typically 2–3 weeks in cartilage. HA is removed from the ECM as a consequence of local catabolism and/or drainage into the lymphatic system for catabolism in regional lymph nodes. HA can be catabolized by a number of enzymes in the hyaluronidase (HAase) family. Hyal1 and Hyal2 are the two most common and ubiquitously important HAases. Both enzymes are found in almost all somatic tissues.[206] Hyal1 is present in two isoforms, the first being a 57 kDa glycosylated protein, and the second being a 45 kDa form with ~100 amino acids deleted.[207,208] Both in vivo and in vitro studies have demonstrated that the larger isoform is probably secreted by the cell, while the smaller isoform is retained in acidic intracellular vesicles.[209] Hyal2 is often found in a glycosylphosphatidylinositol (GPI)-anchored form, tethered to the extracellular side of the plasma membrane.[210,211]

Hyal3 and PH-20 are more specialized HAase. Hyal3 has been poorly studied, but has been shown to be an intracellular HAase expressed in specific tissues.[212] PH-20 is classically known as the sperm HAase involved in fertilization, and is rare in other human tissues. Like Hyal1, PH-20 has two forms: a larger, GPI-linked isoform that is anchored to the plasma membrane, and a smaller, soluble isoform caused by removal of 56 amino acids at the C-terminus.[213]

The HAases have differential activities in the HA fragment sizes they generate and the pH at which they show optimal activity. Hyal1 is only active at very low pH values from 3.5 to 3.8. The enzyme cleaves large or small molecular weight HA into tetramers.[214] Hyal2 shows optimal activity at pH 6.0–7.0, but is active over a large pH range. This enzyme cleaves high molecular weight HA into intermediate size fragments of ~20 kDa.[215] PH-20 is active over a relatively wide pH range between 3.0 and 9.0. PH-20 degrades high molecular weight HA into small fragments, although some intermediate size fragments also are present.[214]

Hyal1 and Hyal2 work in concert to degrade HA in somatic cells. GPI-anchored Hyal2 binds HA extracellularly, probably in concert with HA receptors, then internalizes HA and performs preliminary cleavages on the full length HA polymer in acidic endocytic vesicles.[216] From there, Hyal1 can further process HA oligomers in these vesicles with the help of β-exoglycosidases, which can cleave sugar groups off each terminus.[209] Gene knock-out studies have supported this theory, demonstrating that the action of Hyal1 can be largely compensated for by β-exoglycosidases,[217] whereas Hyal2-deficient mice are either embryonic lethal or have severe defects.[218]

In addition to the enzymatic degradation, HA can be fragmented by reactive oxygen species generated by many types of cells under stressed conditions,[219] and

HA degradation by superoxide and peroxynitrite in various injury models has been studied.[220–225] Interestingly, HA and its degraded fragments have extraordinarily wide-ranging and often opposing biological functions, owing to the activation of different signal transduction pathways. This variation might be a mechanism by which nature diversifies the functions of a simple polysaccharide.[226] High molecular weight HA species with >1000–5000 saccharide repeats are space-filling, anti-angiogenic and immunosuppressive; they impede differentiation, possibly by suppressing cell–cell interactions, or ligand access to cell surface receptors. HA chains up to 20 MDa are involved in ovulation, embryogenesis, wound repair and tissue regeneration.[226] Studies have shown that, in response to HA of 40–400 kDa, the NF-κB-mediated gene expression is activated by HA binding with HA receptor for endocytosis.[227] Malignant cells produce HA polysaccharides in order to co-opt normal cellular functions. However, the ability of the naked mole rat to synthesize high molecular mass HA (five times larger than human HA) is correlated to the cancer resistance and longevity of this species.[228] Contrarily, HA fragments of lower molecular weight are inflammatory (1000 repeats), immuno-stimulatory and pro-angiogenic (8–32 saccharide repeats), and they competitively bind HA receptors on cell surfaces. Under certain conditions, low-molecular-weight HA species (20–200 kDa) function as endogenous ‘‘danger signals’’, while even smaller fragments can ameliorate these effects.[229]

1.3.3 HA-protein interactions

While HA alone has distinct biophysical and biomechanical properties, the biological functions of HA are manifested through its interactions with a large number of HA-binding proteins (HABPs or hyaladherins) that exhibit significant differences in

their tissue expression, cellular localization, specificity, affinity and regulation.[230,231] A number of HABP bind HA through binding motifs with the sequence B(X7)B, where B is a basic residue, arginine or lysine, and the Xs contain at least one basic amino acid, but can be any other non-acidic amino acids.[232] Additionally, a second HA binding motif, known as the link module, consists of a span of ~100 amino acids, which binds HA when oriented in the correct tertiary structure.[233] A third possible binding motif is an arginine-arginine (R-R) sequence that has been shown biochemically to bind HA, but has not been thoroughly studied in full-length proteins.[234]

HABPs can be classified based on the binding motif that is used to bind HA. Members of the family that use the link module in binding HA include a cluster of differentiation 44 (CD44), hyaluronectin, aggrecan, versican, lymphatic vessel endothelial receptor 1 (LYVE-1) and tumor necrosis factor-α stimulated gene 6 (TSG-6). The family of proteins that use the B(X7)B motif includes the receptor for hyaluronan mediated motility (RHAMM), cdc37, P-32 and sialo protein associated with cones and rods (SPACR). Given that HABP generally interact with a minimum of 6–10 sugar repeats of HA,[226] a single chain of high molecular weight HA can theoretically accommodate in the order of 1000 protein molecules.[235] In general, cellular signaling responses induced by HA/HABP interactions are strongly dependent on the HA molecular weight and the cell phenotype.[236]

CD44 is a multi-domain, ubiquitous HA receptor protein that spans the plasma membrane of the cell. It contains highly conserved membrane spanning, cytoplasmic and HA binding domains, while the membrane proximal region is poorly conserved among mammalian species. Ten alternatively spliced exons reside in the poorly

conserved, extracellular region. The standard version of CD44 (CD44s) has all ten of these variant exons removed. Estimated mathematically, over 800 variant forms of CD44 (CD44v) could be created with the 10 alternatively spliced exons, although not all these combinations are expressed. Over 20 unique forms of CD44v have been identified to date.[237] The core protein of CD44s is only 37 kDa in size, but is increased to between 80 and 90 kDa through the addition of multiple oligosaccharide and GAG additions. CD44v can contain additional modifications, because many of the variant exons contain sites for additional oligosaccharide and GAG additions.[238] These variant exons therefore affect the affinity of CD44 for HA binding, based on the concept that the N-linked glycosylation pattern dictates the activation state of CD44. Specifically, a high degree of N-linked glycosylation activates CD44 to bind HA, while a low degree inactivates CD44 so that it binds HA poorly or not at all.[238] The activation patterns of CD44 are also affected by the type of cell, phosphorylation state of the cytoplasmic tail and clustering in the membrane.[239] CD44/HA binding is involved in diverse functions, including attachment, organization and turnover of the ECM at the cell surface, as well as the mediation of lymphocyte migration during inflammation.

Another HABP, RHAMM, also known as CD168, was originally discovered as a soluble protein that altered migratory cell behavior.[240] In contrast to CD44 and other cell-surface receptors that contain the classical membrane spanning domain and signal sequence for secretion from the endoplasmic reticulum (ER)/Golgi complex, RHAMM does not contain a membrane spanning domain nor does the mRNA transcript contain a signal sequence. RHAMM is normally localized inside the cell and is only released by certain, poorly defined stimuli. The transport of RHAMM to the

extracellular space is still unclear, but may involve transport channels or proteins, flippase activity or exocytosis.[241] Intracellularly, RHAMM associates with microtubules and, working with breast cancer-2 susceptibility protein (BRCA2) and BRCA1-associated RING domain protein 1 (BARD1), plays a role in the regulation of mitosis.[242] Extracellularly, RHAMM associates with CD44 and, upon binding to HA, activates intracellular signaling pathways.[243] Variants of RHAMM caused by alternative splicing have been observed, but not thoroughly studied. Preliminary reports have suggested that alternatively spliced forms of RHAMM may be upregulated in some tumor types, promoting tumor progression.[244]

Expressed on the endothelial cells of the lymphatic sinus and in reticular cells in the lymph nodes, LYVE-1 binds HA via the link module to mediate the transport of HA from tissue ECM to lymph for cell uptake and degradation.[245] Based on the amino acid sequence, LYVE-1 is predicted to be a type I transmembrane glycoprotein, with a single copy of CD44-like link module located at the N-terminus of the extracellular domain that binds both soluble and immobilized HA.[246,247] LYVE-1 has been widely used as a lymphatic vessel specific marker, and offers a prognostic parameter for head and neck squamous cell carcinomas. Although the HA binding capacity of LYVE-1 is highly regulated, HA homeostasis in LYVE-deficient mice is not perturbed.[248] Further investigations are necessary to identify the role of LYVE-1 in normal lymphatic development and function, as well as its involvement in lymphatic HA metabolism or HA-mediated cell migration.

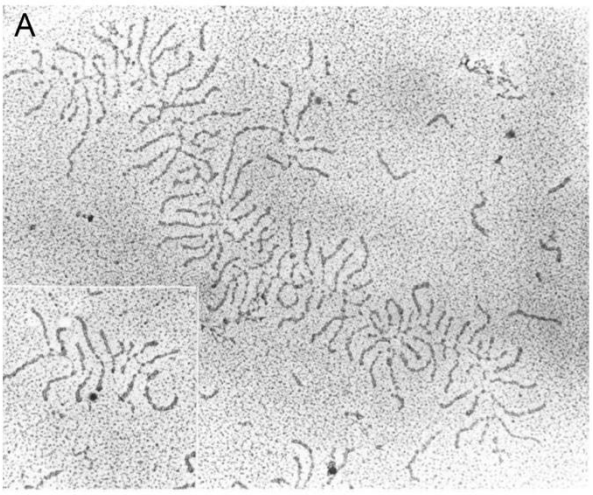

Figure 1.4 HA organizes the cartilage ECM via non-covalent binding with aggrecan. Reproduced with permission,[249] Copyright 1996, Orthopaedic Research Society. Electron micrograph of an aggrecan/HA aggregate (from fetal bovine cartilage) shadowed with platinum. Each aggregate consists of ~100 aggrecan monomers bound to HA. With a molecular weight $>10^8$, such a complex occupies a volume equivalent to that of a bacterium.

HA can be organized into supramolecular assemblies via its association with multiple binding proteins.[235,250] In the ECM of connective tissues, HA binds certain proteoglycans, such as aggrecan (Figure 1.4), versican and brevican, to form large complexes that provide the structural integrity and mechanical functions to the tissues.[251–253] The protein product of TSG-6, secreted in response to inflammatory stimuli, also binds HA via a single link module. Binding of TSG-6 with HA results in the formation of fibrils or ‘‘cables’’ (Figure 1.5A) that are pro-adhesive to lymphocytic cell lines. Adhesion of leukocytes to the HA complexes prevents the direct contact of inflammation-promoting receptors to the underlying tissues, thereby maintaining leukocytes in a non-activated state. In response to ER stress or when exposed to high concentrations of glucose, a variety of cells produce HA cables.[254]

TSG-6 catalyzes the covalent transfer of heavy chains (HC) from inter-alpha- trypsin inhibitor (IαI) and pre-α-inhibitor (PαI) to HA, and HC–HC crosslinks result in stabilized HA cables.[255–257] Certain HA cables, for example, those synthesized by airway smooth muscle cells, can form without TSG-6 and are independent of HC attachment.[258] With an overall length >200 μm, these cables are capable of supporting the binding of a large number of leukocytes. Versican is found to associate with the cables, extending and hydrating these structures, as well as providing a means of sequestering proinflammatory chemokines through interactions with its chondroitin sulfate and dermatan sulfate chains.[259]

The pericellular coat (Figure 1.5B-C), an HA-rich, 5–10 ım thick gel-like layer surrounding many types of cells, is also organized and stabilized by HABPs. The HA coat is organized by aggregating proteoglycan and cell surface HA receptors (CD44) and is crosslinked by various proteins such as tenascin, TSG-6, IαI, pentraxin (PTX) and thrombospondin 1 (TSP-1). The pericellular coat plays complex roles in cell adhesion/de-adhesion and cell shape changes associated with proliferation and locomotion, thereby contributing to the regulation of inflammation, morphogenesis, tissue regeneration and healing. The elastomeric pericellular matrix has also been implicated in cellular mechanotransduction.[190,260] The HA coat, formed between the cumulus cells surrounding the oocyte during ovulation, is responsible for the integrity of the cumulus–oocyte complex, providing protection and facilitating the transport of the oocyte into the oviduct for fertilization. Sperm-associated HAases allow penetration of this matrix at fertilization.[168,261]

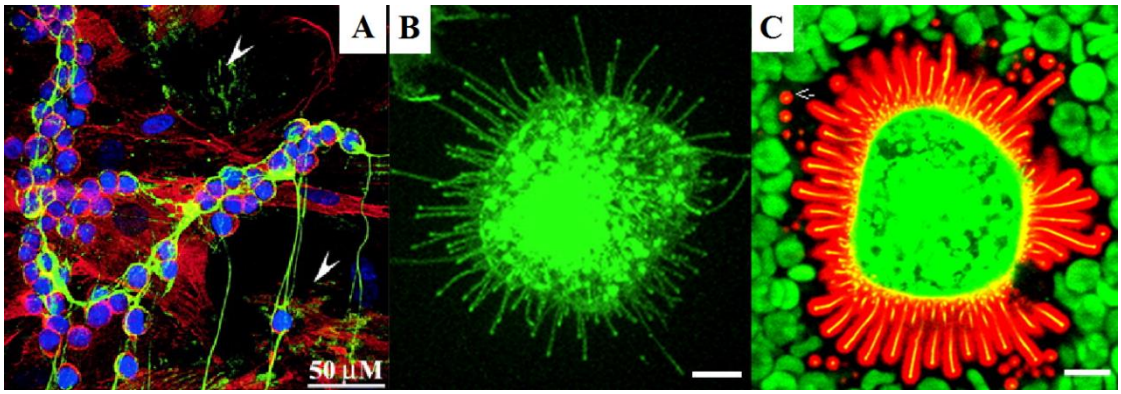

Figure 1.5 HA organized as (A) monocyte-adhesive cables or (B, C) pericellular coat. (A) Monocyte-adhesive HA cable, produced by treating human colon smooth muscle cells with poly I:C for 17 h:green, HA; red, CD44; and blue, nuclei. Scale bar, 50 ım. Arrowheads point to areas without any leukocytes. (B, C) HA coat around a MCF-7 cell, as revealed by confocal imaging a probe made of aggrecan G1 domain and link protein tagged with Alexa Fluor 594®(red). Green staining represents green fluorescent protein tagged HAS3 (GFP-HAS3). The HA coat was visualized by particle exclusion using red blood cells (green). Scale bar, 10 µm. (A) Reproduced with permission,[254] Copyright 2003, Elsevier. (B, C): Reproduced with permission,[260] Copyright 2008, Elsevier.

1.3.4 HA in morphogenesis and wound healing

Mounting evidence points to the involvement of HA in morphogenesis. HA-rich matrix can either facilitate cell migration by creating hydrated and non-adhesive milieu or inhibit cell migration via the increased binding of proteoglycans to pericellular HA.[262] HA exerts a profound effect on the ‘‘stemness’’ of hematopoietic stem cells (HSC), human embryonic stem cells and mesenchymal stem cells (MSCs). All three types of stem cells reside in specific HA-rich microenvironments that maintain cells in a quiescent state with low levels of proliferation. The maintenance and differentiation of stem cells are also intimately mediated by HA/ HABP interactions. Specifically, HA/CD44 and HA/RHAMM interactions are essential for the trafficking of HSCs and their homing into the bone marrow, where they are

maintained in an undifferentiated state.[263] In embryonic tissues, RHAMM plays an important role in the maintenance of hESC pluripotency, viability and cell cycle. During stem cell differentiation, RHAMM expression is significantly down-regulated and, at the same time, HAS2 expression is markedly enhanced, resulting in a 13–24-fold increase in HA production.[264] MSCs are resident stem cells in adult tissues, and CD44 has long been used as a marker for MSCs.[265] In response to platelet-derived growth factor stimulation, MSCs express high levels of CD44 standard isoform, which facilitates cell migration through interaction with extracellular HA. Such a migratory mechanism could be critical for the recruitment of MSC into wound sites for the preparation of tissue regeneration.[266] From a biomedical engineering perspective, delivering stem cells in HA matrices not only improves cell survival, but also allows the cells to be released to contribute to tissue regeneration, owing to the susceptibility of the HA matrices to enzymatic degradation.

HA, alone or through its interaction with its binding partners, has been shown to be crucial for the morphogenesis of many tissues/organs. For example, HA produced by endocardial cells during embryonic development contributes to the formation of endocardial cushions and facilitates the endothelial-to-mesenchymal transformation in the development of cardiac valves. The maintenance of HA homeostasis, thereby the size of the endocardial cushions, is achieved through balanced activity of positive and negative regulators of HAS2.[267] HA is also widely distributed throughout the developing central nervous system, playing a role in regulating neural crest cell migration from the dorsal neural tube. Specifically, HA promotes the separation of neural crest cells from the dorsal neural tube. In addition to regulating neuronal function and cell migration, HA may influence progenitor cell

differentiation and maturation. It has been reported that the presence of HA, either in vivo or in vitro, blocked the maturation of oligodendrocyte progenitor cells into myelin-forming oligodendrocytes, suggesting that HA blocks remyelination by maintaining progenitor cells in an undifferentiated or immature state. Neural stem cells (NSCs) may be influenced similarly by exposure to HA in stem cell niches and in injury microenvironments, where they may synthesize their own pericellular HA.[231] Delivery of NSCs in a HA-containing hydrogel into stroke cavity promotes NSC maturation and proliferation.[268] Being a major component of the ECM of the developing limb bud, HA is involved in various aspects of limb morphogenesis. Importantly, down-regulation of HA is necessary for the cell positioning, cell–cell interaction and cartilage differentiation during condensation. The over expression of HAS2 in the mesoderm of the chick limb bud in vivo results in the formation of shortened and severely malformed limbs that lack one or more skeletal elements.[269–271]

The tissue injury and repair process is characterized by the turnover of the matrix components, and HA plays important and multifaceted roles in this dynamic process.[272] Interactions between HA and its signaling receptors initiate inflammatory responses, maintain structural cell integrity and promote recovery from tissue injury. Studies have shown that RHAMM is critical for the recruitment of macrophage to areas of tissue injury,[273] whereas CD44 is critical for abrogation of inflammation.[274] Moreover, Toll-like receptors cooperate with HA receptors, particularly with CD44, to activate the innate immune system.[275–279] The ability of HA to facilitate tissue repair and wound healing depends on its molecular weight and tissue location, as well as the specific cell population with which HA interacts. The HA-rich matrix, both in the

early inflammatory phase of wound repair and in the granulation tissue, facilitates cell migration into the provisional wound matrix by providing an open hydrated matrix and through direct interaction with cells via HABP.[231] Fibroblasts recruited to the wound bed produce proinflammatory cytokines that, in turn, stimulate endothelial cells to produce HA, further promoting the adhesion of cytokine-activated lymphocytes through the HA-binding variant of CD44.[280] HA also facilitates the cell detachment from the matrix and cell mitosis, thereby fostering cell proliferation.[281] Through its interaction with HABP and aggregating proteoglycan, HA contributes to the organization of the granulation tissue matrix. Experimental results suggest that CD44 may contribute to the organization and/or stability of developing endothelial tubular networks.[282] Finally, the physiological role of HA and its oligosaccharide are central to angiogenesis, an important step in wound healing.[272] As mentioned above and consistent with this idea, high molecular weight HA has been shown to inhibit angiogenesis, while the low molecular weight counterparts promote angiogenesis and enhance the production of collagens by endothelial cells.[283] It is noteworthy that intact, high molecular weight HA, not the fragmented HA, promotes the induction of regulatory T-cells.[284] Thus, the induction signals can be recapitulated using HA-containing synthetic matrices.

In the later stage of wound healing, HA may function as a moderator of inflammation by protecting against free radical damage to cells.[285] The TSG-6/IαI complex, through its interaction with HA both on the cell surface and in the ECM, may serve as a potent negative feedback loop to moderate inflammation and to stabilize the granulation tissue as healing progresses. The final stages of wound healing include re-epithelialization and remodeling. In healing wounds, HA is

expressed in the wound margin, in the connective tissue matrix, and collocating with CD44 expression in migrating keratinocytes.[286] Interestingly, fetal wound healing is characterized by a lack of fibrous scarring. HA in fetal wounds remains high for longer periods than in adult wounds, probably reducing the deposition of disorganized collagen matrix. The persistent HA-rich environment can affect cell–cell and cell–matrix interactions, ultimately contributing to scarless wound healing, as can occur in the HA-rich young organism[2].[272] In adult tissues, studies show that blocking signaling of HA fragments using a RHAMM-mimetic peptide results in skin wound healing with reduced fibrosis.[287]

1.3.5 HA in cancer

Tumor progression and metastasis are accompanied by the alteration of organ microenvironment. HA is enriched in many types of tumors and has been implicated in the progression and metastasis of carcinomas.[190] Enrichment of HA in tumors can be attributed to increased production by tumor cells themselves or by tumor-associated stromal cells through tumor–stroma crosstalk.[288] For example, normally absent in healthy epithelial tissues, HA is upregulated when the epithelial cells undergo malignant transformation.[262] The involvement of HA in the growth and spreading of cancers of epithelial origin is complex and multifaceted. During tumorigenesis, epithelial cells can undergo epithelial-to-mesenchymal transition and detach themselves from the epithelial compartment for invasion, accompanied by enhanced HA synthesis. HA, in turn, supports cell proliferation, prevents apoptosis, maintains intercellular space to facilitate nutrient diffusion, and enhances cell locomotion that stimulates invasion. In addition, cancer cells disguise themselves with a coat of HA

from the cytotoxic effects of T-lymphocytes. HA cables, in contrast, bind tissue macrophages and modulate their activity to favor tumor growth.[262]

The upregulation of HAS expression results in the accumulation of HA in tumor tissues and, consequently, the creation of a prometastatic microenvironment.[177] Using a clone of breast cancer cell line MDA-MB-231 that forms bone metastases in an *in vivo*-like basement membrane model, researchers discovered that the increased expression of HAS2 in metastatic cells resulted in a 7-fold higher HA-synthesizing capacity compared with MDA-MB-231 cells.[289] Further, knockdown of HAS2 completely suppressed the invasive capability of these cells by the induction of tissue metalloproteinase inhibitor 1 (TIMP-1) and dephosphorylation of focal adhesion kinase (FAK). HAS2 knockdown-mediated inhibition of basement membrane remodeling was rescued by HAS2 overexpression, transfection with TIMP-1 siRNA or addition of TIMP-1-blocking antibodies. Moreover, knockdown of HAS2 suppressed the EGF-mediated induction of the FAK/PI3K/Akt signaling pathway. [289] HAS2 has also been shown to be critical for the interaction of cancer stem cells (CSCs) with tumor-associated macrophages (TAM), leading to enhanced secretion of platelet-derived growth factor-BB from TAM. This secretion could then activate stromal cells and enhance CSC self-renewal. Loss of HAS2 in CSCs or inhibition of HAS activity drastically reduced the incidence and growth of metastatic lesions in vitro or in vivo, respectively.[290]

It is noteworthy that, while a moderate increase in HA production correlates with tumor growth and metastasis, a large excess of HA can suppress tumor growth.[291] Because HA accumulation is the result of a balance between the activities of HAS isozymes and HAases, the presence of HAases may promote HA turnover in

the cancer cells and overcome tumor suppression by excess amounts of HA. By degrading the HA-rich matrix surrounding the tumor, HAases help the cancer cells to escape from the primary tumor mass and play a major role in intravasation by allowing degradation of the basement membrane of the lymph or blood vessel. HAases play roles in the establishment of a metastatic lesion by helping with extravasation and clearing the ECM of the secondary site.[292] Finally, HAases produce HA fragments to stimulate endothelial cell proliferation and budding of new capillaries that promote angiogenesis to allow tumor expansion.[293] Interestingly, hypoxia also increases production of HA and activity of HAases.[294]

Each of the HAases discussed above can play a role in cancer progression, although the roles they play and the cancers they contribute to may differ. Earlier in vitro cell culture experiments suggested that Hyal1 expression prevented tumor growth from the results of cells cultured in vitro.[295] Furthermore, when directly injected, Hyal-1 was found to inhibit tumor formation in vivo.[296] Subsequently, it was discovered that context matters in the case of the role of Hyal1 in cancer progression. Hyal1 plays a role in metastasis mainly via interactions with the ECM, and a lack of this tumor microenvironment would probably complicate the data in an in vitro setting. Additionally, Hyal1 functions predominantly in an intracellular fashion, explaining why direct injection of this enzyme may produce conflicting results. Clinically, there is considerable interest in using Hyal1 levels in blood or urine to predict a patient's prognosis. Studies among bladder cancer patients show that Hyal1 levels correlated positively with poor prognosis, muscle invasion and recurrence.[297,298] In prostate cancer (PCa) patients, high Hyal1 levels correlate with progression 84% of the time.[299] Hyal1 is also the predominant HAase responsible for

lung cancers.[300] Laboratory studies have shown similar results. PCa cells that over-express Hyal1 form significantly more metastases than do controls that express lower levels of the enzyme.[301]

Some research has been performed to examine the role of Hyal2 in cancer metastasis, but the accumulated data indicate that Hyal2 probably plays a role. A clinical study found that endometrial cancer cells express more Hyal2 than Hyal1, pointing to its importance in that type of cancer.[302] Additionally, a cell-based study found that highly invasive breast cancer cell lines express more Hyal2 than poorly invasive lines.[303] When Hyal2 was over-expressed in astrocytoma cells, these cells formed more aggressive, invasive tumors in the cranium compared with control. Interestingly, the same result was not found when the cells were injected subcutaneously, indicating that the microenvironment matters for the role of Hyal2 in cancer progression.[304]

The role of Hyal3 in cancer progression is poorly studied, and the few studies that have investigated this HAase report contradictory results. A study of breast cancer cell lines demonstrated that poorly invasive lines express more Hyal3 than do highly invasive lines.[303] In contrast, a study of endometrial cancer found that Hyal3 was expressed at levels 1000 times higher than Hyal1 and 33 times higher than Hyal2 suggesting that Hyal3 is the main HAase necessary for endometrial cancer progression.[302] The finding that PH-20 is normally expressed only in the testes is of interest to the medical community, because it could provide a good prognostic indicator of the existence of cancer and the likelihood to metastasize. Two studies on laryngeal cancer have shown that PH-20 expression increased in late stage tumors, or those likely to metastasize.[305,306] A similar correlation was shown for breast

cancer.[307,308] African-American women with breast cancer were shown to have a higher expression of PH-20 compared with Caucasian women, an interesting observation considering that African-Americans have a higher likelihood of breast cancer metastasis.[309] Collectively, the existing data demonstrate that PH-20 plays a strong role in cancer metastasis, at least for some cancers.

HA also interacts with its receptors to modulate cell behavior during tumor progression and metastasis. Among the HA receptors, CD44 has been best studied. Numerous clinical studies have shown that increased expression of CD44 correlates with increased metastasis of a variety of different tumors.[310] In addition to a wealth of clinical data, the pathways by which CD44 affects cancer metastasis have also been largely determined. Collectively, CD44 affects adhesion of cancer cells, rearranges the cytoskeleton through activation of Rho GTPases, and increases the activity of ECM degrading enzymes.

When a cell remains epithelial in nature by expressing E-cadherin, CD44/HA binding is low, preventing the activation of metastatic signaling pathways.[311] When a cell becomes cancerous, E-cadherin is down-regulated, leading to higher CD44/HA binding. After binding with HA, CD44 signals for the activation of a number of ECM degrading proteins, which allow cancer cells to detach from the primary tumor mass and migrate. CD44 increases matrix metalloproteinase-9 (MMP-9) localization to the plasma membrane and optimizes Hyal-2 activity by adjusting extracellular pH through activation of a Na^+/H^+ exchanger.[312,313] CD44 itself can be cleaved by MMP, again helping cancer cells release themselves from the tumor mass.[314,315] An intracellular cleavage product of CD44 produced by c-secretase can participate in signal transduction, leading to increased migration.[316]

CD44 activates a number of Rho GTPase that remodel the actin cytoskeleton to allow for migration to occur. Binding of CD44 to HA controls activation of RhoA, Rac1 and Cdc42 GTPases, and subsequently the downstream targets of these GTPases.[317–319] Along with remodeling the actin cytoskeleton, CD44 also activates FAK, which allows for focal adhesion formation and turnover, another key step in the process of cell motility.[320] Another molecule that promotes invasion that CD44 activates is Snail2, through the NFκB pathway.[321] Other downstream targets of CD44 probably exist, but have not yet been discovered. While it is important that CD44 molecules be cleaved for the cancer cells to release from the primary tumor mass, interactions between the receptor and HA and other ECM molecules during the metastatic process are also important. Several isoforms of CD44v are necessary for cell motility by binding with HA and other ECM components.[322–324] Additionally, CD44 is indispensable during the processes of intravasation and extravasation, because it regulates binding of the cancer cell to endothelial cells.[325]

While RHAMM has been less well studied than CD44 in the progression of cancer metastasis, the research that has been produced shows that it is probably just as important in this process and probably plays a larger role in cell motility than does CD44. Increased RHAMM expression is correlated with metastases in colorectal cancer, among others.[326,327] Mechanistically, RHAMM promotes cell motility through a number of different pathways. As is seen with CD44, RHAMM can promote focal adhesion turnover by controlling FAK phosphorylation and by cooperating with the $\alpha_4\beta_1$ and $\alpha_5\beta_1$ integrins.[328,329] RHAMM also activates a number of downstream kinases including Erk 1/2 through the mitogen-activated protein kinase (MAPK) pathway, pp60 (c-src), and the downstream targets of Rho kinase (ROK).[330–332]

Finally, once a metastatic lesion has been established, RHAMM can cooperate with CD44 to promote angiogenesis by promoting migration of neighboring endothelial cells towards the tumor.[333]

The understanding of HA in cancer biology has led to successful clinical use of HA for cancer treatment. For example, to improve the treatment of tumors, Halozyme Therapeutics[334] uses recombinant human HAase (PH-20) to temporarily degrade HA, thereby facilitating the penetration and diffusion of other drugs and fluids that are injected under the skin. The use of HA by Tracey Brown and her team as drug carriers[335] for the treatment of cancer has been successfully demonstrated in clinical trials.[336]

1.3.6 HA in biomedical applications

The ubiquitous presence of HA in various tissues, combined with its inherent biocompatibility and biodegradability, has motivated researchers to explore the utility of HA-based materials for tissue growth, repair and regeneration.[181,337] In this special issue, Segura and colleagues have summarized strategies for preparing HA-based hydrogel scaffolds with desired cell-instructive features for tissue engineering and regenerative medicine applications. Many HA-derived medical products have been developed and tested, and readers are referred to recent reviews[104,338] for in-depth analyses. This paper highlights the present authors' own experiences in the application of HA-based hydrogels for the repair and regeneration of healthy functional tissues, such as vocal folds,[117,339–341] cartilage[342,343] and salivary glands,[344,345] as well as the creation of pathological tissue models, such as tumor spheroids.[113,346,347]

Using chemically modified HA derivatives as modular building blocks, the present authors have engineered HA hydrogel particles (HGPs) and complex networks

with defined biological functions and robust mechanical properties.[181] For example, nanoporous, micron-sized HA HGPs were synthesized using different inverse emulsion systems and crosslinking reactions. The resultant particles either contained residual functional groups or were rendered reactive by subsequent chemical modifications. HA-based doubly crosslinked networks (DXNs) were synthesized via covalent crosslinking of HA HGPs with soluble HA macromers carrying mutually reactive functional groups. These hybrid matrices are hierarchical in nature, consisting of densely crosslinked HGPs integrated in a loosely connected secondary matrix.[340] Their mechanical properties and degradation kinetics can be readily tuned by varying the particle size, functional group density and intra- and inter-particle crosslinking. Using a custom-designed torsional wave apparatus,[348] the present authors demonstrated that the viscoelastic properties of HA DXNs can be matched to those of the vocal fold tissue samples[349] at frequencies close to human phonation. Thus, these materials are attractive injectables for the elimination of vocal fold scarring.[117,340] Separately, HA hydrogels containing self-assembled collagen fibrils provide instructive matrices for the three-dimensional (3-D) culture of primary vocal fold fibroblasts (PVFFs). PVFFs are found to attach and spread in the matrix and proliferate readily. TWA analysis suggests that PVFFs residing in gels alter the matrix organization, chemical compositions and viscoelasticity through cell-mediated remodeling processes.[341]

HA-based complex networks have also been evaluated for the repair of cartilage and the regeneration of the cartilage–bone interface. In this context, the nanoporous HA HGPs are ideal growth factor depots for chondrogenic cytokines and growth factors. To improve the biological functions of HA HGPs, perlecan/HSPG2

domain I (PlnDI), a basement membrane proteoglycan that has strong affinity for various heparin (HP) binding growth factors, was successfully conjugated to the particles through the core protein via a flexible poly(ethylene glycol) (PEG) linker. The immobilized PlnDI maintains its ability to bind bone morphogenetic proteins (BMP-2) and modulates its release.[118] The chondrogenic potential of the HGPs and the stimulatory effects of the injectable formulation were confirmed in vitro using micromass culture of multipotent MSCs and in vivo in a reversible animal model of osteoarthritis (OA). Finally, cell-adhesive HA DXNs were fabricated by encapsulating gelatin or collagen-like peptide-decorated HA HGPs in a secondary HA matrix.[121] Human MSCs were shown to adhere to the composite matrix through the focal adhesion sites clustered on particle surfaces. The cell-adhesive composite matrices supported hMSC proliferation and migration into the gels. Human MSCs were undifferentiated during the early time points of culture. However, they differentiated into osteoblast phenotype after 28 days of culture.[122]

Cartilage is routinely exposed to regular compression during locomotion. Integrating mechano-responsive elements in HA hydrogels is a novel strategy to harvest the compressive forces in the tissue to direct cellular behavior effectively. To achieve this goal, self-assembled block copolymer micelles (BCMs) containing a hydrophobic, rubbery core and a hydrophilic shell with chemically addressable groups were used as the dynamic building blocks and microscopic crosslinkers.[350,93] Covalent integration of dexamethasone (DEX)-loaded BCMs in HA gels significantly reduced the initial burst release and provided sustained DEX release over a prolonged period. Importantly, DEX release from BCM-HA gels was accelerated by intermittently applied external compression in a strain-dependent manner. Culturing

macrophages in the presence of DEX-releasing BCM-HA gels significantly reduced cellular production of inflammatory cytokines, possibly through the synergistic actions of HA and the released DEX.[351] Incorporating mechano-responsive modules in synthetic matrices offers a novel strategy to harvest mechanical stress present in the healing wounds to initiate tissue repair.

Although not present at high levels in healthy salivary glands, the biocompatibility and the bioactivity of HA motivated the present authors to investigate HA-based gels for the creation of artificial salivary glands for the treatment of xerostomia, or dry mouth. Parotid cells encapsulated in 3-D HA hydrogels self-assembled into acini-like structures and expressed functional neurotransmitter receptors.[345] Structures in 3-D hydrogels merged to form organized 50 ım spheroids that could be maintained in culture for over 100 days and merged to form structures over 500 ım in size. Treatment of acini-like structures with the badrenergic agonists increased granule production and α-amylase staining in treated structures, demonstrating regain of protein secretion. Upon treatment with the M3 muscarinic agonist acetylcholine, acini-like structures activated the fluid production pathway by increasing intracellular calcium levels. Encapsulated cells in 3-D retained their spheroid structure and structural integrity, along with the salivary biomarkers, and maintained viability for over 3 weeks in vivo. Thus, the HA hydrogels are capable of maintaining for long periods in vitro functional 3-D salivary spheroid structures that retain both fluid and protein secreting functions and are suitable for tissue restoration.[345]

The utility of HA-based matrices for the engineering of healthy replacement tissues has been expanded to the construction of pathological tissue models. The

present authors have developed a biologically relevant hydrogel culture system[113] that recaptures the essential feature of PCa and its associated stroma. Cell-laden hydrogels were prepared by mixing HA derivatives carrying complementary reactive groups. The resultant viscoelastic hydrogels are biodegradable and can interact with PCa cells through its receptors, activating specific signaling pathways.[346] PCa cells entrapped in HA matrices formed distinct multicellular aggregates, which grew and merged, reminiscent of real tumors, whereas cells cultured on a two-dimensional (2-D) monolayer adopted an atypical spread-out morphology.

The engineered tumor model was used successfully to test the efficacy of anti-cancer drugs, including camptothecin, docetaxel and rapamycin, alone and in combination, including specificity, dose and time responses. Responses of cells to anti-neoplastics differed between the 3-D HA hydrogel and 2-D monolayer systems.[113] The engineered tumor models also have the potential to provide predictable results for the in vivo assessment of nanomedicine. Specifically, doxorubicin (Dox)-loaded nanoparticles (NPs) with an average diameter of 54 ± 1 nm were able to diffuse into the hydrogel matrices, reach and penetrate into the tumoroids, be internalized by LNCaP PCa cells through caveolae-mediated endocytosis and macropinocytosis pathways, and finally release the drug intracellularly. A drug efficacy study revealed that LNCaP PCa cells cultured in the 3-D hydrogel were more resistant to Dox in both soluble and NP-based form than were cells on 2-D culture. In addition, the NP-based Dox formulation may bypass the drug efflux function of MRP1, thereby partially reversing drug resistance in 3-D cultures.[138]

To simulate the tumor–stroma cross-talk, a bilayer construct was developed and characterized. The top hydrogel layer contains HP-decorated, HA-based HGPs

presenting HP-binding epidermal growth factor-like growth factor (HB-EGF) in a sustained manner. LNCaP cells were embedded within the bottom hydrogel layer and received growth stimuli from the top. It was demonstrated that tumoroids grown in bilayer HA hydrogels reflect features reminiscent of native carcinoma, and exhibit promising angiogenic potential through the upregulation of pro-angiogenic factors, at both gene and protein levels. These structured 3-D units provide a novel means to study cancer and stroma invasiveness, cell–cell interactions and drug responses.[347]

To study the individual functions of HA interacting proteins in PCa motility through connective tissues, the present authors have developed an invasion assay[346] based on the 3-D HA hydrogel, which provides a flexible, quantifiable and physiologically relevant alternative to current methods. Metastatic PCa cells in these hydrogels develop fingerlike structures, ‘‘invadopodia’’, consistent with their invasive properties. The number of invadopodia, as well as cluster size, shape and convergence, can provide a quantifiable measure of invasive potential. It was found that culture in the HA hydrogel triggers invasive PCa cells to differentially express and localize RHAMM/CD168 which, in the absence of CD44, appears to contribute to PCa motility and invasion by interacting with the HA hydrogel components. PCa cell invasion through the HA hydrogel also was found to depend on the activity of HAases. While HAase activity was necessary for invadopodia and interconnecting cluster formation, activity alone was not sufficient for acquisition of invasiveness to occur. The results suggest that development of invasive behavior in 3-D HA-based systems requires development of additional cellular features, such as activation of motility associated pathways that regulate formation of invadopodia.

1.3.7 Summary and outlook

This review highlights the fundamental functions of HA in the context of biological systems, as a structural support and a signaling molecule. HA biosynthesis, tissue turnover and homeostasis are coordinately maintained by three synthases and several HAases. Traditionally known as an ECM molecule, HA is also found pericellularly and intracellularly, although its intracellular function is largely speculative. HA provides structural frameworks for cells, functions as an extracellular molecule transmitting signals, and regulates a variety of cell behaviors, including cell adhesion, motility, growth and differentiation. Binding of HA to cell surface receptors activates various intracellular signaling cascades, such as c-Src, Ras and MAPKs,[236] thereby regulating cell growth and survival, cytoskeletal rearrangement and active cell migration. The biological functions of HA depend on the molecular size of HA, the HA binding proteins, its spatial and temporal distribution in tissues, and the cellular background and tissue stages. Mounting evidence confirms the involvement of HA in morphogenesis and wound healing, and its role in cancer progression and metastasis.

HA has been widely used by the biomedical community as a starting material for the fabrication of hydrogel matrices, tissue engineering tools, drug delivery vehicles or drug depot systems, and tissue filler or surgical devices.[180,352–354] HA-based materials may impart biological activity to cells, as evidenced by changes in cellular behavior, owing to the cells' ability to interact with biomaterials based on HA compared with synthetic polymers, such as PEG. For example, the ability of HA to maintain stem cells in an undifferentiated state[355] and the involvement of HA-interacting proteins in tumor metastasis in HA gels[346] have been investigated. In drug delivery, the ability of HA to bind cell surface receptors has been explored for drug targeting purposes.[335] Notably, excessive chemical modification of HA alters its

biological functions. Real-time imaging of quantum dot (QD)-tagged HA derivatives revealed that HA-QD conjugates with 35 mol.% HA modification maintained the ability to bind HA receptors and accumulated mainly in the liver, while those with 68 mol.% HA modification lost many HA characteristics and were evenly distributed throughout the body.[356]

Considering the complexity of the biological functions of HA, particularly the connection with pathologies including inflammation and cancer, care must be taken to ensure the long-term safety of HA-based biomaterials. For example, the intra-articular injection of HA is widely used for symptomatic knee OA. In a systematic review of randomized trials in any language, comparing visco supplementation with sham or non-intervention control in adults with knee OA, Reichenbach and co-workers found that, in patients with knee OA, visco supplementation is associated with a small and clinically irrelevant benefit and an increased risk of serious adverse events. The authors cautioned that trial quality was generally low, and safety data were often not reported.[357] Concerns also exist for using HA-based materials for cell delivery and other modalities in tissue engineering as potentially causing/exacerbating cell migration and metastasis of the residual tumor cells following chemotherapy.[358] In a landmark paper, Khaldoyanidi's team[359] provided experimental evidence that HA treatment does not stimulate but delays the growth of residual cancer cells, which is an important parameter in establishing whether the use of HA can enhance current chemotherapeutic strategies. As researchers continue to unravel the complex functions of HA under different biological conditions and disease states, advanced engineering strategies and surgical interventions will lead to the potential utility of HA-based materials in translational applications.

1.4 Dissertation Summary

In this dissertation, we report on the design of a novel interfacial, diffusion-controlled crosslinking platform which can be utilized to fabricate covalently crosslinked hydrogel spheres and channels with 3D spatial patterns for *in vitro* tissue engineering models. In **Chapter 1**, several topics relevant to this work including modular and orthogonal reactions and their application in tissue engineering[360] and the biology and utility of Hyaluronic Acid in tissue engineering was introduced.[361] In **Chapter 2**, the interfacial, diffusion-controlled crosslinking platform fueled by the rapid bioorthogonal tetrazine *trans*-cyclooctene (TCO) ligation was first displayed. Proof of concept methods for the formation of hydrogel spheres and hydrogel channels were provided. Using this platform, 3D spatial patterning of a TCO conjugated fluorophore was achieved without external triggers or templates. Prostate cancer cells maintain high viability, proliferate readily, and form large tissue-like aggregates when encapsulated in the hydrogel spheres. In **Chapter 3**, 3D spatial patterning of hydrogel spheres was further explored. Incorporation of MMP-degradable and cell adhesive peptides in the 3D microenvironment compared to a blank hydrogel was reflected in the response of 3D encapsulated hMSCs. The utility of using a mono functional capper molecule to alter the modulus of desired regions was characterized by a custom micromaterials tester. Further, core-shell patterns within the microspheres of varying degradability, adhesiveness, and stiffness were described and the response of encapsulated hMSCs in each region in terms of morphology, alignment and viability was assessed. In **Chapter 4**, the liquid-filled hydrogel channels were further explored. 3D spatial patterning within the channel wall was shown by perfusion of TCO conjugated molecules into the lumen of the channel with subsequent diffusion through the channel wall. 3D spatial patterning of different cell populations was shown

through time-dependent altering of the cell laden HA-Tz reservoir. Vascular endothelial cells, smooth muscle cells, and adventitial fibroblasts maintained high viability and were able to be patterned in to the hydrogel channels in anatomically relevant order. In **Chapter 5**, this dissertation work is concluded by summarizing key discoveries and potential impact this has had on the field. Also, future directions are provided for further investigations using the described systems.

REFERENCES

[1] B. Alberts, A. Johnson, J. Lewis, M. Raff, K. Roberts, P. Walter, *New York Garland, Sci.* **2002**, *4th ed.*

[2] E. F. Hounsell, M. J. Davies, D. V Renouf, *Glycoconj. J.* **1996**, *13*, 19.

[3] L. L. Kiessling, J. E. Gestwicki, L. E. Strong, *Curr. Opin. Chem. Biol.* **2000**, *4*, 696.

[4] B. Vrhovski, A. S. Weiss, *Eur. J. Biochem.* **1998**, *258*, 1.

[5] P. Friedl, E. B. Brocker, *Cell. Mol. Life Sci.* **2000**, *57*, 41.

[6] J. Gosline, M. Lillie, E. Carrington, P. Guerette, C. Ortlepp, K. Savage, *Phil. Trans. R. Soc. Lond. B* **2002**, *357*, 121.

[7] F. Rosso, A. Giordano, M. Barbarisi, A. Barbarisi, *J. Cell. Physiol.* **2004**, *199*, 174.

[8] T. H. Barker, *Biomaterials* **2011**, *32*, 4211.

[9] G. W. M. Vandermeulen, H. A. Klok, *Macromol. Biosci.* **2004**, *4*, 383.

[10] M. P. Lutolf, J. A. Hubbell, *Nat. Biotechnol.* **2005**, *23*, 47.

[11] X. Jia, K. L. Kiick, *Macromol. Biosci.* **2009**, *9*, 140.

[12] M. A. Azagarsamy, K. S. Anseth, *ACS Macro Lett.* **2013**, *2*, 5.

[13] R. K. Iha, K. L. Wooley, A. M. Nystrom, D. J. Burke, M. J. Kade, C. J. Hawker, *Chem. Rev.* **2009**, *109*, 5620.

[14] C. J. Hawker, K. L. Wooley, *Science (80-.).* **2005**, *309*, 1200.

[15] C. P. Ramil, Q. Lin, *Chem. Commun.* **2013**, *49*, 11007.

[16] M. King, A. Wagner, *Bioconjug. Chem.* **2014**, *25*, 825.

[17] C. S. McKay, M. G. Finn, *Chem. Biol.* **2014**, *21*, 1075.

[18] H. W. Shih, D. N. Kamber, J. A. Prescher, *Curr. Opin. Chem. Biol.* **2014**, *21*, 103.

[19] A. Dirksen, P. E. Dawson, *Bioconj. Chem.* **2008**, *19*, 2543.

[20] S. Ulrich, D. Boturyn, A. Marra, O. Renaudet, P. Dumy, *Chem. Eur. J.* **2014**, *20*, 34.

[21] B. D. Mather, K. Viswanathan, K. M. Miller, T. E. Long, *Prog. Polym. Sci.* **2006**, *31*, 487.

[22] C. E. Hoyle, C. N. Bowman, *Angew. Chemie-International Ed.* **2010**, *49*, 1540.

[23] M. Ghirardello, K. Oberg, S. Staderini, O. Renaudet, N. Berthet, P. Dumy, Y. Hed, A. Marra, M. Malkoch, A. Dondoni, *J. Polym. Sci. Part a-Polymer Chem.* **2014**, *52*, 2422.

[24] K. C. Nicolaou, S. A. Snyder, T. Montagnon, G. Vassilikogiannakis, *Angew. Chemie-International Ed.* **2002**, *41*, 1668.

[25] A. Sanyal, *Macromol. Chem. Phys.* **2010**, *211*, 1417.

[26] H. C. Kolb, M. G. Finn, K. B. Sharpless, *Angew. Chem., Int. Ed.* **2001**, *40*, 2004.

[27] N. J. Agard, J. A. Prescher, C. R. Bertozzi, *J. Am. Chem. Soc.* **2004**, *126*, 15046.

[28] E. M. Sletten, C. R. Bertozzi, *Acc. Chem. Res.* **2011**, *44*, 666.

[29] N. K. Devaraj, R. Weissleder, *Acc. Chem. Res.* **2011**, *44*, 816.

[30] A.-C. Knall, C. Slugovc, *Chem. Soc. Rev.* **2013**, *42*, 5131.

[31] R. Selvaraj, J. M. Fox, *Curr. Opin. Chem. Biol.* **2013**, *17*, 753.

[32] G. T. Hermanson, *Bioconjugate Techniques*, Elsevier/Academic Press, Amsterdam, **2008**.

[33] A. Dirksen, S. Dirksen, T. M. Hackeng, P. E. Dawson, *J. Am. Chem. Soc.* **2006**, *128*, 15602.

[34] E. T. Kool, D. H. Park, P. Crisalli, *J. Am. Chem. Soc.* **2013**, *135*, 17663.

[35] P. Schmidt, L. N. Zhou, K. Tishinov, K. Zimmermann, D. Gillingham, *Angew. Chemie-International Ed.* **2014**, *53*, 10928.

[36] J. Kalia, R. T. Raines, *Angew. Chemie-International Ed.* **2008**, *47*, 7523.

[37] S. C. Rizzi, M. Ehrbar, S. Halstenberg, G. P. Raeber, H. G. Schmoekel, H. Hagenmuller, R. Muller, F. E. Weber, J. A. Hubbell, *Biomacromolecules* **2006**, *7*, 3019.

[38] A. D. Baldwin, K. L. Kiick, *Bioconjug. Chem.* **2011**, *22*, 1946.

[39] C. E. Hoyle, T. Y. Lee, T. Roper, *J. Polym. Sci. Part a-Polymer Chem.* **2004**, *42*, 5301.

[40] A. B. Lowe, *Polym. Chem.* **2014**, *5*, 4820.

[41] B. H. Northrop, R. N. Coffey, *J. Am. Chem. Soc.* **2012**, *134*, 13804.

[42] M. H. Stenzel, *ACS Macro Lett.* **2013**, *2*, 14.

[43] A. Gandini, *Prog. Polym. Sci.* **2013**, *38*, 1.

[44] X. X. Chen, M. A. Dam, K. Ono, A. Mal, H. B. Shen, S. R. Nutt, K. Sheran, F. Wudl, *Science (80-.).* **2002**, *295*, 1698.

[45] A. J. Inglis, L. Nebhani, O. Altintas, F. G. Schmidt, C. Barner-Kowollik, *Macromolecules* **2010**, *43*, 5515.

[46] R. Berg, B. F. Straub, *Beilstein J. Org. Chem.* **2013**, *9*, 2715.

[47] S. I. Presolski, V. Hong, S. H. Cho, M. G. Finn, *J. Am. Chem. Soc.* **2010**, *132*, 14570.

[48] P. Appukkuttan, V. P. Mehta, E. V Van der Eycken, *Chem. Soc. Rev.* **2010**, *39*, 1467.

[49] V. Hong, S. I. Presolski, C. Ma, M. G. Finn, *Angew. Chemie-International Ed.* **2009**, *48*, 9879.

[50] T. R. Chan, R. Hilgraf, K. B. Sharpless, V. V Fokin, *Org. Lett.* **2004**, *6*, 2853.

[51] D. S. del Amo, W. Wang, H. Jiang, C. Besanceney, A. C. Yan, M. Levy, Y. Liu, F. L. Marlow, P. Wu, *J. Am. Chem. Soc.* **2010**, *132*, 16893.

[52] C. Besanceney-Webler, H. Jiang, T. Q. Zheng, L. Feng, D. S. del Amo, W. Wang, L. M. Klivansky, F. L. Marlow, Y. Liu, P. Wu, *Angew. Chemie-International Ed.* **2011**, *50*, 8051.

[53] C. Uttamapinant, A. Tangpeerachaikul, S. Grecian, S. Clarke, U. Singh, P. Slade, K. R. Gee, A. Y. Ting, *Angew. Chemie-International Ed.* **2012**, *51*, 5852.

[54] C. Uttamapinant, M. I. Sanchez, D. S. Liu, J. Z. Yao, A. Y. Ting, *Nat. Protoc.* **2013**, *8*, 1620.

[55] G. J. Brewer, *Chem. Res. Toxicol.* **2010**, *23*, 319.

[56] P. Kay, J. R. Wagner, H. Gagnon, R. Day, K. Klarskov, *Chem. Res. Toxicol.* **2013**, *26*, 1333.

[57] J. M. Baskin, J. A. Prescher, S. T. Laughlin, N. J. Agard, P. V Chang, I. A. Miller, A. Lo, J. A. Codelli, C. R. Bertozzi, *Proc. Natl. Acad. Sci.* **2007**, *104*, 16793.

[58] J. C. Jewett, C. R. Bertozzi, *Chem. Soc. Rev.* **2010**, *39*, 1272.

[59] M. L. Blackman, M. Royzen, J. M. Fox, *J. Am. Chem. Soc.* **2008**, *130*, 13518.

[60] F. Thalhammer, U. Wallfahrer, J. Sauer, *Tetrahedron Lett.* **1990**, *31*, 6851.

[61] M. T. Taylor, M. L. Blackman, O. Dmitrenko, J. M. Fox, *J. Am. Chem. Soc.* **2011**, *133*, 9646.

[62] K. Lang, L. Davis, S. Wallace, M. Mahesh, D. J. Cox, M. L. Blackman, J. M. Fox, J. W. Chin, *J. Am. Chem. Soc.* **2012**, *134*, 10317.

[63] N. K. Devaraj, R. Weissleder, S. A. Hilderbrand, *Bioconj. Chem.* **2008**, *19*, 2297.

[64] D. N. Kamber, L. A. Nazarova, Y. Liang, S. A. Lopez, D. M. Patterson, H.-W. Shih, K. N. Houk, J. A. Prescher, *J. Am. Chem. Soc.* **2013**, *135*, 13680.

[65] D. M. Patterson, K. A. Jones, J. A. Prescher, *Mol. Biosyst.* **2014**, *10*, 1693.

[66] D. M. Patterson, L. A. Nazarova, B. Xie, D. N. Kamber, J. A. Prescher, *J. Am. Chem. Soc.* **2012**, *134*, 18638.

[67] A. Sachdeva, K. H. Wang, T. Elliott, J. W. Chin, *J. Am. Chem. Soc.* **2014**, *136*, 7785.

[68] J. Seckute, J. Yang, N. K. Devaraj, *Nucleic Acids Res.* **2013**, *41*, 9.

[69] J. Yang, J. Šečkutė, C. M. Cole, N. K. Devaraj, *Angew. Chem. Int. Ed.* **2012**, *51*, 7476.

[70] W. Chen, D. Wang, C. Dai, D. Hamelberg, B. Wang, *Chem. Commun.* **2012**, *48*, 1736.

[71] M. R. Karver, R. Weissleder, S. A. Hilderbrand, *Angew. Chem. Int. Ed.* **2012**, *51*, 920.

[72] A. Niederwieser, A.-K. Späte, L. D. Nguyen, C. Jüngst, W. Reutter, V. Wittmann, *Angew. Chem. Int. Ed.* **2013**, *52*, 4265.

[73] J. B. Haun, N. K. Devaraj, S. A. Hilderbrand, H. Lee, R. Weissleder, *Nat. Nano.* **2010**, *5*, 660.

[74] E. J. Keliher, T. Reiner, A. Turetsky, S. A. Hilderbrand, R. Weissleder, *ChemMedChem* **2011**, *6*, 424.

[75] C. F. Hansell, P. Espeel, M. M. Stamenovic, I. A. Barker, A. P. Dove, F. E. Du Prez, R. K. O'Reilly, *J. Am. Chem. Soc.* **2011**, *133*, 13828.

[76] D. L. Alge, M. A. Azagarsamy, D. F. Donohue, K. S. Anseth, *Biomacromolecules* **2013**, *14*, 949.

[77] A. M. . Cok, H. . Zhou, J. A. Johnson, *Macromol. Symp.* **2013**, *329*, 108.

[78] H. Zhang, K. T. Dicker, X. Xu, X. Jia, J. M. Fox, *ACS Macro Lett.* **2014**, *3*, 727.

[79] E. Saxon, C. R. Bertozzi, *Science (80-.).* **2000**, *287*, 2007.

[80] B. L. Nilsson, L. L. Kiessling, R. T. Raines, *Org. Lett.* **2000**, *2*, 1939.

[81] P. E. Dawson, T. W. Muir, I. Clarklewis, S. B. H. Kent, *Science (80-.).* **1994**, *266*, 776.

[82] R. W. Armstrong, A. P. Combs, P. A. Tempest, S. D. Brown, T. A. Keating, *Acc. Chem. Res.* **1996**, *29*, 123.

[83] C. O. Kappe, *Molecules* **1998**, *3*, 1.

[84] B. Yang, Y. Zhao, S. Q. Wang, Y. L. Zhang, C. K. Fu, Y. Wei, L. Tao, *Macromolecules* **2014**, *47*, 5607.

[85] K. M. Koeller, C. H. Wong, *Nature* **2001**, *409*, 232.

[86] M. P. Lutolf, J. L. Lauer-Fields, H. G. Schmoekel, A. T. Metters, F. E. Weber, G. B. Fields, J. A. Hubbell, *Proc. Natl. Acad. Sci.* **2003**, *100*, 5413.

[87] C. J. Kloxin, C. N. Bowman, *Chem. Soc. Rev.* **2013**, *42*, 7161.

[88] K. Ulbrich, V. Subr, P. Podperova, M. Buresova, *J. Control. Release* **1995**, *34*, 155.

[89] S. Sahoo, C. Chung, S. Khetan, J. A. Burdick, *Biomacromolecules* **2008**, *9*, 1088.

[90] A. M. Kloxin, A. M. Kasko, C. N. Salinas, K. S. Anseth, *Science (80-.).* **2009**, *324*, 59.

[91] P. M. Kharkar, K. L. Kiick, A. M. Kloxin, *Chem. Soc. Rev.* **2013**, *42*, 7335.

[92] M. P. Lutolf, G. P. Raeber, A. H. Zisch, N. Tirelli, J. A. Hubbell, *Adv. Mater.* **2003**, *15*, 888.

[93] L. X. Xiao, J. H. Zhu, J. D. Londono, D. J. Pochan, X. Q. Jia, *Soft Matter* **2012**, *8*, 10233.

[94] J. M. Hu, G. Q. Zhang, S. Y. Liu, *Chem. Soc. Rev.* **2012**, *41*, 5933.

[95] A. Higuchi, Q. D. Ling, S. S. Kumar, Y. Chang, T. C. Kao, M. A. Munusamy, A. A. Alarfaj, S. T. Hsu, A. Umezawa, *Prog. Polym. Sci.* **2014**, *39*, 1585.

[96] P. M. Kharkar, A. M. Kloxin, K. L. Kiick, *J. Mater. Chem. B* **2014**, *2*, 5511.

[97] C. A. DeForest, B. D. Polizzotti, K. S. Anseth, *Nat. Mater.* **2009**, *8*, 659.

[98] C. Mangold, F. Wurm, H. Frey, *Polym. Chem.* **2012**, *3*, 1714.

[99] B. Schulte, A. Walther, H. Keul, M. Moller, *Macromolecules* **2014**, *47*, 1633.

[100] A. Thomas, S. S. Muller, H. Frey, *Biomacromolecules* **2014**, *15*, 1935.

[101] H. B. Jin, W. Huang, X. Y. Zhu, Y. F. Zhou, D. Y. Yan, *Chem. Soc. Rev.* **2012**, *41*, 5986.

[102] M. A. Serban, G. D. Prestwich, *Methods* **2008**, *45*, 93.

[103] K. T. Dicker, L. A. Gurski, S. Pradhan-Bhatt, R. L. Witt, M. C. Farach-Carson, X. Jia, *Acta Biomater.* **2014**, *10*, 1558.

[104] J. A. Burdick, G. D. Prestwich, *Adv. Mater.* **2011**, *23*, H41.

[105] X. Xu, A. K. Jha, D. a Harrington, M. C. Farach-Carson, X. Jia, *Soft Matter* **2012**, *8*, 3280.

[106] K. Chawla, T. B. Yu, L. Stutts, M. Yen, Z. B. Guan, *Biomaterials* **2012**, *33*, 6052.

[107] A. M. Kushner, Z. B. Guan, *Angew. Chemie-International Ed.* **2011**, *50*, 9026.

[108] S. W. Liao, J. Rawson, K. Omori, K. Ishiyama, D. Mozhdehi, A. R. Oancea, T. Ito, Z. B. Guan, Y. Mullen, *Biomaterials* **2013**, *34*, 3984.

[109] M. Metzke, N. O'Connor, S. Maiti, E. Nelson, Z. B. Guan, *Angew. Chemie-International Ed.* **2005**, *44*, 6529.

[110] J. T. Roland, Z. Guan, *J Am Chem Soc* **2004**, *126*, 14328.

[111] S. W. Liao, T. B. Yu, Z. B. Guan, *J. Am. Chem. Soc.* **2009**, *131*, 17638.

[112] X. Jia, G. Colombo, R. Padera, R. Langer, D. S. Kohane, *Biomaterials* **2004**, *25*, 4797.

[113] L. A. Gurski, A. K. Jha, C. Zhang, X. Jia, M. C. Farach-Carson, *Biomaterials* **2009**, *30*, 6076.

[114] L. A. Gurski, X. Xu, L. N. Labrada, N. T. Nguyen, L. X. Xiao, K. L. van Golen, X. Q. Jia, M. C. Farach-Carson, *PLoS One* **2012**, *7*, e50075.

[115] X. Xu, M. C. Farach-Carson, X. Jia, *Biotechnol. Adv.* **2014**, *32*, 1256.

[116] A. J. Farran, S. S. Teller, A. K. Jha, T. Jiao, R. A. Hule, R. J. Clifton, D. P. Pochan, R. L. Duncan, X. Jia, *Tissue Eng Part A* **2010**, *16*, 1247.

[117] X. Jia, Y. Yeo, R. J. Clifton, T. Jiao, D. S. Kohane, J. B. Kobler, S. M. Zeitels, R. Langer, *Biomacromolecules* **2006**, *7*, 3336.

[118] A. K. Jha, W. Yang, C. B. Kirn-Safran, M. C. Farach-Carson, X. Jia, *Biomaterials* **2009**, *30*, 6964.

[119] A. K. Jha, R. a Hule, T. Jiao, S. S. Teller, R. J. Clifton, R. L. Duncan, D. J. Pochan, X. Jia, *Macromolecules* **2009**, *42*, 537.

[120] A. K. Jha, M. S. Malik, M. C. Farach-Carson, R. L. Duncan, X. Jia, *Soft Matter* **2010**, *6*, 5045.

[121] O. D. Krishna, A. K. Jha, X. Jia, K. L. Kiick, *Biomaterials* **2011**, *32*, 6412.

[122] A. K. Jha, X. Xu, R. L. Duncan, X. Jia, *Biomaterials* **2011**, *32*, 2466.

[123] M. Patenaude, T. Hoare, *Biomacromolecules* **2012**, *13*, 369.

[124] K. Y. Lee, K. H. Bouhadir, D. J. Mooney, *Macromolecules* **2000**, *33*, 97.

[125] D. D. McKinnon, D. W. Domaille, J. N. Cha, K. S. Anseth, *Chem. Mater.* **2014**, *26*, 2382.

[126] D. D. McKinnon, D. W. Domaille, J. N. Cha, K. S. Anseth, *Adv. Mater.* **2014**, *26*, 865.

[127] X. Z. Shu, Y. C. Liu, F. Palumbo, G. D. Prestwich, *Biomaterials* **2003**, *24*, 3825.

[128] X. Z. Shu, Y. C. Liu, F. S. Palumbo, Y. Lu, G. D. Prestwich, *Biomaterials* **2004**, *25*, 1339.

[129] X. Z. Shu, G. D. Prestwich, in *Chem. Biol. Hyaluronan* (Eds.: H.G. Garg, C.A. Hales), Elsevier Ltd., Oxford, **2004**, pp. 475–504.

[130] G. D. Prestwich, J. W. Kuo, *Curr. Pharm. Biotechnol.* **2008**, *9*, 242.

[131] K. Ghosh, X. Z. Shu, R. Mou, J. Lombardi, G. D. Prestwich, M. H. Rafailovich, R. A. F. Clark, *Biomacromolecules* **2005**, *6*, 2857.

[132] R. J. Seelbach, P. Fransen, M. Peroglio, D. Pulido, P. Lopez-Chicon, F. Duttenhoefer, S. Sauerbier, T. Freiman, P. Niemeyer, C. Semino, F. Albericio, M. Alini, M. Royo, A. Mata, D. Eglin, *Acta Biomater.* **2014**, *10*, 4340.

[133] J. L. Vanderhooft, M. Alcoutlabi, J. J. Magda, G. D. Prestwich, *Macromol. Biosci.* **2009**, *9*, 20.

[134] L. W. Hosack, M. A. Firpo, J. A. Scott, G. D. Prestwich, R. A. Peattie, *Biomaterials* **2008**, *29*, 2336.

[135] X. Chen, S. L. Thibeault, *Tissue Eng. Part A* **2012**, *18*, 2528.

[136] Y. Lei, S. Gojgini, J. Lam, T. Segura, *Biomaterials* **2011**, *32*, 39.

[137] X. Xu, L. A. Gurski, C. Zhang, D. A. Harrington, M. C. Farach-Carson, X. Jia, *Biomaterials* **2012**, *33*, 9049.

[138] X. Xu, C. R. Sabanayagam, D. a Harrington, M. C. Farach-Carson, X. Jia, *Biomaterials* **2014**, *35*, 3319.

[139] T. Rossow, J. A. Heyman, A. J. Ehrlicher, A. Langhoff, D. A. Weitz, R. Haag, S. Seiffert, *J. Am. Chem. Soc.* **2012**, *134*, 4983.

[140] A. A. Aimetti, A. J. Machen, K. S. Anseth, *Biomaterials* **2009**, *30*, 6048.

[141] J. D. McCall, K. S. Anseth, *Biomacromolecules* **2012**, *13*, 2410.

[142] J. J. Roberts, S. J. Bryant, *Biomaterials* **2013**, *34*, 9969.

[143] S. B. Anderson, C. C. Lin, D. V Kuntzler, K. S. Anseth, *Biomaterials* **2011**, *32*, 3564.

[144] A. Raza, C. S. Ki, C.-C. Lin, *Biomaterials* **2013**, *34*, 5117.

[145] W. M. Gramlich, I. L. Kim, J. A. Burdick, *Biomaterials* **2013**, *34*, 9803.

[146] H. Shih, A. K. Fraser, C. C. Lin, *ACS Appl Mater Interfaces* **2013**, *5*, 1673.

[147] S. C. Owen, S. A. Fisher, R. Y. Tam, C. M. Nimmo, M. S. Shoichet, *Langmuir* **2013**, *29*, 7393.

[148] M. Malkoch, R. Vestberg, N. Gupta, L. Mespouille, P. Dubois, A. F. Mason, J. L. Hedrick, Q. Liao, C. W. Frank, K. Kingsbury, C. J. Hawker, *Chem. Commun.* **2006**, 2774.

[149] Y. Yuan, A. K. Zhang, J. Ling, L. H. Yin, Y. Chen, G. D. Fu, *Soft Matter* **2013**, *9*, 6309.

[150] D. Steinhilber, T. Rossow, S. Wedepohl, F. Paulus, S. Seiffert, R. Haag, *Angew. Chemie-International Ed.* **2013**, *52*, 13538.

[151] K. M. Gattas-Asfura, C. L. Stabler, *Biomacromolecules* **2009**, *10*, 3122.

[152] B. H. Hu, J. Su, P. B. Messersmith, *Biomacromolecules* **2009**, *10*, 2194.

[153] J. Su, B. H. Hu, W. L. Lowe, D. B. Kaufman, P. B. Messersmith, *Biomaterials* **2010**, *31*, 308.

[154] I. Strehin, D. Gourevitch, Y. Zhang, E. Heber-Katz, P. B. Messersmith, *Biomater. Sci.* **2013**, *1*, 603.

[155] M. Ehrbar, S. C. Rizzi, R. Hlushchuk, V. Djonov, A. H. Zisch, J. A. Hubbell, F. E. Weber, M. P. Lutolf, *Biomaterials* **2007**, *28*, 3856.

[156] K. A. Mosiewicz, L. Kolb, A. J. Van Der Vlies, M. M. Martino, P. S. Lienemann, J. A. Hubbell, M. Ehrbar, M. P. Lutolf, *Nat. Mater.* **2013**, *12*, 1072.

[157] K. A. Mosiewicz, K. Johnsson, M. P. Lutolf, *J. Am. Chem. Soc.* **2010**, *132*, 5972.

[158] S. E. Grieshaber, A. K. Jha, A. J. E. farran, X. Jia, in *Biomater. Tissue Eng. A Rev. Past Futur. Trends* (Eds.: J.A. Burdick, R.L. Mauck), Springer, New York, **2011**, pp. 9–46.

[159] M. Guvendiren, J. A. Burdick, *Nat. Commun.* **2012**, *3*, 792.

[160] S. Khetan, M. Guvendiren, W. R. Legant, D. M. Cohen, C. S. Chen, J. A. Burdick, *Nat. Mater.* **2013**, *12*, 458.

[161] F. Lin, J. Y. Yu, W. Tang, J. K. Zheng, A. Defante, K. Guo, C. Wesdemiotis, M. L. Becker, *Biomacromolecules* **2013**, *14*, 3749.

[162] H. Zhou, J. Woo, A. M. Cok, M. Wang, B. D. Olsen, J. a Johnson, *Proc. Natl. Acad. Sci. U. S. A.* **2012**, *109*, 19119.

[163] E. Elacqua, D. S. Lye, M. Weck, *Acc Chem Res* **2014**, *47*, 2405.

[164] W. Palmer, K. M. John, *Ophthalmology* **n.d.**, 629.

[165] K. MEYER, *Fed. Proc.* **1958**, *17*, 1075.

[166] E. A. Balazs, T. C. Laurent, R. W. Jeanloz, *Biochem. J.* **1986**, *235*, 903.

[167] J. R. E. Fraser, T. C. Laurent, U. B. G. Laurent, *J. Intern. Med.* **1997**, *242*, 27.

[168] L. Zhuo, K. Kimata, *Cell Struct. Funct.* **2001**, *26*, 189.

[169] D. Russell, A. Salustri, *Semin. Reprod. Med.* **2006**, *24*, 217.

[170] K. Furukawa, H. Terayama, **1977**, *499*, 278.

[171] R. K. Margolis, C. P. Crockett, W.-L. Kiang, R. U. Margolis, *Biochim. Biophys. Acta* **1976**, *451*, 465.

[172] P. S. Eggli, W. Graber, *J. Histochem. Cytochem.* **1995**, *43*, 689.

[173] S. P. Evanko, T. N. Wight, *J. Histochem. Cytochem.* **1999**, *47*, 1331.

[174] F. W. K. Kan, *Anat. Rec.* **1990**, *228*, 370.

[175] J. A. Ripellino, M. Bailo, R. U. Margolis, R. K. Margolis, *J. Cell Biol.* **1988**, *106*, 845.

[176] V. C. Hascall, A. K. Majors, C. A. De La Motte, S. P. Evanko, A. Wang, J. A. Drazba, S. A. Strong, T. N. Wight, **2004**, DOI 10.1016/j.bbagen.2004.02.013.

[177] N. Itano, K. Kimata, *Semin. Cancer Biol.* **2008**, *18*, 268.

[178] A. Almond, *Cell. Mol. Life Sci.* **2007**, *64*, 1591.

[179] H. G. Garg, C. A. Hales, *Chemistry and Biology of Hyaluronan*, Elsevier Ltd., Oxford, **2004**.

[180] D. D. Allison, K. J. Grande-Allen, *Tissue Eng.* **2006**, *12*, 2131.

[181] X. Xu, A. K. Jha, D. A. Harrington, M. C. Farach-Carson, X. Jia, *Soft Matter* **2012**, *8*, 3280.

[182] T. C. Laurent, J. R. Fraser, *FASEB J.* **1992**, *6*, 2397.

[183] A. P. Spicer, J. A. McDonald, *J. Biol. Chem.* **1998**, *273*, 1923.

[184] P. Prehm, *Ciba Found. Symp.* **1989**, *143*, 21.

[185] N. Itano, T. Sawai, M. Yoshida, P. Lenas, Y. Yamada, M. Imagawa, T. Shinomura, M. Hamaguchi, Y. Yoshida, Y. Ohnuki, S. Miyauchi, A. P. Spicer, J. A. McDonald, K. Kimata, *J. Biol. Chem.* **1999**, *274*, 25085.

[186] K. Rilla, S. Oikari, T. A. Jokela, J. M. T. Hyttinen, R. Kärnä, R. H. Tammi, M. I. Tammi, *J. Biol. Chem.* **2013**, *288*, 5973.

[187] N. Itano, K. Kimata, *IUBMB Life (International Union Biochem. Mol. Biol. Life)* **2002**, *54*, 195.

[188] T. D. Camenisch, J. Biesterfeldt, T. Brehm-Gibson, J. Bradley, J. A. McDonald, *Exp. Clin. Cardiol.* **2001**, *6*, 4.

[189] P. H. Weigel, V. C. Hascall, M. Tammi, *J. Biol. Chem.* **1997**, *272*, 13997.

[190] B. P. Toole, *Semin. Cell Dev. Biol.* **2001**, *12*, 79.

[191] K. Sato, M. Hirano, T. Nakashima, *Ann. Otol. Rhinol. Laryngol.* **2001**, *110*, 417.

[192] S. Gray, *Otolaryngol Clin North Am* **2000**, *33*, 679.

[193] J. . and Lubomír Lapčík, L. Lapčík, §,‖ and Stefaan De Smedt*, J. Demeester§, P. Chabreček, **1998**, DOI 10.1021/CR941199Z.

[194] I. Hargittai, M. Hargittai, *Struct. Chem.* **2008**, *19*, 697.

[195] A. Almond, A. Brass, J. K. Sheehan, **1998**.

[196] J. E. Scott, F. Heatley, *Proc. Natl. Acad. Sci. U. S. A.* **1999**, *96*, 4850.

[197] M. K. Cowman, S. Matsuoka, **n.d.**, DOI 10.1016/j.carres.2005.01.022.

[198] * Mary K. Cowman, and Joan Feder-Davis, D. M. Hittner, **2000**, DOI 10.1021/MA001082E.

[199] M. K. Cowman, C. Spagnoli, D. Kudasheva, M. Li, A. Dyal, S. Kanai, E. A. Balazs, *Biophys. J.* **n.d.**, *88*, 590.

[200] P. Gribbon, B. C. Heng, T. E. Hardingham, *Biophys. J.* **n.d.**, *77*, 2210.

[201] R. W. Chan, I. R. Titze, *http://dx.doi.org/10.1121/1.427947* **1999**, DOI 10.1121/1.427947.

[202] R. W. Chan, I. R. Titze, *http://dx.doi.org/10.1121/1.428354* **1999**, DOI 10.1121/1.428354.

[203] R. W. Chan, S. D. Gray, I. R. Titze, *Otolaryngol. - Head Neck Surg.* **2001**, DOI 10.1067/mhn.2001.115906.

[204] E. A. Turley, *Cancer Metastasis Rev.* **1992**, *11*, 21.

[205] N. Itano, *J. Biochem.* **2008**, *144*, 131.

[206] A. B. Csó, S. W. Scherer, R. Stern, **n.d.**

[207] A. B. Csóka, G. I. Frost, H. H. Heng, S. W. Scherer, G. Mohapatra, R. Stern, T. B. Csóka, *Genomics* **1998**, *48*, 63.

[208] G. I. Frost, T. B. Csóka, T. Wong, R. Stern, **1997**, *236*, 10.

[209] A. B. Csoka, G. I. Frost, R. Stern, **n.d.**

[210] G. Lepperdinger, B. Strobl, G. Kreil, *J. Biol. Chem.* **1998**, *273*, 22466.

[211] S. K. Rai, F. M. Duh, V. Vigdorovich, A. Danilkovitch-Miagkova, M. I. Lerman, A. D. Miller, *Proc. Natl. Acad. Sci. U. S. A.* **2001**, *98*, 4443.

[212] R. Hemming, D. C. Martin, E. Slominski, J. I. Nagy, A. J. Halayko, S. Pind, B. Triggs-Raine, *Glycobiology* **2008**, *18*, 280.

[213] M. F. Meyer, G. Kreil, H. Aschauer, *FEBS Lett.* **1997**, *413*, 385.

[214] E. S. A. Hofinger, J. Hoechstetter, M. Oettl, G. Bernhardt, A. Buschauer, *Glycoconj. J.* **2008**, *25*, 101.

[215] H. Harada, M. Takahashi, *J. Biol. Chem.* **2007**, *282*, 5597.

[216] R. Tammi, K. Rilla, J. P. Pienimaki, D. K. MacCallum, M. Hogg, M. Luukkonen, V. C. Hascall, M. Tammi, *J. Biol. Chem.* **2001**, *276*, 35111.

[217] D. C. Martin, V. Atmuri, R. J. Hemming, J. Farley, J. S. Mort, S. Byers, S. Hombach-Klonisch, R. Stern, B. L. Triggs-Raine, *Hum. Mol. Genet.* **2008**, *17*, 1904.

[218] L. Jadin, X. Wu, H. Ding, G. I. Frost, C. Onclinx, B. Triggs-Raine, B. Flamion, *FASEB J.* **2008**, *22*, 4316.

[219] G. Kogan, L. Šoltés, R. Stern, R. Mendichi, *Pethrick RA, Ballad. A, Zaikov GE, Ed. Handb. Polym. Res. monomers, oligomers, Polym. Compos. Nov. Sci. Publ.* **2007**, 393.

[220] F. Gao, J. R. Koenitzer, J. M. Tobolewski, D. Jiang, J. Liang, P. W. Noble, et al., *J Biol Chem* **2008**, *283*, 6058.

[221] D. Manzanares, M.-E. Monzon, R. C. Savani, M. Salathe, *Am. J. Respir. Cell Mol. Biol.* **2007**, *37*, 160.

[222] R. Moseley, R. J. Waddington, G. Embery, *Biochim. Biophys. Acta* **1997**, *1362*, 221.

[223] H. C. Osterholt, I. Dannevig, M. H. Wyckoff, J. Liao, Y. Akgul, M. Ramgopal, et al., *PLoS One* **2012**, 7:11.

[224] E. Hrabarova, I. Juranek, L. Soltes, *Gen Physiol Biophys* **2011**, *30*, 223.

[225] M. Li, L. Rosenfeld, R. E. Vilar, M. K. Cowman, *Arch. Biochem. Biophys.* **1997**, *341*, 245.

[226] R. Stern, A. A. Asari, K. N. Sugahara, *Eur. J. Cell Biol.* **2006**, *85*, 699.

[227] M. S. Pandey, B. A. Baggenstoss, J. Washburn, E. N. Harris, P. H. Weigel, *J. Biol. Chem.* **2013**, *288*, 14068.

[228] X. Tian, J. Azpurua, C. Hine, A. Vaidya, M. Myakishev-Rempel, J. Ablaeva, et al., *Nature* **2013**, *499*, U122.

[229] R. Stern, *Glycobiology* **2003**, *13*, 105R.

[230] E. A. Turley, *Adv. Drug Deliv. Rev.* **1991**, *7*, 257.

[231] C. B. Knudson, W. Knudson, *FASEB J.* **1993**, *7*, 1233.

[232] B. Yang, B. L. Yang, R. C. Savani, E. A. Turley, *EMBO J.* **1994**, *13*, 286.

[233] D. Kohda, C. J. Morton, A. A. Parkar, *Cell* **1996**, *86*, 767.

[234] K. Amemiya, T. Nakatani, A. Saito, A. Suzuki, H. Munakata, **2005**, DOI 10.1016/j.bbagen.2005.04.029.

[235] A. J. Day, C. A. De La Motte, **n.d.**, DOI 10.1016/j.it.2005.09.009.

[236] E. A. Turley, P. W. Noble, L. Y. W. Bourguignon, *J. Biol. Chem.* **2002**, *277*, 4589.

[237] D. Naor, S. B. Wallach-Dayan, M. A. Zahalka, R. V. Sionov, *Semin. Cancer Biol.* **2008**, *18*, 260.

[238] J. Lesley, N. English, A. Perschl, J. Gregoroff, R. Hyman, *J. Exp. Med.* **1995**, *182*, 431.

[239] C. M. Isacke, H. Yarwood, *Int. J. Biochem. Cell Biol.* **2002**, *34*, 718.

[240] E. A. Turley, *Biochem. Biophys. Res. Commun. Oct.* **1982**, *108*, 1016.

[241] C. A. Maxwell, J. McCarthy, E. Turley, M. Göttlicher, J. Sleeman, R. Plug, N. Howells, O. von Stein, H. Ponta, P. Herrlich, *J. Cell Sci.* **2008**, *121*, 925.

[242] C. A. Maxwell, J. J. Keats, M. Crainie, X. Sun, T. Yen, E. Shibuya, M. Hendzel, G. Chan, L. M. Pilarski, *Mol. Biol. Cell* **2003**, *14*, 2262.

[243] E. A. Turley, L. Austen, K. Vandeligt, C. Clary, *J. Cell Biol.* **1991**, *112*, 1041.

[244] M. Crainie, A. Belch, M. Mant, L. Pilarski, *Blood* **1999**, *93*, 1684.

[245] D. G. Jackson, *Br. Rev. TCM* **2003**, *13*.

[246] S. Banerji, J. Ni, S. X. Wang, S. Clasper, J. Su, R. Tammi, M. Jones, D. G. Jackson, *J. Cell Biol.* **1999**, *144*, 789.

[247] D. G. Jackson, R. Prevo, S. Clasper, S. Banerji, *TRENDS Immunol.* **2001**, *22*.

[248] N. W. Gale, R. Prevo, J. Espinosa, D. J. Ferguson, M. G. Dominguez, G. D. Yancopoulos, G. Thurston, D. G. Jackson, *Mol. Cell. Biol.* **2007**, *27*, 595.

[249] L.-H. Tang, J. A. Buckwalter, L. C. Rosenberg, *J. Orthop. Res.* **1996**, *14*, 334.

[250] A. J. Day, G. D. Prestwich, *J. Biol. Chem.* **2002**, *277*, 4585.

[251] H. Watanabe, S. C. Cheung, N. Itano, K. Kimata, Y. Yamada, *J. Biol. Chem.* **1997**, *272*, 28057.

[252] Y. Yamaguchi, *Cell. Mol. Life Sci.* **2000**, *57*, 276.

[253] T. N. Wight, *Curr. Opin. Cell Biol.* **2002**, *14*, 617.

[254] C. A. De La Motte, V. C. Hascall, J. Drazba, S. K. Bandyopadhyay, S. A. Strong, *Am. J. Pathol.* **2003**, *163*, 121.

[255] L. S. Zhuo, V. C. Hascall, K. Kimata, *J Biol Chem* **2004**, *279*, 38079.

[256] K. W. Sanggaard, C. S. Sonne-Schmidt, T. P. Krogager, T. Kristensen, H. G. Wisniewski, I. B. Thogersen, et al., *J Biol Chem* **2008**, *283*, 33919.

[257] N. S. Baranova, S. J. Foulcer, D. C. Briggs, V. Tilakaratna, J. J. Enghild, C. M. Milner, et al., *J Biol Chem* **2013**, *288*, 29642.

[258] M. E. Lauer, C. Fulop, D. Mukhopadhyay, S. Comhair, S. C. Erzurum, V. C. Hascall, *J. Biol. Chem.* **2009**, *284*, 5313.

[259] C. M. Milner, W. Tongsoongnoen, M. S. Rugg, A. J. Day, *Biochem. Soc. Trans.* **2007**, *35*, 672.

[260] S. P. Evanko, M. I. Tammi, R. H. Tammi, T. N. Wight, **2007**, DOI 10.1016/j.addr.2007.08.008.

[261] D. Mukhopadhyay, A. Asari, M. S. Rugg, A. J. Day, C. Fülöp, *J. Biol. Chem.* **2004**, *279*, 11119.

[262] R. H. Tammi, A. Kultti, V. M. Kosma, R. Pirinen, P. Auvinen, M. I. Tammi, *Semin Cancer Biol* **2008**, *18*, 288.

[263] D. N. Haylock, S. K. Nilsson, *Regen. Med* **2006**, *1*, 437.

[264] M. Choudhary, X. Zhang, P. Stojković, L. Hyslop, G. Anyfantis, M. Herbert, A. P. Murdoch, M. Stojković, M. Lako, *Stem Cells* **2007**, *25*, 3045.

[265] M. F. Pittenger, A. M. Mackay, S. C. Beck, R. K. Jaiswal, R. Douglas, J. D. Mosca, et al., *Science (80-.).* **1999**, *284*, 143.

[266] H. Zhu, N. Mitsuhashi, A. Klein, L. W. Barsky, K. Weinberg, M. L. Barr, A. Demetriou, G. D. Wu, *Stem Cells* **2006**, *24*, 928.

[267] A. K. Lagendijk, A. S. Szabó, R. M. H. Merks, J. Bakkers, *Trends Cardiovasc. Med.* **2013**, *23*, 135.

[268] J. Zhong, A. Chan, L. Morad, H. I. Kornblum, G. Guoping Fan, S. T. Carmichael, *Neurorehabil. Neural Repair* **2010**, *24*, 636.

[269] Y. Li, B. P. Toole, C. N. Dealy, R. A. Kosher, **2007**, DOI 10.1016/j.ydbio.2007.02.023.

[270] K. Matsumoto, Y. Li, C. Jakuba, Y. Sugiyama, T. Sayo, M. Okuno, C. N. Dealy, B. P. Toole, J. Takeda, Y. Yamaguchi, R. A. Kosher, *Development* **2009**, *136*, 2825.

[271] J. Liu, Q. Li, M. R. Kuehn, Y. Litingtung, S. A. Vokes, C. Chiang, *Dev Biol* **2013**, *375*, 160.

[272] W. Y. J. CHEN, G. ABATANGELO, *Wound Repair Regen.* **1999**, *7*, 79.

[273] A. Zaman, Z. Cui, J. P. Foley, H. Zhao, P. C. Grimm, H. M. DeLisser, R. C. Savani, *Am. J. Respir. Cell Mol. Biol.* **2005**, *33*, 447.

[274] R. C. Savani, G. Hou, P. Liu, C. Wang, E. Simons, P. C. Grimm, et al., *Am J Respir Cell Mol Biol* **2000**, *23*, 475.

[275] D. Jiang, J. Liang, J. Fan, S. Yu, S. Chen, Y. Luo, et al., *Nat Med* **2005**, *11*, 1173.

[276] D. Jiang, J. Liang, P. W. Noble, *Annu. Rev. Cell Dev. Biol.* **2007**, *23*, 435.

[277] K. A. Scheibner, M. A. Lutz, S. Boodoo, M. J. Fenton, J. D. Powell, M. R. Horton, *J. Immunol.* **2006**, *177*, 1272.

[278] K. R. Taylor, J. M. Trowbridge, J. A. Rudisill, C. C. Termeer, J. C. Simon, R. L. Gallo, *J Biol Chem* **2004**, *279*, 17079.

[279] K. R. Taylor, K. Yamasaki, K. A. Radek, A. Di Nardo, H. Goodarzi, D. Golenbock, et al., *J Biol Chem* **2007**, *282*, 18265.

[280] K. R. Taylor, R. L. Gallo, *FASEB J.* **2006**, *20*, 9.

[281] G. Abatangelo, R. Cortivo, M. Martelli, P. Vecchia: ', *Exp. Cell Res.* **1982**, *137*, 73.

[282] G. Cao, R. C. Savani, M. Fehrenbach, C. Lyons, L. Zhang, G. Coukos, H. M. Delisser, *Am. J. Pathol.* **2006**, *169*, 325.

[283] M. Slevin, J. Krupinski, J. Gaffney, S. Matou, D. West, H. Delisser, R. C. Savani, S. Kumar, **n.d.**, DOI 10.1016/j.matbio.2006.08.261.

[284] P. L. Bollyky, R. P. Wu, B. A. Falk, J. D. Lord, S. A. Long, A. Preisinger, et al., *Proc Natl Acad Sci U S A* **2011**, *108*, 7938.

[285] H. G. Wisniewski, R. Maier, M. Lotz, S. Lee, L. Klampfer, T. H. Lee, J. Vilcek, *J. Immunol.* **1993**, *151*, 6593.

[286] S. Pasonen-Seppänen, J. M. T. Hyttinen, K. Rilla, T. Jokela, P. W. Noble, M. Tammi, R. Tammi, *Histochem. Cell Biol.* **2012**, *137*, 107.

[287] C. Tolg, S. R. Hamilton, E. Zalinska, L. Mcculloch, R. Amin, N. Akentieva, F. Winnik, R. Savani, D. J. Bagli, L. G. Luyt, M. K. Cowman, J. B. Mccarthy, E. A. Turley, *AJPA* **2012**, *181*, 1250.

[288] B. P. Toole, *Nat. Rev. Cancer* **2004**, *4*, 528.

[289] B. Bernert, H. Porsch, P. Heldin, *J. Biol. Chem.* **2011**, *286*, 42349.

[290] H. Okuda, A. Kobayashi, B. Xia, M. Watabe, S. K. Pai, S. Hirota, F. Xing, W. Liu, P. R. Pandey, K. Fukuda, V. Modur, A. Ghosh, A. Wilber, K. Watabe, *Cancer Res.* **2012**, *72*, 537.

[291] R. Stern, *Trends Glycosci Glycotechnol* **2004**, *16*, 171.

[292] A. G. Bharadwaj, K. Rector, M. A. Simpson, *J. Biol. Chem.* **2007**, *282*, 20561.

[293] F. Gao, C. X. Yang, W. Mo, Y. W. Liu, Y. Q. He, *Clin. Invest. Med.* **2008**, *31*, E106.

[294] F. Gao, P. Okunieff, Z. Han, I. Ding, L. Wang, W. Liu, J. Zhang, S. Yang, J. Chen, C. B. Underhill, S. Kim, L. Zhang, in *Oxyg. Transp. to Tissue XXVI*, Springer-Verlag, New York, **2005**, pp. 249–256.

[295] E. de Maeyer, J. De Maeyer-Guignard, *Int. J. Cancer* **1992**, *51*, 657.

[296] F. Wang, E. V. Grigorieva, J. Li, V. N. Senchenko, T. V. Pavlova, E. A. Anedchenko, A. V. Kudryavtseva, A. Tsimanis, D. Angeloni, M. I. Lerman, V. I. Kashuba, G. Klein, E. R. Zabarovsky, *PLoS One* **2008**, *3*, e3031.

[297] A. H. Aboughalia, **n.d.**, DOI 10.1016/j.arcmed.2005.04.019.

[298] M. W. Kramer, R. Golshani, A. S. Merseburger, J. Knapp, A. Garcia, J. Hennenlotter, R. C. Duncan, M. S. Soloway, M. Jorda, M. A. Kuczyk, A. Stenzl, V. B. Lokeshwar, *Eur. Urol.* **2010**, *57*, 86.

[299] S. Ekici, W. H. Cerwinka, R. Duncan, P. Gomez, F. Civantos, M. S. Soloway, V. B. Lokeshwar, *Int. J. Cancer* **2004**, *112*, 121.

[300] N. Junker, S. Latini, L. N. Petersen, P. E. G. Kristjansen, *Oncol. Rep.* **n.d.**, *10*, 609.

[301] S. Patel, P. R. Turner, C. Stubberfield, E. Barry, C. R. Rohlff, A. Stamps, K. Tyson, J. Terrett, G. Box, S. Eccles, M. J. Page, *Int. J. Cancer* **2002**, *97*, 416.

[302] P. Paiva, M.-P. Van Damme, M. Tellbach, R. L. Jones, T. Jobling, L. A. Salamonsen, *Gynecol. Oncol.* **2005**, DOI 10.1016/j.ygyno.2005.02.031.

[303] L. Udabage, G. R. Brownlee, S. K. Nilsson, T. J. Brown, *Exp. Cell Res.* **2005**, *310*, 204.

[304] U. Novak, S. S. Stylli, A. H. Kaye, G. Lepperdinger, *Cancer Res.* **1999**, *59*, 6246.

[305] T. A. Christopoulos, N. Papageorgakopoulou, D. A. Theocharis, N. S. Mastronikolis, T. A. Papadas, D. H. Vynios, *Biochem. Biophys. Acta* **2006**, *1760*, 1039.

[306] D. A. Godin, P. C. Fitzpatrick, A. B. Scandurro, P. C. Belafsky, B. A. Woodworth, R. G. Amedee, D. J. Beech, B. S. Beckman, *Arch. Otolaryngol. Neck Surg.* **2000**, *126*, 402.

[307] A. K. Madan, K. Yu, N. Dhurandhar, C. Cullinane, Y. Pang, D. J. Beech, *Oncol. Rep.* **n.d.**, *6*, 607.

[308] L. Wang, X. Xu, H. Ning, S.-M. Yang, J. Chen, J. Yu, H. Ding, C. B. Underhill, L. Zhang, *Zhonghua bing li xue za zhi = Chinese J. Pathol.* **2004**, *33*, 320.

[309] D. J. Beech, A. K. Madan, N. Deng, *J. Surg. Res.* **2002**, *103*, 203.

[310] A. Ouhtit, Z. Y. A. Elmageed, M. E. Abdraboh, T. F. Lioe, M. H. G. Raj, *Am. J. Pathol.* **2007**, *171*, 2033.

[311] Y. Xu, Q. Yu, *J. Biol. Chem.* **2003**, *278*, 8661.

[312] S.-T. Peng, C.-H. Su, C.-C. Kuo, C.-F. Shaw, H.-S. Wang, *Int. J. Oncol.* **2007**, *31*, 1119.

[313] G. Tzircotis, R. F. Thorne, C. M. Isacke, *J. Cell Sci.* **2005**, *118*, 5119.

[314] Y.-C. Kuo, C.-H. Su, C.-Y. Liu, T.-H. Chen, C.-P. Chen, H.-S. Wang, *Int. J. Cancer* **2009**, *124*, 2568.

[315] K. Sugahara, T. Hirata, T. Tanaka, S. Ogino, M. Takeda, H. Terasawa, E. Al., *Cancer Res* **2008**, *68*, 7191.

[316] O. Nagano, H. Saya, *Cancer Sci.* **2004**, *95*, 930.

[317] L. Y. W. Bourguignon, E. Gilad, K. Rothman, K. Peyrollier, *J. Biol. Chem.* **2005**, *280*, 11961.

[318] L. Y. W. Bourguignon, P. A. Singleton, H. Zhu, F. Diedrich, *J. Biol. Chem.* **2003**, *278*, 29420.

[319] T. Murai, Y. Miyazaki, H. Nishinakamura, K. N. Sugahara, T. Miyauchi, Y. Sako, T. Yanagida, M. Miyasaka, *J. Biol. Chem.* **2004**, *279*, 4541.

[320] Y. Fujita, M. Kitagawa, S. Nakamura, K. Azuma, G. Ishii, M. Higashi, H. Kishi, T. Hiwasa, K. Koda, N. Nakajima, K. Harigaya, *FEBS Lett.* **2002**, *528*, 101.

[321] E. A. Craig, P. Parker, T. D. Camenisch, *Glycobiology* **2009**, *19*, 890.

[322] A. Afify, P. Purnell, L. Nguyen, *Exp. Mol. Pathol.* **2009**, *86*, 95.

[323] A. P. Barbour, J. A. Reeder, M. D. Walsh, J. Fawcett, T. M. Antalis, D. C. Gotley, *Cancer Res.* **2003**, *63*, 887.

[324] K. A. Iczkowski, A. L. Omara-Opyene, G. V Shah, *Anticancer Res.* **n.d.**, *26*, 2863.

[325] A. Hill, S. McFarlane, K. Mulligan, H. Gillespie, J. E. Draffin, A. Trimble, A. Ouhtit, P. G. Johnston, D. P. Harkin, D. McCormick, D. J. J. Waugh, *Oncogene* **2006**, *25*, 6079.

[326] H. Li, L. Guo, J. Li, N. Liu, J. Liu, *Chinese J. Med. Genet.* **2000**, *17*, 343.

[327] I. Zlobec, K. Baker, P. Minoo, J. Jass, L. Terracciano, A. Lugli, *Clin Cancer Res* **2008**, *14*, 143.

[328] C. L. Hall, C. Wang, L. A. Lange, E. A. Turley, *J. Cell Biol.* **1994**, *126*, 575.

[329] S. L. Gares, L. M. Pilarski, *Dev. Immunol.* **2000**, *7*, 209.

[330] C. L. Hall, L. A. Lange, D. A. Prober, S. Zhang, E. A. Turley, *Oncogene* **1996**, *13*, 2213.

[331] S. R. Hamilton, S. F. Fard, F. F. Paiwand, C. Tolg, M. Veiseh, C. Wang, J. B. McCarthy, M. J. Bissell, J. Koropatnick, E. A. Turley, *J. Biol. Chem.* **2007**, *282*, 16667.

[332] S.-L. Lin, D. Chang, A. Chiang, S.-Y. Ying, *Carcinogenesis* **2008**, *29*, 282.

[333] R. C. Savani, G. Cao, P. M. Pooler, A. Zaman, Z. Zhou, H. M. DeLisser, *J. Biol. Chem.* **2001**, *276*, 36770.

[334] C. B. Thompson, H. M. Shepard, P. M. O'Connor, S. Kadhim, P. Jiang, R. J. Osgood, L. H. Bookbinder, X. Li, B. J. Sugarman, R. J. Connor, S. Nadjsombati, G. I. Frost, *Mol. Cancer Ther.* **2010**, *9*, 3052.

[335] T. J. Brown, *Curr Pharm Biotechnol* **2008**, *9*, 253.

[336] P. Gibbs, P. R. Clingan, V. Ganju, A. H. Strickland, S. S. Wong, N. C. Tebbutt, et al., *Cancer Chemother Pharmacol* **2011**, *67*, 153.

[337] X. Jia, K. L. Kiick, *Macromol Biosci* **2009**, *9*, 140.

[338] J.-W. Kuo, G. D. Prestwich, *Compr. Biomater.* **2011**, 239.

[339] N. Sahiner, A. K. Jha, D. Nguyen, X. Jia, *J. Biomater. Sci. Polym. Ed.* **2008**, *19*, 223.

[340] A. K. Jha, R. A. Hule, T. Jiao, S. S. Teller, R. J. Clifton, R. L. Duncan, D. J. Pochan, X. Jia, *Macromolecules* **2009**, *42*, 537.

[341] A. J. E. Farran, S. S. Teller, A. K. Jha, T. Jiao, R. A. Hule, R. J. Clifton, D. P. Pochan, R. L. Duncan, X. Jia, *Tissue Eng. Part A* **2010**, *16*, 1247.

[342] A. K. Jha, M. S. Malik, M. C. Farach-Carson, R. L. Duncan, X. Jia, *Soft Matter* **2010**, *6*, 5045.

[343] P. P. Srinivasan, S. Y. McCoy, A. K. Jha, W. Yang, X. Jia, M. C. Farach-Carson, C. B. Kirn-Safran, *Biomed. Mater.* **2012**, *7*, 24109.

[344] S. Pradhan, C. Zhang, X. Jia, D. D. Carson, R. Witt, M. C. Farach-Carson, **2009**.

[345] S. Pradhan-Bhatt, D. A. Harrington, R. L. Duncan, X. Jia, R. L. Witt, M. C. Farach-Carson, *Tissue Eng. Part A* **2013**, *19*, 1610.

[346] L. A. Gurski, X. Xu, L. N. Labrada, N. T. Nguyen, L. Xiao, K. L. van Golen, X. Jia, M. C. Farach-Carson, *PLoS One* **2012**, *7*, e50075.

[347] X. Xu, L. A. Gurski, C. Zhang, D. A. Harrington, M. C. Farach-Carson, X. Q. Jia, *Biomaterials* **2012**, *33*, 9049.

[348] T. Jiao, A. Farran, X. Jia, R. J. Clifton, *Exp. Mech.* **2009**, *49*, 235.

[349] S. S. Teller, A. J. E. Farran, L. Xiao, T. Jiao, R. L. Duncan, R. J. Clifton, X. Jia, *Tissue Eng Part A.* **2012**, *18*, 2008.

[350] L. Xiao, C. Liu, J. Zhu, D. J. Pochan, X. Jia, *Soft Matter* **2010**, *6*, 5293.

[351] L. Xiao, Z. Tong, Y. Chen, D. J. Pochan, C. R. Sabanayagam, X. Jia, *Biomacromolecules* **2013**, *14*, 3808.

[352] N. E. Larsen, E. A. Balazs, *Adv. Drug Deliv. Rev.* **1991**, *7*, 279.

[353] G. D. Prestwich, *Acc. Chem. Res.* **2008**, *41*, 139.

[354] A. Fakhari, C. Berkland, *Acta Biomater.* **2013**, *9*, 7081.

[355] S. Gerecht, J. A. Burdick, L. S. Ferreira, S. A. Townsend, R. Langer, G. Vunjak-Novakovic, *Proc. Natl. Acad. Sci. U. S. A.* **2007**, *104*, 11298.

[356] J. Kim, K. S. Kim, G. Jiang, H. Kang, S. Kim, B.-S. Kim, M. H. Park, S. K. Hahn, *Biopolymers* **2008**, *89*, 1144.

[357] A. W. S. Rutjes, P. Jüni, B. R. da Costa, S. Trelle, E. Nüesch, S. Reichenbach, *Ann. Intern. Med.* **2012**, *157*, 180.

[358] R. Kosaki, K. Watanabe, Y. Yamaguchi, *Cancer Res* **1999**, *59*, 1141.

[359] B. M. Mueller, I. U. Schraufstatter, V. Goncharova, T. Povaliy, R. DiScipio, S. K. Khaldoyanidi, *Mol Cancer Ther* **2010**, *9*, 3024.

[360] Liu, S., Dicker, K. T., Jia, X. *Chem Commun* **2015**, *15*, 5218.

[361] Dicker, K. T., Gurski, L. A., Pradhan-Bhatt, S., Witt, R. L., Farach-Carson, M. C., Jia, X. *Acta Biomater* **2014**, *10*, 1558.

Chapter 2

INTERFACIAL BIOORTHOGONAL CROSSLINKING

2.1 Introduction

The construction of complex, cell-instructive hydrogel networks represents the first step towards *in vitro* engineering of functional tissues.[1-2] For the advancement of tissue engineering, it is essential that synthetic matrices mimic the properties of the natural extracellular matrix (ECM) by controllably introducing biochemical cues in a spatially-defined manner without adversely effecting living cells. Although various modes of reactivity have been explored for the synthesis of covalently crosslinked hydrogels, efficient network formation at well-defined interfaces with close to 100% overall cell viability has not yet been reported.

Advances in synthesis have provided a diverse set of bioorthogonal reactions that proceed efficiently without interference from biological functionality. The Cu-catalyzed cycloaddition of azides with alkynes, first described in 2002,[3-4] has become a ubiquitous tool for polymer synthesis and materials development.[5] In 2004, Bertozzi and coworkers[6] reported that strain-driven [3+2] cycloadditions between cyclooctyne and azide derivatives are effective for bioorthogonal ligation without the necessary addition of a Cu-catalyst.[7-9] Cu-free procedures have represented an advance to the field of hydrogel formation by ameliorating cytotoxicity concerns due to copper and the need to remove catalysts from biomaterial products.[10-11]

In 2008, the Fox group described a bioorthogonal and extremely rapid reaction between *s*-tetrazine (Tz) and *trans*-cyclooctene (TCO) derivatives.[12] With more

recently developed TCO derivatives,[13] rate constants of $k_2 > 10^5$ $M^{-1}s^{-1}$ have been measured under aqueous conditions.[14-15] Contemporaneous with the initial study of TCO, several groups described reactions of tetrazines with derivatives of norbornene[16] or the Reppe anhydride,[17] with a measured rate constant of k_2 1.9 $M^{-1}s^{-1}$ at 20 °C in PBS for norbornene conjugation. Recently, cyclopropenes,[18-19] cyclooctynes[15,20-21] and terminal alkenes[22] have also been used as dienophiles for tetrazine ligation. While each of these dienophiles offers complementary advantages, TCO derivatives display the fastest rate constants. Accordingly, tetrazine-TCO ligation has been used for a host of applications in nuclear medicine and cellular imaging.[23-27]

In recent years, tetrazine-norbornene chemistry, alone or in combination with a separate, independent click reaction, has been applied to polymer synthesis and hydrogel fabrication.[28-30] Separately, TCO- or Tz-modified polymers have functioned as scavenging/clearing agents for radiochemical labeling, and TCO has been used for the conjugating nanoparticles and quantum dots to antibody-pretargeted cells.[23,31] However, tetrazine-TCO ligation has not been used as a method for the crosslinking or polymerization of biomaterials. I projected that the unique kinetic properties of TCO could enable the first interfacial processes based on a bioorthogonal reaction. Interfacial reactions are extensively utilized in polymer science, with the interfacial polymerization of nylon serving as the archetypical example.[32] Interfacial crosslinking processes have also been used for cell encapsulation purposes, most typically employing the anionic polysaccharide alginic acid.[33] While alginate capsules meet many of the requirements for the immunoisolation of cells, they can lack *in vivo* stability and strength, due to weakening of the hydrogel core by exchange

of calcium.[34] In addition, the calcium crosslinking is not amenable for further modulation of gel mechanics and the spatial distribution of biochemical signals.

Herein, I demonstrate the first example of bioorthogonal interfacial crosslinking—the use of bioorthogonal chemistry to create hydrogel materials through rapid crosslinking at the gel-liquid interface. The gel/liquid interface is formed upon contact of a solution of a tetrazine-modified hyaluronic acid (HA-Tz) with an octadecaethylene glycol (OEG) crosslinker flanked by *trans*-cyclooctenes (bis-TCO). Because the tetrazine-TCO ligation is extremely fast, crosslinking occurs at a rate which is diffusion controlled, resulting in the advancement of a distinct gel/liquid interface as the crosslinking reaction proceeds (Figure 2.1). Interfacial bioorthogonal crosslinking enables the construction of spherical particles and tubular structures via a simple syringe injection process, and I demonstrate the utility of the tetrazine-TCO ligation for *in situ* encapsulation and subsequent 3D culture of prostate cancer LNCaP cells in HA hydrogel microspheres which maintain almost full cell viability. With spatially resolved functionalization in 3D and without having to resort to multiple independent reactions or specialized equipment such as two-photon or photomasks, the bioorthogonal interfacial crosslinking of hydrogels offers a new approach to the modulating the display of functional molecule in cell culture matrices.

2.2 Materials and Methods

2.2.1 Materials

All reactions were carried out in glassware that was flame-dried under vacuum and cooled under nitrogen. (1*R*,8*S*,9*R*,4*E*)-bicyclo[6.1.0]non-4-en-9-ylmethyl(4-nitrophenyl) carbonate was prepared following a known procedure.[13] *O*,*O*'-Bis(2-

aminoethyl)octadecaethylene glycol (≥ 95% oligomer purity) and *O*-(2-Aminoethyl)-*O*-[2-(Boc-amino)ethyl] decaethylene glycol (≥ 90% oligomer purity) were purchased from Sigma Aldrich. Hyaluronic acid (sodium salt) was a generous gift from Genzyme Corporation. Dialysis membranes were purchased from Spectrum Labs (MWCO: 10 kDa). Flash Chromatography was performed using normal phase Silicycle silica gel (40-63D, 60Å). Deactivated silica gel was prepared by treating silica gel with $EtSiCl_3$.[48] An APT pulse sequence was used for ^{13}C NMR spectra, where methylene and quaternary carbons appear 'up' (u), and methine and methyl carbons appear 'down' (d). The abbreviation 'app' stands for 'apparent.' Other reagents were purchased from commercial sources without additional purification.

2.2.2 Synthesis of Hydrogel Precursors

2.2.2.1 sTCO-OH

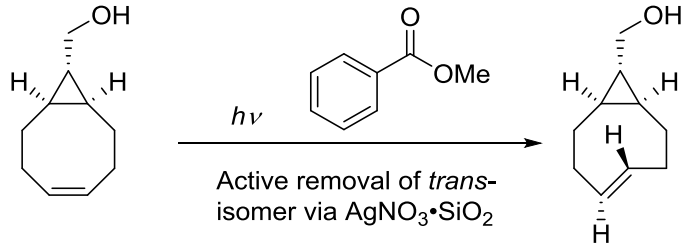

The continuous flow apparatus described previously[49] was used for the photoisomerization, Biotage SNAP cartridges (Biotage part no. FSK0-1107-0050) was filled with a bed of unmodified silica gel that was topped with 14.5 g of silica gel which was impregnated with $AgNO_3$(1.45 g, 8.55 mmol). (1R,8S,9R,4Z)-Bicyclo [6.1.0]non-4-ene-9-ylmethanol(1.00 g, 6.58 mmol) and methyl benzoate (1.80g, 13.2 mmol) were placed in a quartz flask and dissolved in 500 mL of 1:1 Et_2O:hexanes. Dodecane (1.12g, 6.58 mmol) was also added to the flask to allow for GC monitoring.

The solution was equilibrated through the continuous flow system at a 100 mL/min flow rate. The solution in the quartz flask was then irradiated (254nm) under continuous flow conditions (100 mL/min) for 4 hours, at which point GC analysis indicated that the reaction was complete. The SNAP cartridges were flushed with 400 mL of 1:1 Et_2O/hexanes and then dried with compressed air. To the dried silica gel was sequentially added NH_4OH (200 mL) and methylene chloride (200 mL) and the resulting mixture was filtered. The filtrate was transferred to a separatory funnel and partitioned. The aqueous layer was extracted twice with methylene chloride. The organic layers were combined, washed twice with water then dried with magnesium sulfate and filtered. The solvent was removed with a rotary evaporator, column chromatography (20% ethyl acetate/hexanes) afforded 820 mg of 7 (82%) (rel-1R,8S,9R,4E)-Bicyclo [6.1.0]non-4-ene-9-ylmethanol as a colorless oil. ^{1}H and ^{13}C NMR data agreed with the previously reported data.[13] Synthesis of sTCO-OH was done by my collaborator, Han Zhang.

2.2.2.2 sTCO-carbonate(2)

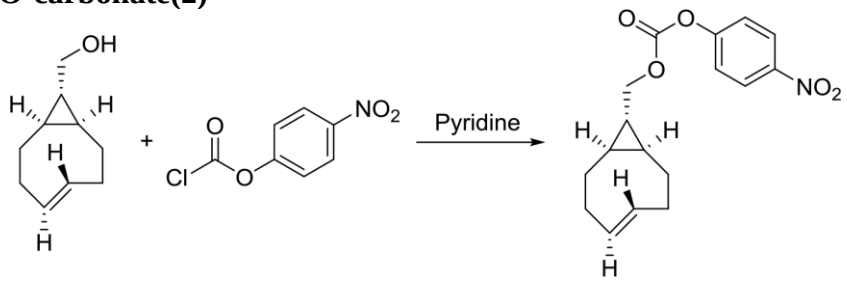

A dry round-bottled flask was charged with (rel-1R,8S,9R,4E)-Bicyclo [6.1.0]non-4-ene-9-ylmethanol (820 mg, 5.39 mmol). Anhydrous dichloromethane (100 mL) and pyridine (1.09 mL, 13.5 mmol) were added to the flask. A solution of 4-nitrophenylchloroformate (1.30 g, 6.47 mmol) in anhydrous dichloromethane (14 mL) was added to the flask via syringe and the solution was stirred for 1 h at room

temperature. Saturated NH_4Cl aqueous solution was added to the mixture and the layers were separated, and the aqueous layer was extracted twice with dichloromethane. The organic layers were combined, dried with $MgSO_4$, filtered, solvent was removed using a rotary evaporator. Purification by column chromatography (5% ethyl actetate/hexanes) yielded afforded 1.18 g (3.72 mmol, 69%) of (rel-1R,8S,9R,4E)-Bicyclo[6.1.0]non-4-ene-9-ylmethyl (4-nitrophenyl) carbonate as a white solid. ^1H and ^{13}C NMR data agreed with the previously reported data.[13] Synthesis of sTCO-carbonate was done by my collaborator, Han Zhang.

2.2.2.3 sTCO-PEG18-sTCO

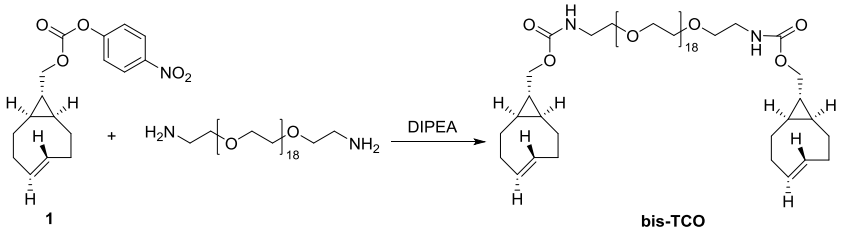

A dry round-bottled flask was sequentially charged via syringe with a solution of *O,O*'-Bis(2-aminoethyl)octadecaethylene glycol (64 mg, 0.071 mmol) in anhydrous dichloromethane (2 mL) and *N,N*-diisopropylethylamine (49.9 µL, 0.29 mmol), followed by a solution of (1*R*,8*S*,9*R*,4*E*)-bicyclo[6.1.0]non-4-en-9-ylmethyl(4-nitrophenyl) carbonate[1] (50 mg, 0.16 mmol) in anhydrous dichloromethane (3 mL). The mixture was stirred overnight at room temperature. The solvent was removed with a rotary evaporator. Purification by column chromatography using 0-5% methanol in dichloromethane yielded 80 mg (0.064 mmol, 90%) of bis-TCO as a water-soluble clear oil. ^1H NMR ($CDCl_3$, 400 MHz, δ): 5.77-5.90 (m, 2H), 5.17-5.31 (m, 2H), 5.04-5.16 (m, 2H), 3.86-3.97 (m, 4H), 3.48-3.68 (m, 72H), 3.50-3.56 (m, 4H), 3.30-3.38 (m, 4H), 2.29-2.38 (m, 2H), 2.12-2.29 (m, 6H), 1.82-1.97 (m, 4H), 0.75-0.88 (m, 2H),

0.47-0.60 (m, 4H), 0.32-0.46 (m, 4H). ^{13}C NMR ($CDCl_3$, 100 MHz, δ): 157.0 (u, 2C), 138.5 (d, 2C), 131.4 (d, 2C), 70.7-70.5 (u, 34C), 70.4 (u, 2C), 70.2 (u, 2C), 69.5 (u, 2C), 40.8 (u, 2C), 38.8 (u, 2C), 33.9 (u, 2C), 32.7 (u, 2C), 27.7 (u, 2C), 24.8 (d, 2C), 22.0 (d, 2C), 21.0 (d, 2C). HRMS (ESI) [M+H]: calcd. for $C_{62}H_{113}N_2O_{23}^+$, 1253.7729; found 1253.7745. Initial synthesis of PEG-bisTCO was conducted by my collaborator, Han Zhang.

2.2.2.4 sTCO-PEG11-Boc(6)

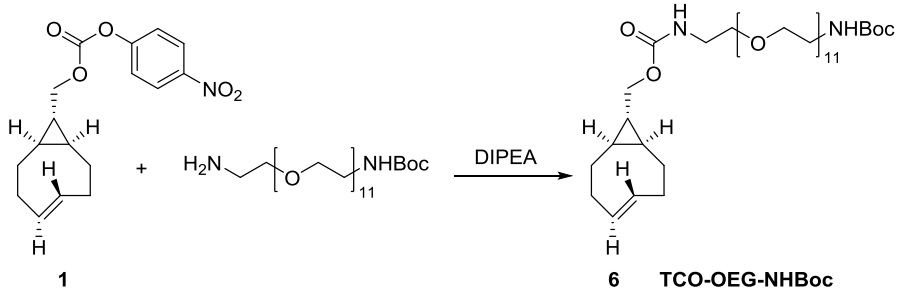

1 6 TCO-OEG-NHBoc

A dry round-bottled flask was charged with an anhydrous dichloromethane (2 mL) solution of *O*-(2-aminoethyl)-*O*-[2-(Boc-amino)ethyl] decaethylene glycol (75 mg, 0.12 mmol) and *N*,*N*-diisopropylethylamine (30 mg, 0.233 mmol). A solution of (1*R*,8*S*,9*R*,4*E*)-bicyclo[6.1.0]non-4-en-9-ylmethyl(4-nitrophenyl) carbonate[1] (44 mg, 0.14 mmol) in anhydrous dichloromethane (2 mL) was added to the flask via a syringe. The mixture was then stirred overnight at room temperature. Solvent was removed with rotary evaporator. Purification by column chromatography using 0-5% methanol in dichloromethane yielded 84 mg (0.10 mmol, 88%) of **6** as a water-soluble clear oil. ^{1}H NMR (MeOD, 600 MHz, δ): 5.78-5.94 (m, 1H), 5.04-5.20 (m, 1H), 3.87-3.97 (m, 2H), 3.58-3.66 (m, 42H), 3.47-3.53 (m, 4H), 3.25-3.28 (m, 2H), 3.20-3.23 (m, 2H), 2.32-2.36 (m, 1H), 2.15-2.27 (m, 3H), 1.86-1.96 (m, 2H), 1.44 (s, 9H), 0.85-0.93 (m, 1H), 0.54-0.65 (m, 2H), 0.40-0.47 (m, 2H). ^{13}C NMR (MeOD, 150 MHz, δ):

159.3 (u, 2C), 139.4 (d, 1C), 132.4 (d, 1C), 80.2 (u, 1C), 71.8-71.4 (u, 20C), 71.3-71.1 (u, 2C), 70.5 (u, 1C), 41.8 (u, 1C), 41.5 (u, 1C), 39.9 (u, 1C), 34.8 (u, 1C), 33.8 (u, 1C), 29.0 (d, 3C), 28.7 (u, 1C), 26.3 (d, 1C), 23.4 (d, 1C), 22.4 (d, 1C). HRMS (ESI) [M+H]: calcd. for $C_{40}H_{74}N_2O_{15}Na^+$, 845.4981; found 845.4982. Initial synthesis was conducted by my collaborator, Han Zhang.

2.2.2.5 sTCO-Alexa Fluor® 647(5)

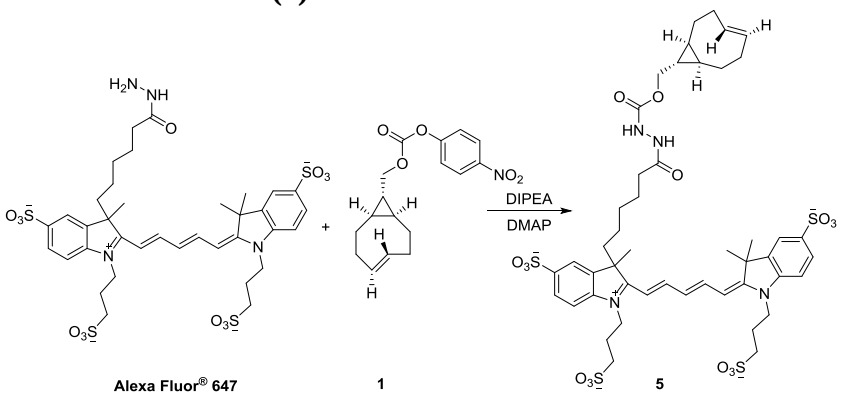

(1*R*,8*S*,9*R*,4*E*)-Bicyclo[6.1.0]non-4-en-9-ylmethyl(4-nitrophenyl) carbonate (**1**) (1.3 mg, 4.2 μmol) was added to a vial that contained Alexa Fluor® 647 hydrazide, tris(triethylammonium) salt (1.0 mg, 0.83 μmol). A DMF solution (200 μL, anhydrous) containing *N*,*N*-diisopropylethylamine (215 μg, 1.67 μmol) and 4-dimethylaminopyridine (DMAP, 50 μg, 0.41 μmol) was added to the vial. The mixture was stirred overnight at ambient temperature and was purified with reverse phase HPLC, generating 0.49 mg (47 μmol, 56%) of **5** as a blue solid. LC-MS (Figure S2.18) and HPLC (Figure S2.19) analyses indicated that the purity of a compound with a mass of 1047 Da. was >98%. Synthesis of Alexa-TCO was done by my collaborator, Han Zhang.

2.2.2.6 Diphenyl-Tetrazine-OH(2)

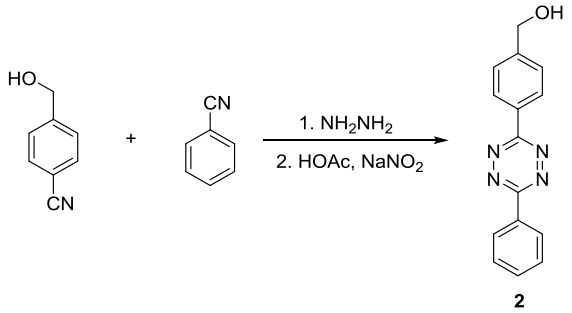

2

A dry round-bottomed flask was charged with 4-(hydroxymethyl)benzonitrile (5.80 g, 43.6 mmol), benzonitrile (18.0 g, 175 mmol) and anhydrous hydrazine (21.4 mL, 440 mmol). The flask was equipped with a reflux condenser, and the mixture was heated to 90 °C for 20 h behind a blast shield. The mixture was allowed to cool down to room temperature and was diluted with ethyl acetate (300 mL), washed twice with H_2O (150 mL), and dried over $MgSO_4$. The solution was filtered and the filtrate was concentrated under reduced pressure. The residual solid was dissolved in acetic acid (84 mL), and an aqueous solution of $NaNO_2$ (23.2 mL of a 9.40 M solution, 218 mmol) was added at 0 °C via Pasteur pipette. After stirring for 30 min at room temperature, the mixture was diluted with dichloromethane (300 mL). An aqueous solution of saturated $NaHCO_3$ was added then carefully added to neutralize the acetic acid. The mixture was partitioned and the organic phase was washed three times with saturated $NaHCO_3$ aqueous solution, and then dried over $MgSO_4$, filtered, and concentrated onto silica gel using a rotary evaporator. Column chromatography using a gradient (0-70 %) of acetone in hexanes afforded 2.46 g (9.32 mmol, 22%) of **2** as a purple solid. ^{1}H NMR (DMSO-d_6, 400 MHz, δ): 8.40-8.60 (m, 4H), 7.58-7.75 (m, 5H), 5.46 (t, J=5.7 Hz 1H), 4.65 (d, J=5.6 Hz, 2H). ^{13}C NMR (DMSO-d_6, 100 MHz, δ): 163.4 (u, 1C), 163.3 (u, 1C), 147.7 (u, 1C), 132.6 (d, 1C), 132.0 (u, 1C), 130.2 (u, 1C), 129.6 (d, 2C), 127.6 (d, 2C), 127.5 (d, 2C), 127.2 (d, 2C), 62.5 (u, 1C). HRMS

(ESI) [M+H]: calcd. for $C_{15}H_{13}N_4O^+$, 265.1084; found 265.1098. Synthesis of Tz-OH was done by my collaborator, Han Zhang.

2.2.2.7 Diphenyl-Tetrazine-carbonate(3)

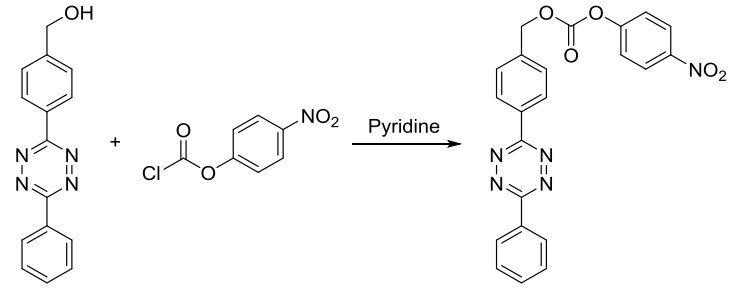

A dry round-bottled flask was charged with (4-(6-phenyl-1,2,4,5-tetrazin-3-yl)phenyl)methanol **2** (157 mg, 0.595 mmol). Anhydrous dichloromethane (12 mL) and pyridine (0.12 mL, 1.5 mmol) were added to the flask. A solution of 4-nitrophenylchloroformate (180 mg, 0.892 mmol) in anhydrous dichloromethane (3 mL) was added to the flask via syringe and the solution was stirred for 2 h at room temperature. Saturated NH_4Cl aqueous solution was added to the mixture and the layers were separated, and the aqueous layer was extracted twice with dichloromethane. The organic layers were combined, dried with $MgSO_4$, filtered, and concentrated onto silica gel using a rotary evaporator. Column chromatography using a gradient (30-70%) of dichloromethane in hexanes afforded 0.211 g (0.492 mmol, 83%) of **3** as a purple solid. ^{1}H NMR ($CDCl_3$, 400 MHz, δ): 8.63-8.76 (m, 4H), 8.26-8.34 (m, 2H), 7.60-7.75 (m, 5H), 7.38-7.46 (m, 2H), 5.43 (s, 2H). ^{13}C NMR ($CDCl_3$, 100 MHz, δ): 164.2 (u, 1C) 163.7 (u, 1C) 155.5 (u, 1C) 152.7 (u, 1C) 145.6 (u, 1C) 138.9 (u, 1C) 133.0 (d, 1C) 132.5 (u, 1C) 131.8 (u, 1C) 129.5 (d, 2C) 129.2 (d, 2C) 128.5 (d, 2C) 128.2 (d, 2C) 125.5 (d, 2C) 121.9 (d, 2C) 70.3 (u, 1C). HRMS (ESI)

[M+H]: calcd. for $C_{22}H_{16}N_5O_5^+$, 430.1146; found 430.1154. Synthesis of Tz-carbonate was done by my collaborator, Han Zhang.

2.2.2.8 Diphenyl-Tetrazine-PEG18-Amine(4)

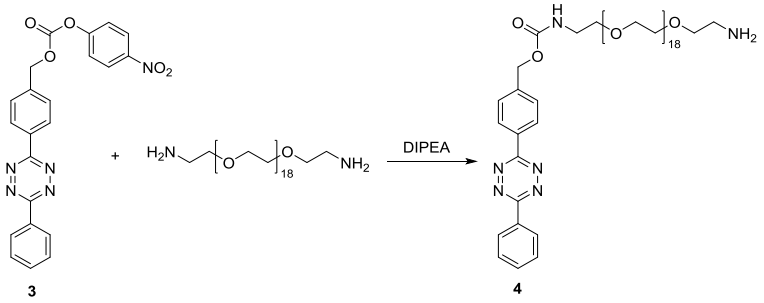

A dry round-bottled flask was charged with a solution of *O*,*O*'-bis(2-aminoethyl)octadecaethylene glycol (141 mg, 0.157 mmol) in anhydrous dichloromethane (4 mL) and *N*,*N*-diisopropylethylamine (DIPEA, 36.5 µL, 0.209 mmol). A solution of 4-nitrophenyl 4-(6-phenyl-1,2,4,5-tetrazin-3-yl)benzyl carbonate (45 mg, 0.11 mmol) in anhydrous dichloromethane (6 mL) was added to the flask via a syringe pump over 3 h. The mixture was then allowed to stir overnight at room temperature. The solvent was removed with a rotary evaporator and the residue was washed three times with hexanes. Column chromatography on deactivated silica gel[3] using a gradient 30-100% acetone in hexanes followed by 10% methanol in dichloromethane afforded 88 mg (0.074 mmol, 71%) of **4** as a water-soluble purple solid. ^{1}H NMR ($CDCl_3$, 400 MHz, δ): 8.55-8.75 (m, 4H), 7.86-7.99 (br, 2H), 7.50-7.70 (m, 5H), 5.50-5.61 (br, 1H), 5.21 (s, 2H), 3.91 (m, 2H), 3.59-3.73 (m, 74H), 3.41 (m, 2H), 3.10-3.24 (m, 2H). ^{13}C NMR ($CDCl_3$, 100 MHz, δ): 164.1(1C), 163.8(1C), 156.4(1C), 141.8(1C), 132.9(1C), 131.8(1C), 131.4(1C), 129.5(2C), 128.6(2C), 128.2(2C), 128.1(2C), 70.7-70.0(35C), 69.9(1C), 69.7(1C), 66.8(1C), 66.0(1C), 41.1(1C), 40.7(1C). HRMS (ESI) [M+H]: calcd. for $C_{56}H_{95}N_6O_{21}^+$, 1187.6545; found

1187.6541. UV-vis (27.5 μM in H_2O): λ_{max} 300 nm. Synthesis of Tz-PEG-NH_2 was done by my collaborator, Han Zhang.

2.2.2.9 Diphenyl-Tetrazine Modified Hyaluronic Acid

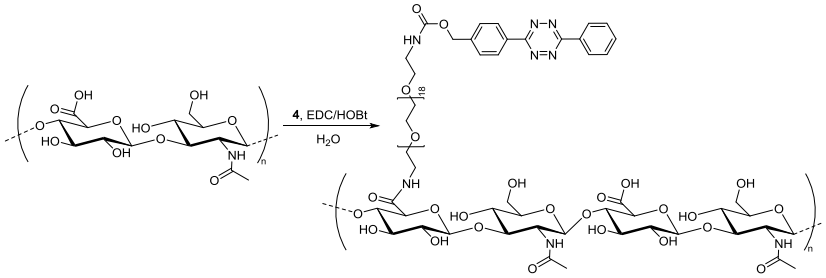

Hyaluronic acid (30.1 mg, 792 μmol) was dissolved in H_2O (6.7 mL) at a concentration of 4.5 mg/mL. Tetrazine-OEG-amine (**4**) (447 mg, 0.376 mmol) dissolved in H_2O (3.2 mL) was then added dropwise to the HA solution. To this mixture was slowly added a solution of 1-ethyl-3-[3-(dimethylamino)propyl]-carbodiimide (EDC) (57.8 mg, 301 μmol) in DMSO/H_2O (1:1, 302 μL), followed by a solution of 1-hydroxybenzotriazole (HOBt) (40.6 mg, 301 μmol) in DMSO/H_2O (1:1, 302 μL). The resulting mixture was stirred at 37 °C for 24 h. The HA derivative was then precipitated in ice-cold ethanol (100 mL, 10 vol. excess). The precipitates were then collected by centrifugation at 4,000 rpm for 8 min. The pellet was then re-dissolved in H_2O at approximately 3 mg/mL and exhaustively dialyzed (Spectra 10 kDa MWCO) against H_2O. The purified product was lyophilized to afford 29 mg (0.063 mmol, 80%) HA-Tz as a pink fluffy solid. The product was stored at 4 °C prior to use.

The percent tetrazine incorporation in HA-Tz was determined collectively by UV-vis and ^{1}H NMR analyses. UV-vis quantification was based on the tetrazine absorption at λ_{max} 300 nm employing Beer-Lambert law. Using an aqueous solution of compound **4** at a concentration of 27.5 μM as the standard (Figure S2.2a), the molar

extinction coefficient of the tetrazine moiety (ε_{Tz}) was determined as 3.2×10^4 L Mol^{-1} cm^{-1}. Taking into consideration the change of the molecular weight for HA disaccharide repeats after tetrazine incorporation, the degree of tetrazine incorporation in HA-Tz was calculated as 7% (Figure S2.2b). By ^{1}H NMR (Figure S2.3), the degree of modification was analyzed by comparing the integration between the aromatic protons (7.4-8.4 ppm) to that the acetamido moiety of the N-acetyl-d-glucosamine residue of HA. Initial UV-Vis quantification was conducted by my collaborator, Han Zhang.

2.2.3 Kinetic analysis of the reaction between TCO (4) and 3,6-diphenyl-s-tetrazine (6) in H_2O

The reaction was run under pseudo-first order conditions and monitored by UV-Vis spectroscopy at 294 nm using an Applied Photophysics SX.18MV-R stopped-flow dual mixing spectrometer. The reactants were separately dissolved in H_2O and mixed in the stopped-flow device. The final concentrations of **4** and **6** were 2.50×10^{-5} M and 2.50×10^{-4} M, respectively. A spectrum was acquired every 5×10^{-4} seconds for 4×10^{-2} seconds (95% conversion). The k_{obs} was determined by fitting a linear curve to $\ln(A/A_0)$, where A = absorbance and A_0 = absorbance at t = 0, respectively. The kinetic runs were measured in triplicate, and k_{obs} was 71.6 s^{-1}(+/- 1.9). The second order rate constant (k_2) was calculated to be 71.6 s^{-1} / (2.5×10^{-4} M) = 2.86×10^5 $M^{-1}s^{-1}$ (+/- 1.3×10^4). Stopped flow experiments were conducted by my collaborator, Han Zhang.

2.2.4 Determination of molecular weight and solution viscosity.

Viscosity average molecular weight (M_v) of HA and HA-Tz was determined using a viscometer (Cannon Instrument Company, State College, Pa) in 0.2 M NaCl at

room temperature. Efflux times for HA and HA-Tz solutions at concentrations of 0.2, 0.1, 0.05, 0.025, and 0 wt% were determined in triplicate. Using the Mark-Houwink equation with parameters of a=0.816 and K=0.0228 mL/g, M_v[4] was calculated to be 543 kDa and 218 kDa for the parent HA and the tetrazine derivative, respectively. The viscosity of HA and HA-Tz (both 2 wt%) was determined using a rheometer (AR-G2, TA Instrument, New Castle, DE) with a 20 mm aluminum parallel plate geometry with 100 μm gap size at ambient temperature where the shear rate was stepped from 1 to 100 s^{-1}.

2.2.5 Interfacial bioorthogonal crosslinking.

HA-Tz and bis-TCO were separately dissolved in PBS at a concentration of 2 wt% and 400 μM, respectively. To prepare HA microspheres, HA-Tz was dropped via a 25G syringe into a 500 μL solution of bis-TCO solution in a 48 well plate (BD Falcon™). The interfacial crosslinking was allowed to occur at 37 °C for 2 hours without any agitation. The bis-TCO solution was then replaced with fresh PBS. The gel particles were dehydrated in graded ethanol solutions and vacuum dried. The swelling ratio, reported as an average of three repeats, was determined as the ratio of the initial weight of the wet gel to the weight of the dry product.

To prepare crosslinked hydrogel channels while simultaneously monitoring the channel formation via confocal microscopy, a glass cylinder (I.D. = 5 mm, h = 10 mm), mounted onto an imaging chamber (Lab-Tek™), was filled with ~200 μL HA-Tz (2 wt%). A syringe containing 2 mM bis-TCO and 2 μM Alexa-TCO was inserted to the bottom of the HA-Tz-filled cylinder. The syringe was pulled out of the cylinder while injecting ~ 30 μL of the solution, leaving behind a liquid channel. The channel

was monitored and imaged for 60 minutes using a Zeiss 510 NLO confocal microscope (Carl Zeiss, Maple Grove, MN).

2.2.6 Rheological characterization.

The rheological properties of the hydrogel microspheres were evaluated using a controlled stress rheometer (AR-G2, TA Instruments, New Castle, DE) with a parallel plate geometry (8 mm diameter). After the gelation was complete, the hydrogel microsphere was loaded onto the geometry, and mineral oil was applied around the sample to prevent water evaporation during the measurement. Samples were tested at 25°C with a gap size of 175 μm. The linear viscoelastic region was determined by a strain sweep from 0.1 to 1000% at an angular frequency of 1 Hz. A time sweep experiment was conducted for 60 minutes at a frequency of 1 Hz and a strain of 1%. A frequency sweep experiment within the linear viscoelastic range was performed after the time sweep measurement at 1% strain from 0.1 to 10 Hz. All measurements were performed in triplicate.

2.2.7 Selective interfacial tagging.

Selective interfacial tagging was achieved by timed exposure of the crosslinking HA-Tz droplet, originally dissolved in PBS at 2 wt%, to aqueous baths of bis-TCO (400 μM) alone or bis-TCO (399 μM and 1 μM Alexa-TCO) in an alternating fashion. The total exposure time was maintained at 2 hours to ensure complete gelation. For example, alternating exposure of the HA-Tz droplet to the dye-free and dye-containing baths for 15 min each for 3 cycles, followed by a 30-min exposure to the dye-containing bath resulted in a crosslinked microsphere with 7 distinct layers. To tag the microspheres with Alexa-TCO in a gradient fashion, HA-Tz

was dropped into a bis-TCO bath (1 mL, 400 μM) and Alexa-TCO was added to the bath using a syringe pump gradually over the course of 2 hours, reaching a final concentration of 0.47 μM. Upon completion of the tagging experiment, the bath was replaced with PBS and the gels were images using a Zeiss 510 NLO confocal microscope.

2.2.8 Interfacial cell encapsulation and 3D culture.

LNCaP cells were maintained in a RPMI-1640 medium supplemented with 5% (v/v) fetal bovine serum (FBS), 100U/mL penicillin G sodium and 100 μg/mL streptomycin sulfate in 0.085% (v/v) saline (P/S), as previously described.[41] The dialyzed HA-Tz solution was sterile-filtered using a Steriflip® filter tube (EMD Millipore, Billerica, MA) before lyophilization and the dry product was dissolved in the medium at a concentration of 2 wt%. Bis-TCO (400 μM) was sterilized using a 0.22 μm poly(vinylidene fluoride) (PVDF) sterile syringe filter (Thermo Fisher Scientific, Waltham, MA). Cell-laden HA microspheres were prepared by dropping LNCaP cells suspended in HA-Tz solution (1×10^6/mL) into a bis-TCO bath, allowing the interfacial crosslinking to occur for 2 hours at 37 °C. The bath was then replaced with fresh media and cells were incubated at 37 ºC for up to 14 days, with media refreshed every other day. Cell viability was assessed by Live/Dead staining using Syto 13 and propidium iodide (PI). Selected samples were also stained for F-actin using Alexa Fluor 488 phalloidin, with the nuclei counter stained by Draq 5, following previous protocols.[41] Stained samples were imaged using a Zeiss 510 NLO confocal microscope. Percent viability was analyzed by taking z-stacks of 105 μm with 15 μm slices at days 1 and 5 and cell counting of the maximum intensity projections was conducted using Image J. To quantify cell proliferation, cell-laden gel constructs were

treated with hyaluronidase (14.8 KU/mL, PBS) at 37 °C for 2 hours and the mixture was centrifuged at 1,500 rpm for 3 min. The collected pellets were trypsinized (0.25% Trypsin-EDTA) at 37 °C for 5 min and the suspension was homogenous mixed. Ten microliters of the cell suspension was removed and mixed with 20 μL of 0.4% Trypan Blue (Sigma, St. Louis, MO). The live cells were counted using a hemocytometer with a light microscope (Nikon Eclipse TS100). Analyses were performed on three replicate samples and statistical significance was evaluated by analysis of variance (one-way ANOVA), followed by Tukey's post-hoc test. A P-value of < 0.05 was considered to be statistically different.

2.3 Results and Discussion

2.3.1 Hydrogel Preparation

Hyaluronic acid (HA) was employed as the primary building block for the preparation of hydrogel microspheres and water-filled channels. HA is a ubiquitous non-sulfated glycosaminoglycan present in extracellular matrices (ECM) of all vertebrates and is involved in diverse biological processes including wound healing and tumor metastasis.[35] HA derivatives carrying complementary functional groups have been exploited for the preparation of hydrogels with tunable properties for drug delivery and tissue engineering.[36-37] Here, I describe the synthesis of HA hydrogels via a well-defined interfacial crosslinking procedure using bis-TCO and a 3,6-diphenyl-*s*-tetrazine modified HA (HA-Tz). The tetrazine was chosen both for its fast reactivity and excellent stability toward exogenous nucleophiles. The crosslinker was capped with the strained cyclooctene **1,** a TCO designed to have exceptionally fast

reactivity in the tetrazine ligation.[13] In each case, OEG spacers were utilized to ensure aqueous solubility of the hydrogel precursors.

Bis-TCO was prepared by combining *O,O'*-bis(2-aminoethyl)-octadecaethylene glycol with **1** (2.2 equiv) in 71% yield. TCO-tagged Alexa Fluor 647 (Alexa-TCO, **5**) was similarly synthesized for labeling purposes. 4-Hydroxymethylphenyl-*s*-tetrazine **2** was prepared in 22% yield on multigram scale. Derivatization to **3** was followed by coupling with *O,O'*-bis(2-aminoethyl)-octadecaethylene glycol to give **4** in 71% yield. Stopped flow UV-vis analysis (Figure S1) was used to measure the rate of reactivity between **4** and the mono-TCO adduct **6** from **1** and *N*-Boc-*O,O'*-bis(2-aminoethyl)-dodecaethylene glycol. A fast second-order rate constant of k_2 284,000 (+/– 13,000) $M^{-1}s^{-1}$ was observed. HA-Tz was synthesized by carbodiimide-mediated coupling reaction between the HA and compound **4**. The degree of tetrazine incorporation in HA-Tz was found to be 7%, as judged by UV-Vis (Figure S2.2) and ^{1}H NMR (Figure S2.3) analyses. Using the Mark-Houwink equation and reported parameters for HA,[38] the viscosity average molecular weight (M_v) of HA and HA-Tz was calculated as 543 kDa and 218 kDa, respectively. These results agree with the common observation that chemical modifications inevitably result in partial HA degradation.[36,39] However, compared to 2 wt% HA in PBS, HA-Tz of the same concentration is >3 times more viscous (Figure S2.4).

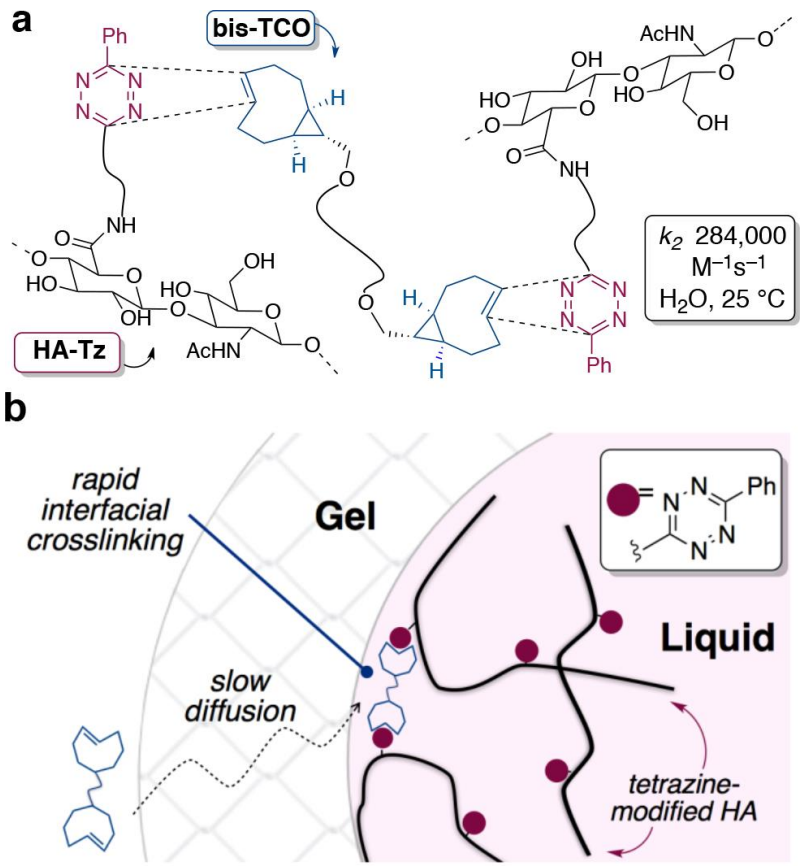

Figure 2.1 **a**) Instantaneous crosslinking via tetrazine-TCO ligation. **b**) Gel interface forms when a droplet of tetrazine modified hyaluronic acid (HA-Tz) contacts a solution of bis-trans cyclooctene crosslinker (bis-TCO). Crosslinking at the gel/liquid interface is faster than the rate of diffusion through the gel interface.

With HA-Tz and bis-TCO in hand, I devised an interfacial crosslinking protocol for the synthesis of HA hydrogel microspheres (Figure 2.1b). The pink color of the tetrazine chromophore and its disappearance upon reaction with TCO allows qualitative monitoring by the naked eye. Microspheres were prepared via syringe delivery of a solution of HA-Tz (2 wt%) to an aqueous solution of bis-TCO (400 μM). When the droplet containing HA-Tz encounters the bis-TCO solution, a crosslinked

shell forms on contact, as evidenced by the appearance of a colorless layer around the pink core (Figure 2.2a). The high viscosity of HA-Tz promotes the formation of a sharp interface once dropped into the bis-TCO solution. Subsequent crosslinking occurs at a rate controlled by diffusion, resulting in the advancement of a distinct gel/liquid interface that advances toward the core. While the bis-TCO crosslinker with a molar mass of 1,253 g/mol can diffuse across the gel layer readily, HA-Tz (M_v>10^5) cannot diffuse through the hydrogel at an appreciable rate. Thus, interfacial crosslinking takes place at the interior of the microsphere, with the volume of the pink HA-Tz core steadily decreasing over the course of 2 hours (Figure 2.2a). Consequently, the microsphere wall thickness increases linearly with time until it is fully gelled (Figure 2.2b). Throughout the crosslinking process, microspheres remain buoyant, possibly due to the nitrogen gas produced by the tetrazine ligation. The HA hydrogel microspheres prepared from HA-Tz and bis-TCO are fully-swollen after the synthesis in PBS, and the estimated equilibrium swelling ratio was 49 ± 2.

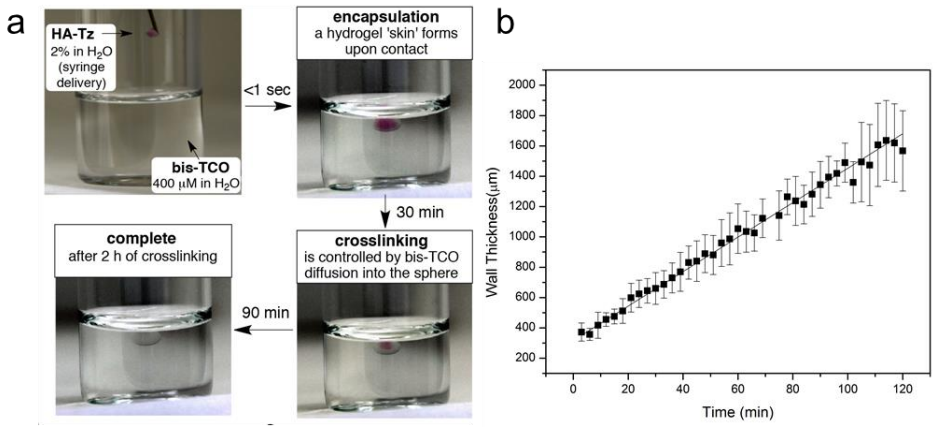

Figure 2.2 Interfacial crosslinking of HA-Tz droplets. **a**. HA-Tz droplet (pink) dropped into a bath of bis-TCO. Upon contact with the bath, an instantaneous crosslinked shell forms on the outside of the droplet. As the crosslinking is allowed to proceed, bis-TCO will diffuse across the crosslinked shell, reacting with HA-Tz at the gel-liquid interface until completely crosslinked (2 Hr). **b**. The crosslinked wall thickness of the microsphere over the two hour crosslinking period monitors by the disappearance of the pink chromophore.

The viscoelastic properties of the fully swollen hydrogel microspheres after 2 h of interfacial crosslinking were evaluated by oscillatory rheometry (Figure 2.3). The time-sweep (Figure 2.3a) experiments reveal that the HA microspheres are soft and elastic, having an elastic modulus (G') value of 135 ± 5 Pa and a loss modulus (G") of <10 Pa. Overall, G' is at least two orders of magnitude higher than G" and tan(δ) is less than 0.01. The modulus values are independent of testing time, confirming the complete consumption of HA-Tz in the droplet during the 2 hours interfacial crosslinking. The insensitivity of G' in the sample gels (Figure 2.3b) to the frequency change from 0.1 to 10 Hz confirms the elastic nature of covalently crosslinked, gel-like response with infinite relaxation time.

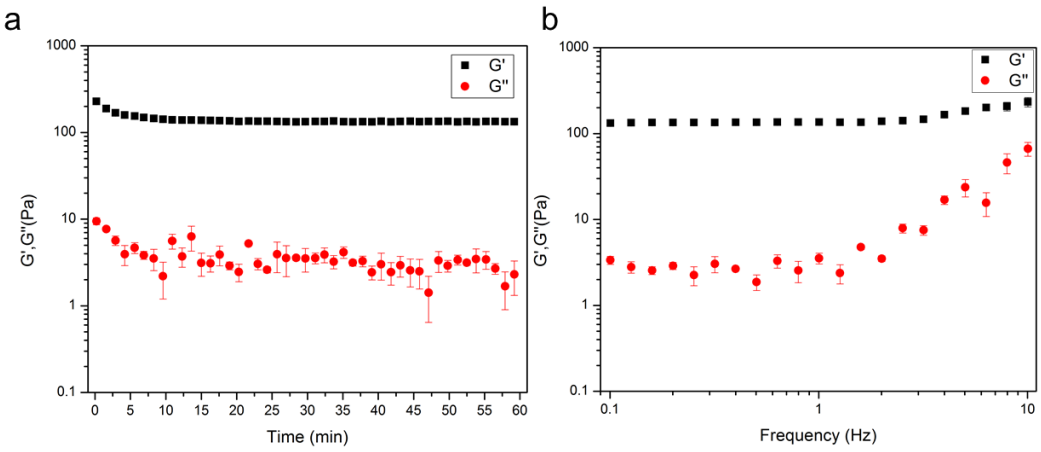

Figure 2.3 Rheological properties of the crosslinked hydrogel microspheres. Elastic (G') and loss modulus (G") as a function of time (**a**) and frequency (**b**).

2.3.2 Liquid-Filled Hydrogel Channel Formation

The tetrazine ligation not only enables the preparation of crosslinked hydrogel particles but also permits the construction of tubular structures with water filled channels (Figure 2.4). When the bis-TCO solution (2 mM) was introduced to a reservoir of HA-Tz (2 wt%) through a syringe needle, a crosslinked wall formed instantaneously following the path of the needle.

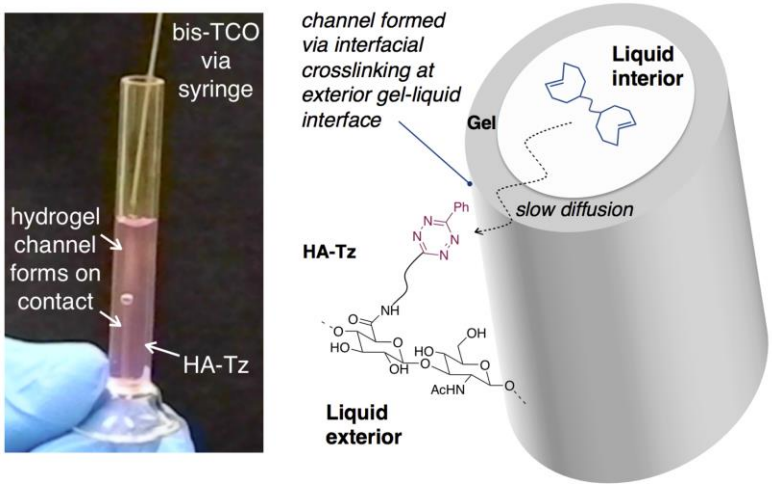

Figure 2.4 Hydrogel channels via interfacial bioorthogonal crosslinking. Channel structures were pulled by injecting while withdrawing an aqeous solution of bis-TCO (2 mM) and Alexa-TCO (2 μM) into a vessel containing HA-Tz (2 wt%). A crosslinked channel wall forms at the interface between the two liquids and the channel wall continues to grow with diffusion of the bis-TCO crosslinker until fully depleted.

To visualize channel formation, Alexa-TCO was included in the bis-TCO solution at a concentration of 2 μM. Thus, while the HA-Tz was being crosslinked at the gel-solution interface, it was simultaneously labeled by Alexa-TCO (Figure 2.5a-c). One minute after the channel was created, the wall thickness was 155 ± 13 μm and free Alexa-TCO remained inside the channel (Figure 2.5a). After 15 minutes when the structure was reimaged, the thickness of the fluorescently-labeled wall had increased to 254 ± 18 μm and the fluorescent signal inside the channel had decreased significantly. I reason that bis-TCO and Alexa-TCO exhibit a similar rate of diffusion across the crosslinked shell, whereas HA-Tz in the reservoir is excluded from penetrating into the channel due to its large size. Thus, the crosslinking front extends outward and generates water-filled channels. As Alexa-TCO diffused outwards into

the reservoir, it effectively functionalized the growing wall via ligation with the tetrazine groups at the interface. The wall thickness at 30 minutes was 262 ± 18 μm, and no significant thickness increase was observed thereafter until 60 minutes (Figure 2.5b-d) when the experiment was terminated. These observations on wall thickness are consistent with a limiting amount of the bis-TCO crosslinker within the lumen of the channel, as the wall ceased to thicken when the crosslinker was depleted. The projected confocal images (Figure 2.5c) convincingly show the creation of a hollow channel by this simple injection process.

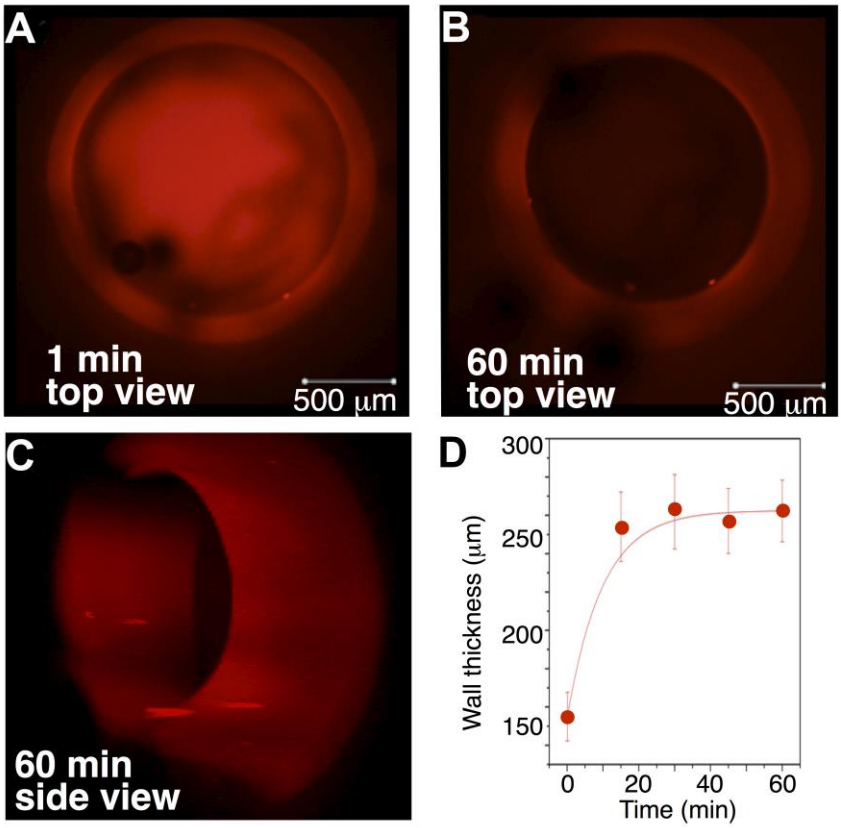

Figure 2.5 Visualization of hydrogel channel formation. **a–c**, Top and side views of Z-stack confocal images show the formation of a 3-D channel structure. **a**. Confocal imaging 1 minute after creating the channel showed distinct walls (153 ± 13 μM) had formed at the interface. The interior of the channel still contained unreacted dye. **b**. After 60 min, the same channel structure was reimaged. The dye from the interior of the channel had almost completely migrated to the walls, which had thickened to 254 ± 18 μM , consistent with an interfacial polymerization at the exterior of the structures. **c**. Imaging of the same channel after 60 min shown from a side view. **d**. Plot of channel wall thickness over time.

2.3.3 Interfacial Hydrogel Microsphere Patterning

The fast rate of crosslinking and the relatively slow rate of molecular diffusion presented an extremely simple method for introducing functional molecules to hydrogel microspheres with 3-D spatial resolution. As described above, crosslinking

of HA-Tz by bis-TCO occurs at the gel-liquid interface. I reasoned that diffusible TCO conjugates could also be covalently introduced at the gel-solution interface, and that the thickness of the resulting 'tagged' gel layer would be a function of the crosslinking time. Subsequently exposing the microsphere to a solution containing only the bis-TCO crosslinker would lead to gels with distinct tagged and untagged gel layers. The concept is outlined in Figure 2.6a.

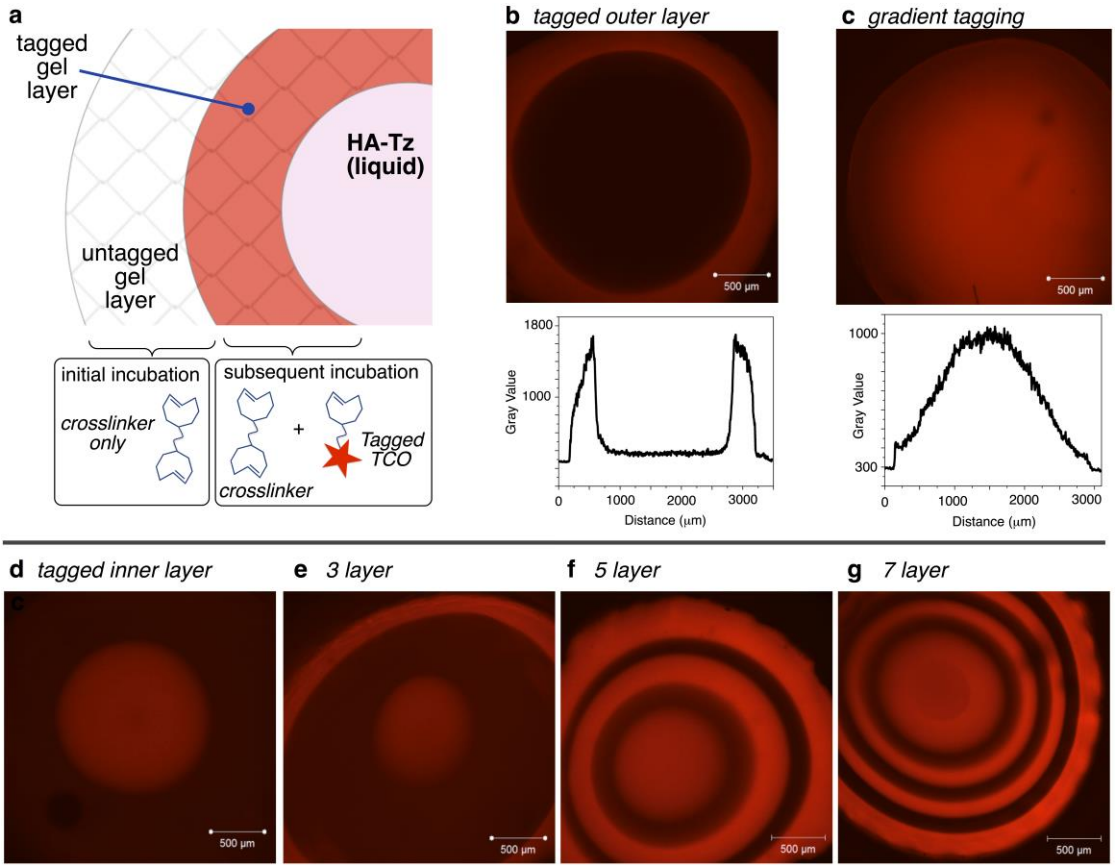
a
tagged gel layer
HA-Tz (liquid)
untagged gel layer
initial incubation
crosslinker only
subsequent incubation
+
Tagged TCO
crosslinker
b tagged outer layer
500 µm
1800
1000
Gray Value
0
1000
2000
3000
Distance (µm)
c gradient tagging
500 µm
1000
300
Gray Value
0
1000
2000
3000
Distance (µm)
d tagged inner layer
e 3 layer
f 5 layer
g 7 layer
500 µm

Figure 2.6 Fluorescent tagging with 3D spatial resolution. **a**, Schematic depiction of a small molecule-TCO conjugate being covalently introduced at the gel-solution interface during crosslinking of HA-Tz by bis-TCO. Alternating the presence/absence of Alexa-TCO leads to gels with distinct tagged and untagged gel layers. **b–g,** Confocal microscopy images of microspheres with spatially resolved 3-D tagging by Alexa-TCO. Displayed beneath images **b** and **c** are image density profile plots. **b,** Interfacial crosslinking the presence of Alexa-TCO for 30 min, and then in the absence of Alexa-TCO for 90 min gave microspheres that were labeled on the exterior. **c**, Confocal microscopy image of a microsphere with a radial gradient of 3-D tagging by Alexa-TCO, with increasing concentration of Alexa-TCO toward the center of the capsule. Interfacial crosslinking was carried out with 0.5 mL of a 400 μM bis-TCO solution. Initially, no Alexa-TCO was present. Once crosslinking was initiated, a syringe pump was used to add 200 μL of a 2.8 μM Alexa-TCO/400 μM bis-TCO solution over the course of 90 min, and crosslinking was continued for an additional 30 min without further addition of Alexa-TCO. **d,** Crosslinking in the absence and then presence of Alexa-TCO gave capsules that were labeled at the core. **e-g** Onion-like structures could be created by alternating the presence and absence of Alexa-TCO during the crosslinking procedure. Images of three, five and seven layered gels are displayed.

Alexa-TCO was again employed to demonstrate this concept. Thus, a droplet of HA-Tz (2 wt%) was added to a solution of bis-TCO (400 μM) and Alexa-TCO (1 μM) and was aged for 30 minutes. Subsequently, the bath solution was replaced with a dye-free solution of bis-TCO (400 μM), and crosslinking was continued for the remainder of 2 hours. Confocal imaging showed that the resulting microspheres were peripherally functionalized by a ~400 μm thick fluorescent shell (Figure 2.6b) with sharp contrast between the colorless core and the fluorescent outer layer. In another experiment, a HA-Tz droplet was initially exposed to the bis-TCO solution for 60 min. Alexa-TCO was then added to reach a final dye concentration of 1 μM, and crosslinking was continued for the remainder of 2 hours. This process produced microspheres that were fluorescently labeled at the core (1.45 mm diameter) with a

900 μm thick shell that was only faintly stained (Figure 2.6d), perhaps due to Alexa-TCO reacting with residual tetrazines in the crosslinked shell layer.

Microspheres with radial gradients of fluorescent tags were readily created by gradually increasing the concentration of Alexa-TCO during the crosslinking process (Figure 2.6c). Thus, during the crosslinking of an HA-Tz droplet with bis-TCO, a solution of Alexa-TCO was added via syringe pump over 2 hours. The concentration of Alexa-TCO was nil when the shell of the microsphere was crosslinked, and the concentration of the fluorescent tag was gradually increased as interfacial crosslinking proceeded toward the center of microsphere, with an Alexa-TCO concentration of 0.47 μM when the core of the microsphere was crosslinked. As shown by the confocal images in Figure 2.6c, this protocol produced microspheres with distinct radial gradients where fluorescence intensity is highest at the core.

By incubating the polymerizing HA-Tz droplet in bis-TCO crosslinker solutions with the alternating presence/absence of Alexa-TCO, it was possible to create microspheres with onion-like layers that were alternately tagged by fluorescent TCO-conjugates. Shown in Figure 2.6e is a fluorescence microscopy image of an HA microsphere containing three distinct layers, prepared by an initial 15 min exposure to an Alexa-TCO/bis-TCO mixture, followed by 45 min exposure to a dye-free solution of bis-TCO, and ultimately by 60 min re-exposure to the Alexa-TCO/bis-TCO mixture. Analogously, it is possible to create microsphere with 5- or 7-layers, where alternate layers were fluorescently tagged (Figure 2.6f-g). These experiments not only confirm the diffusion controlled nature of the bioorthogonal crosslinking, but also illustrate how complex 3-D patterns of functionalized molecules in hydrogels can be created using only a syringe and a stopwatch. Ultimately, I envision this technique

serving as a straightforward method for spatially controlled introduction of biologically relevant molecular cues. This simple method for making gradients of covalently attached molecules in 3-D should find future utility for the preparation of cell culture matrices that can mimic ligand density and clustering effects known to be important in cell adhesion and signaling.

2.3.4 3D Encapsulation of Prostate Cancer Cells

There is current interest in the engineering of physiologically relevant *in vitro* models of prostate cancer (PCa) that can serve as reliable and predictive platforms for drug discovery.[40] Towards this end, HA-based hydrogel systems have been utilized to mimic the HA-rich tumor associated stromal environment and PCa cells were encapsulated in HA gels *in situ* during the gelation process.[41-42] Prior to the work described below, a considerable challenge was to retain full cell viability in the presence of the crosslinking chemistry, as even bioorthogonal crosslinking reactions can adversely affect cell viability.[30] I show here that LNCaP cells retain near full viability after encapsulation in HA-gels using tetrazine-TCO ligation. Thus, LNCaP cells were suspended in a solution of HA-Tz (2 wt%) and interfacial crosslinking with a bis–TCO (400 μM) solution resulted in the formation of cell-laden constructs. Cell counting of the maximum intensity projections of confocal images (Figure 2.7a) revealed 99% cell viability after day 1 and 98% viability after day 5. These results confirm the cytocompatible nature of the crosslinking chemistry.

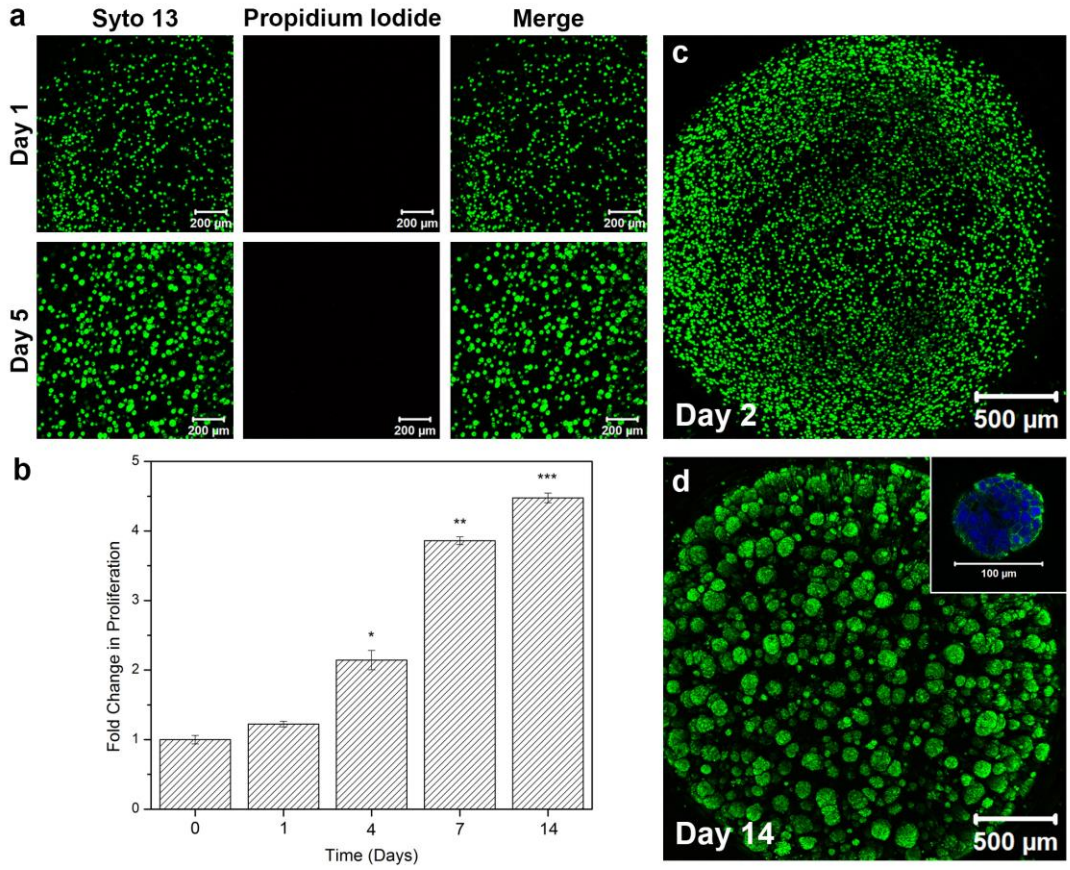

Figure 2.7 Use of interfacial bioorthogonal crosslinking to encapsulate LNCaP cells in HA microspheres. **a**. Live/dead staining of cells cultured in HA microspheres at day 1 and day 5. Live cells were stained green by Syto 13 and dead cells were stained red by propidium iodide. **b**. Cell proliferation analyzed by Trypan Blue exclusion showed a steady increase in cell number over 14 days of culture. *$p < 0.05$. **c**. Confocal image of an entire microsphere after live/dead staining showing individually dispersed LNCaP cells at day 2. **d**. Confocal image of an entire microsphere after live/dead staining showing the presence of dispersed tumoroids with aggregated cells at day 14. The insert shows a ~100 µm tumoroid strained for F-actin (green) and nuceli (blue) at day 14. All confocal images shown are maximum intensity projections of z-stacks.

Cell counting by Trypan Blue exclusion revealed a significant cell proliferation during the first week of culture, with the total number of cells increased by ~4 fold at day 7. The proliferation rate decreased during week two of 3-D culture, and by day 14, a total of 96,000 ± 2,600 cells were found per gel construct, representing a 4.5 fold increase over day 0 (Figure 2.7b). LNCaP cells were initially entrapped homogenously in the microspheres in a single cell state (Figure 2.7c). Over time, individual cells proliferated and neighboring cell clusters merged within the microsphere. Isolated tumoroids varied in diameter from 30 to 200 μm were observed at day 14 (Figure 2.7d).

Cells in individual aggregates displayed a rounded, clustered morphology with apparent cortical organization of actin (Figure 2.7d, insert), in agreement with the cell morphology that is observed *in vivo*, and in sharp contrast to the flat, spread out morphology with mature cytoskeletal stress fibers seen in 2-D cultures.[41] Individual microspheres were completely populated by cauliflower-like structures that were 2.7 mm across, containing an estimated 200 dispersed spheroids greater than 50 μm, displaying a morphology analogous to growing tumors in the body.

2.4 Conclusions

My experiments highlight the utility of tetrazine-TCO ligation for the construction of hydrogel networks with well-defined spatial heterogeneity through instantaneous crosslinking at the gel-solution interface. The interfacial nature of the crosslinking reaction enables the creation of hydrogel microspheres or crosslinked channels using the same hydrogel precursors. My 3-D channel with crosslinked shell was created without using any sacrificial template, and due to the straightforward nature, should be readily adaptable to high throughput platforms. Another important

consequence of interfacial crosslinking is the ability to pattern layers or gradients of functional molecules in 3-D by simply controlling the concentration, as illustrated by using a model compound, Alexa-TCO. The interfacial approach described here allows for the creation of gradient or layered structures without external triggers[43,44] or pre-existing templates,[45,46] and two independent reactions for crosslinking and patterning purposes are not required.[10,47] The method described here is simple, highly reproducible and does not require specialized equipment.

With interfacial bioorthogonal crosslinking, LNCaP cells can be entrapped in the gelling microsphere with 99% viability. This high cellular viability reflects the biocompatibility of the gels, and the bioorthogonality of the chemistry as well as the gelation process itself. The combination of fast, interfacial bioorthogonal crosslinking and a relatively slow rate of molecular diffusion allows the cells in the droplet to adapt to the changing environment over the course of 2 hours before the "covalent cage" is finally set. Moreover, the gels described here are synthesized in their equilibrium swelling state, thereby presenting a consistent environment to the cells before and after the gelation.

I anticipate that interfacial bioorthogonal crosslinking will serve as a generally useful tool for introducing the 3-D localization of molecular cues needed to initiate and guide the formation of artificial tissues in *in vitro* cultures. I envision that cells encapsulated within 3-D structures can be induced to undergo tissue specific differentiation, via the guidance of spatially restricted biological signaling molecules. This approach also holds promise for the creation synthetic tissue models with distinct cell populations. Ongoing studies include the adaption of this hydrogel platform for the creation of complex structures using 3-D bioprinting, the creation of cell-

instructive environments via a delayed, bioorthogonal addition of cellular guidance cues, and 3-D tissue engineering by cultivation of multiple cells in different time and space domains.

2.5 Spectral Data for Chapter 2

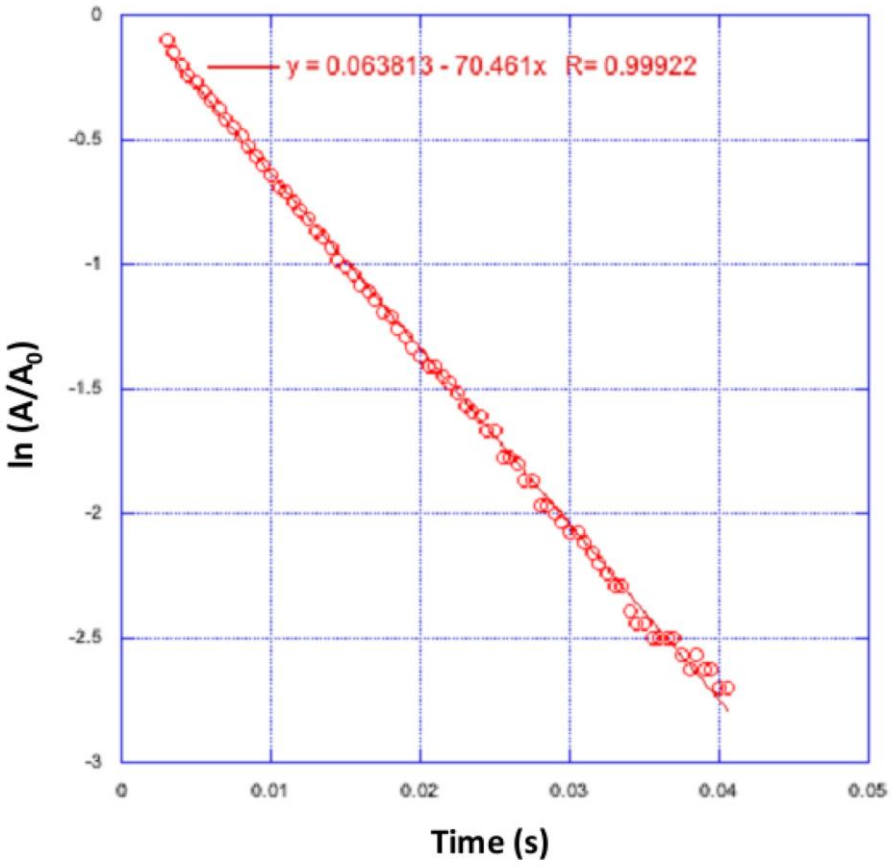

Figure 2.8 A representative stopped-flow kinetic run for determining the second order rate constant for the reaction between **4** and **6** in H_2O. Linear correlation was found between time(s) and ln (A/A_0).

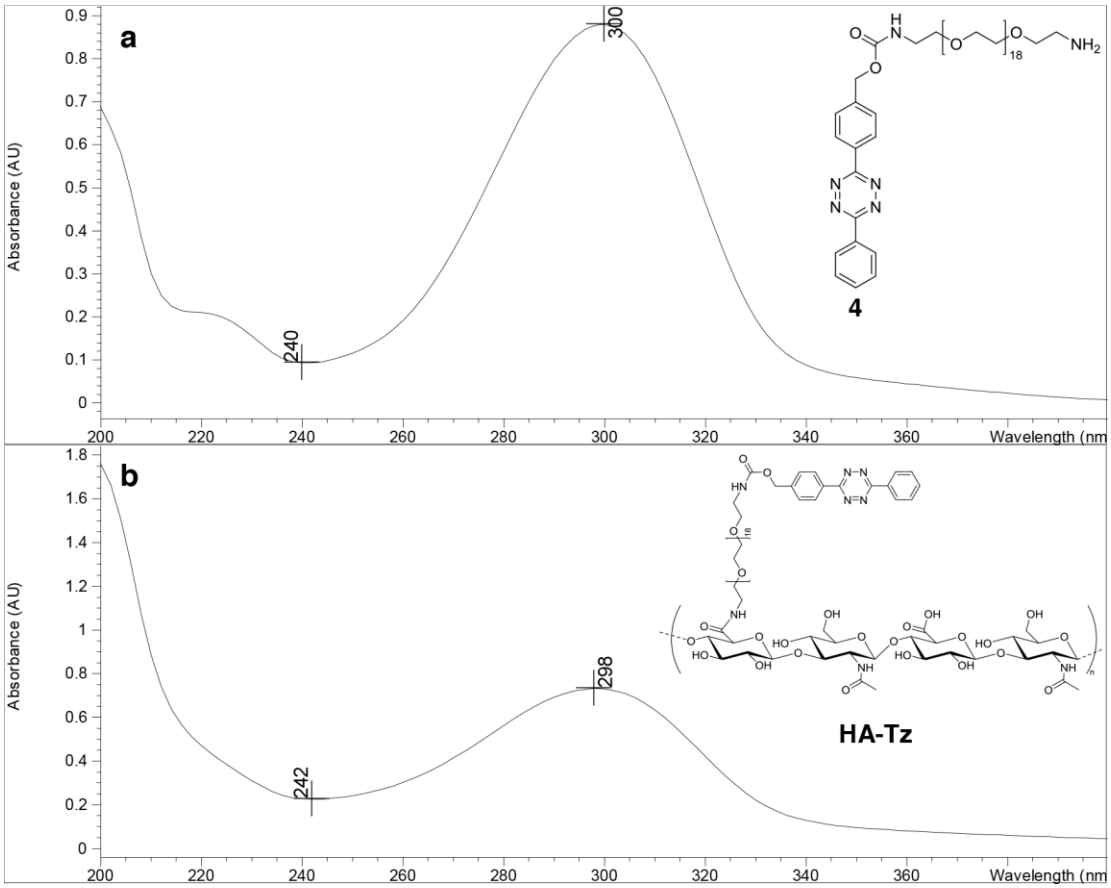

Figure 2.9 UV-vis spectra of aqueous solutions of (a) compound **4** at a concentration of 27.5 μM and (b) HA-Tz at a concentration of 0.153 g/L. In both measurements, a UV cuvette with a pathlength of 1 cm was used.

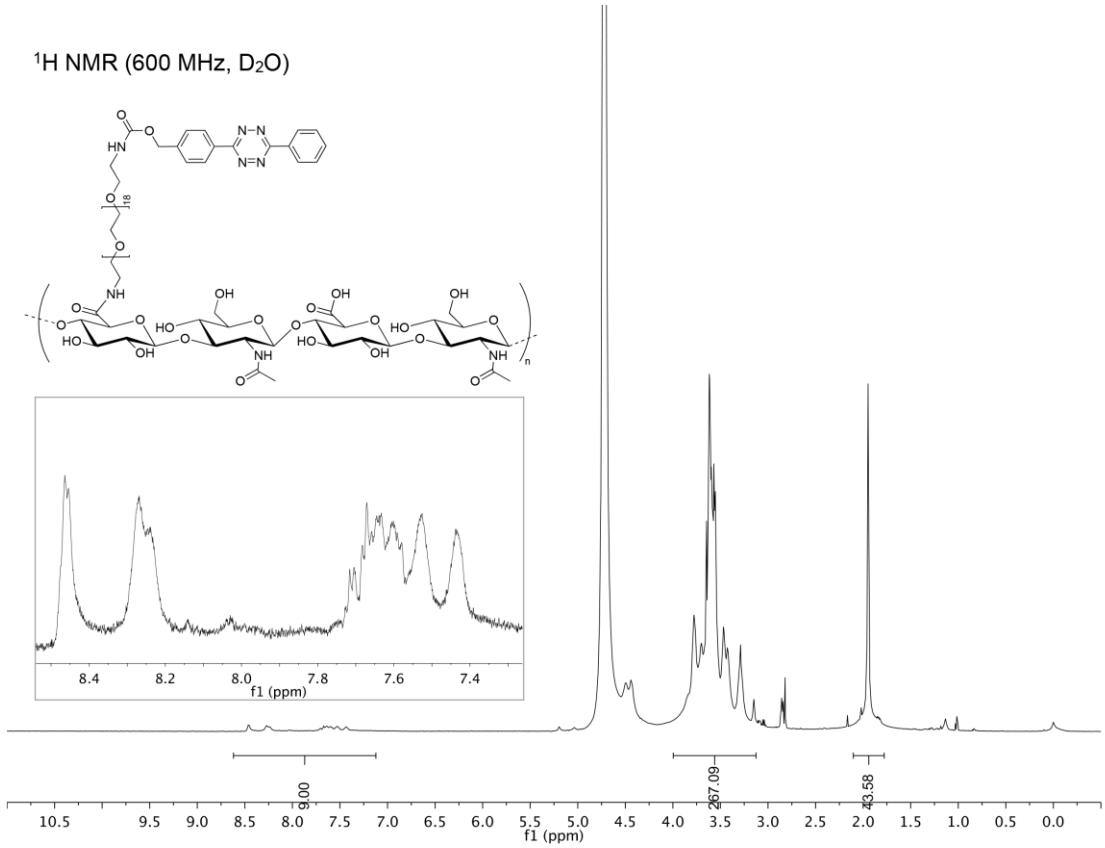

Figure 2.10 ^{1}H NMR spectrum of HA-Tz in D_2O.

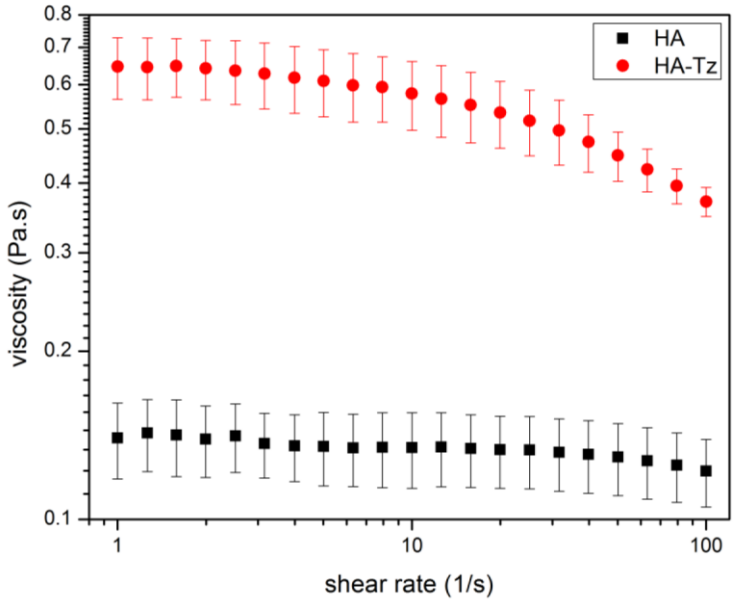

Figure 2.11 Viscosity profile of 2 wt% HA (black) and HA-Tz (red) in PBS.

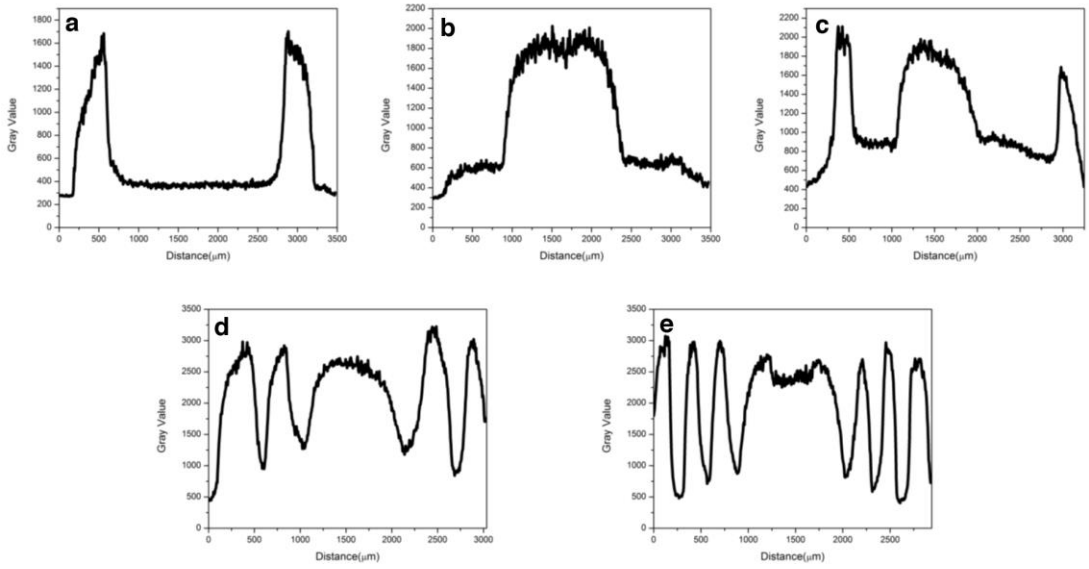

Figure 2.12 a-e) Color intensity plots of Figure 2.4b-f, respectively.

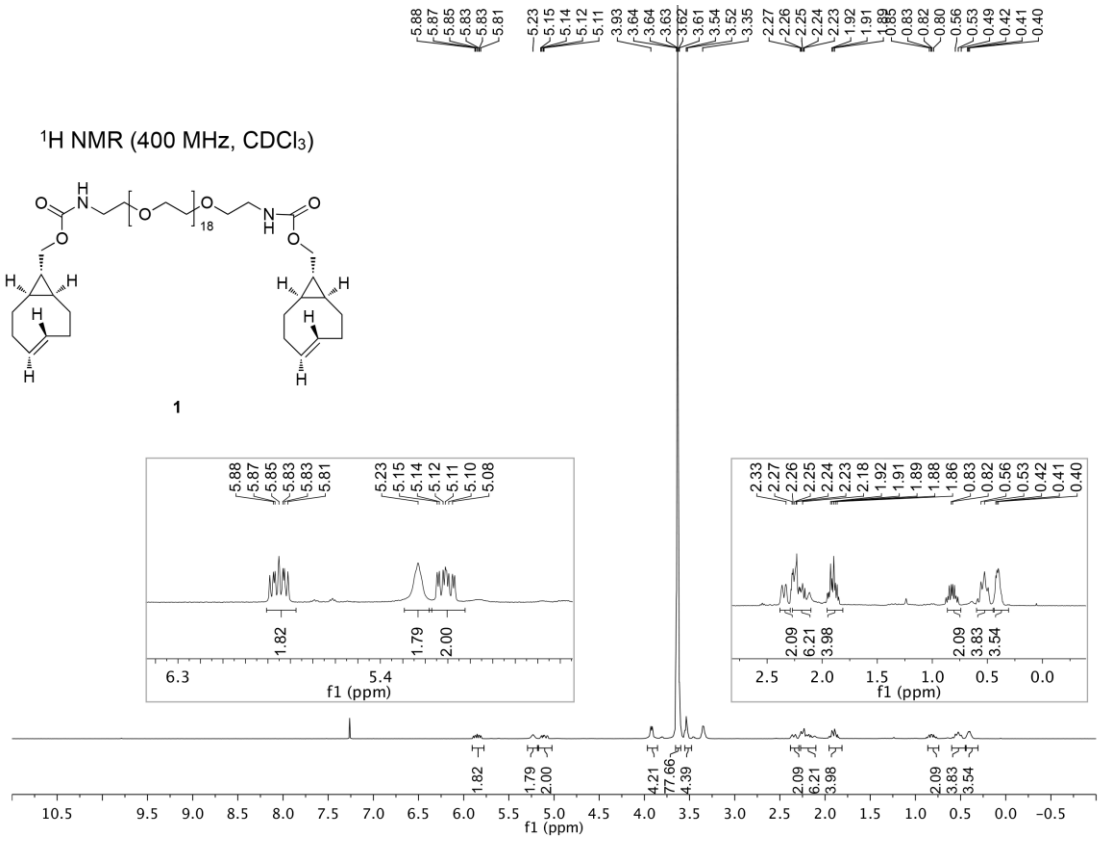

Figure 2.13 ^{1}H NMR spectrum of bis-TCO in $CDCl_3$.

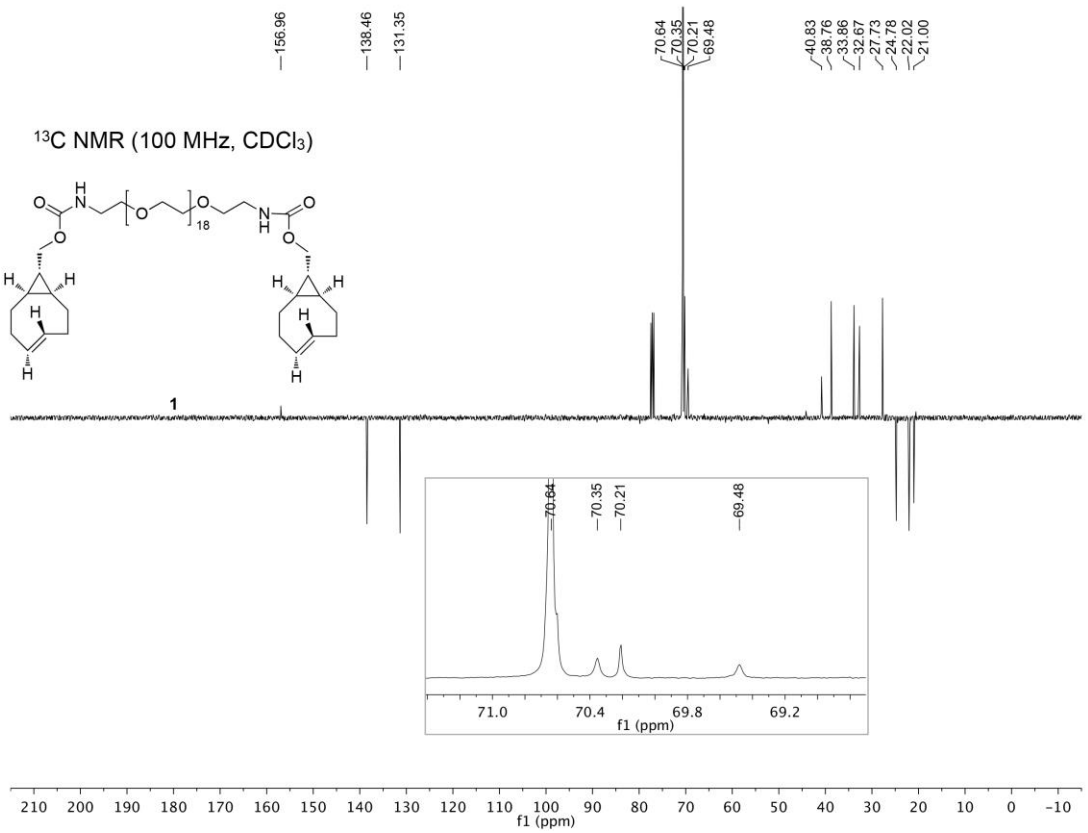

Figure 2.14 ^{13}C NMR spectrum of bis-TCO in $CDCl_3$.

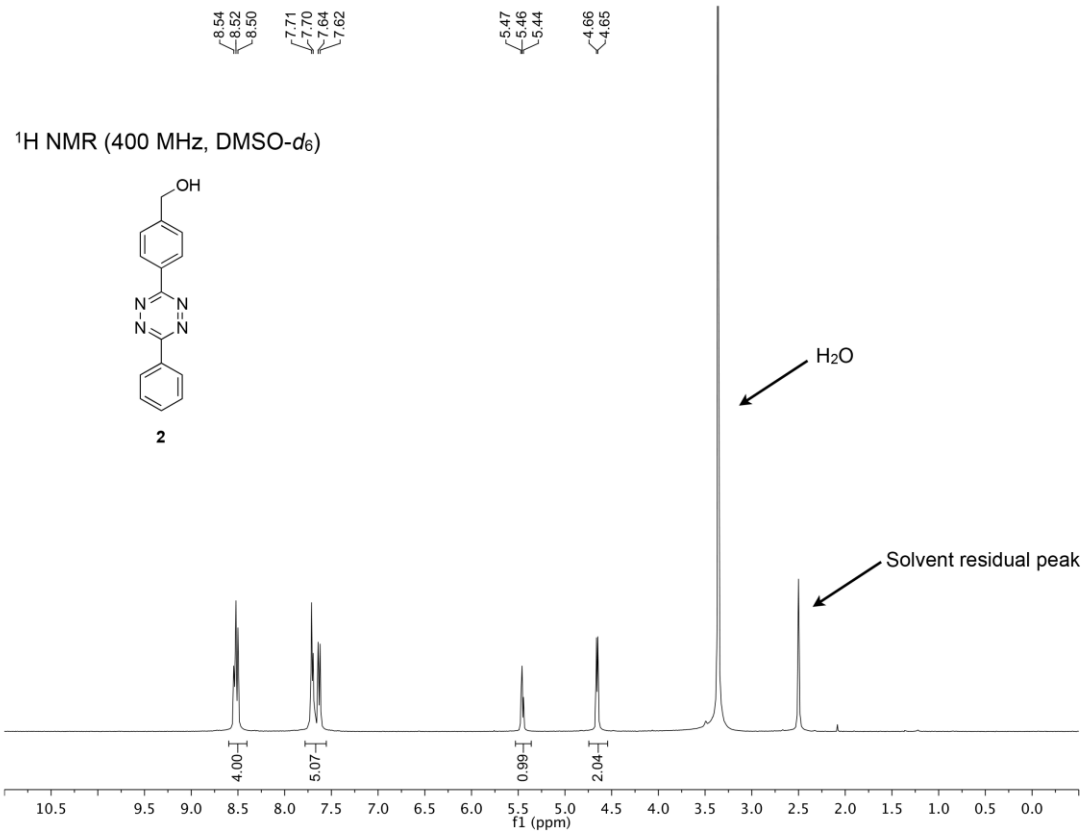

Figure 2.15 ^{1}H NMR spectrum of (4-(6-phenyl-1,2,4,5-tetrazin-3-yl)phenyl)methanol in DMSO-d_6.

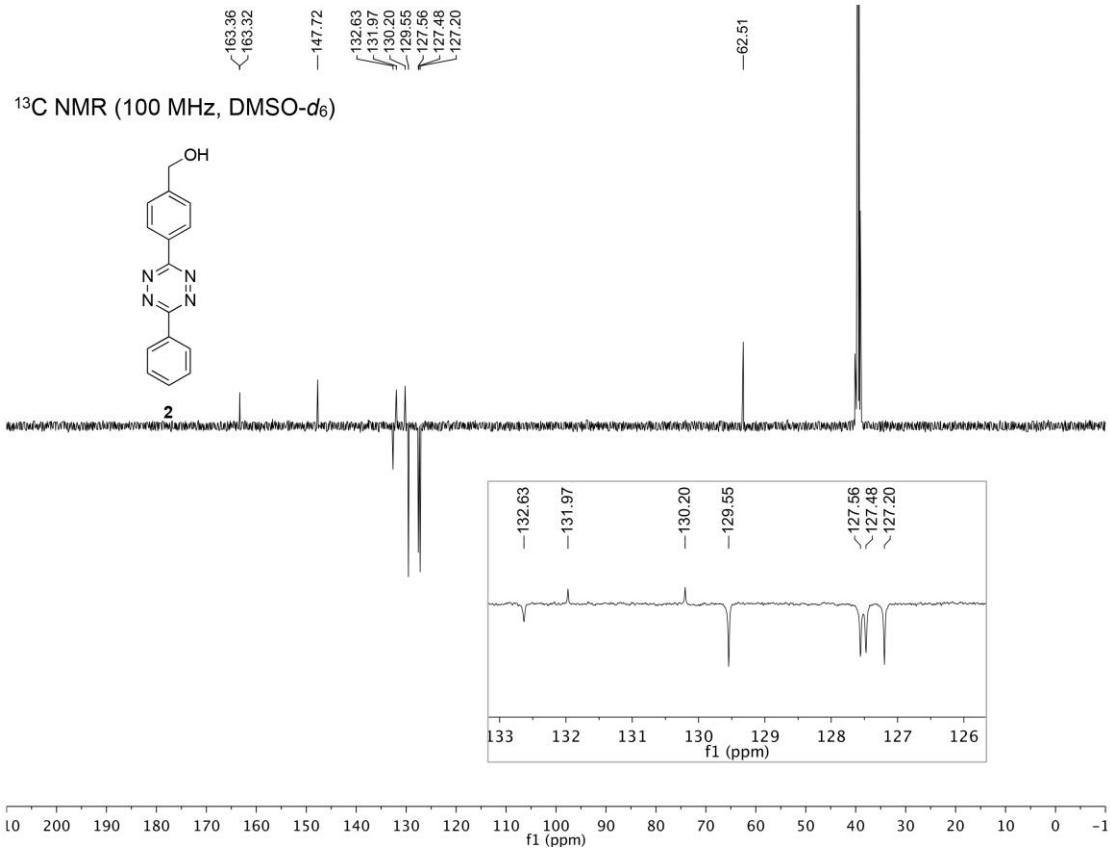

Figure 2.16 ^{13}C NMR spectrum of (4-(6-phenyl-1,2,4,5-tetrazin-3-yl)phenyl)methanol in DMSO-d_6.

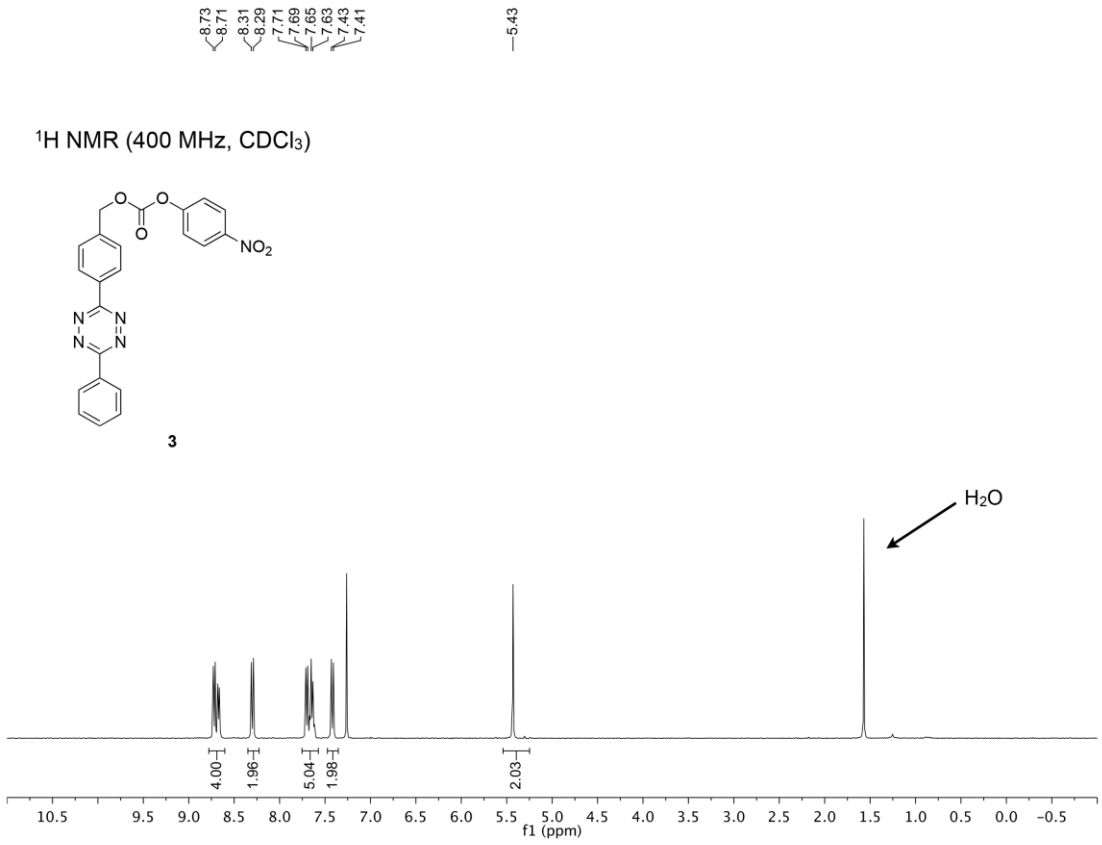

Figure 2.17 ^{1}H NMR spectrum of 4-nitrophenyl 4-(6-phenyl-1,2,4,5-tetrazin-3-yl)benzyl carbonate in $CDCl_3$.

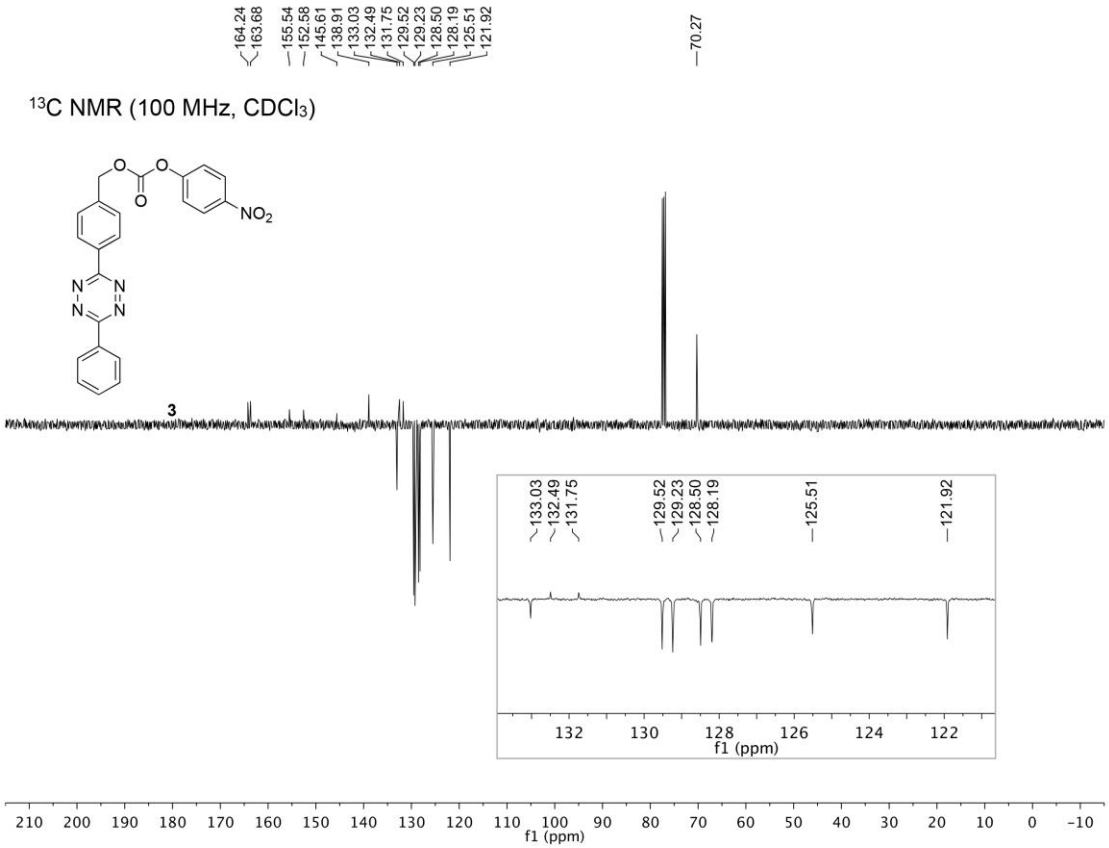

Figure 2.18 ^{13}C NMR spectrum of 4-nitrophenyl 4-(6-phenyl-1,2,4,5-tetrazin-3-yl)benzyl carbonate in $CDCl_3$.

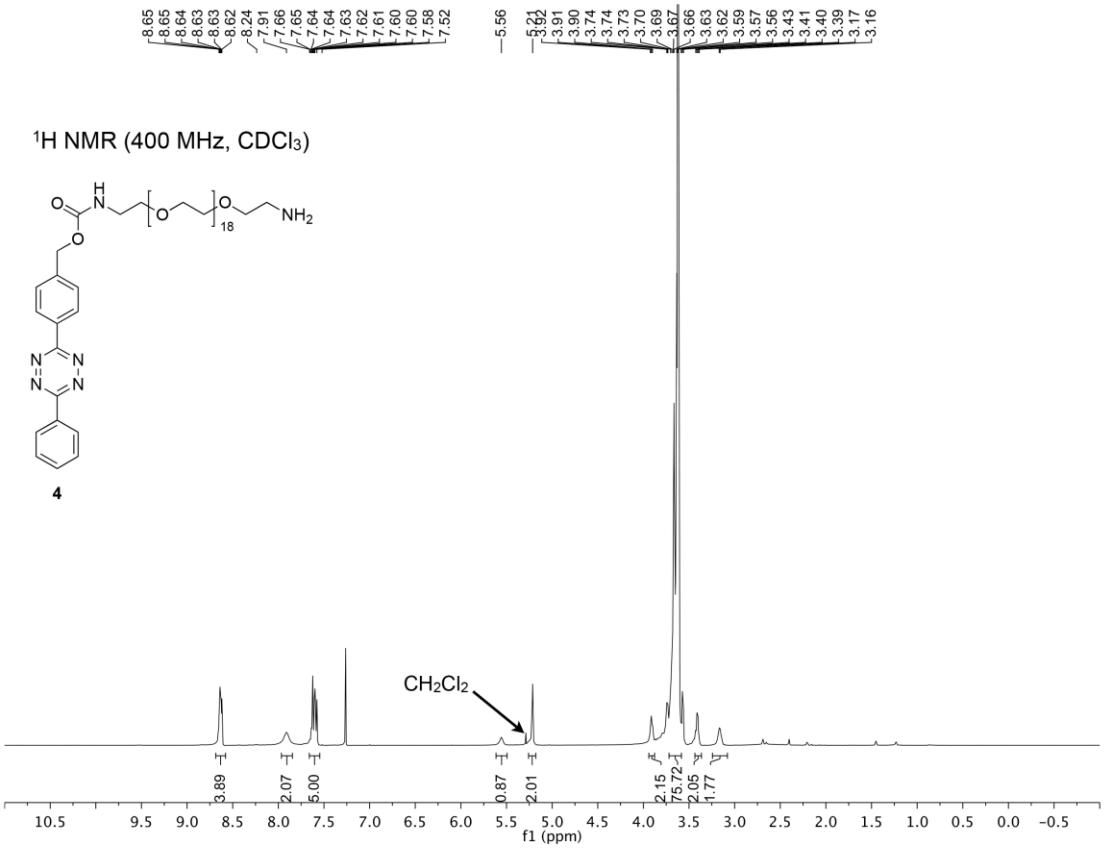

Figure 2.19 ^{1}H NMR spectrum of tetrazine-OEG-amine in $CDCl_3$.

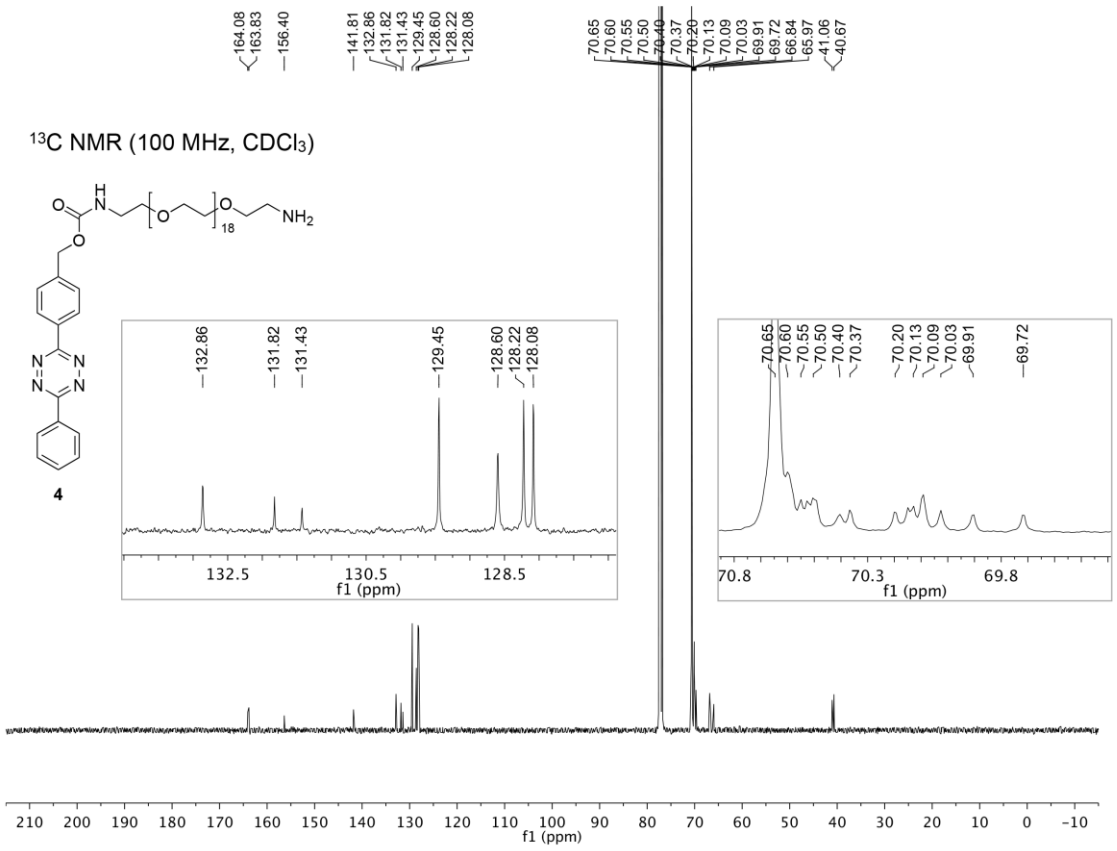

Figure 2.20 ^{13}C NMR spectrum of tetrazine-OEG-amine in $CDCl_3$.

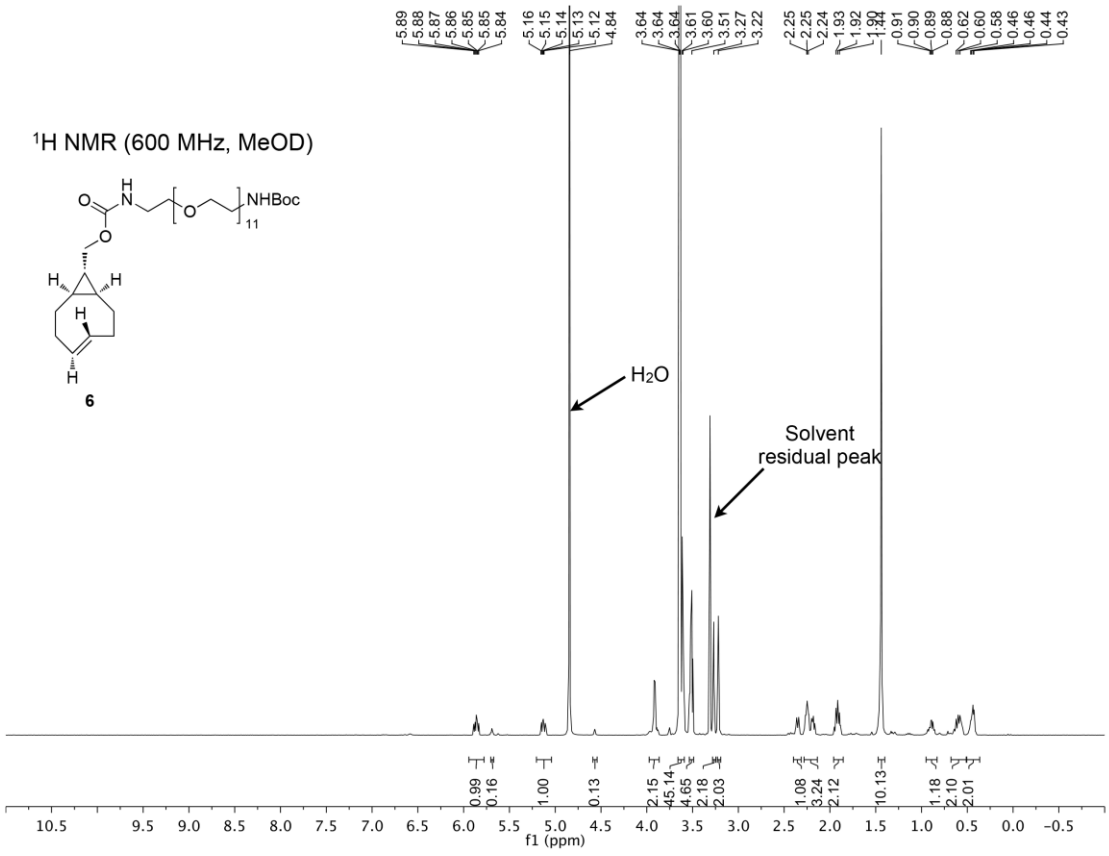

Figure 2.21 ^{1}H NMR spectrum of TCO-OEG-NHBoc in MeOD.

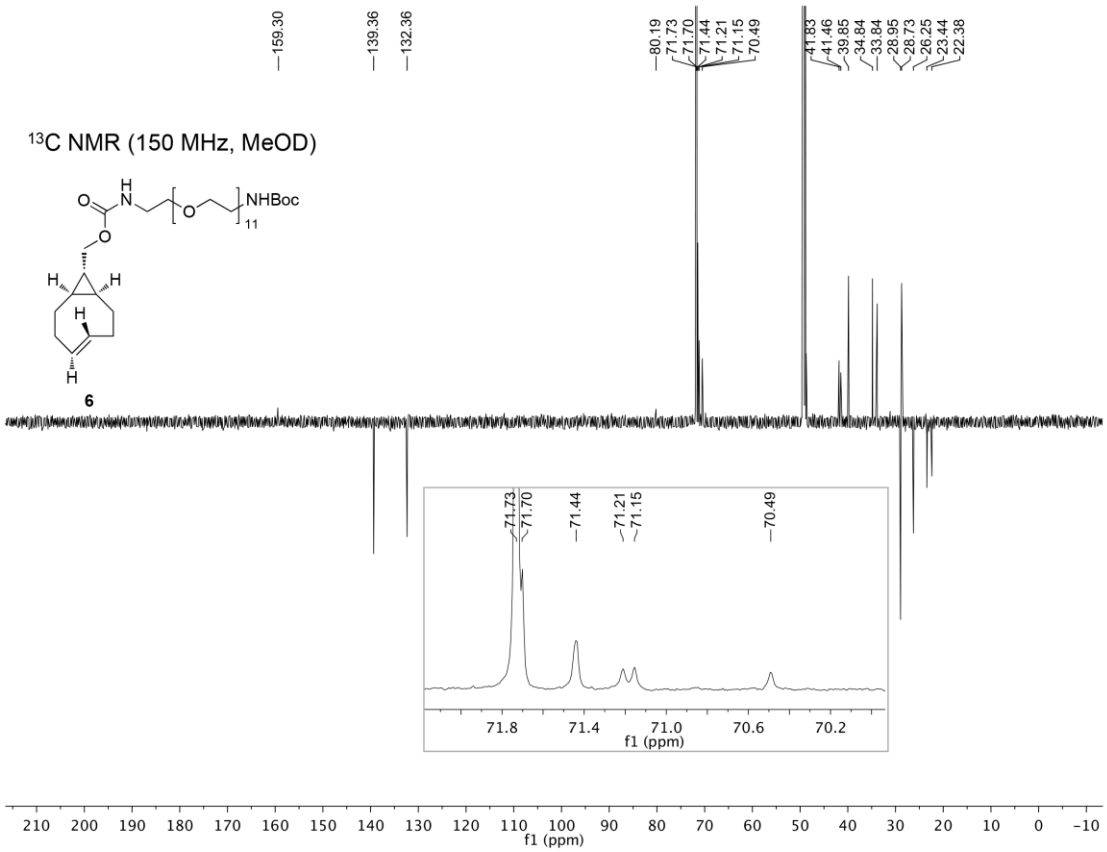

Figure 2.22 ^{13}C NMR spectrum of TCO-OEG-NHBoc in MeOD.

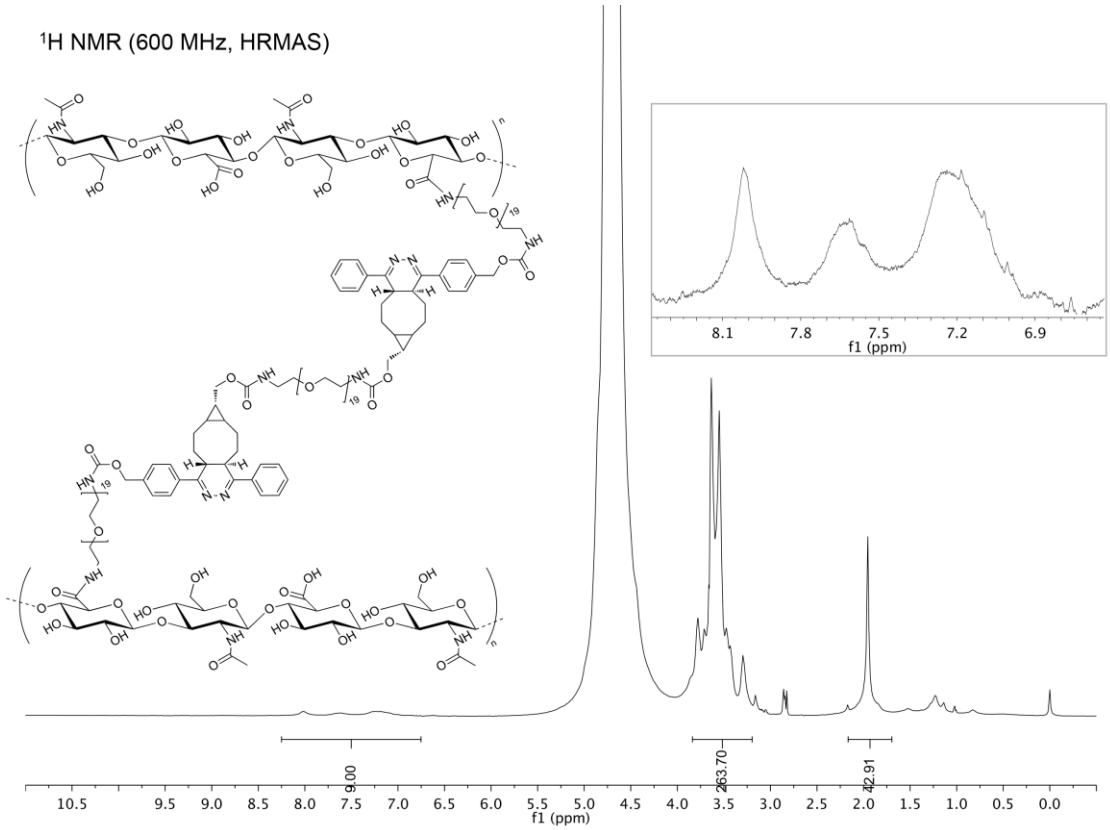

Figure 2.23 High resolution magic angle spinning (HR MAS) ^{1}H NMR spectrum of crosslinked HA-Tz/bis-TCO gels.

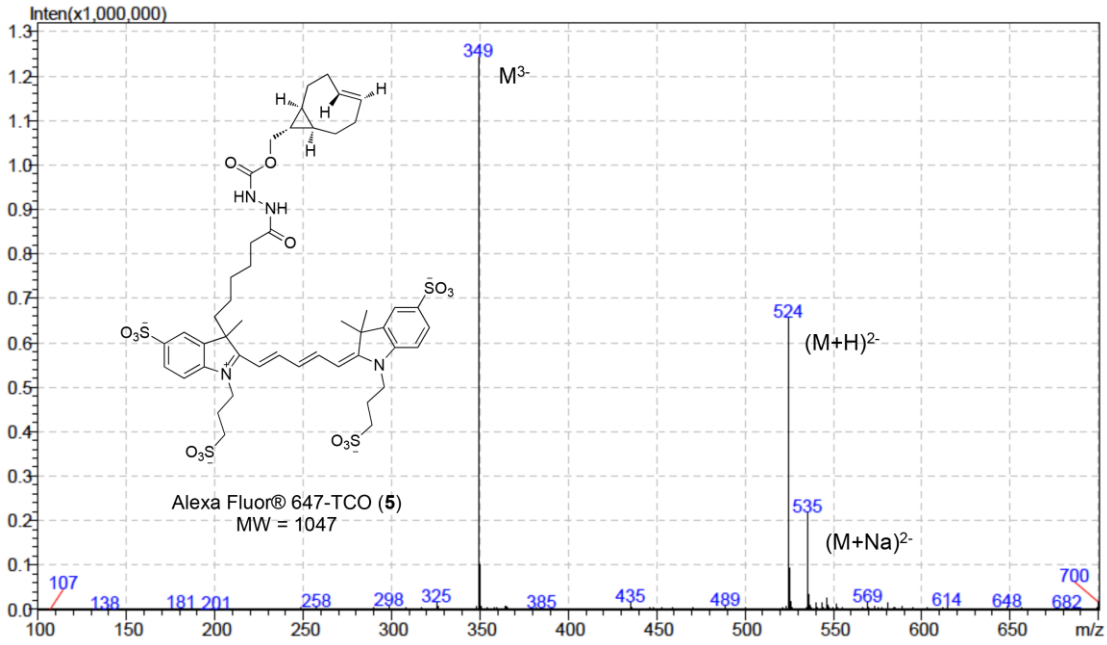

Figure 2.24 LC-MS analysis of Alexa-TCO with Shimadzu LCMS-2020. (ESI negative mode, 60% ACN/H_2O)

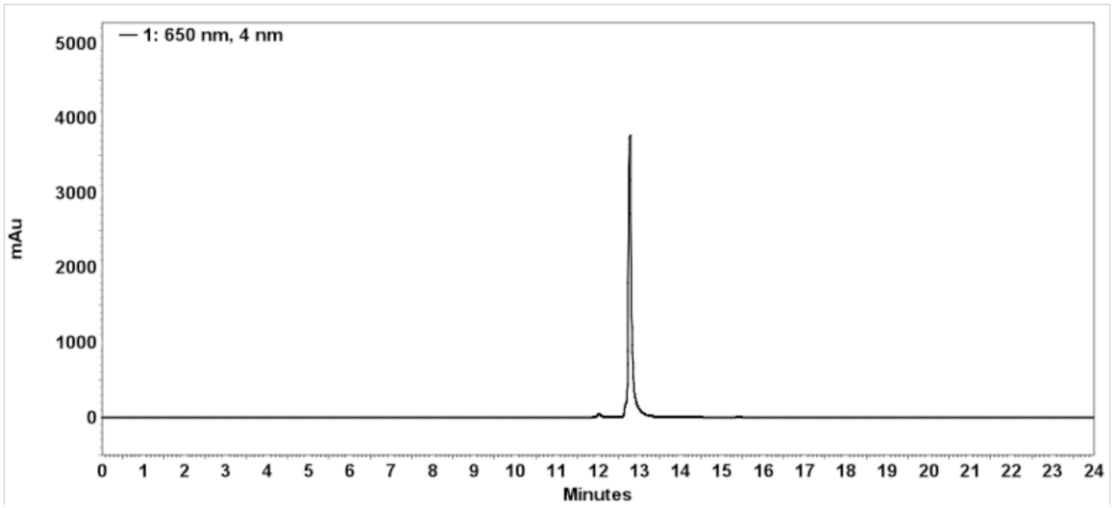

Figure 2.25 HPLC analysis of Alexa-TCO with Shimadzu prominence HPLC with SPD-M20A diode array detector (5 min: 5% ACN/H_2O; 22 min: 100% ACN; 24 min: 100% ACN).

Figures 2.8-10,13-25 were collected by my collaborator, Han Zhang.[50]

REFERENCES

[1] Lutolf M. P., Gilbert P. M.& Blau H. M. Nature **2009**, 462, 433-441.

[2] Huebsch N.& Mooney D. J. Nature **2009**, 462, 426-432.

[3] Rostovtsev V. V., Green L. G., Fokin V. V.& Sharpless K. B. Angew. Chem. Int. Ed. **2002**, 41, 2596-2599.

[4] Tornøe C. W., Christensen C.& Meldal M. J. Org. Chem. **2002**, 67, 3057-3062.

[5] Hawker C. J.& Wooley K. L. Science **2005**, 309, 1200-1205.

[6] Agard N. J., Prescher J. A.& Bertozzi C. R. J. Am. Chem. Soc. **2004**, 126, 15046-15047.

[7] Jewett J. C.& Bertozzi C. Chem. Soc. Rev. **2010**, 39, 1272-1279.

[8] Sanders B. C. et al. J. Am. Chem. Soc. **2010**, 133, 949-957.

[9] Moran J., McKay C. S.& Pezacki J. P. Can. J. Chem. **2011**, 89, 148-151.

[10] DeForest C. A.& Anseth K. S. Nature Chem. **2011**, 3, 925-931.

[11] DeForest C. A.& Anseth K. S. Angew. Chem. Int. Ed. **2012**, 51, 1816-1819.

[12] Blackman M. L., Royzen M.& Fox J. M. J. Am. Chem. Soc. **2008**, 130, 13518-13519.

[13] Taylor M. T., Blackman M. L., Dmitrenko O.& Fox J. M. J. Am. Chem. Soc. **2011**, 133, 9646-9649.

[14] Rossin R. et al. Bioconj. Chem. **2013**, 24, 1210-1217.

[15] Lang K. et al. J. Am. Chem. Soc. **2012**, 134, 10317-10320.

[16] Devaraj N. K., Weissleder R.& Hilderbrand S. A. Bioconj. Chem. **2008**, 19, 2297-2299.

[17] Pipkorn R. et al. J. Peptide Sci. **2009**, 15, 235-241.

[18] Patterson D. M., Nazarova L. A., Xie B., Kamber D. N.& Prescher J. A. J. Am. Chem. Soc. **2012**, 134, 18638-18643.

[19] Yang J., Šečkutė J., Cole C. M.& Devaraj N. K. Angew. Chem. Int. Ed. **2012**, 51, 7476-7479.

[20] Chen W., Wang D., Dai C., Hamelberg D.& Wang B. Chem. Commun. **2012**, 48, 1736-1738.

[21] Karver M. R., Weissleder R.& Hilderbrand S. A. Angew. Chem. Int. Ed. **2012**, 51, 920-922.

[22] Niederwieser A. et al. Angew. Chem. Int. Ed. **2013**, 52, 4265-4268.

[23] Keliher E. J., Reiner T., Turetsky A., Hilderbrand S. A.& Weissleder R. Chem. Med. Chem., **2011**, 6, 424-427.

[24] Reiner T., Keliher E. J., Earley S., Marinelli B.& Weissleder R. Angew. Chem. Int. Ed. **2011**, 50, 1922-1925.

[25] Knall A.-C.& Slugovc C. Chem. Soc. Rev. **2013**, 42, 5131-5142.

[26] Liu S. et al. Mol. Imaging, **2013**, 12, 121-128.

[27] Cole C. M., Yang J., Seckute J.& Devaraj N. K. Chem. Bio. Chem., **2013**, 14, 205-208.

[28] Hansell C. F. et al. J. Am. Chem. Soc., **2011**, 133, 13828-13831.

[29] Cok A. M., Zhou H.& Johnson J. A. Macromol. Symp. **2013**, 329, 108-112.

[30] Alge D. L., Azagarsamy M. A., Donohue D. F.& Anseth K. S. Biomacromolecules, **2013**, 14, 949-953.

[31] Haun J. B., Devaraj N. K., Hilderbrand S. A., Lee H.& Weissleder R. Nat. Nano. **2010**, 5, 660-665.

[32] Odian G. Principles of Polymerization, 4th edn. (John Wiley & Sons, Inc., 2004).

[33] Lim F.& Sun A. M. Science, **1980**, 210, 908-910.

[34] Dumitriu S., Popa, V. Polymeric Biomaterials: Structure and Function, vol. 1. (CRC Press, **2013**).

[35] Garg H. G.& Hales C. A. Chemistry and biology of hyaluronan, 1st edn. (Elsevier Ltd., **2004**).

[36] Burdick J. A.& Prestwich G. D., Adv. Mater., **2011**, 23, H41-H56.

[37] Xu X., Jha A. K., Harrington D. A., Farach-Carson M. C.& Jia X., Soft Matter **2012**, 8, 3280-3294.

[38] Cleland R. L.& Wang J. L., Biopolymers, **1970**, 9, 799-810.

[39] Jia X. et al., Biomacromolecules **2006**, 7, 3336-3344.

[40] Hutmacher D. W. et al.,Trends Biotechnol., **2010**, 28, 125-133.

[41] Xu X. et al. Biomaterials, **2012**, 33, 9049-9060.

[42] Gurski L. A. et al. PLoS One, 2012, 7, e50075.

[43] Bajaj P., Marchwiany D., Duarte C.& Bashir R. Adv. Healthc. Mater., **2013**, 2, 450-458.

[44] Luo Y.& Shoichet M. S., Nat. Mater., **2004**, 3, 249-253.

[45] Lee W.& Park J. Adv. Mater., 2012, 24, 5339-5344.

[46] Occhetta P. et al. Biofabrication, **2013**, 5, doi:10.1088/1758-5082/1085/1083/035002.

[47] Khetan S.& Burdick J. A., Soft Matter, **2011**, 7, 830-838.

[48] Panne, P., Fox, J.M., J. Am. Chem. Soc. **2007**, 129, 22-23.

[49] Royzen, M., Yap, G. P. A., Fox, J. M., J. Am. Chem. Soc. **2008**, *130*, 3760.

[50] Zhang, H., Dicker, K.T., Xu. X., Jia, X., Fox, J. M., ACS Macro Lett. **2014**, *3*, 727.

Chapter 3

3D PATTERNING OF SYNTHETIC HYDROGELS VIA INTERFACIAL BIOORTHOGONAL CHEMISTRY FOR SPATIAL CONTROL OF STEM CELL BEHAVIOR

3.1 Introduction

Rational design of synthetic matrices with tissue-specific biochemical compositions and biomechanical properties represents an important step toward the regeneration of functional tissues *in vitro*.[1-2] Synthetic scaffolds must fulfill the functions of native ECM until cells produce their own support structures to form an engineered tissue.[3-5] Hence, it is important to create an adequate cellular microenvironment with spatial variations of mechanical properties, cell-binding motifs, and morphogenic cues in hydrogel scaffolds.[6-8] Photolithography and stereolithography have enabled spatial tailoring of the cell microenvironment based on photochemistry.[9-10] For example, a secondary, radical-mediated photo-crosslinking reaction was utilized to spatially tune the stiffness of a hydrogel matrix established by Michael addition.[11] Alternatively, photolabile peptide substrates were incorporated in a hydrogel network to afford localized biomolecule tethering through photoactivation.[12] Finally, the chemical and physical properties of a PEG-based hydrogel were dynamically and spatially modulated using a nitrobenzyl ether-derived photodegradable functionality.[13] These materials fabrication strategies rely on the usage of an external trigger, e.g. UV light, to module cell morphology and differentiation in a spatial manner. Complementary approaches that do not rely on

UV-light, which may not be well tolerated by all cell types, or specialized equipment, as required for two-photon processes, have the potential to expand the scope of 3D cell culture methods.

Bioorthogonal reactions,[14] unnatural chemical transformations that occur efficiently in biological context, have recently attracted attention as tools for the fabrication of functional biomaterials.[15] Tetrazine ligation, an inverse-electron-demand Diels-Alder cycloaddition between *s*-tetrazines and strained alkenes, produces nitrogen gas as the only byproduct.[16-17] With *trans*-cyclooctene as the dienophile, this bioorthogonal reaction features fast kinetics, high selectivity at low concentration and compatibility with biological systems.[18-19] The conformationally strained *trans*-cyclooctenes, s-TCO and d-TCO, combine with tetrazines with the fastest rate constants reported to date for a biorthogonal reaction.[20] Based on these rapid reactions, we have developed diffusion-controlled strategies for the creation of protein-mimetic polymer microfibers[19,21] and 3D patterned hydrogel spheres,[18] via *interfacial bioorthogonal polymerization* and *interfacial bioorthgonal crosslinking* respectively. The fabrication of 3D patterned hydrogels can be carried out in one-step without having to rely on a template or photomask, potentially cytotoxic external triggers[22], or step-by-step addition/curing cycles.[23] Because tetrazine ligation is inherently cytocompatible and specific, inclusion of hMSCs during hydrogel fabrication can produce a cellular construct with high viability. The network properties can be systematically tuned in a spatially-defined manner to guide stem cells through stages of differentiation and maturation.

Described herein is the use of interfacial bioorthogonal crosslinking to engineer biomimetic hydrogels with a 3D core-shell structure that can spatially dictate

the behavior of encapsulated hMSCs (Figure 3.1). Hydrogels were fabricated using tetrazine-modified hyaluronic acid (HA-Tz) along with mono- and bi-functional TCO-derivatives (Figure 3.2) *via* a diffusion-controlled interfacial crosslinking mechanism. Time-dependent alteration of the TCO reservoir composition resulted in the creation of hydrogels with a 3D core-shell structure. Biochemical signals, including matrix metalloprotease (MMP)-degradable peptide and integrin binding motifs, and biomechanical cues were patterned into the hydrogels to spatially direct cellular behavior.[24-25] I envision that this synthetic platform should ultimately be useful for the engineering of complex tissues with layered structures.

3.2 Materials and Methods

3.2.1 Materials

All reactions were carried out in glassware that was flame-dried under vacuum and cooled under nitrogen. Cy3-TCO was purchased from AAT Bioquest. O,O′-Bis(2-aminoethyl)hexacosaethylene glycol (≥ 95% oligomer purity) was purchased from Santa Cruz Biotechnology. Hyaluronic acid (sodium salt, 430 kDa) was a generous gift from Sanofi/Genzyme Corporation. Reactive intermediates or products, including (rel-1R,8S,9R,4E)-bicyclo[6.1.0]non-4-ene-9-ylmethanol,[20] d-TCO-carbonate,[43] RGD-TCO[21] and Alexa-TCO[18] were prepared following known procedures. Peptides were synthesized using CEM Liberty Blue Peptide Synthesizer. Dialysis membranes were purchased from Spectrum Labs (MWCO: 10 kDa). Flash Chromatography was performed using normal phase Silicycle silica gel (40-63D, 60Å). Other reagents were purchased from commercial sources without additional

purification. The detailed synthesis of hydrogel precursors can be found in the supporting information.

3.2.2 Synthesis of Hydrogel Precursors

3.2.2.1 Synthesis of 2-(4-(6-methyl-1,2,4,5-tetrazin-3-yl)phenyl)acetohydrazide (Tz-hydrazide)

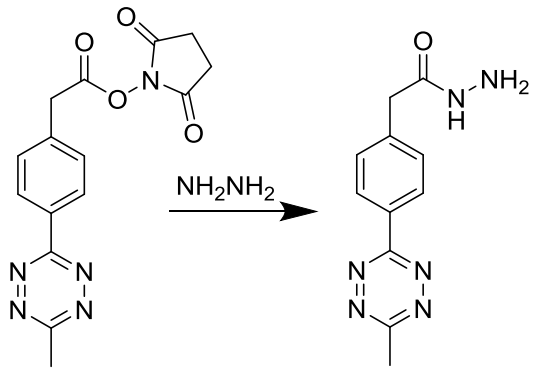

Hydrazine anhydrous (73.4 mg, 2.29 mmol) dissolved in dichloromethane (3 mL) was slowly added a solution of 2,5-dioxopyrrolidin-1-yl 2-(4-(6-methyl-1,2,4,5-tetrazin-3-yl)phenyl)acetate (purchased from Kerafast, 150 mg, 0.46 mmol) in dichloromethane (15 mL). The mixture was stirred at room temperature for 5 minutes, and then directly loaded onto silica gel in a flash column. Column chromatography using a gradient (2 to 5 %) of methanol in dichloromethane afforded 101 mg (0.41 mmol, 90%) of the title compound as a purple solid. ^{1}H NMR (600 MHz, CD_4O) δ 8.51 (s, 2H), 7.57 (s, 2H), 3.61 (s, 0H), 3.03 (s, 0H). ^{13}C NMR (100 MHz, CD_4O) δ 172.39 (1 C), 168.74 (1 C), 165.19 (1 C), 141.60 (1 C), 132.19 (1 C), 131.06 (2 CH), 128.91 (2 CH), 41.65 (1 CH_2), 21.06 (1 CH_3). Initial hydrazine treatment was performed by my collaborator, Han Zhang.

3.2.2.2 Synthesis of tetrazine functionalized hyaluronic Acid (HA-Tz)

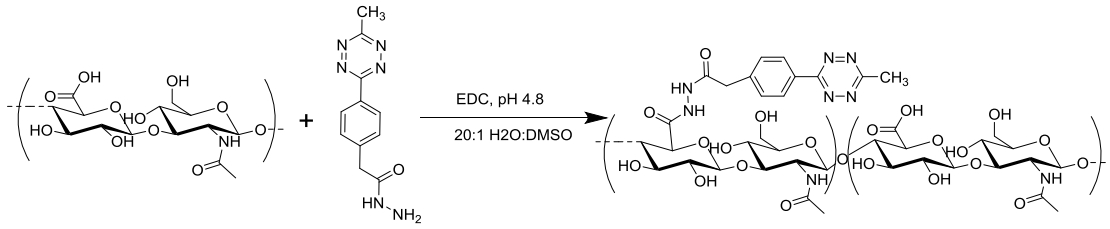

Hyaluronic acid (HA, sodium salt, 430 kDa, 275.9 mg, 0.69 mmol) was dissolved in DI H_2O (92 mL) at a concentration of 3 mg/mL. To this solution was added 1-ethyl-3-[3-(dimethylamino)propyl]-carbodiimide hydrochloride (EDC, 264.9 mg, 1.38 mmol), Tz-hydrazide (67.6 mg, 0.28 mmol) dissolved in DMSO (5 mL). The solution was then added dropwise to the HA solution. The resulting mixture was stirred at room temperature for 24 h with pH controlled around 4.8 by adding 0.1 M HCl aqueous solution. The resulting solution was diluted with DI H_2O to a final volume of 200 mL and was exhaustively dialyzed (Spectra 10 kDa MWCO) first against 0.1 M NaCl solution, then against DI H_2O. The purified solution was lyophilized to afford 267.2 mg (0.60 mmol, 88%) HA-Tz as a pink fluffy solid. The product was stored at -20 °C prior to use.

The percent tetrazine incorporation in HA-Tz was determined collectively by UV-vis and ^{1}H NMR analyses. UV-vis quantification was based on the tetrazine absorption at λ_{max} 267 nm, employing Beer-Lambert law. Using an aqueous solution of Tz-hydrazide at a concentrations from 4.7 mM to 0.47 mM as the standard (Figure S1A-B), the molar extinction coefficient of the tetrazine moiety (ε_{Tz}) was determined as 2.3×10^4 L Mol^{-1} cm^{-1}. Taking into consideration the change of the molecular weight for HA disaccharide repeats after tetrazine incorporation, the degree of tetrazine incorporation was calculated as 18.6% (Figure S1C). By ^{1}H NMR (Figure S11), tetrazine incorporation in HA was calculated as 18.0%, analyzed by comparing

the integration between the aromatic protons (7.4-8.4 ppm) to the anomeric protons of HA. As expected, some EDC-activated carboxyl groups in HA were transformed to N-acylurea.[5] HA-Tz was initially synthesized by my collaborator, Han Zhang.

3.2.2.3 Synthesis of PEG-based TCO crosslinker (PEG-bisTCO)

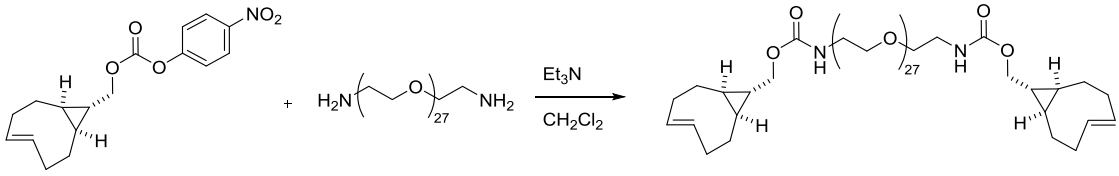

To a round bottom flask was added PEG_{27}-diamine (125 mg, 0.10 mmol), CH_2Cl_2 (2 mL) and Et_3N (56 µL, 0.40 mmol). After the addotopm of sTCO nitrophenyl carbonate[20] (80 mg, 0.25 mmol), the reaction mixture was stirred at room temperature overnight. Upon completion of the reaction, based on UPLC-MS analysis, the solvent was evaporated under reduced pressure and the residue was purified by flash chromatography on silica gel using 30% acetone in hexanes and then a gradient of 2-5% MeOH in CH_2Cl_2 to give the product (113 mg, 0.070 mmol, 70% yield) as water soluble semi-solid. ^{1}H NMR (600 MHz, $CDCl_3$) δ 5.83 (ddd, *J* = 16.1, 9.3, 6.2 Hz, 2H), 5.26 (s, 2H), 5.09 (ddd, *J* = 15.9, 10.2, 3.5 Hz, 2H), 3.90 (d, *J* = 6.2 Hz, 4H), 3.63 – 3.59 (m, 104H), 3.52 (t, *J* = 5.1 Hz, 4H), 3.33 (d, *J* = 5.0 Hz, 4H), 2.37 – 2.30 (m, 2H), 2.23 (m, 4H), 2.18 (m, 2H), 1.90 – 1.84 (m, 4H), 0.80 (m, 2H), 0.58 – 0.47 (m, 4H), 0.43 – 0.36 (m, 4H). ^{13}C NMR (100 MHz, $CDCl_3$) δ 156.9 (2 C), 138.4 (2 CH), 131.3 (2 CH), 70.6 (CH_2 on PEG), 70.26 (2 CH_2), 70.18 (2 CH_2), 69.41 (2 CH_2), 40.76 (2 CH_2), 38.69 (2 CH_2), 33.79 (2 CH_2), 32.60 (2 CH_2), 27.66 (2 CH_2), 24.71 (2 CH), 21.95 (2 CH), 20.93 (2 CH). LC-MS t_R= 2.48 mins, $[M+H_3O]^+$ found at 1623.90,

HRMS-ESI *m/z*, ($M+2H^+$ /2) calculated for $C_{78}H_{146}N_2O_{31}^{2+}$ 803.4949, found, 803.4990.

3.2.2.4 Synthesis of MMP-degradable TCO crosslinker (GIW-bisTCO)

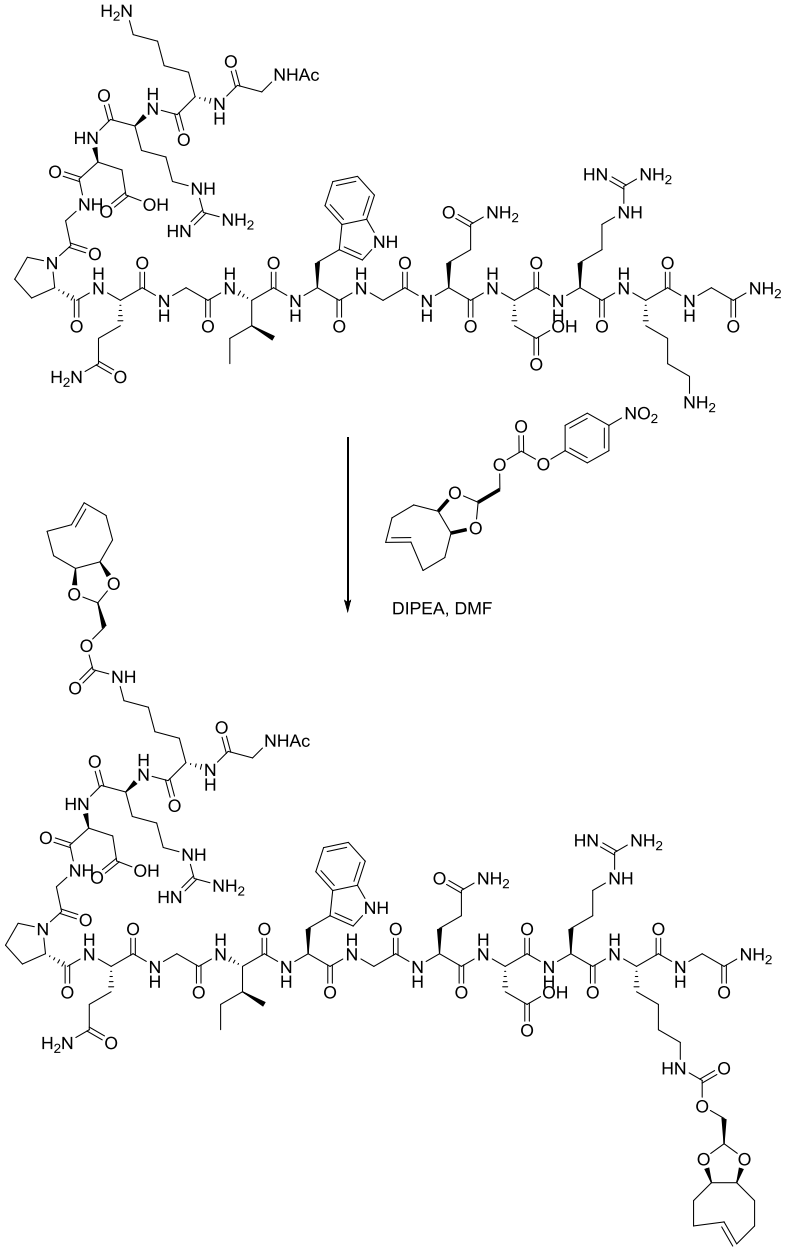

MMP-degradable peptide with a sequence of Ac-GKRDGPQGIWGQDRKG-NH_2 (abbreviated as GIW, 73 mg, 40.6 μmol), prepared by solid phase peptide synthesis, was dissolved in anhydrous DMF (1.5 mL). *N*, *N*-diisopropylethylamine (28 μL, 162 μmol) was added followed by dTCO-4-nitrophenyl carbonate[43] (36 mg, 102 μmol). The solution was stirred at room temperature for 2 hours. The reaction was deemed complete when only the desired bis-modification product was observed by UPLC-MS. The resulting solution was added dropwise to 35 mL of ice cold diethyl ether. Then it was centrifuged at 4000 rpm for 5 mins, and the clear ethereal solution was removed. The solid was re-dissolved in 2 mL of DMF and precipitated into ice cold diethyl ether. The precipitation/re-dissolve cycle was repeated for a total 3 times. Analytical grade sample was obtained by purification of the white powder by reverse phase chromatography on C_{18} silica gel using a gradient of 5% to 95% MeOH in neutral water. LC-MS for GIW-bisTCO: t_R = 1.72 mins, $[M+2H]^{2+}$ found 1109.21. HRMS-ESI for GIW-bisTCO: *m/z*, $(M+2H^+/2)$ calculated for $C_{98}H_{153}N_{28}O_{31}^{2+}$ 1109.0623, found, 1109.0621. LC-MS for GIW: t_R = 1.10 mins, $[M+4H]^{4+}$ found 449.94. HRMS-ESI for GIW, *m/z*, $(M+2H^+/2)$ calculated for $C_{76}H_{125}N_{28}O_{23}^{2+}$ 898.9731, found, 898.9726. TCO conjugation onto lysine amines was initially performed by my collaborator, Yi Li.

3.2.2.5 Synthesis of RGD-TCO

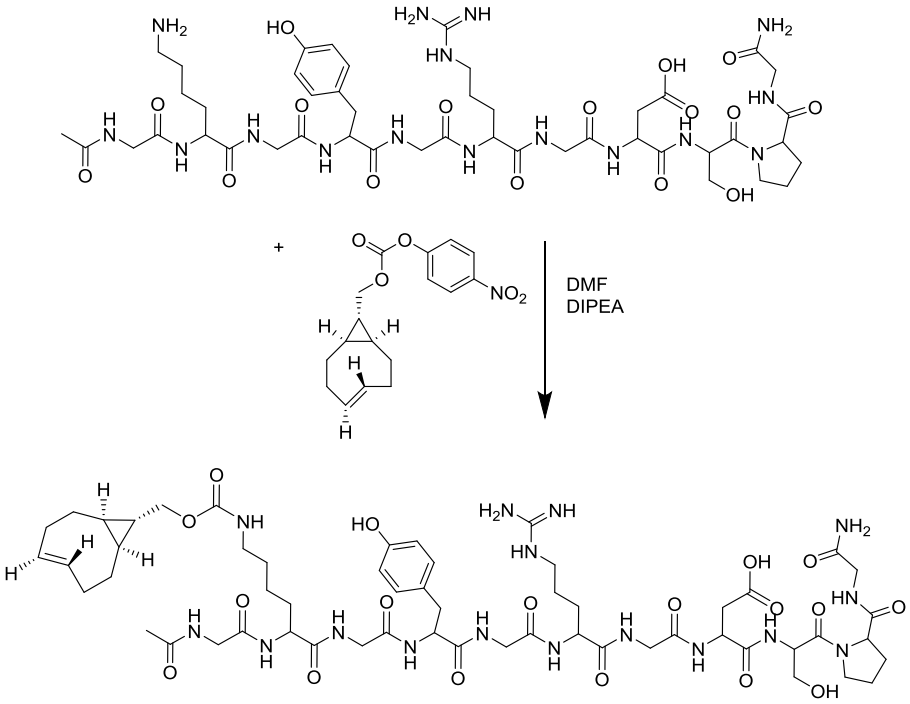

Prior to TCO conjugation, RGD peptide with a sequence of GKGYGRGDSPG was synthesized following standard solid phase peptide synthesis protocol. The cleaved product, with C-amidated and N-acetylated, was allowed to react with nitrophenyl carbonate-derived sTCO in anhydrous DMF to install TCO through the lysine amine. The product was purified by HPLC and analyzed by ESI-MS, as reported previously.[21]

3.2.2.6 Synthesis of PEG-TCO

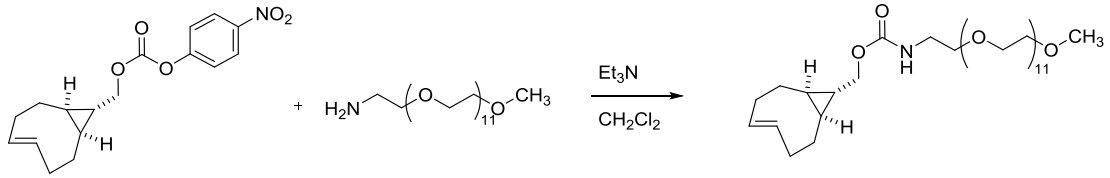

To a round bottom flask was added the MeO-PEG_{12}-amine (67 mg, 98% purity, 0.116mmol), CH_2Cl_2 (2 mL) and Et_3N (65µL, 0.464mmol). After the addition

of sTCO 4-nitrophenyl carbonate (55 mg, 0.175 mmol), the solution was stirred at room temperature overnight, at which point the reaction was analyzed for completion by UPLC-MS analysis. The solvent was evaporated under reduced pressure and the residue was passed through a short column of deactivated C_2 silica gel first eluting with CH_2Cl_2 to remove the excess carbonate and then 10% MeOH in CH_2Cl_2 to elute fractions containing the product. The solvent was concentrated under reduced pressure and the yellow crude product was purified by reverse phase chromatography using a Biotageon C_{18} silica gel using a gradient of 10% to 90% MeOH in neutral water to give the product (63 mg, 0.085 mmol, 74% yield) as a pale yellow oil. ^{1}H NMR (600 MHz, $CDCl_3$) δ 5.83 (ddd, *J* = 16.1, 9.3, 6.2 Hz, 1H), 5.23 (s, 1H), 5.09 (ddd, *J* = 15.9, 10.5, 3.1 Hz, 1H), 3.91 (d, *J* = 6.1 Hz, 2H), 3.66 – 3.58 (m, 42H), 3.55 – 3.49 (m, 4H), 3.35 (s, 3H), 3.33 (d, *J* = 5.1 Hz, 2H), 2.38 – 2.29 (m, 1H), 2.28 – 2.20 (m, 2H), 2.18 (dt, *J* = 12.7, 8.2 Hz, 1H), 1.93 – 1.84 (m, 2H), 0.80 (td, *J* = 12.1, 7.1 Hz, 1H), 0.55 – 0.46 (m, 2H), 0.42 – 0.34 (m, 2H). ^{13}C NMR (100 MHz, $CDCl_3$) δ 156.9 (C), 138.4 (CH), 131.3 (CH), 71.9 (CH_2), 70.60 (CH_2 on PEG), 70.56 (CH_2 on PEG), 70.52 (CH_2 on PEG), 70.3 (CH_2), 70.2 (CH_2), 69.4 (CH_2), 59.1 (CH_3), 40.8 (CH_2), 38.7 (CH_2), 33.8 (CH_2), 32.6 (CH_2), 27.7 (CH_2), 24.70 (CH), 21.95 (CH), 20.93 (CH). LC-MS t_R = 2.11 mins, $[M+NH_4]^+$ found at 755.71, HRMS-ESI *m/z*, $(M+H^+)$ calculated for $C_{36}H_{68}NO_{14}$ 738.4634, found, 738.4651. PEG-TCO was initially synthesized by my collaborator, Yi Li.

3.2.2.7 PEG-dTCO

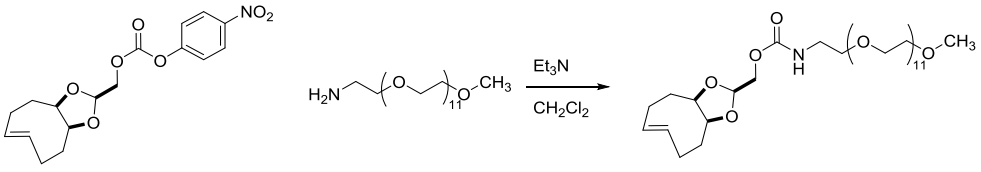

To a round bottom flask was added the MeO-PEG_{12}-amine (58mg, 98% purity, 0.102mmol), CH_2Cl_2 (2 mL) and Et_3N (56µL, 0.400mmol). The dTCO 4-nitrophenyl carbonate (53mg, 0.152mmol,91:9 ratio of 2 diastereomers) was added to the solution and it was stirred at r.t. overnight. The reaction was completed judged by UPLC-MS analysis. The solvent was evaporated under reduced pressure and the residue was passed through a short C_2 deactivated silica gel column first eluting with CH_2Cl_2 to remove the excess carbonate and then 10% MeOH in CH_2Cl_2 to get fractions containing the product. The solvent was concentrated under reduced pressure and the yellow crude product was purified by reverse phase chromatography on C_{18} silica gel using a gradient of 10% to 90% MeOH in neutral water to give the product (60mg, 0.078mmol, 76% yield) as a pale yellow oil. ^{1}H NMR (400 MHz, $CDCl_3$) δ 5.64 – 5.54 (m, 1H), 5.54 – 5.43 (m, 1H), 5.30 (s, 1H), 4.89 (m, 1H), 4.15 – 4.01 (m, 2H), 3.99 – 3.86 (m, 2H), 3.64 – 3.55 (m, 42H), 3.51 (q, *J* = 5.2, 4.5 Hz, 4H), 3.35 (s, 3H), 3.34 – 3.23 (m, 2H), 2.38 (m, 1H), 2.20 (m, 2H), 2.13 – 2.02 (m, 1H), 1.85 (m, 1H), 1.78 (m, 1H), 1.74 – 1.59 (m, 1H), 1.59 – 1.42 (m, 1H). ^{13}C NMR (100 MHz, $CDCl_3$) δ 156.0 (C), 136.5 (CH), 131.1 (CH), 99.1 (CH), 82.8 (CH), 80.7 (CH), 71.9 (CH_2), 70.6 (CH_2 on PEG), 70.6 (CH_2 on PEG), 70.5 (CH_2 on PEG), 70.3 (CH_2), 70.0 (CH_2), 65.2 (CH_2), 59.1 (CH_3), 40.9 (CH_2), 38.7 (CH_2), 33.6 (CH_2), 25.5 (CH_2). LC-MS t_R = 1.89 mins, $[M+NH_4]^+$ found at 787.67 HRMS-ESI *m/z*, ($M+H^+$) calculated for $C_{36}H_{68}NO_{16}$ 770.4533, found, 770.4550. PEG-dTCO was synthesized by my collaborator, Yi Li.

3.2.3 Analysis of reaction kinetics.

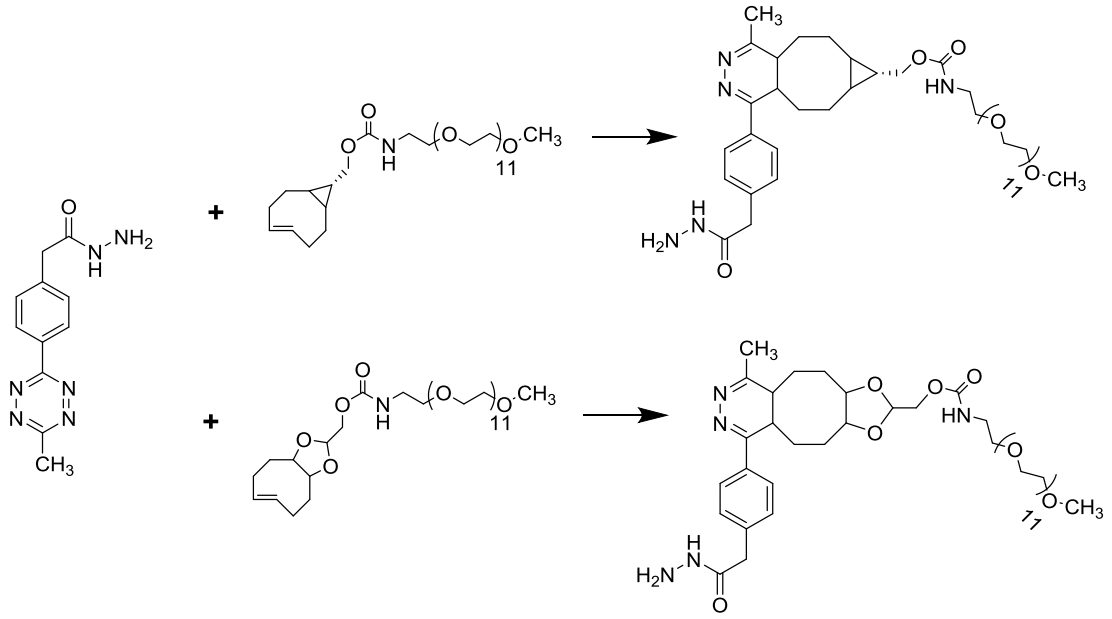

The reaction was run under pseudo-first order conditions and monitored by UV-Vis spectroscopy at 267 nm using an Applied Photophysics SX.18MV-R stopped-flow dual mixing spectrometer. The reactants were separately dissolved in H_2O and mixed in the stopped-flow device. The initial concentrations of Tz-hydrazide, PEG-TCO and PEG-dTCO were 4.43 × 10^{-5} M, 4.02 ×10^{-4} M and 4.28 ×10^{-4} M, respectively, with a 1:1 volume mixing. The spectrum was acquired every 5 × 10^{-4} seconds for 1 second and 2.5 × 10^{-3} for 5 seconds for PEG-TCO and PEG-dTCO, respectively. The K_{obs} was determined by fitting a non-linear curve of $\ln(A/A_0)$ vs time, where A_0 and A was absorbance at time 0 and t, respectively. The kinetic runs were measured in triplicate, and the average K_{obs} was 13.51 ± 0.01 s^{-1} and 2.130 ± 0.003 s^{-1} for PEG-TCO and PEG-dTCO, respectively. The second order rate constant (k_2) was calculated to be 6.70 × 10^4 $M^{-1}s^{-1}$ and 9.94 x 10^3 $M^{-1}s^{-1}$ for PEG-TCO and

PEG-dTCO**,** respectively. The experiment was conducted by my collaborator, Han Zhang.

3.2.4 Hydrogel Synthesis.

HA-Tz and the bisTCO crosslinker (PEG-bisTCO or GIW-bisTCO) were separately dissolved in PBS at a concentration of 5wt% and 0.3 wt%, respectively. Next, HA-Tz was dropped via a 25G syringe into the bis-TCO solution (300 µL for PEG-bisTCO and 414 µL for GIW-bisTCO) in a 48 well plate (BD Falcon™). The interfacial crosslinking process was allowed to occur at 37 °C for 4 h without any agitation until the tetrazime chromophore (pink) disappeared from the droplet. The bis-TCO solution was then replaced with fresh PBS. Hydrogels with a lower crosslinking density were prepared via the incorporation of PEG-TCO in the crosslinking bath at a bisTCO-to-monoTCO molar ratio of 4/1. Homogeneous matrices (Gels A-D) used for 3D culture studies were prepared similarly by adding HA-Tz to a TCO reservoir with a composition depicted in Table 1. Hydrogels with a core-shell structure were prepared by incubating the HA-Tz droplet in the first reservoir for 1 h to establish the shell, followed by a 3 h exposure to a second reservoir to complete the core.

3.2.5 Hydrogel Swelling and Degradation

The as-synthesized hydrogels were dehydrated in graded ethanol solutions and vacuum dried. The swelling ratio, reported as an average of three repeats, was determined as the ratio of the initial weight of the wet gel to the weight of the dry product. For degradation studies, hydrogels were washed with HBSS and allowed to equilibrate overnight. Hydrogels were then weighed to record the starting mass.

Hydrogels were then placed in HBSS solutions with or without 100 U/mL Collagenase Type IV. The supernatant was removed and the gel mass was recorded every 30 min for up to 4 h. Values were normalized to the starting mass.

3.2.6 Fluorescent Tagging

HA-Tz (5 wt% PBS) was dropped into a reservoir containing PEG-bisTCO (1.87 mM) and Alexa-TCO (3 μM). The reaction was allowed to proceed at 37°C for 1 h. The partially crosslinked gel was transferred to a different reservoir containing PEG-bisTCO (1.87 mM) and Cy3-TCO (6 μM). The reaction was allowed to continue for an additional 3 h. The hydrogels were washed with PBS overnight before imaging using a Zeiss 710 NLO confocal microscope with a 5× objective.

3.2.7 Mechanical Properties

Compression experiments were conducted using a custom-made micro-materials tester,[34] modified for parallel plate ramp compression of hydrogels (Figure 4A). The parallel plates were made of 1-mm thick borosilicate glass microscope slides (12-550-A3, Fisher Scientific). One glass flat was fixed to an XY table while the other was fixed to the free end of a calibrated cantilever beam load cell with a μN resolution. The fixed end of the beam was driven by a piezoelectric stage (0-800 ± 0.002 μm). Hydrogels were placed on the lower glass flat and a small droplet of PBS was placed at the base. Prior to contact, the hydrogel was aligned using the XY table and positioned ~200 μm below the moving glass flat. Subsequently, the piezoelectric stage was driven toward the sample over a travel range of 700 μm at a rate of 45 μm/s; the compression rate of the sample was lower at ~40 μm/s due to deformation of the load cell. Compressive modulus was determined based on the approaching curve using

the Hertzian model, and was converted to Young's modulus based on the assumed Poisson ratio of 0.5.[35] Compression testing was done by my collaborator, Axel Moore.

3.2.8 Cell Maintenance and 3D Culture

hMSC cells were maintained in a MSC growth BulletKit medium (Lonza, Walkersville, MD). HA-Tz was dissolved in the PBS at a concentration of 5wt% and was sterilized by exposure to germicidal UV light for 15 min. All TCO-conjugated molecules were dissolved in PBS and sterile-filtered using a 0.22 μm Poly(vinylidene fluoride) (PVDF) syringe filter (Thermo Fisher Scientific, Waltham, MA). Cellular constructs were prepared following procedures described above for hydrogel synthesis and using HA-Tz containing suspended hMSCs (1×10^6/mL). Upon completion of the crosslinking reaction, the constructs were transferred to wells containing fresh media and were incubated at 37 ºC for up to 7 days, with media refreshed every other day.

3.2.9 Cell Viability Study

Percent cell viability was assessed by Live/Dead staining using calcein AM and ethidium homodimer after 1, 4 and 7 days of culture. Short z-stacks of 105 μm with 15 μm slices were taken with Zeiss 710 NLO confocal microscope with a 10X objective. The images were flattened in Zeiss's Zen software to produce maximum intensity projections. By using Image J and counting the live and dead cells in each image, percent viability was quantified. Values are presented as a percentage of live cells compared with the total number of cells.

3.2.10 Cell Morphology

Cell morphology was assessed by staining hydrogel constructs after 1 and 7 days of culture for F-actin using Alexa Fluor 568 phalloidin, with the nuclei counter stained by DAPI, following previous protocols.[44] Selected samples were incubated with primary integrin β1 antibody (Santa Cruz Biotechnology) at a 1:100 dilution in 1× PBS containing 3% BSA for 2 h at room temperature. Samples were then treated with Alexa Fluor 488-conjugated secondary antibody at a 1:200 dilution in the same buffer for 2 h at room temperature. Stained samples were imaged using a Zeiss 710 NLO confocal microscope with a 10X objective. Short z-stacks of 106.7 μm with 6.2 μm slices were taken and converted into maximum intensity projections using Zen. Using Image J, cell body was accessed for total area, Feret's diameter, circularity and roundness. Values were plotted as a histogram with a fitted Gaussian curve.

3.2.11 Statistical Analysis

All quantitative analyses were performed in triplicate and results were expressed as the mean ± standard deviation. Statistical significance was evaluated by analysis of variance (Two-way ANOVA), followed by Tukey-Kramer post-hoc test. A P-value of <0.05 was considered to be statistically different.

3.3 Results and Discussion

Hydrogel precursors were derived from defined-length PEG, bioactive peptides, and HA, a natural non-sulfated glycosaminoglycan abundant in connective tissue ECM. Thus, high molecular weight HA (430 kDa) was coupled with Tz-hydrazide through 1-ethyl-(3,3-dimethylaminopropyl) carbodiimide (EDC)-mediated coupling chemistry at pH 4.75 to yield a tetrazine-functionalized HA (HA-Tz, Figure 2B) with 18 mol% tetrazine incorporation, as quantified by UV-Vis spectroscopy

(Figure S1) and ^{1}H NMR and (Figure S11). Separately, s-TCO nitrophenyl carbonate was combined with PEG_{27}-diamine to produce a non-degradable crosslinker (PEG-bisTCO, Figure 2B) with a molecular weight of 1.6 kDa. Degradability of the matrix by cell-secreted proteases is desirable to maintain cell viability and to enhance cell spreading and migration.[25-26] Accordingly, an MMP-cleavable peptide with a basic sequence of GPQG↓IWGQ flanked with charged amino acid residues (abbreviated as GIW) was modified with d-TCO nitrophenyl carbonate through lysine amines to produce GIW-bisTCO (2.2 kDa, Figure 2B). To enable spatial control of gel mechanics in a diffusion-controlled manner, a mono-functional 'capper' molecule was synthesized by conjugating s-TCO to the amino end of $mPEG_{12}$-NH_2 (PEG-TCO, Figure 2B). To introduce cell adhesive ligands to the synthetic matrix, s-TCO was conjugated to the GKGYGRGDSPG peptide through the lysine amine (RGD-TCO, 1.3 kDa, Figure 2B). Previous investigation[21] showed that such derivation does not compromise the cells' ability to bind to the RGD peptide.

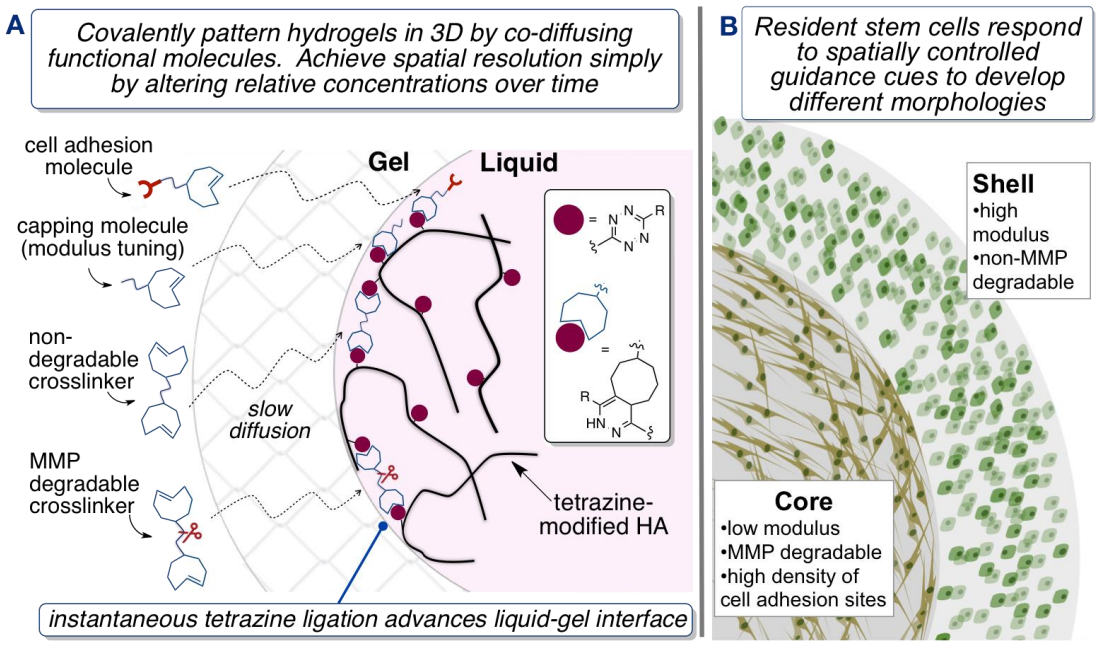

Figure 3.1 Fabrication of biomimetic hydrogels with a 3D core-shell pattern to provide spatial guidance cues to encapsulated hMSCs. (**A**) TCO-conjugated molecules diffuse across the crosslinked shell to react at the gel-liquid interface. (**B**) hMSCs adopt different morphologies depending their spatial localization within the matrix.

Covalently crosslinked hydrogels were fabricated via the addition of an HA-Tz droplet into a reservoir containing mono- and bifunctional TCO molecules. The bioorthogonal nature of tetrazine ligation (Figure 2A) allows for the hydrogel to be formed under physiological conditions in either phosphate buffered saline (PBS) or cell culture media. Stopped-flow experiments (Figure S2) conducted in water at 25 °C revealed that PEG-TCO and PEG-dTCO reacted with Tz-hydrazide with a second order rate constant, *k2*, of 6.70×10^4 $M^{-1}s^{-1}$ and 9.94×10^3 $M^{-1}s^{-1}$, respectively. Thus, both s-TCO and d-TCO react with HA-Tz with rates that are more rapid than the rate of diffusion through a crosslinked hydrogel. As shown in Figure 1A, as soon as a

droplet of HA-Tz (5% in PBS) was added to the TCO reservoir, a crosslinked shell formed instantaneously between the two liquids. As the reaction was allowed to proceed, the low molecular weight TCO species continued to diffuse across the crosslinked shell to react with the high molecular weight HA-Tz at the gel-liquid interface, crosslinking the droplet radially towards the core, until all tetrazine sites on HA were consumed (~4 h). The resultant hydrogels had a diameter of ~2-3 mm.

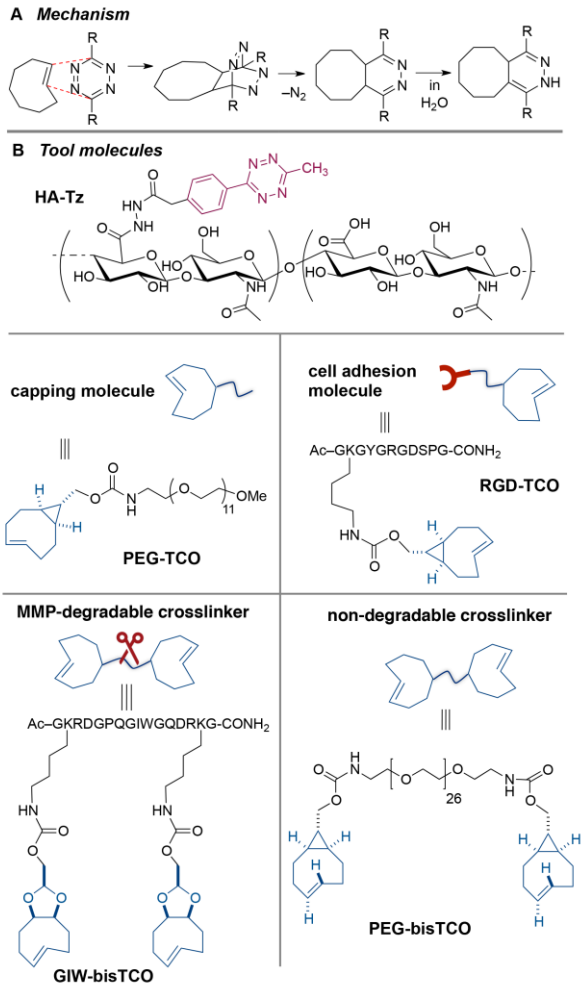

Figure 3.2 Synthetic toolbox for core-shell patterning. (**A**) Tetrazine-TCO ligation mechanism. (**B**) Hydrogel building blocks include tetrazine-modified HA (HA-Tz), non-degradable and MMP-degradable TCO crosslinkers (PEG-bisTCO and GIW-bisTCO) and monofunctional molecules (PEG-TCO, and RGD-TCO).

To illustrate that the diffusion-controlled kinetics can be used to pattern hydrogels in 3D, fluorescent TCO-conjugates of Cy3 (Ex: 555 nm; Em: 565 nm) and Alexa Fluor® 647 (Ex: 650 nm; Em: 665 nm) were used to covalently tag the gels during the crosslinking process. At time zero, a droplet of HA-Tz was introduced to a

crosslinking reservoir containing Alexa-TCO[18] (3 μM) and PEG-bisTCO (1.87 mM). The crosslinking reaction was allowed to proceed for 1 h, and the reservoir was switched to one containing Cy3-TCO (6 μM) and PEG-bisTCO (1.87 mM). The mixture was left undisturbed at ambient temperature for additional 3 h to produce a fully crosslinked hydrogel. As shown in Figure 3, Alexa was covalently tagged only to the outer shell of the hydrogel (~300 μm) during the initial 1 h crosslinking, whereas Cy3 was incorporated only into the hydrogel core during the remaining 3 h. There was also a sharp interface where the Alexa signal stopped and the Cy3 signal started, confirming that the fluorescent tags are introduced simultaneously with crosslinking at the gel-liquid interface. Thus, changing the TCO reservoir composition as a function of time provides a simple way to covalently pattern hydrogels in 3D.

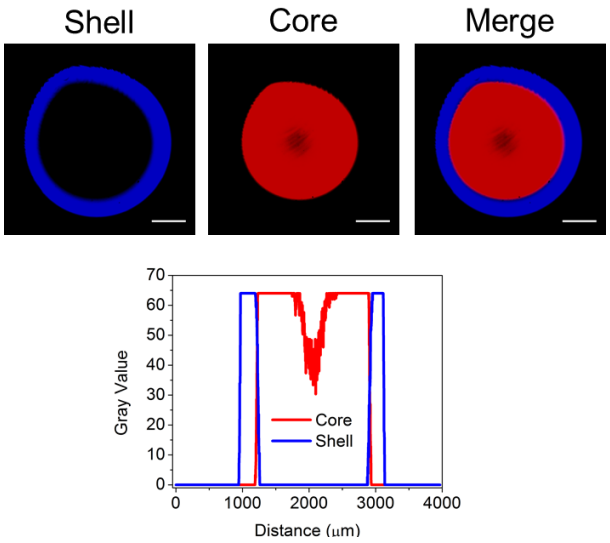

Figure 3.3 Covalent tagging of fluorescent dyes in a spatial core-shell pattern. (**A**) Confocal microscopy images of the hydrogel showing a distinct core-shell structure (central slice). (**B**) Intensity plot across the gel showing the presence of a sharp interface between the core and the shell regions.

Mechanical properties of hydrogels can directly influence cellular behaviors.[27-29] Under 2D culture, hMSCs cultured on softer hydrogels have been shown to differentiate into a neural phenotype while those cultured on stiffer substrates tended to go towards an osteoblastic fate.[30-31] Traditionally, hydrogel stiffness was altered by varying the concentration or the functionality of the macromers or crosslinkers. In my system, matrix stiffness was tuned by changing the ratio of mono-functional TCO capper and bifunctional TCO crosslinker, both exhibiting a similar diffusivity. The capper molecule consumes tetrazine groups on HA to generate network defects as a dangling chain.[32-33] As such, it effectively removes reactive sites that would otherwise contribute to the establishment of elastically active connections. The mechanical properties of the hydrogels were quantified by compression experiments using a custom micro-materials tester (Figure 3.4A) under hydrated conditions.[34] Normal force was measured as a function of compression and the resulting compression response (based on the approaching curve only) was fit to a Hertzian model of parallel plate compression of an elastic sphere (Figure 3.4B). The compressive modulus was converted to Young's modulus, assuming a Poisson ratio of 0.5.[35]

A

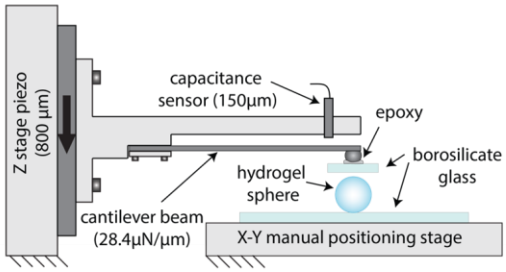

B

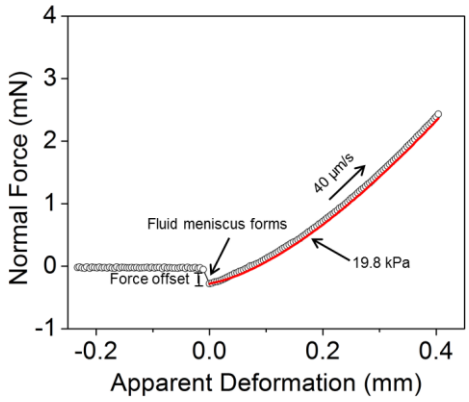

C **Effect of Capper on Gel Mechanical Properties**

Gel	Young's Modulus	
100% PEG-bisTCO	16.4 ± 2.1 kPa	*
75% PEG-bisTCO 25% PEG-TCO	8.7 ± 1.1 kPa	
100% GIW-bisTCO	12.8 ± 0.7 kPa	*
75% GIW-bisTCO 25% PEG-TCO	5.0 ± 0.3 kPa	

D **Mechanical Properties of Multi-component Gels**

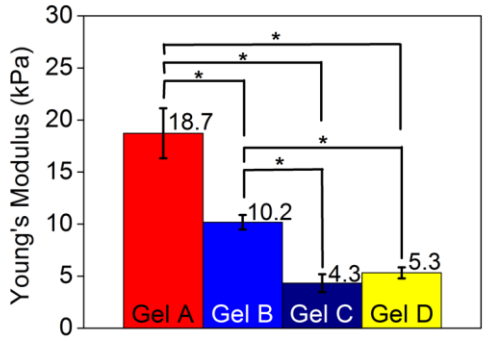

Figure 3.4 Characterization of hydrogel mechanical properties using a custom-built, micro-materials tester. (A) Schematic of the micro-materials tester used in this study. The hydrogel rested on the lower glass flat was compressed by a borosilicate plate. (B) Representative force-displacement curve demonstrating the top plate approach, contact with and compress the hydrogel. (C) Young's modulus of hydrogels prepared using different and mono- and bis-TCO derivatives. Hertzian model of parallel plate compression was used and Young's modulus was calculated assuming a Poisson ratio of 0.5. The crosslinking reservoir contained 0% or 25% monofunctional TCO capper. (D) Young's modulus of hydrogels formulated according to Table 1 and used for subsequent cell culture studies. * $p < 0.05$

As shown in Figures 3.4C and S3.6, I demonstrated that inclusion of a PEG-TCO capping molecule in the bisTCO reservoir resulted in the reduction of gel stiffness, for gels crosslinked by PEG-bisTCO or GIW-bisTCO. Hydrogel samples prepared using 100% PEG-bisTCO (1.87 mM) or GIW-bisTCO (1.35 mM) had a Young's modulus of 16.4 ± 2.1 kPa and 12.8 ± 0.7 kPa, respectively (Figures 3.4C, S3.5-6). The equilibrium swelling ratio was found to be 25 ± 4 and 39 ± 5 for gels crosslinked with PEG-bisTCO and GIW-bisTCO, respectively. The MMP-degradable network swells more due to the large number of charged amino acid residues in the peptide sequence. Inclusion of monofunctional PEG-TCO in the bisTCO reservoir produced hydrogels that were significantly softer. At a 1/4 capper (PEG-TCO)/crosslinker (PEG-bisTCO or GIW-bisTCO) ratio, an average Young's modulus of 8.7 ± 1.1 kPa and 5.0 ± 0.3 kPa were detected for non-degradable and MMP-degradable networks, respectively (Figures 3.4C and 3.6A-B).

Table 3.1 Preparation of HA-based hydrogels with varying stiffness, degradability and adhesivity.

	Formulation	Property
A	5% HA-Tz 1.87 mM PEG-bisTCO	Stiff (18.7kPa), No adhesion sites, Non-degradable
B	5% HA-Tz, 1.29 mM GIW-bisTCO, 0.17 mM RGD-TCO	Stiff (10.2kPa), Low density of adhesion sites, MMP-degradable
C	5% HA-Tz, 1.01 mM GIW-bisTCO, 0.17 mM RGD-TCO, 0.53mM PEG-TCO	Soft (4.3kPa), Low density of adhesion sites, MMP-degradable
D	5% HA-Tz, 1.01 mM GIW-bisTCO, 0.69 mM RGD-TCO	Soft (5.3kPa), High density of adhesion sites, MMP-degradable

Having shown that capping molecules could be used to tune the moduli of gels produced through interfacial crosslinking, I next sought to demonstrate that interfacial chemistry could be used to create more complex gels with varying stiffness, MMP-degradability and cell adhesivity. Four gel types, designated as Gels A, B, C, and D, were produced employing gel formulations outlined in Table 1 and the mechanical properties (Figure 3.4D) were analyzed as described above. Gel A was found to be the stiffest with a Young's modulus of 18.7±2.4 kPa. Gel B made with 5% RGD-TCO and 95% GIW-bisTCO was softer, and had an average Young's modulus of 10.2±0.7 kPa. Gels C and D had 25% mono-functional TCO molecules, thus were the softest with moduli of 4.3±0.9 kPa and 5.3±0.5 kPa, respectively. Having a similar molecular weight, PEG-TCO and RGD-TCO had a comparable capacity in modulating gel stiffness. Statistically, Gel A was significantly stiffer than Gels B-D ($p<0.05$), whereas Gel C and D had comparable stiffness ($p>0.05$). These results further corroborate the ability to tune gel stiffness by introducing the mono-functional capper molecule.

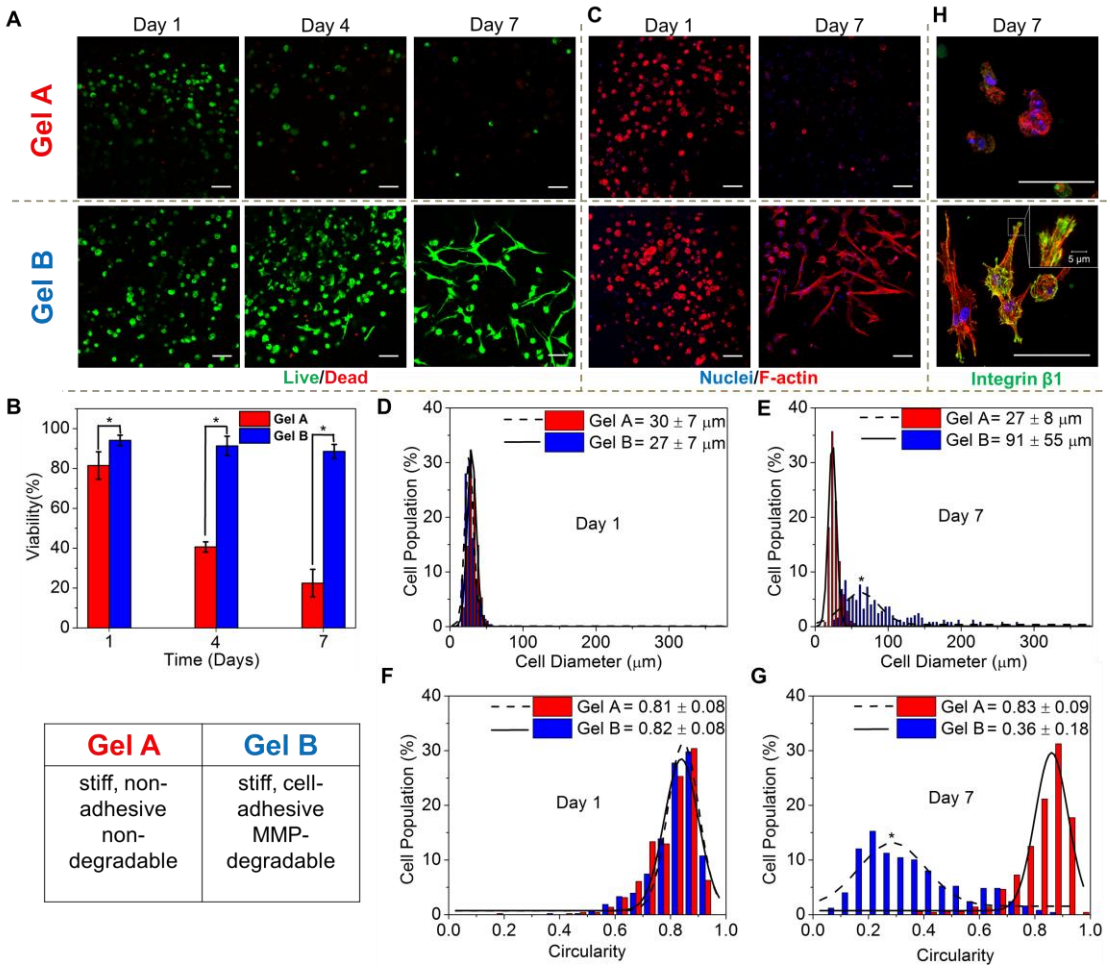

Figure 3.5 3D culture of hMSCs in homogeneous hydrogels prepared using either PEG-bisTCO (Gel A) or GIW- and RGD-TCO (Gel B). (A) Confocal images of 3D cultures stained by calcein AM (green) and ethidium homodimer (red) for live and dead cells, respectively, after 1, 4 and 7 days of culture. (B) Quantification of cell viability based on live/dead assay using ImageJ. (C) Confocal images of 3D cultures stained by F-actin (red) and DAPI (blue) after 1 and 7 days of culture. (D-G) Characterization of cell morphology by Feret diameter (D-E) and circularity (F-G) using ImageJ. (H) Higher magnification (40×) confocal images of hMSCs stained for DAPI (blue), F-actin (Red) and integrin β1 (green) after 7 days of culture. * $p < 0.05$. Scale bar = 100 μm.

The ability of cells to breakdown their ECM is an important prerequisite for maintaining proper cell functions.[36-37] In covalently crosslinked 3D hydrogels, stem cell fate is directly related to the ability of cells to generate traction forces, through MMP-mediated matrix degradation, independent of cell morphology and matrix stiffness.[38] Hydrogel degradation was monitored gravimetrically with or without type IV collagenase. When incubated in Hank's balanced salt solution (HBSS) containing 100 U/mL collagenase at pH 7.4, a significant mass loss was observed within 30 min for gels crosslinked with GIW-bisTCO, and the gels were completely disintegrated within 1 h (Figure 3.6C). By contrast, gels incubated in enzyme-free media were intact. No mass loss was detected from gels made with PEG-bisTCO and incubated with or without the enzyme. These results confirmed the specificity of enzymatic degradation and the absence of hydrolytic degradation within the period of the experiment.

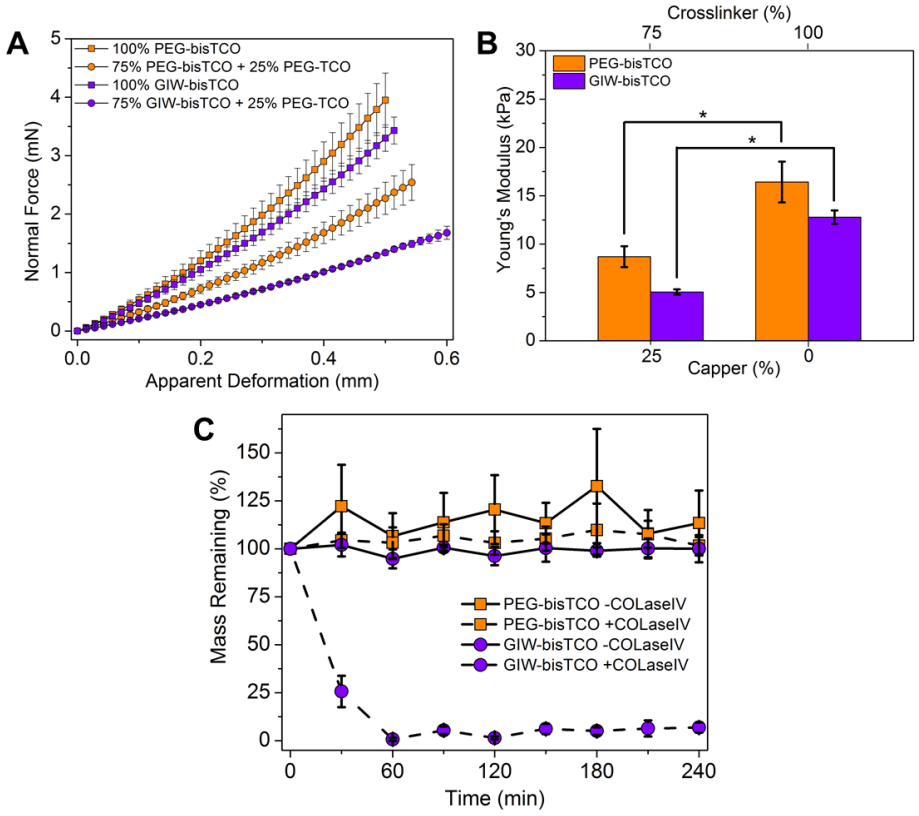

Figure 3.6 (A) Force deformation curves for hydrogels crosslinked with either PEG-bisTCO or GIW-bisTCO. Modulus was altered by tuning the relative concentration of mono-functional capper, PEG-TCO. (B) Young's modulus of hydrogels crosslinked with either PEG-bisTCO or GIW-bisTCO. Modulus was altered by tuning the relative concentration of mono-functional capper, PEG-TCO. * $p < 0.05$. (C) Hydrogel degradation. HA-Tz was crosslinked by either PEG-bisTCO or GIW-bisTCO. Hydrogels were incubated with or without of collagenase type IV and the gel mass was measured every 30 min for 4 h.

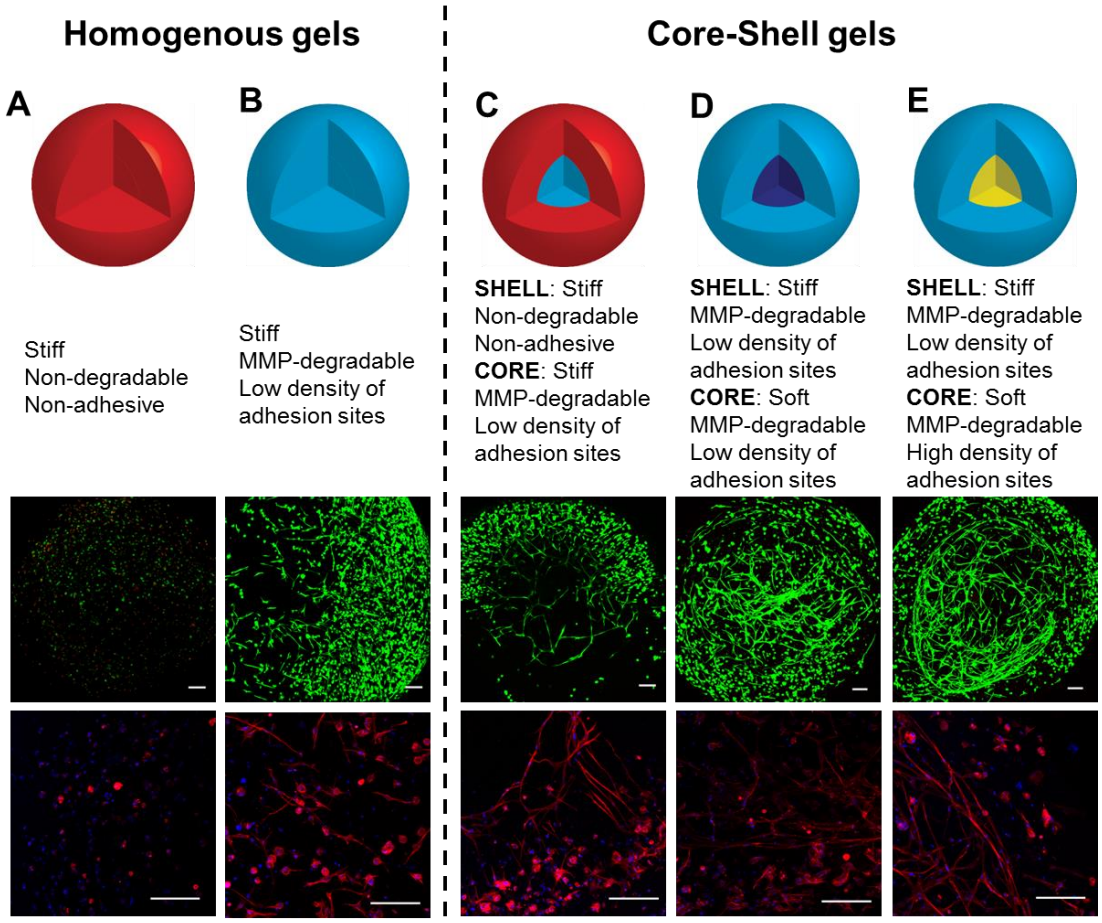

Figure 3.7 3D culture of hMSCs in hydrogels with bioactive core-shell patterning. Cells grown in homogeneous gels (**A-B**), prepared using (**A**) PEG-bisTCO or (**B**) GIW-bisTCO and RGD-TCO (0.17 mM), were included for comparison purposes. Hydrogels with a core-shell pattern (**C, D, E**) were created following conditions outlined in Table 1. Construct in **C**, prepared using PEG-bisTCO and GIW-bisTCO/RGD-TCO had a blank shell (red) and a bioactive core (light blue). Construct in **D**, prepared using GIW-bisTCO/RGD-TCO with or without the PEG-TCO capper had a stiff shell (light blue) and a softer core (dark blue). Construct in **E**, prepared using GIW-bisTCO with low and high concentrations of RGD-TCO, had a stiffer, less adhesive shell and a softer, more adhesive core. Cultures were maintained for 7 days before staining and confocal imaging. Live and dead cells were stained green and red, respectively, F-actin and nuclei were stained red and blue, respectively. Scale bar = 200 μm.

For 3D cell encapsulation, hMSCs were first dispersed in an HA-Tz (5% in PBS) solution and the cell suspension was dropped into a TCO reservoir containing PEG-bisTCO (1.87 mM) only or RGD-TCO (0.17 mM) and GIW-bisTCO (1.29 mM) to establish cell-laden constructs of Gel A and Gel B, respectively. The reaction was complete in 4 h at 37 °C before the TCO reservoir was replaced with fresh hMSC growth media. The 3D cultures were maintained for up to 7 days and cell viability was assessed by counting live (green) and dead (red) cells from fluorescently stained constructs under confocal microscope (Figure 3.5A-B). After 1 day of culture, hMSCs encapsulated in PEG-crosslinked hydrogels had a viability of 80%, confirming the cytocompatible nature of the hydrogel and crosslinking chemistry. Replacing the PEG crosslinker with an MMP-degradable substrate significantly improved the overall viability (94%), highlighting the importance of including key cell-responsive motifs in synthetic matrices. Prolonged culture of hMSCs in Gel A, a non-degradable covalent network, led to a progressive decrease in cell viability, in agreement with previous observations.[39] On the other hand, cells encapsulated in the cell-adhesive and MMP-degradable hydrogels maintained high viability (~90%) throughout the 7-day culture period. The ability of hMSCs to breakdown their matrix through MMP secretion[36,40] led to a significant change in cell morphology, from a rounded shape at day 1 to a spindle shape with long cellular processes by day 7 (Figure 3.5A-B).

Next, the morphology of hMSCs residing in blank (Gel A) or bioactive (Gel B) hydrogels were analyzed by immunefluorescent staining and confocal imaging. After 1 day of culture, cells in both types of hydrogels exhibited a similar, rounded cell shape, with an estimated diameter, and circularity of ~30 μm, and ~80%, respectively (Figure 3.5C-G). By day 7, cells in the two types of gels had developed significantly

different cell morphology. Cells in the non-degradable gels (Gel A) mostly maintained the rounded shape, although a slight decrease diameter were observed, potentially as a result of cells undergoing apoptosis (Figure 3.5C-G). By day 7, only 22 ± 7% cells were viable. hMSCs were distributed in the blank gels as single, rounded cells with distinct cortical actin, with little expression of integrin β1 (Figure 3.5H), a protein of the β subunit which plays a prominent role in RGD attachment and cell motility.[41] By contrast, cells in MMP-degradable/cell-adhesive gels became more elongated and spread-out, having an average diameter and circularity of ~90 μm and 36%, respectively (Figure 3.5C-G). Cells developed polarized, spindle-shaped morphology with bundles of F-actin stress fibers distributed throughout the entire cellular extensions (Figure 3.5C,H). Integrin clustered at the edges of the elongated actin stress fibers, as punctate foci, where they attach to the hydrogel matrix (Figure 3.5H). Organization of actin monomer into stress fibers indicates active actin polymerization events leading to the development of load-bearing cell-matrix binding that is conducive to cell extension in 3D. My observation was in agreement with earlier reports that, when entrapped in a covalent network, cell-mediated matrix degradation is essential to promote integrin-mediated[42] cell-matrix interactions.

Having confirmed the distinctly different cellular responses to blank (Gel A) and bioactive (Gel B) gels, I next spatially patterned the two matrix compositions into an individual hydrogel via diffusion controlled interfacial crosslinking. One hour after HA-Tz was added to the PEG-bisTCO reservoir, the partially crosslinked gel was transferred to a reservoir containing GIW-bisTCO (1.29 mM) and RGD-TCO (0.17 mM) and the reaction was allowed to proceed for 3 h to establish a fully crosslinked hydrogel. As inferred from the dye labeling experiment (Figure 3.3), the resultant

matrix exhibited a core-shell structure, having a core of ~1700 μm in diameter encased by a shell of ~300 μm thick. Based on mechanical evaluations of the homogeneous gels (Figure 3.4D), the outer shell was ~1.8 times stiffer than the inner core. Again, hMSCs cultured in the homogenous and bioinert gel (Gel A) remained round after 7 days (Figure 3. 7A) while those cultured in the homogenous and bioactive hydrogel (Gel B) exhibited a spread-out morphology with elongated stress fibers (Figure 3.7B). Cells elongated along a single axis in 3D to establish an interconnected cellular mesh by day 7. When these two gel compositions were patterned into the same hydrogel in a core-shell geometry, cells maintained the respective shapes in the corresponding regions (Figure 3.7C). Intriguingly, cells at the core-shell boundary were interconnected and those in the outer shell crosslinked with PEG-bisTCO developed inward projections towards this boundary. Because cells residing in the outer shell were unable to degrade and attach to their matrix, they could not migrate to the more favorable region. Instead, they were able to communicate with cells in the core through paracrine signaling to align their cell body towards the more permissive center.[42] Although cells could only remodel the GIW-containing core, hyaluronidase secreted by cells residing in the outer layer may contribute to the development of long projects at the boundary.

Biomechanical cues can be similarly presented in a core-shell fashion in the hydrogels using PEG-TCO capper, along with GIW-bisTCO crosslinker. One hour after HA-Tz was added to the TCO reservoir containing GIW-bisTCO and RGD-TCO, the partially crosslinked hydrogel was transferred to a reservoir containing monoTCO and bisTCO at a molar ratio of 1:4 to complete the crosslinking. RGD-TCO concentration was maintained constant (0.17 mM) throughout the entire crosslinking

process. Thus, the resultant gel had a core and shell with properties of Gel C and B, respectively. As inferred from Figure 3.4D, the shell was approximately two times stiffer than the central core. Because all crosslinks were MMP-degradable, cells in both core and shell regions were able to spread (Figure 3.7D). The ability of cells to perceive the difference in their environment was reflected again by the different morphologies cells adopt. The loosely crosslinked core promote a more rapid spreading and foster the development of longer cellular extensions. By day 7, cells in the more densely crosslinked shell region had just started to extend, and their cell bodies were relatively small.

While decreased stiffness can be achieved through introduction of the PEG-based capper molecule without altering other properties, the same effect can be achieved using RGD-TCO, which essentially functions as a capper from the mechanics perspective. One hour after HA-Tz was added to a reservoir containing GIW-bisTCO (95%) and RGD-TCO (5%), the partially crosslinked hydrogel was transferred to a reservoir with an increased concentration of RGD-TCO (25%) along with GIW-bisTCO (75%) to finish crosslinking. Consequently, the core with a composition of Gel D was softer (~2×) and more cell-adhesive than the shell of Gel B. As shown in Figure 3.6E, hMSCs formed a similar core-shell like structure, with a network of highly spread-out cells residing at the boundary between the core and shell after 7 days of culture. The softer core had a lower GIW concentration, but a higher RGD concentration. In matrices with higher concentrations of RGD peptide, hMSCs show high viability and proliferation as the adhesion supports cells during ECM degradation. Unlike the previous case, cells at the core-shell boundary were aligned along the circumferential direction, rather than projecting inwards. I speculate that, in

this case, because cells in both core and shell can spread, there was no directionality in cytokine secretion.

As shown here, interfacial tetrazine ligation provides a powerful, new method for modulating the biochemical and biomechanical properties of synthetic ECMs. Without any specialized equipment, 3D spatial patterning was achieved via the timed alteration of the TCO bath composition. My work was motivated by the need to create ECM templates for the engineering of mechanically active soft tissues that exhibit characteristic gradient or layered structures, as a consequence of the mechanical roles these tissues perform. Under the influence of the combined biochemical and mechanical factors, cells residing in these tissues exhibit different behaviors depending on their spatial localization within the tissue. Here, I demonstrated the development of a cell-instructive synthetic ECM displaying layered structures to provide the resident stem cells with spatially controlled guidance cues. With further development, I expect that the resident stem cells will actively remodel the synthetic environment and deposit natural matrix components in a spatial fashion reflecting that of the original ECM template. I anticipate that the new method for establishing spatial control of stem cell behavior presented here should find applications in the tissue repair, modeling and regeneration.

3.4 Conclusions

I have demonstrated the use of interfacial bioorthogonal chemistry for the preparation of spatially patterned hydrogels with distinct chemical and mechanical microenvironments. Through temporally controlled introduction of *trans*-cyclooctene (TCO) conjugates during the crosslinking process, the enzymatic degradability, cell adhesivity, and mechanical properties of the synthetic microenvironment can be tuned

with spatial precision. hMSCs encapsulated in the bioactive region were able to degrade their matrix to adopt a spread morphology while those in the blank, non-degradable region remained round. The bioorthogonal platform allows straightforward patterning of cellular microenvironments to trigger desired responses or to promote the formation of multilayer tissues.

3.5 Spectral Data for Chapter 3

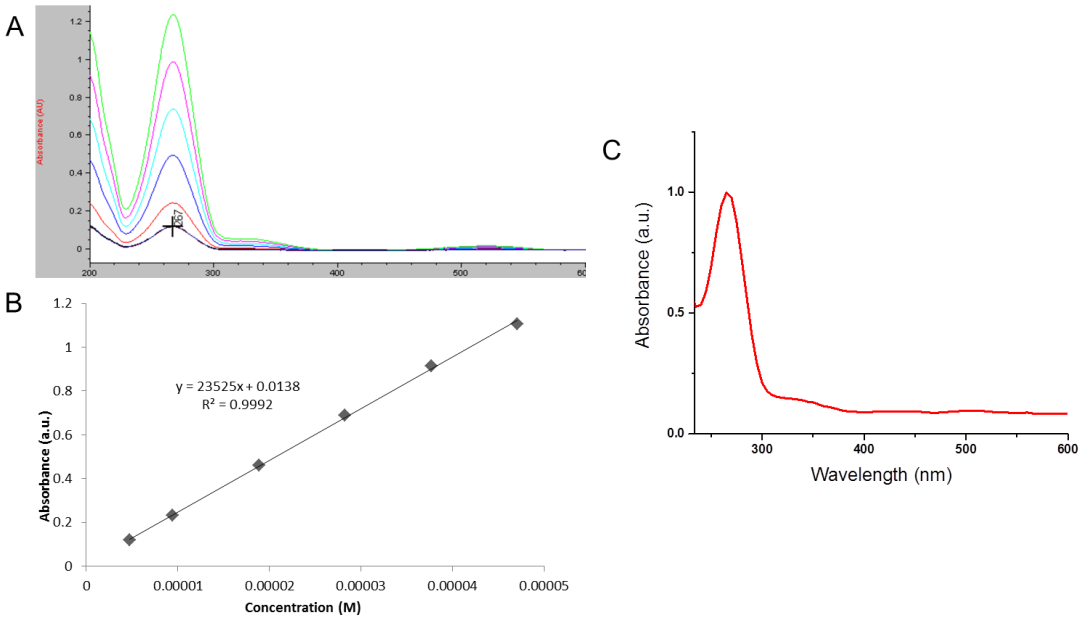

Figure 3.8 UV-Vis spectra of aqueous solutions of Tz-hydrazide (A, 4.7 mM to 0.47 mM) and HA-Tz (C, 0.27mM). The extinction coefficient was determined from the standard curve with a linear regression (B). A UV cuvette with a pathlength of 1 cm was used.

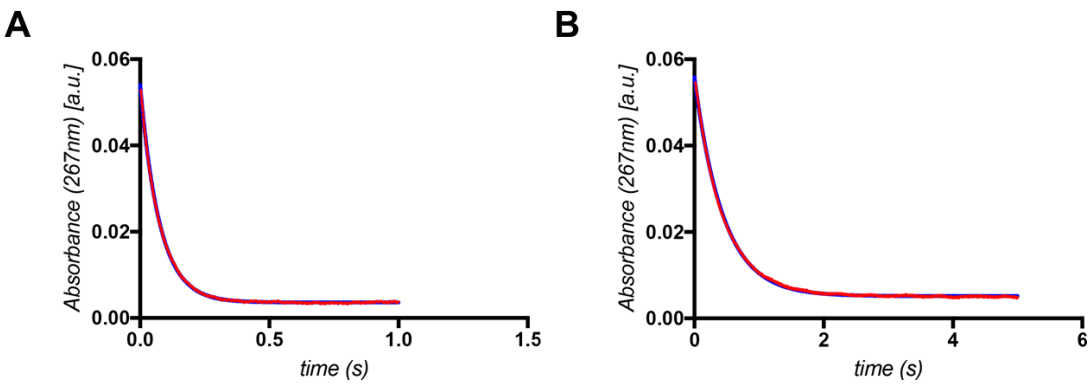

Figure 3.9 Stopped flow results for reactions of Tz-hydrazide with PEG-TCO (**A**) or with PEG-dTCO (**B**). Red circles: raw data; Blue line: fitted curve.

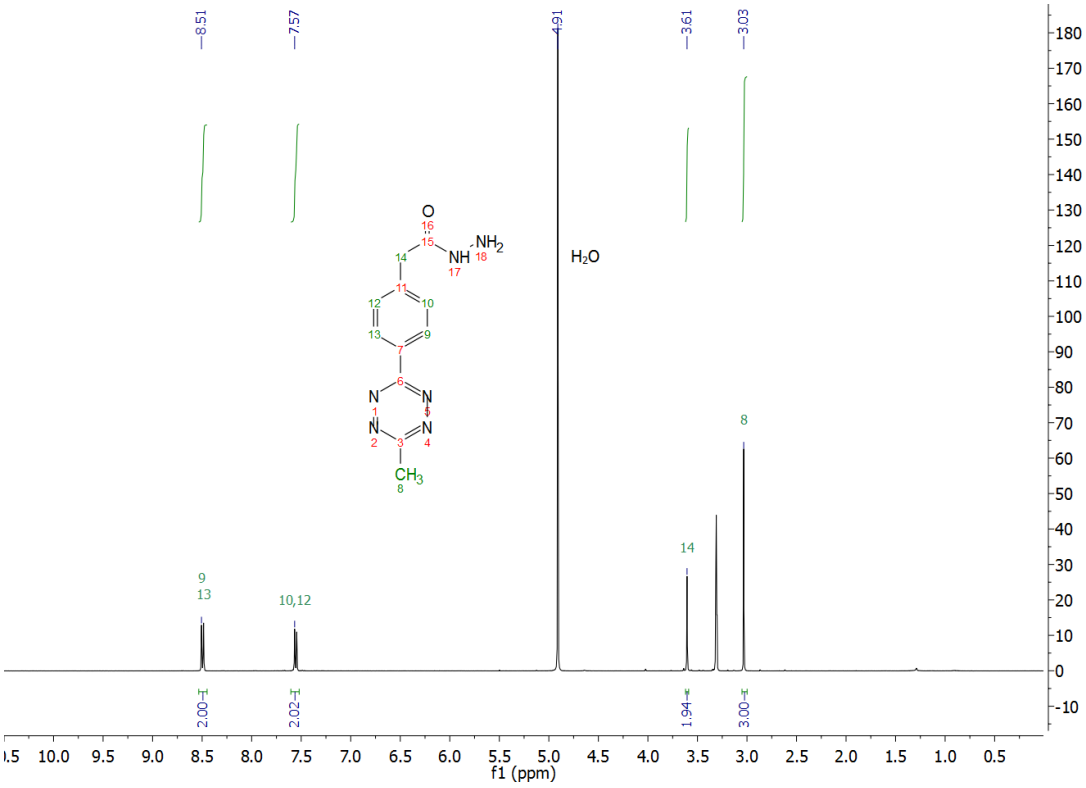

Figure 3.10 ^{1}H NMR spectrum of Tz-hydrazide in methanol-d_4.

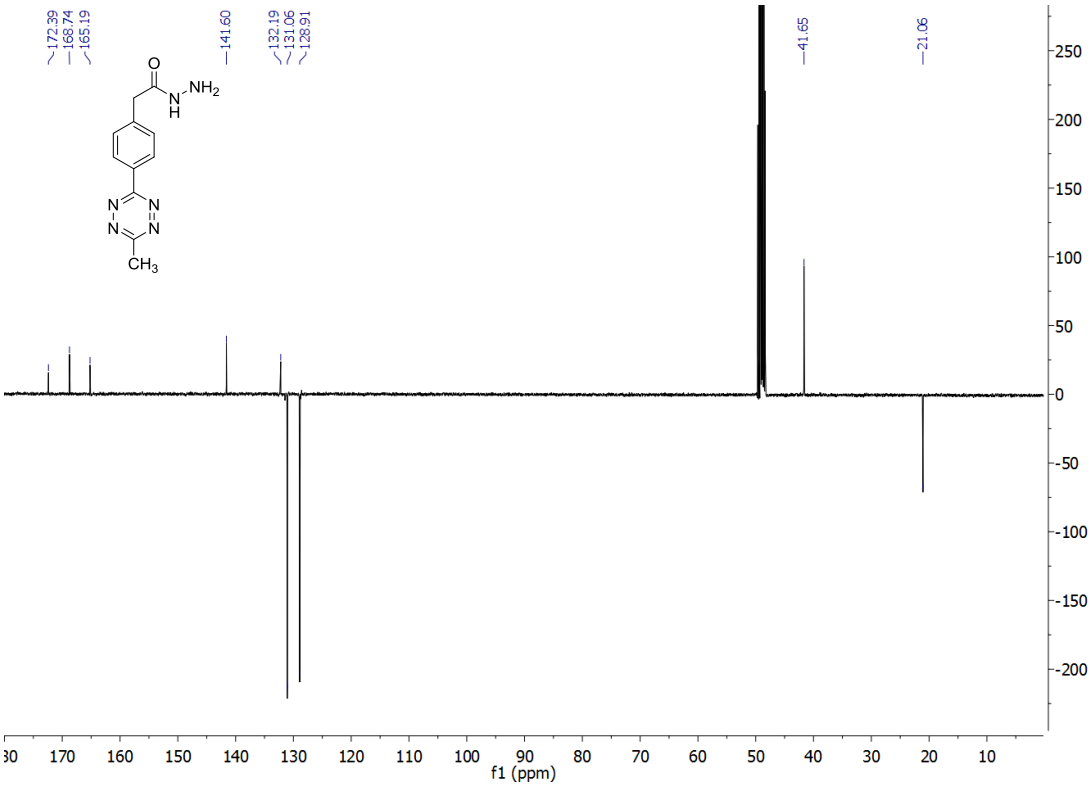

Figure 3.11 ^{13}C NMR spectrum of Tz-hydrazide in $CDCl_3$.

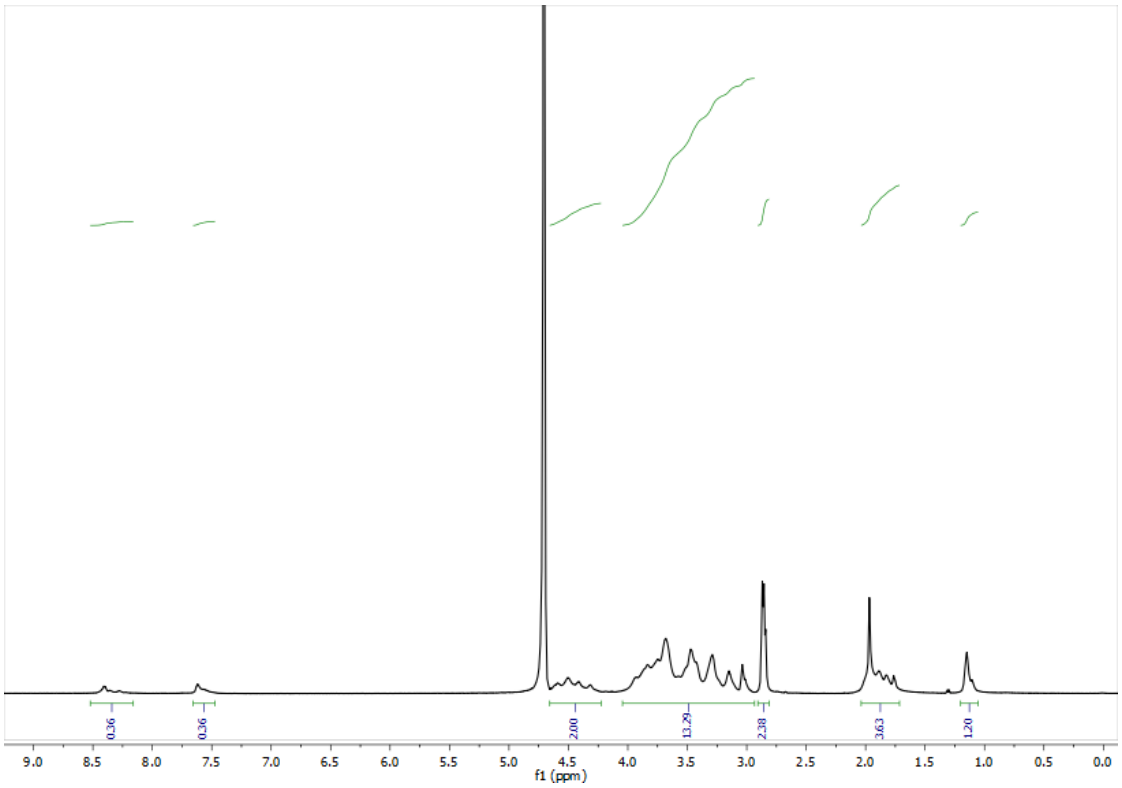

Figure 3.12 ^{1}H NMR spectrum of HA-Tz in D_2O.

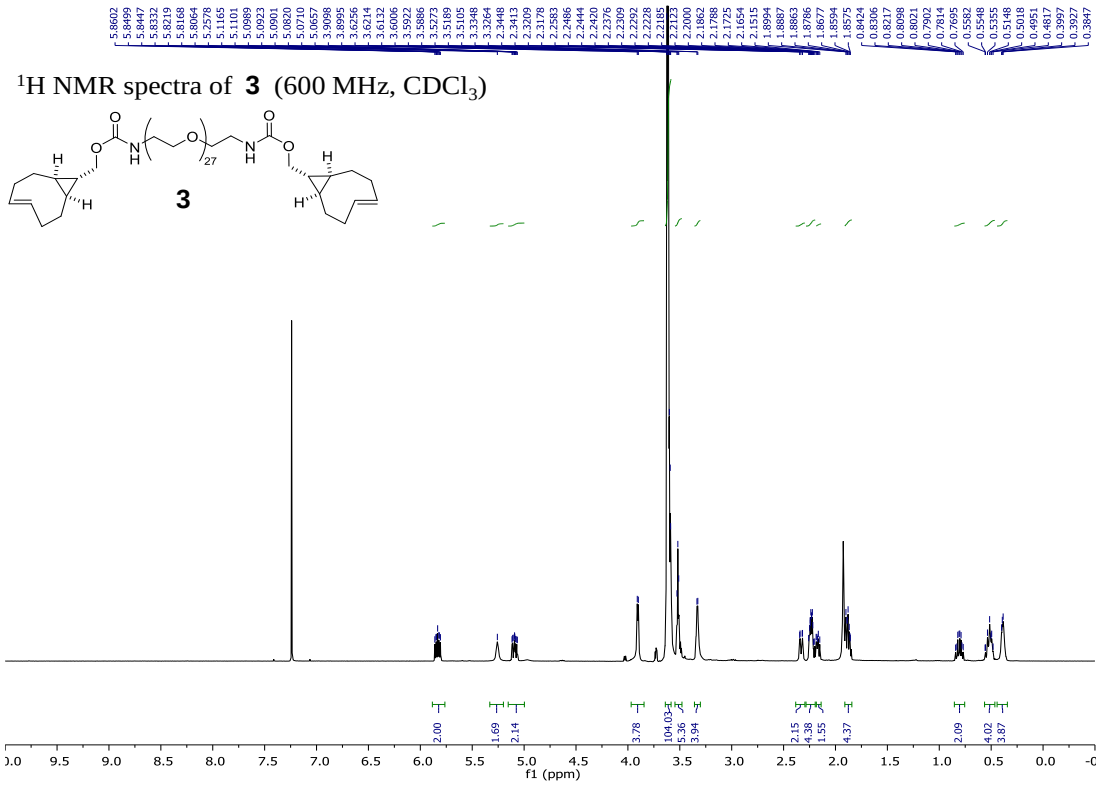

Figure 3.13 ^{1}H NMR spectrum of PEG-bisTCO in $CDCl_3$.

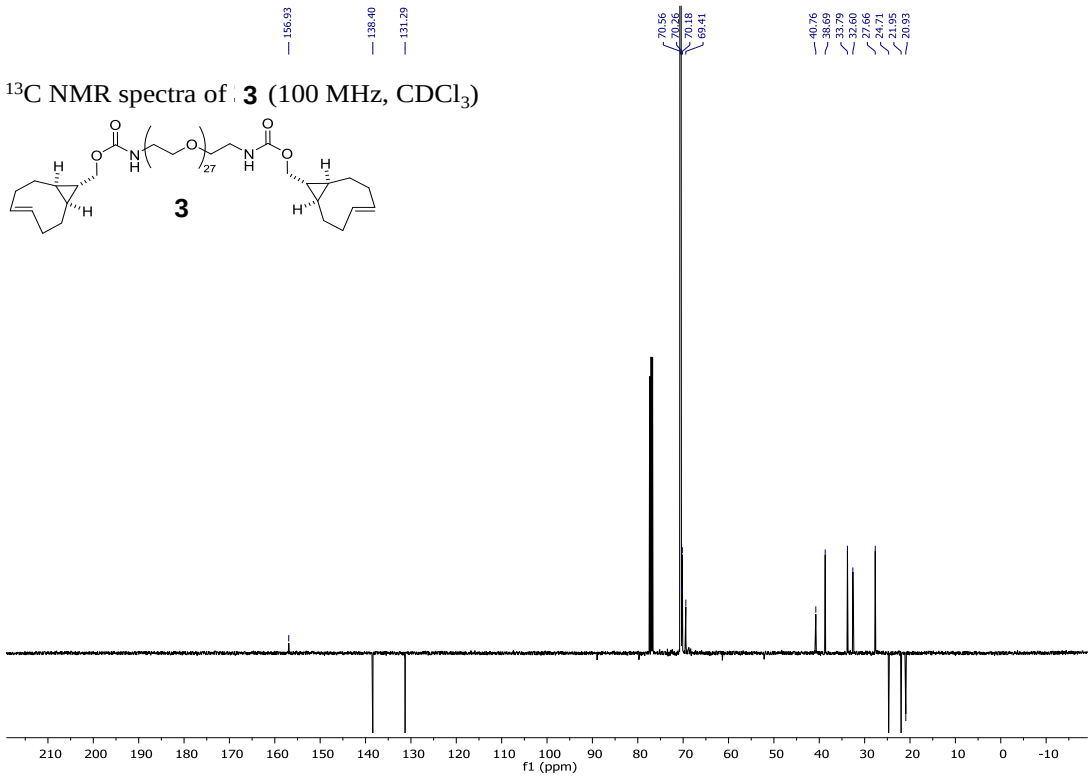

Figure 3.14 ^{13}C NMR spectrum of PEG-bisTCO in $CDCl_3$

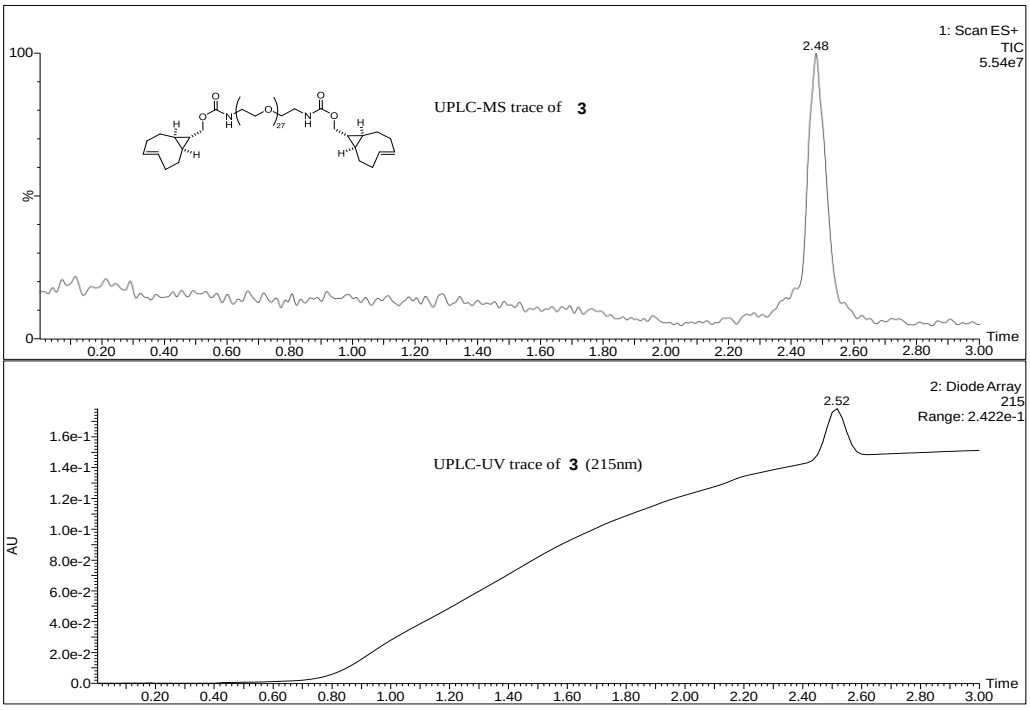

Figure 3.15 UPLC-MS trace of PEG-bisTCO.

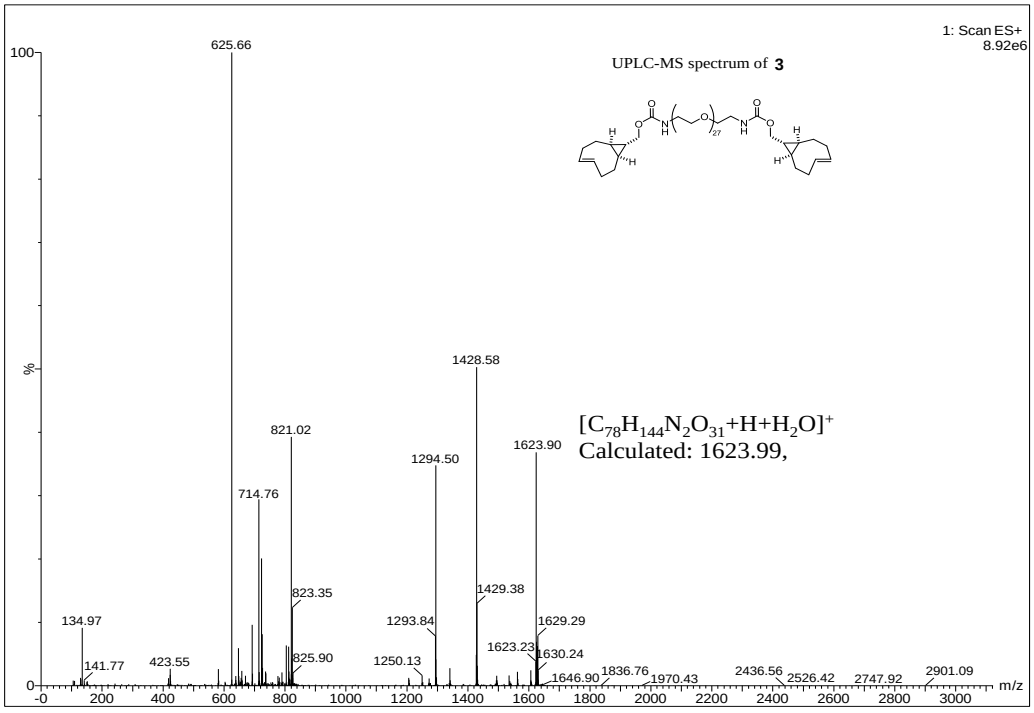

Figure 3.16 UPLC-MS spectrum of PEG-bisTCO.

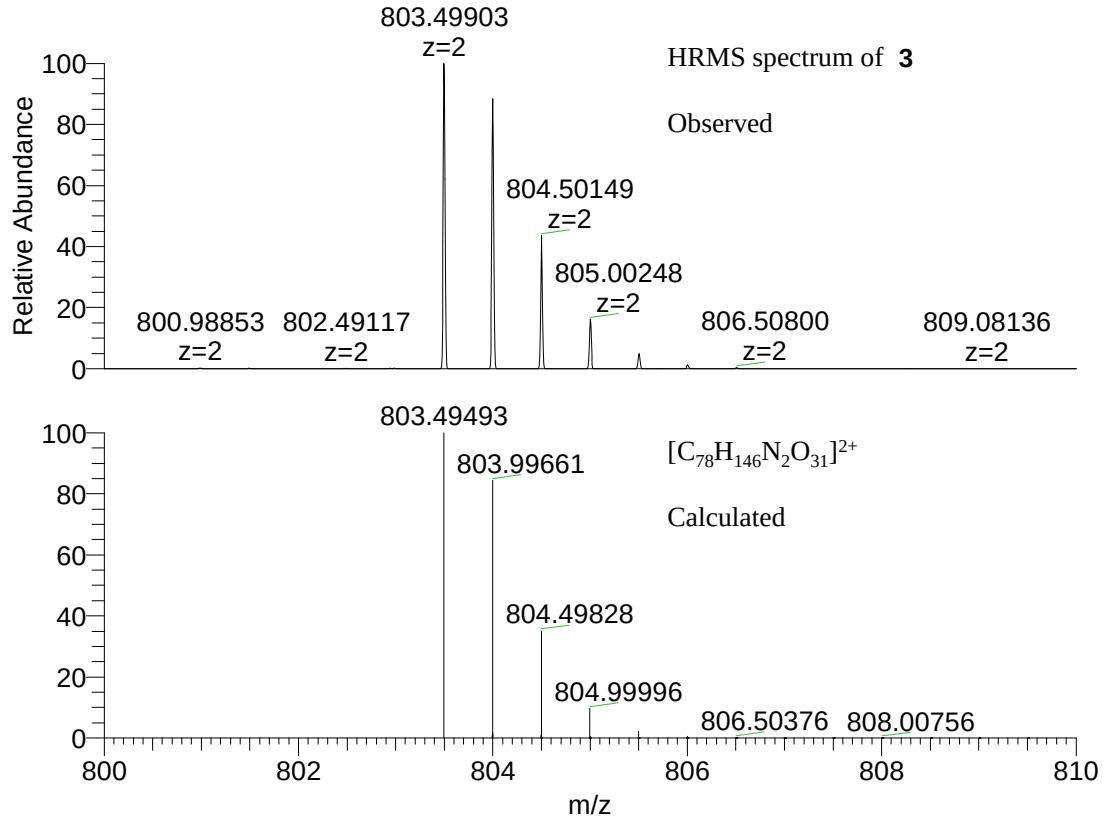

Figure 3.17 HRMS spectrum of PEG-bisTCO.

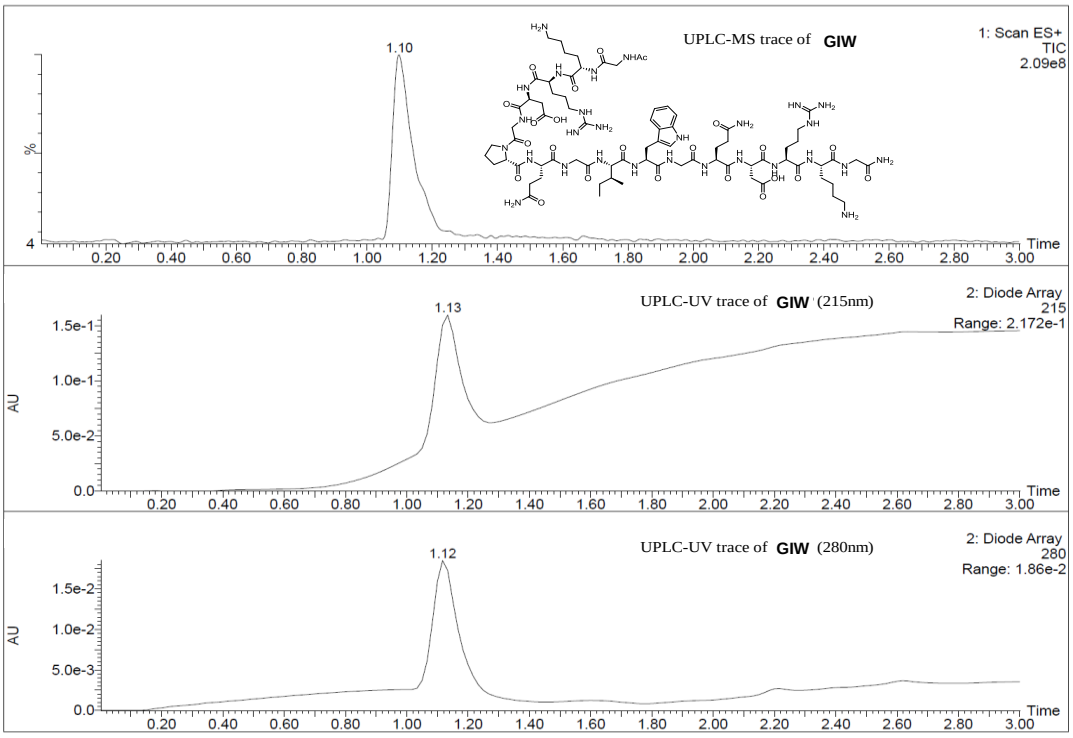

Figure 3.18 UPLC-MS trace of the GIW peptide.

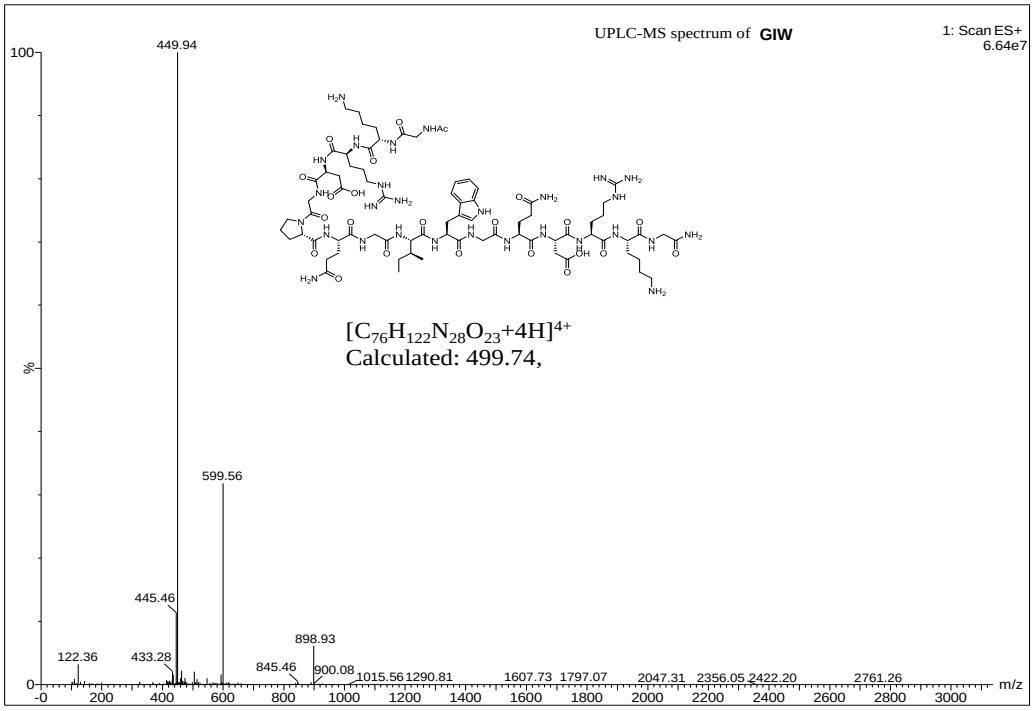

Figure 3.19 UPLC-MS spectrum of the GIW peptide.

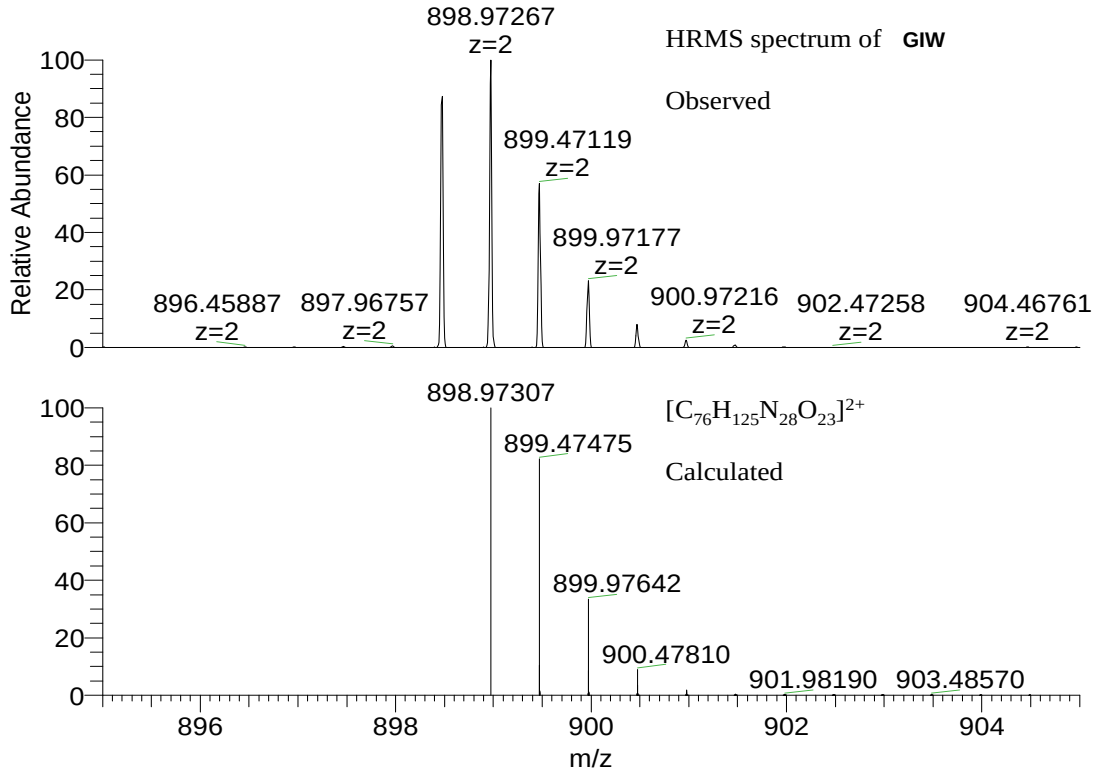

Figure 3.20 HRMS of the GIW peptide.

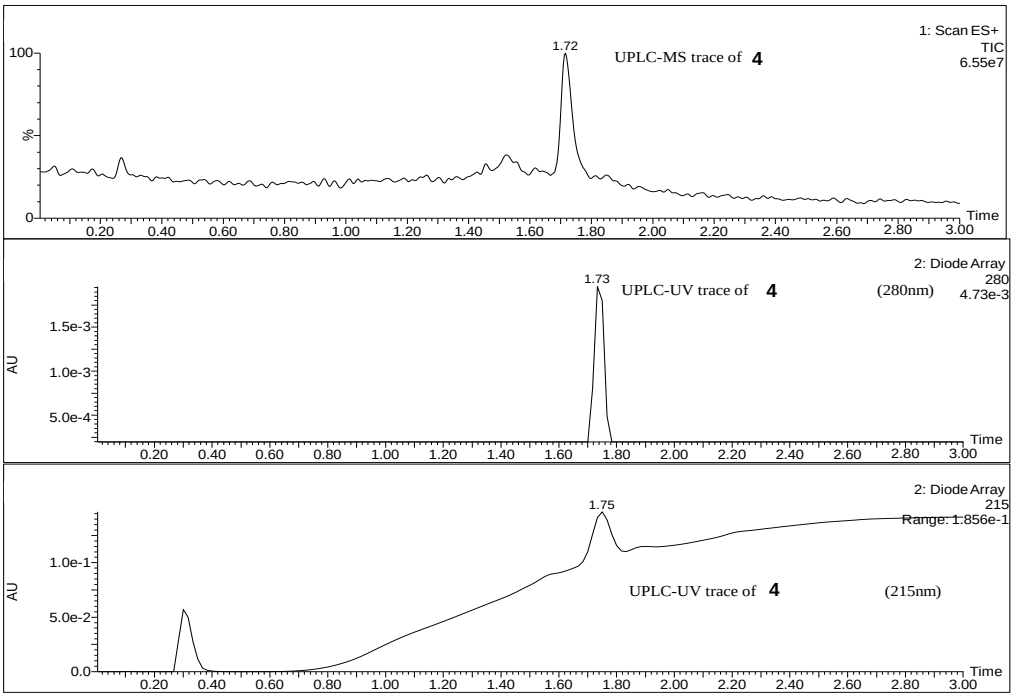

Figure 3.21 UPLC-MS trace of GIW-bisTCO.

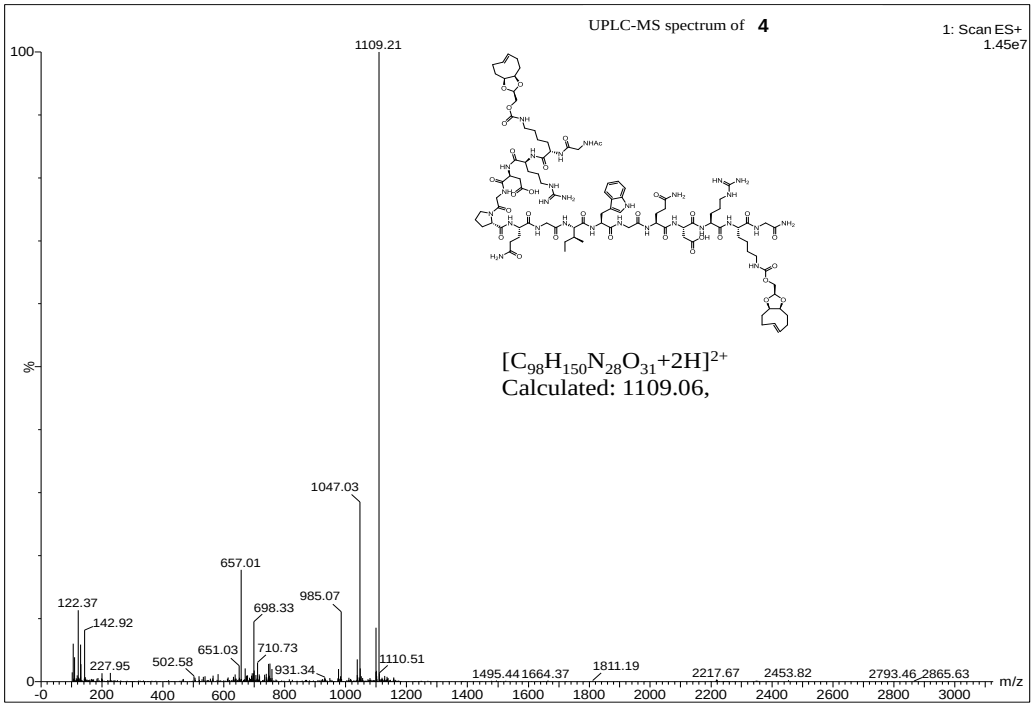

Figure 3.22 UPLC-MS spectrum of GIW-bisTCO.

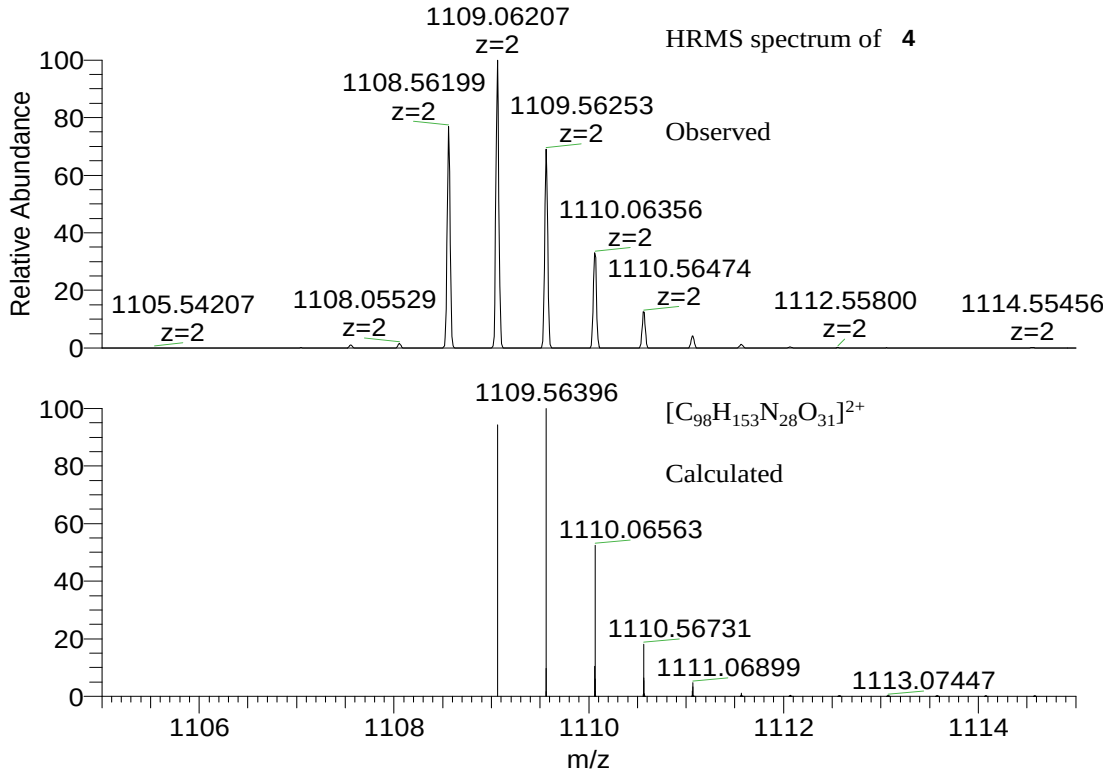

Figure 3.23 HRMS spectrum of GIW-bisTCO.

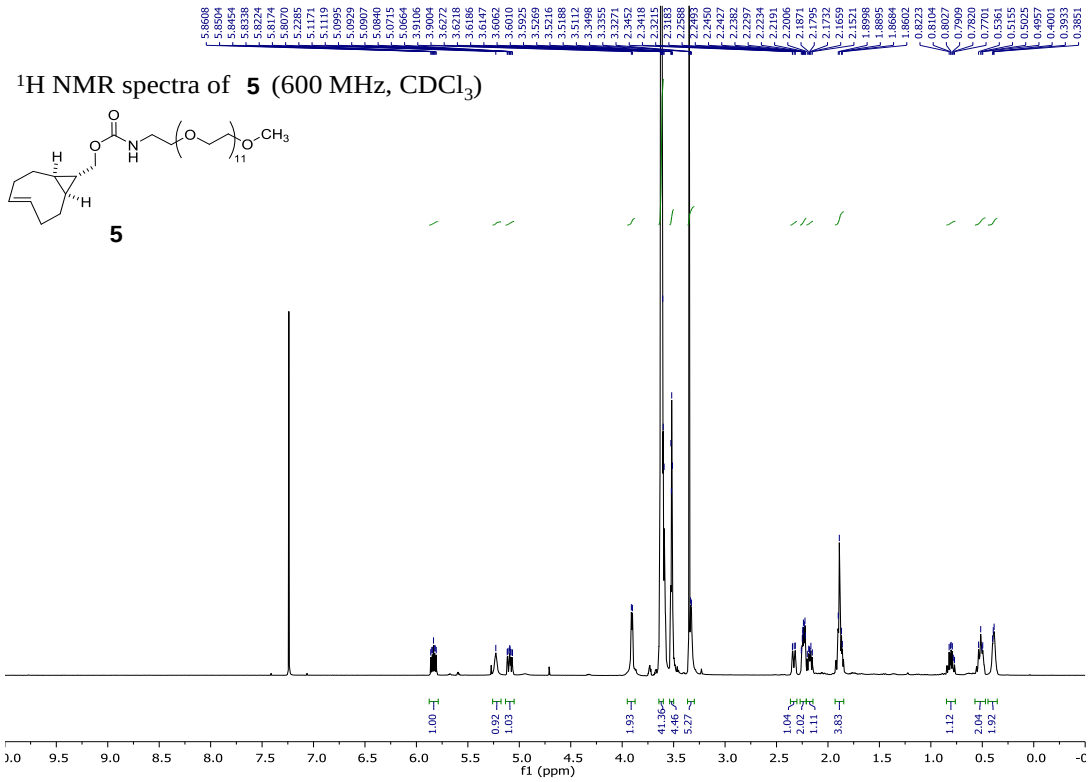

Figure 3.24 ^{1}H NMR spectrum of PEG-TCO in $CDCl_3$

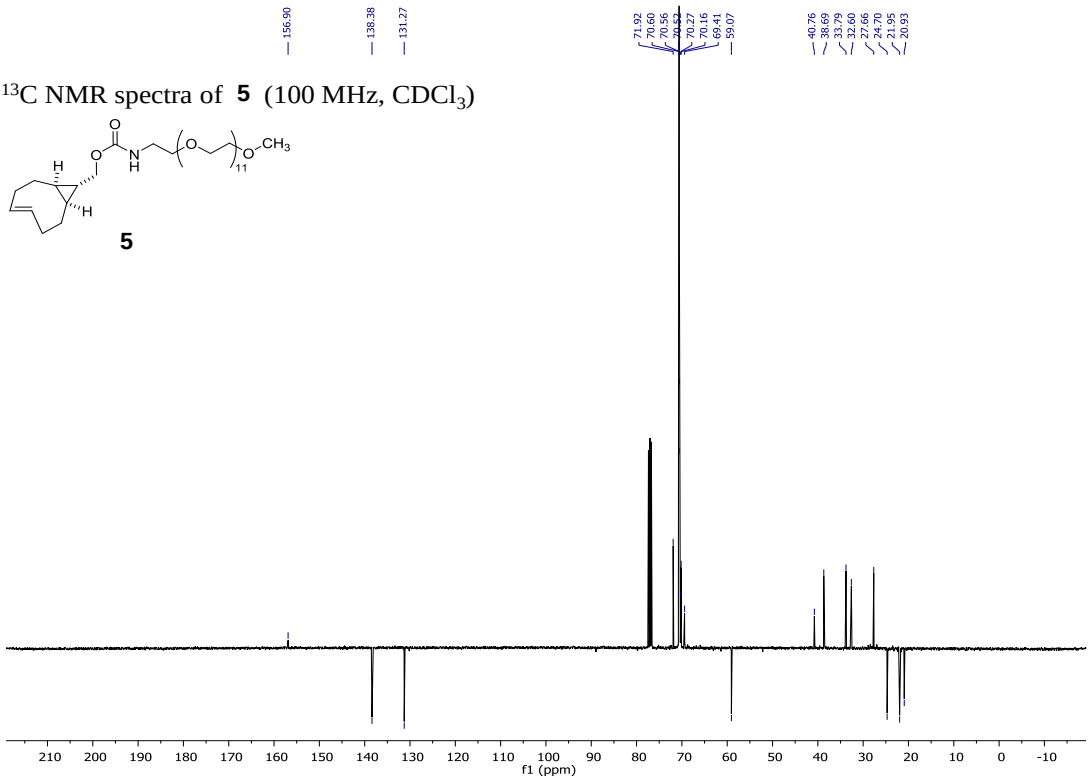

Figure 3.25 ^{13}C NMR spectrum of PEG-TCO in $CDCl_3$.

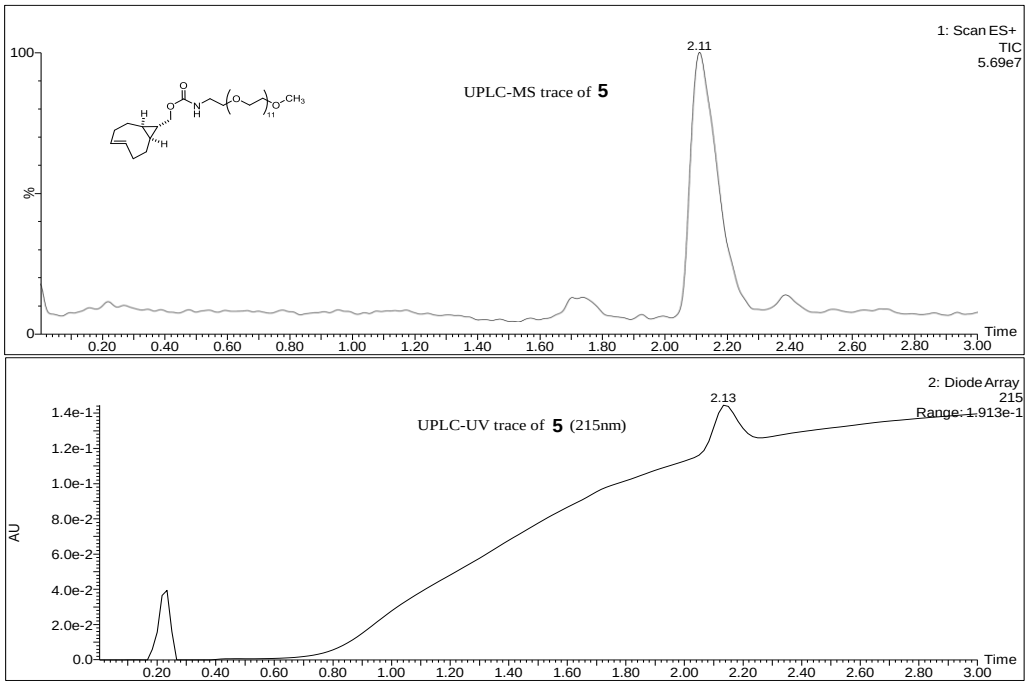

Figure 3.26 UPLC-MS spectrum of PEG-TCO.

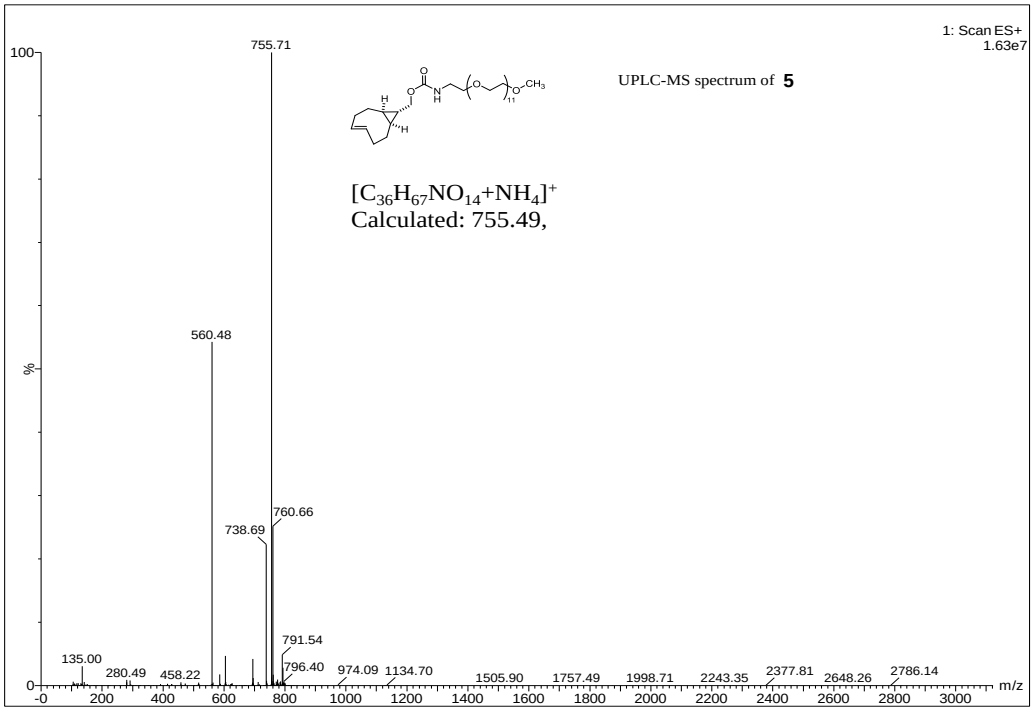

Figure 3.27 UPLC-MS spectrum of PEG-TCO.

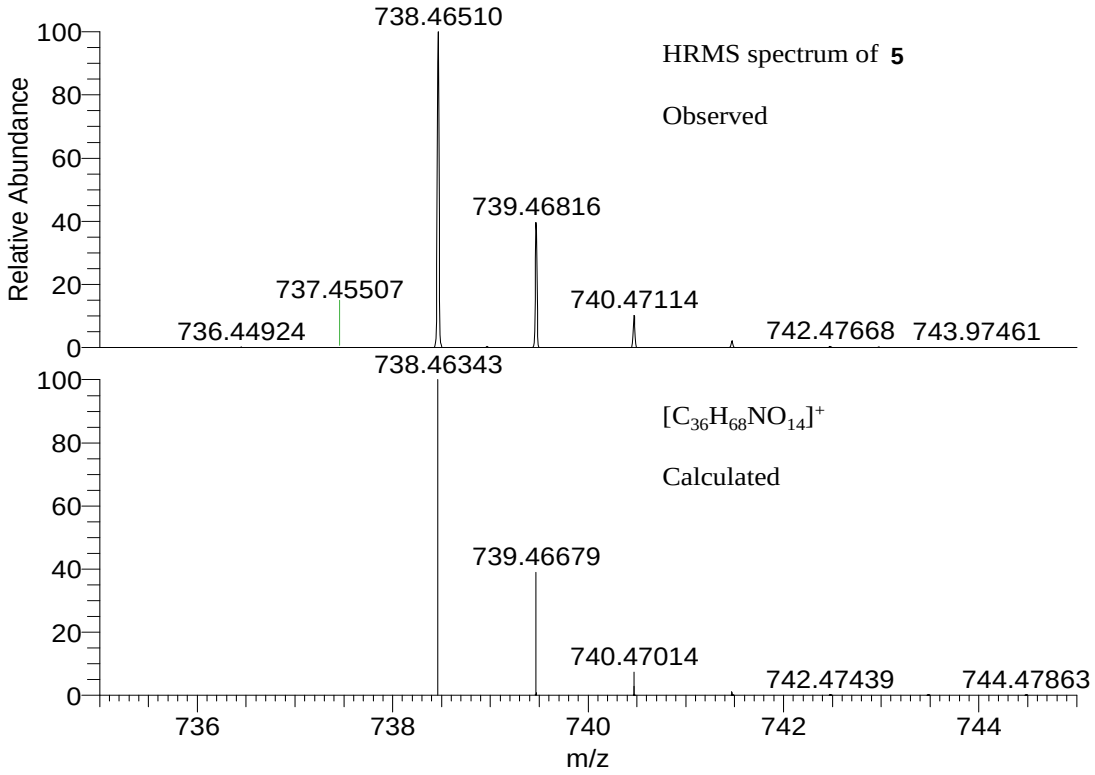

Figure 3.28 HRMS spectrum of PEG-TCO.

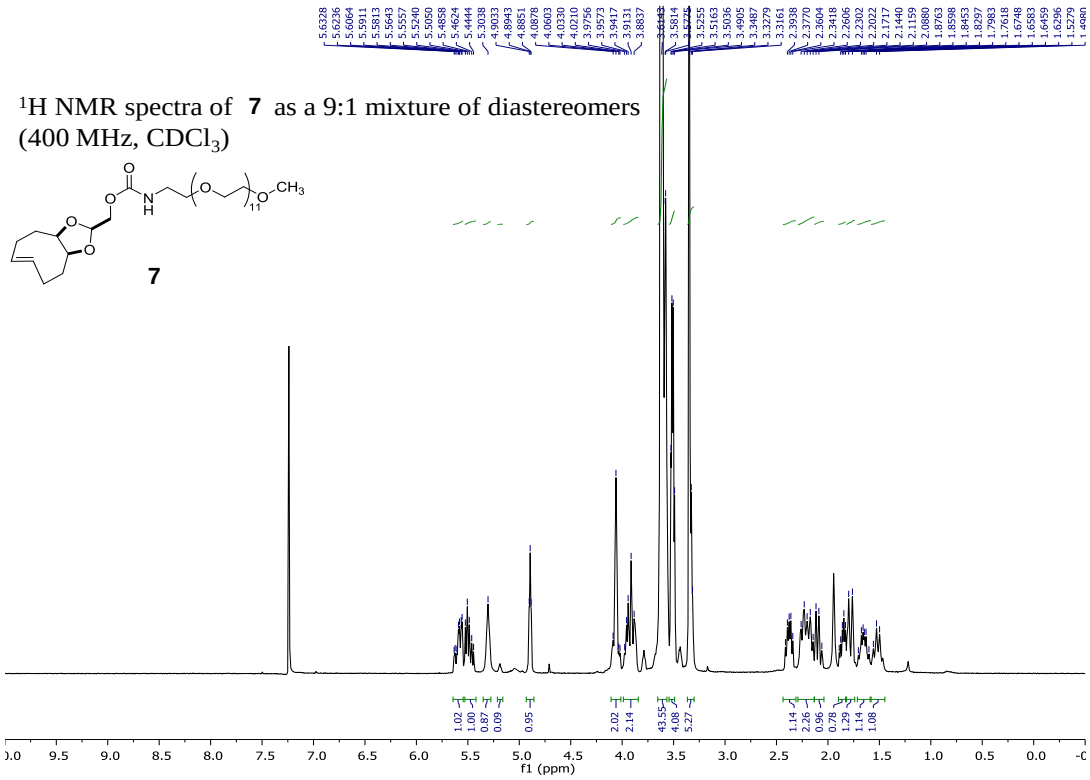

Figure 3.29 ^{1}H NMR spectrum of PEG-dTCO in $CDCl_3$.

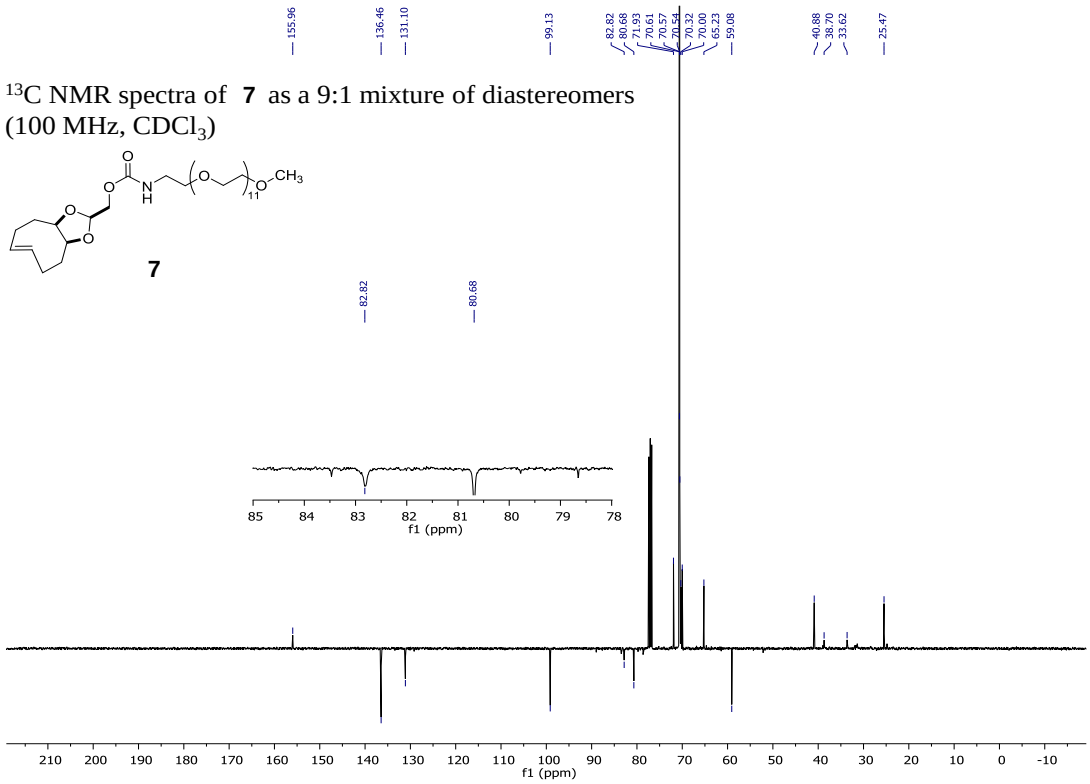

Figure 3.30 ^{13}C NMR spectrum of PEG-dTCO in $CDCl_3$

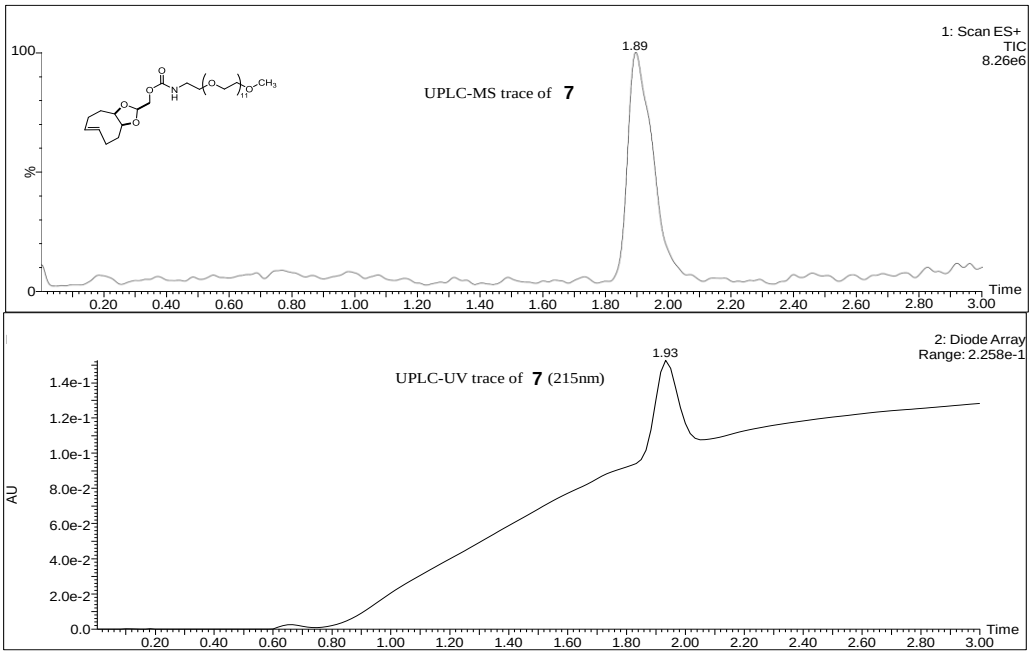

Figure 3.31 UPLC-MS trace of PEG-dTCO.

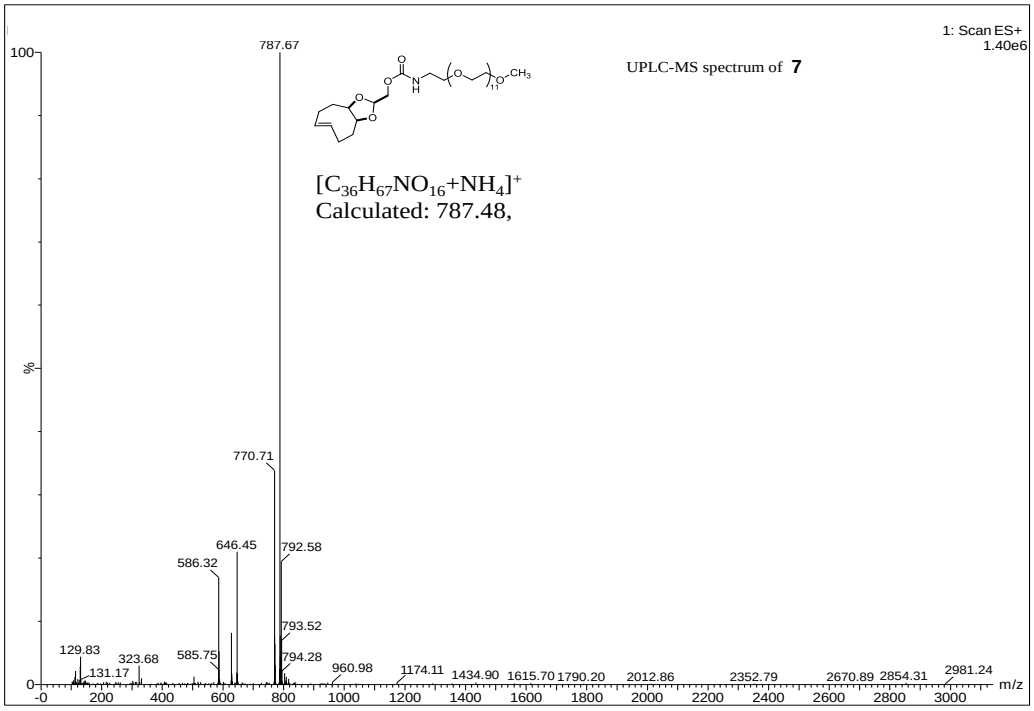

Figure 3.32 UPLC-MS spectrum of PEG-dTCO.

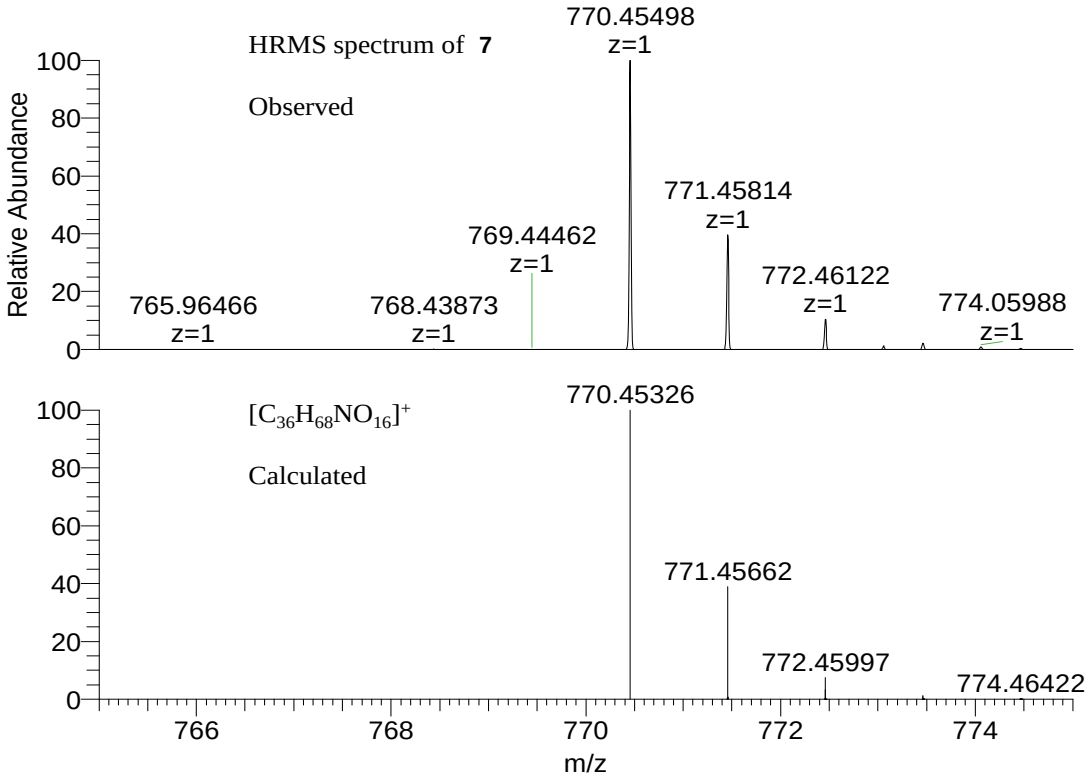

Figure 3.33 HRMS spectrum of PEG-dTCO.

Spectrums shown in Figures 8-33 were collected by my collaborator, Yi Li.

REFERENCES

[1] Li, L.; Stiadle, J. M.; Lau, H. K.; Zerdoum, A. B.; Jia, X.; Thibeault, S. L.; Kiick, K. L. *Biomaterials* **2016,** *108*, 91-110.

[2] Xu, X.; Farach-Carson, M. C.; Jia, X. *Biotechnol. Adv.* **2014,** *32*, 1256-1268.

[3] Ozdemir, T.; Fowler, E. W.; Hao, Y.; Ravikrishnan, A.; Harrington, D. A.; Witt, R. L.; Farach-Carson, M. C.; Pradhan-Bhatt, S.; Jia, X. *Biomater. Sci.* **2016,** *4*, 592-604.

[4] Hinderer, S.; Layland, S. L.; Schenke-Layland, K. *Adv. Drug Delivery Rev.* **2016,** *97*, 260-269.

[5] Tibbitt, M. W.; Anseth, K. S. *Sci. Transl. Med.* **2012,** *4*, 160ps24-160ps24.

[6] Mao, A. S.; Mooney, D. J. *Proc. Natl. Acad. Sci. USA* **2015,** *112*, 14452-14459.

[7] Pashuck, E. T.; Stevens, M. M. *Sci. Transl. Med.* **2012,** *4*, 160sr4-160sr4.

[8] Place, E. S.; Evans, N. D.; Stevens, M. M. *Nat. Mater.* **2009,** *8*, 457.

[9] Sugiura, S.; Cha, J. M.; Yanagawa, F.; Zorlutuna, P.; Bae, H.; Khademhosseini, A. *J. Tissue Eng. Regen. Med.* **2013**, *10*, 690-699.

[10] Billiet, T.; Vandenhaute, M.; Schelfhout, J.; Van Vlierberghe, S.; Dubruel, P. *Biomaterials* **2012,** *33*, 6020-6041.

[11] Khetan, S.; Burdick, J. A. *Biomaterials* **2010,** *31*, 8228-8234.

[12] Mosiewicz, K. A.; Kolb, L.; Van Der Vlies, A. J.; Martino, M. M.; Lienemann, P. S.; Hubbell, J. A.; Ehrbar, M.; Lutolf, M. P. *Nat. Mater.* **2013,** *12*, 1072-1078.

[13] Kloxin, A. M.; Kasko, A. M.; Salinas, C. N.; Anseth, K. S. *Science* **2009,** *324*, 59-63.

[14] Sletten, E. M.; Bertozzi, C. R. *Acc. Chem. Res.* **2011,** *44*, 666-676.

[15] Tang, W.; Becker, M. L. *Chem. Soc. Rev.* **2014,** *43*, 7013-7039.

[16] Sauer, J.; Heldmann, D. K.; Hetzenegger, J.; Krauthan, J.; Sichert, H.; Schuster, J. *Eur. J. Org. Chem.* **1998,** *1998*, 2885-2896.

[17] Blackman, M. L.; Royzen, M.; Fox, J. M. *J. Am. Chem. Soc.* **2008,** *130* (41), 13518-13519.

[18] Zhang, H.; Dicker, K. T.; Xu, X.; Jia, X.; Fox, J. M. *ACS Macro Lett* **2014,** *3*, 727-731.

[19] Liu, S.; Zhang, H.; Remy, R. A.; Deng, F.; Mackay, M. E.; Fox, J. M.; Jia, X., *Adv. Mater.* **2015,** *27*, 2783-90.

[20] Taylor, M. T.; Blackman, M. L.; Dmitrenko, O.; Fox, J. M., *J. Am. Chem. Soc.* **2011,** *133*, 9646-9649.

[21] Zhang, H.; Trout, W. S.; Liu, S.; Andrade, G. A.; Hudson, D. A.; Scinto, S. L.; Dicker, K. T.; Li, Y.; Lazouski, N.; Rosenthal, J. *J. Am. Chem. Soc.* **2016,** *138*, 5978-5983.

[22] DeForest, C. A.; Anseth, K. S. *Nat. Chem.* **2011,** *3*, 925-931.

[23] He, Y.; Yang, F.; Zhao, H.; Gao, Q.; Xia, B.; Fu, J., *Sci. Rep.* **2016,** *6*, 29977.

[24] Sletten, E. M.; Bertozzi, C. R. *Angew. Chem. Int. Ed.* **2009,** *48*, 6974-6998.

[25] Gattazzo, F.; Urciuolo, A.; Bonaldo, P., *Biochim. Biophys. Acta* **2014,** *1840*, 2506-2519.

[26] Lei, Y.; Gojgini, S.; Lam, J.; Segura, T. *Biomaterials* **2011,** *32*, 39-47.

[27] Lutolf, M. P.; Lauer-Fields, J. L.; Schmoekel, H. G.; Metters, A. T.; Weber, F. E.; Fields, G. B.; Hubbell, J. A. *Proc. Natl. Acad. Sci. USA* **2003,** *100*, 5413-8.

[28] Yang, C.; DelRio, F. W.; Ma, H.; Killaars, A. R.; Basta, L. P.; Kyburz, K. A.; Anseth, K. S. *Proc. Nat. Acad. Sci. USA* **2016,** *113*, E4439-45.

[29] Wang, L. S.; Chung, J. E.; Chan, P. P.; Kurisawa, M. *Biomaterials* **2010,** *31*, 1148-57.

[30] Marklein, R. A.; Burdick, J. A. *Soft Matter* **2010,** *6*, 136-143.

[31] Wen, J. H.; Vincent, L. G.; Ruhrmann, A.; Choi, Y. S.; Hribar, K. C.; Taylor-Weiner, H.; Chen, S.; Engler, A. J., *Nat. Mater.* **2014,** *13*, 979-987.

[32] Engler, A. J.; Sen, S.; Sweeney, H. L.; Discher, D. E. *Cell* **2006,** *126*, 677-89.

[33] Zhou, H.; Schon, E. M.; Wang, M.; Glassman, M. J.; Liu, J.; Zhong, M.; Diaz Diaz, D.; Olsen, B. D.; Johnson, J. A. *J. Am. Chem. Soc.* **2014,** *136*, 9464-70.

[34] Moore, A. C.; Zimmerman, B. K.; Chen, X.; Lu, X. L.; Burris, D. L. *Tribol. Int.* **2015,** *89*, 2-8.

[35] Latifi, N.; Miri, A. K.; Mongeau, L. *J. Mech. Behav. Biomed. Mater.* **2014,** *39*, 366-74.

[36] Schultz, K. M.; Kyburz, K. A.; Anseth, K. S. *Proc. Nat. Acad. Sci. USA* **2015,** *112*, E3757-64.

[37] Kyburz, K. A.; Anseth, K. S. *Acta Biomater.* **2013,** *9*, 6381-92.

[38] Khetan, S.; Guvendiren, M.; Legant, W. R.; Cohen, D. M.; Chen, C. S.; Burdick, J. A. *Nat. Mater.* **2013,** *12*, 458-465.

[39] Nuttelman, C. R.; Tripodi, M. C.; Anseth, K. S. *J. Biomed. Mater. Res. A* **2004,** *68A*, 773-782.

[40] Humphries, J. D.; Byron, A.; Humphries, M. J. *J. Cell Sci.* **2006,** *119*, 3901-3903.

[41] Barczyk, M.; Carracedo, S.; Gullberg, D. *Cell Tissue Res.* **2010,** *339*, 269-80.

[42] Fonseca, K. B.; Gomes, D. B.; Lee, K.; Santos, S. G.; Sousa, A.; Silva, E. A.; Mooney, D. J.; Granja, P. L.; Barrias, C. C. *Biomacromolecules* **2014,** *15*, 380-90.

[43] Darko, A.; Wallace, S.; Dmitrenko, O.; Machovina, M. M.; Mehl, R. A.; Chin, J. W.; Fox, J. M. *Chem. Sci.***2014,** *5*, 3770-3776.

[44] Xu, X.; Gurski, L. A.; Zhang, C.; Harrington, D. A.; Farach-Carson, M. C.; Jia, X. Q. *Biomaterials* **2012,** *33*, 9049-9060.

Chapter 4

FORMATION OF LIQUID FILLED HYDROGEL CHANNELS

4.1 Introduction

Cardiovascular disease, including Coronary Heart Disease, is the leading cause of mortality in the United States with nearly 33% of all deaths attributed to these diseases.[1] Treatments of cardiovascular diseases include vascular bypass surgery by means of autografts or allografts. Initially these vascular grafts are able to treat the disease, however, they fail approximately 50% of the time due to vessel wall thickening caused by atherosclerosis or intimal hyperplasia.[2] Engineered biomaterials which are able to mimic the native vascular environment offer an attractive approach for the fabrication of in vitro models which could be utilized to improve treatment of cardiovascular disease.

Recent vascular research efforts have focused on two general approaches: vasculogensis and angiogenesis or prevascularization-based methods.[3] Vasculogenesis and angiogesis methods utilize endothelial cells to create vasculature within a synthetic construct.[4] Prevascularization methods include the formation of channels by utilizing templates or by a layer by layer addition. Templates include SU-8 silicon molds,[5–7] microneedles,[8] SAM-modified gold rods[9] or silica capillary tubes[10] which are removed after forming the construct, leaving behind channels. Another type of template is formed by the fabrication of sacrificial layers made of

carbohydrate glass,[11] pluronic[12] or gelatin[13] followed by subsequent dissolving of the sacrificial layer leaving behind hollow channels. Laser-based hydrogel degradation has also been shown to be able to fabricate vascular microfluidic networks with image-guided laser control.[14,15]

Previously, I described the formation of hydrogel channels via tetrazine ligation.[16] Tetrazine ligation, the inverse electron demand Diels-Alder (iEDDA) reaction between *s*-tetrazines and *trans*-cylcooctenes (Figure 4.1A), is a bioorthogonal reaction which exhibits rapid kinetics ($k_2 > 10^5$ $M^{-1}s^{-1}$)[16,17] and has been shown to be cyto-compatible in both the formation of hydrogels[16] and fibers[18,19]. Herein, I describe the formation and 3D spatial patterning of hydrogel channels without the use of external triggers and multiple reactions or templates through an interfacial bioorthogonal crosslinking process. A pressure-dilation assay was used to characterize the mechanical properties of the hydrogel channels. The interfacial, diffusion-controlled nature of the crosslinking chemistry allows for the spatial patterning of TCO conjugated fluorophores and biomolecules to modulate the local 3D microenvironment of encapsulated fibroblasts. The crosslinking chemistry also permits the facile spatial patterning of different cell populations by systematic changing of the cell laden reservoir to mimic anatomically relevant order found *in vivo*.

4.2 Materials and Methods

4.2.1 Materials

All reactions were carried out in glassware that was flame-dried under vacuum and cooled under nitrogen. Cy3-TCO and Cy5-TCO were purchased from AAT Bioquest. O,O′-Bis(2-aminoethyl)hexacosaethylene glycol (≥ 95% oligomer purity) was purchased from Santa Cruz Biotechnology. Hyaluronic acid (sodium salt, 430 kDa) was a generous gift from Sanofi/Genzyme Corporation. Reactive intermediates or products, including (rel-1R,8S,9R,4E)-bicyclo[6.1.0]non-4-ene-9-ylmethanol,[20] d-TCO-carbonate,[17] RGD-TCO,[21] Alexa-TCO[16] and Clover-TCO[21] were prepared following known procedures. Peptides were synthesized using CEM Liberty Blue Peptide Synthesizer. Dialysis membranes were purchased from Spectrum Labs (MWCO: 10 kDa). Flash Chromatography was performed using normal phase Silicycle silica gel (40-63D, 60Å). Other reagents were purchased from commercial sources without additional purification.

4.2.2 Synthesis of Hydrogel Precursors

4.2.2.1 Synthesis of VPM-bisTCO

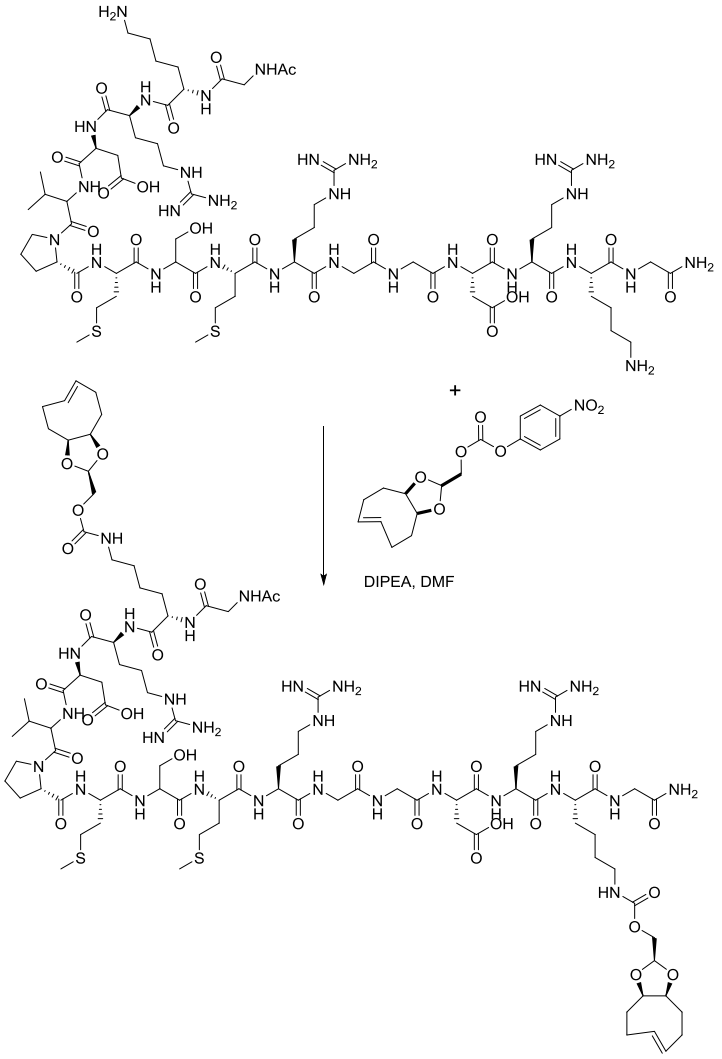

MMP-degradable peptide with a basic sequence of Ac-GKRDVPMSMRGGDRKG-NH_2 (abbreviated as VPM, 144.2 mg, 80.6 μmol), prepared by solid phase peptide synthesis, was dissolved in anhydrous DMF (3 mL). *N*, *N*-diisopropylethylamine (56.2 μL, 322 μmol) was added followed by dTCO-4-nitrophenyl carbonate[17] (70.4 mg, 202 μmol). The solution was stirred at room temperature for 2 hours. The reaction was deemed complete when only the desired

bis-modification product was observed by UPLC-MS. The resulting solution was added dropwise to 45 mL of ice cold diethyl ether. Then it was centrifuged at 4000 rpm for 5 mins, and the clear ethereal solution was removed. The solid was re-dissolved in 3 mL of DMF and precipitated into ice cold diethyl ether. The precipitation/re-dissolve cycle was repeated for a total 3 times. Analytical grade sample was obtained by purification of the white powder by reverse phase chromatography on C_{18} silica gel using a gradient of 5% to 95% MeOH in neutral water. UPLC-MS for VPM-bisTCO: t_R = 1.79 mins, $[M+2H]^{2+}$ found 1105.11. UPLC-MS for VPM: t_R = 1.03 mins, $[M+4H]^{4+}$ found 447.99.

4.2.3 Chamber Fabrication

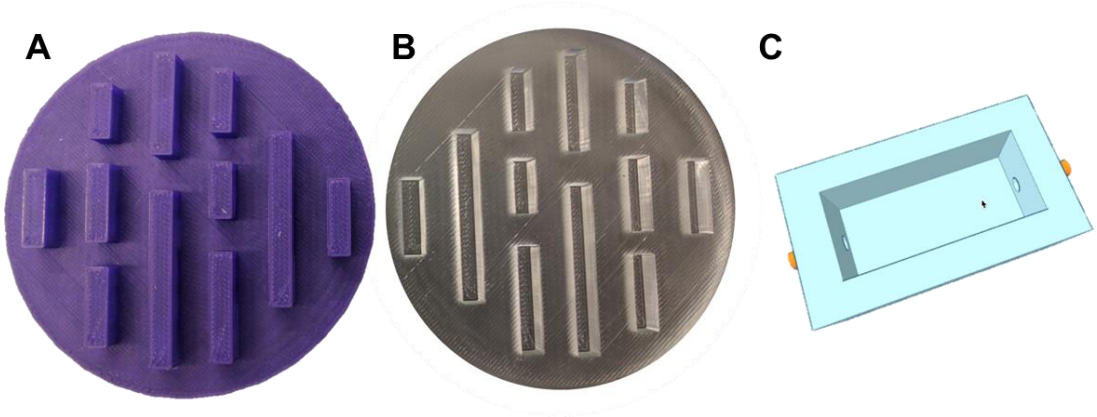

A mold was 3D printed using a Replicator 2 (Makerbot, Brooklyn, NY) 3D printer with ABS resin. Sylgard 184 (Dow Corning, Midland, MI) was poured on top of the mold and cured at 110°C for 30 min. The individual chambers were cut out with a blade and inlet and outlet holes were formed with a 2 mm biopsy punch. Fluorinated ethylene propylene (FEP) tubing (Cole-Parmer, Vernon Hills, IL) with an ID of 1/32" and OD of 1/16" was fit into the inlet and outlet of each chamber. Chambers were sterilized in 70% ethanol with germicidal ultraviolet light prior to cell experiments.

4.2.4 Hydrogel Channel Formation

HA-Tz (2 wt%), bisTCO crosslinker (PEG, GIW or VPM, 1 wt%) and RGD-TCO (1 wt%) were dissolved separately in PBS. HA-Tz (400 μL) was added to the well of the PDMS chamber sitting on a moving stage. A syringe with a 21G blunt needle (Component Supply Company, Fort Meade, FL) containing the bisTCO solution (500 μL) was placed in a syringe pump with the needle placed through the inlet and outlet of the PDMS chamber. The chamber is moved horizontally through the PDMS chamber while bisTCO solution (20 μL) is injected into the HA-Tz bath over 13 s. The channel is allowed to crosslink further for 5 min. The HA-Tz solution is removed and the channel is washed with PBS.

4.2.5 Pressure Dilation Assay

A schematic of this experiment is shown in Figure 4.2. In this configuration, a screw-driven head tank moves relative to the stationary hydrogel channel in 2.54 mm steps. The relationship between fluid pressure (P) and the height (h) of the head tank is given by the following equation:

$$P = h \cdot \gamma = h \cdot \rho \cdot g \qquad \text{Eq. 1}$$

Assuming that the solution (70 ml of 0.15 M saline and 1 ml of India ink) has a density similar to that of pure water (~998 kg/m^3) at room temperature, and that the system is quasi static (i.e. only gravity acts on the fluid column), then it can be assumed that the specific weight (γ) is ~9790 N/m^3. This means that every mm of travel (vertical) produces a pressure differential of ~9.79 Pa.

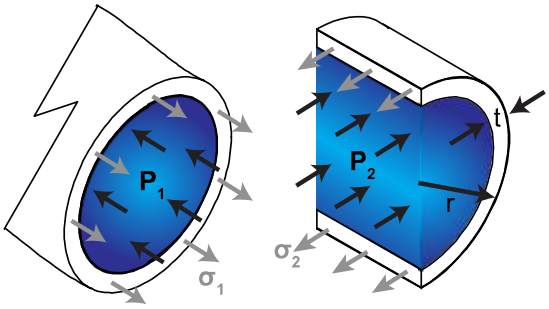

The channel modulus was calculated according to a mechanical model that described the change of diameter as a function of pressure. The relatively higher pressure inside the channels (P) caused them to expand while the pressure was balance by stresses (σ) in the channels' walls. Strain (ε) was calculated by balancing the forces at two principal cuts of the channels and assuming a Poisson's ratio of 0.5 (typical for hydrogels):

$$\varepsilon = \frac{3PD}{8Et} \qquad \text{Eq. 2}$$

where D is the tubes' diameter, E is elastic modulus and t is wall thickness. Using this relation, the change of strain for each pressure rise was numerically integrated to calculate the increase in tube diameter. This model was then best fit to the experimental data of pressure versus diameter and initial wall thickness. The resulting fit had a coefficient of determination $R^2 = 0.99$ and showed that the elastic modulus increases with increasing pressure and diameter while the wall thickness decreases.

The change in channel dilation, in response to the change in fluid pressure, was tracked by taking consecutive microscope images. A custom edge detection code was written in MatLab® to identify the channel boundaries and measure the radial changes. The contrast provided by the India ink and saline solution allowed the algorithm to construct a bimodal distributed histogram of the pixel intensity across the image and separate the darker areas which were representative of the channels' inside

diameter (Figure 4.2). Since the channels were attached to the PDMS chamber at both the inlet and outlet, which likely created edge effects, only the dilation in the central 30%. The pressure-dilation assay was collaborated on with Axel Moore and Nikolay Garabedian.

4.2.6 Covalent Patterning of Fluorophores

HA-Tz (2 wt% PBS) was added to the PDMS chamber well. A syringe containing PEG-bisTCO (4.4 mM) and Clover-TCO (5 μM) was drawn through the well while injected ~20 μL of solution as described above. The channel was allowed to crosslink for 5 min before fresh PBS was perfused through the channel. A solution of PEG-bisTCO (4.4 mM) and Cy3-TCO (5 μM) was injected into the lumen of the channel and allowed to crosslink for 15 min. The channel was flushed with fresh PBS before a solution of PEG-bisTCO (4.4 mM) and Cy5-TCO (5 μM) was injected into the lumen of the channel incubated for 45 min. The channels were washed with PBS overnight before imaging using a Zeiss 710 NLO confocal microscope with a 5X objective.

4.2.7 Cell Maintenance and 3D culture

NIH3T3 fibroblasts were maintained in a DMEM (Corning, Corning, NY) medium supplemented with 10% FBS and 1% PS. NIH3T3-GFP fibroblasts were maintained in a DMEM (Corning, Corning, NY) medium supplemented with 10% FBS, 0.1 mM MEM Non-Essential Amino Acids (NEAA) and 1% PS. HAAE-1 cells were maintained in a F-12K (Corning, Corning, NY) medium supplemented with Heparin (0.1 mg/mL), ECGS (0.03 mg/mL), FBS (10%), and P/S (1%). T/G HA-VSMCs were maintained in a F-12K (ATCC,) medium supplemented with TES

(10mM), HEPES(10mM), Ascorbic acid(0.05 mg/mL), sodium selenite (10 ng/mL), Transferrin (0.01mg/mL), ECGS (0.03 mg/mL), Insulin (0.01 mg/mL), FBS (10%), and P/S (1%). AoAFs were maintained in a stromal cell growth medium BulletKit (Lonza, Walkersville, MD). HA-Tz and all TCO-conjugated molecules were dissolved in PBS and sterile-filtered using a 0.22 μm Poly(vinylidene fluoride) (PVDF) syringe filter (Thermo Fisher Scientific, Waltham, MA). Cellular constructs were prepared following procedures described above for hydrogel synthesis and using HA-Tz containing a suspension of one of the cell types cells described above (excluding the HAAE-1) at 2 x 10^6/mL. Upon completion of the crosslinking reaction, channels were transferred to wells containing fresh media and were incubated at 37°C for up to 7 days, with media refreshed every other day. HAAE-1, dispersed in fresh media (8 x 10^6/mL), were injected into the lumen of the channel after formation and allowed to attach for 16 hours at 37°C. The channels were then transferred to wells containing fresh media and were incubated at 37°C for up to 7 days, with media refreshed every other day.

4.2.8 Three dimensional (3D) matrix patterning

NIH3T3-GFP fibroblasts were dispersed in HA-Tz (2 wt% PBS) and added to the well of the PDMS chamber as described above. A syringe containing PEG-bisTCO (5 mM) and alexa-TCO (2 μM) was drawn through the chamber while injecting 20 μL of the solution. The solution was allowed to incubate for 5 min before being flushed with PBS. A solution of GIW-bisTCO (3.2 mM) and RGD-TCO (0.4 mM) was then perfused into the channel and incubated for 15 min. The channel was flushed with PBS before a fresh solution of PEG-bisTCO (5 mM) and alexa-TCO (2 μM) was perfused into the channel and incubated for 30 min. The cell laden HA-Tz bath was

removed and the chamber was washed with PBS before the the channels were transferred to wells containing fresh media and were incubated at 37°C for up to 28 days, with media refreshed every other day.

4.2.9 Three dimensional (3D) cell patterning

NIH3T3 fibroblasts were stained with either Cell Tracker Red CMTPX (10 μM) or Cell Tracker Green CMFDA (10 μM) (Thermo Fisher, Waltham, MA) for 30 minutes. NIH3T3s stained with cell tracker red were dispersed (2 x 10^6/mL) in HA-Tz (2 wt% PBS) and added to the well of the PDMS chamber. A syringe containing PEG-bisTCO (uM) was drawn through the chamber injecting 20 uL of crosslinking solution. The crosslinker reacted for 5 min before removing the Red cell bath and washing with PBS. A second bath containing cell tracker green cells dispersed (2 x 10^6/mL) in HA-Tz (2 wt% PBS) was added to the chamber well and allowed to crosslink for 15 additional min. The Green cell bath was removed and the chamber was washed with PBS before returning the Red cell bath to the chamber well and incubated for 45 min. The crosslinker in the lumen of the channel was replenished throughout the experiment to maintain sufficient crosslinking. The Red cell bath was removed and washed with PBS. The channels were transferred to a 4-well Nunc chamber (Thermo-Fisher, Waltham, MA) containing fresh media and imaged immediately using a Zeiss 710 NLO confocal microscope with a 5X objective.

4.2.10 Cell Viability

Percent cell viability was assessed by Live/Dead staining with calcein AM and ethidium homodimer after 7 days of culture. Short z-stacks of 225 μm with 15 μm slices were taken with Zeiss 710 NLO confocal microscope with a 5X objective. The

images were flattened in Zeiss's Zen software to produce maximum intensity projections. By using Image J and counting the live and dead cells in each image, percent viability was quantified. Values are presented as a percentage of live cells compared with the total number of cells. Encapsulated cells were subsequently stained for F-actin using Alexa Fluor 568 phalloidin and with the nuclei counter stained by DAPI, following previous protocols.[22] Stained samples were imaged using a Zeiss 710 NLO confocal microscope with a 40X objective.

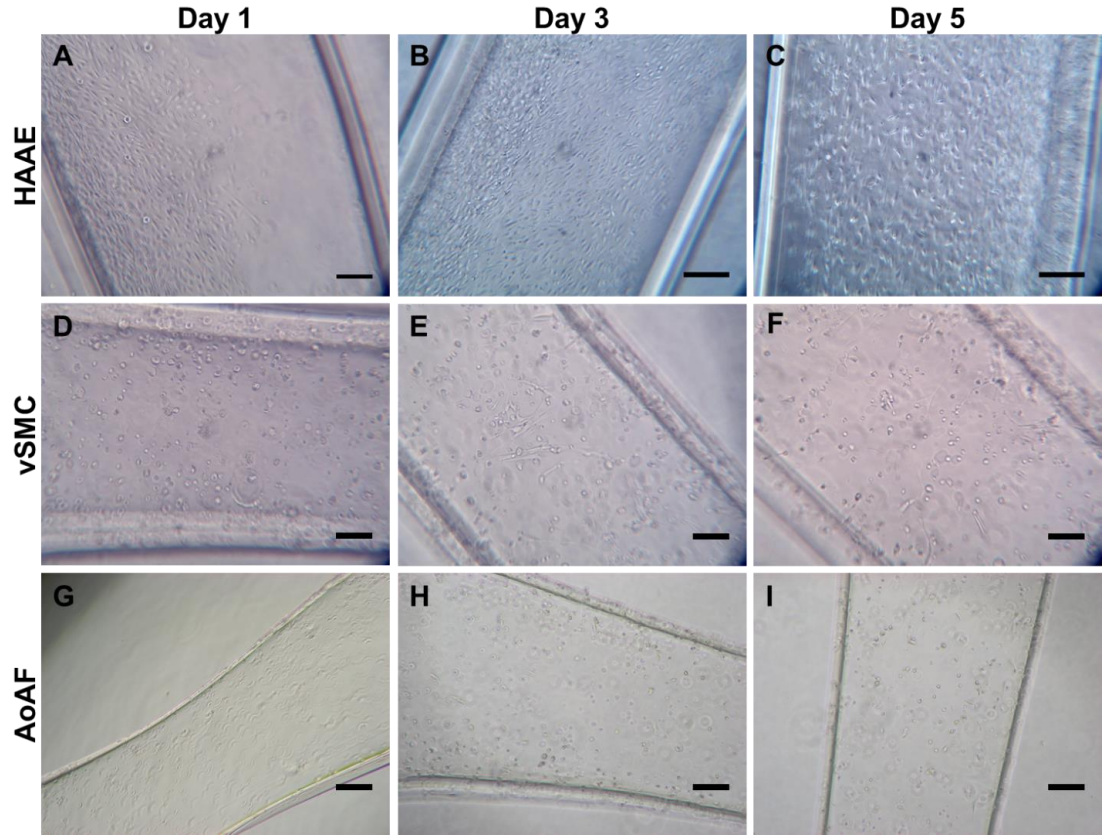

Figure 4.1 Light microscope images of encapsulated vascular cells within the hydrogel channels over 5 days of culture. (A-C) HAAE cells were injected into the lumen of the channel and attach to the inner surface while (D-F) vSMCs and (G-I) AoAFs are encapsulated within the hydrogel. Scale bar = 200 μm.

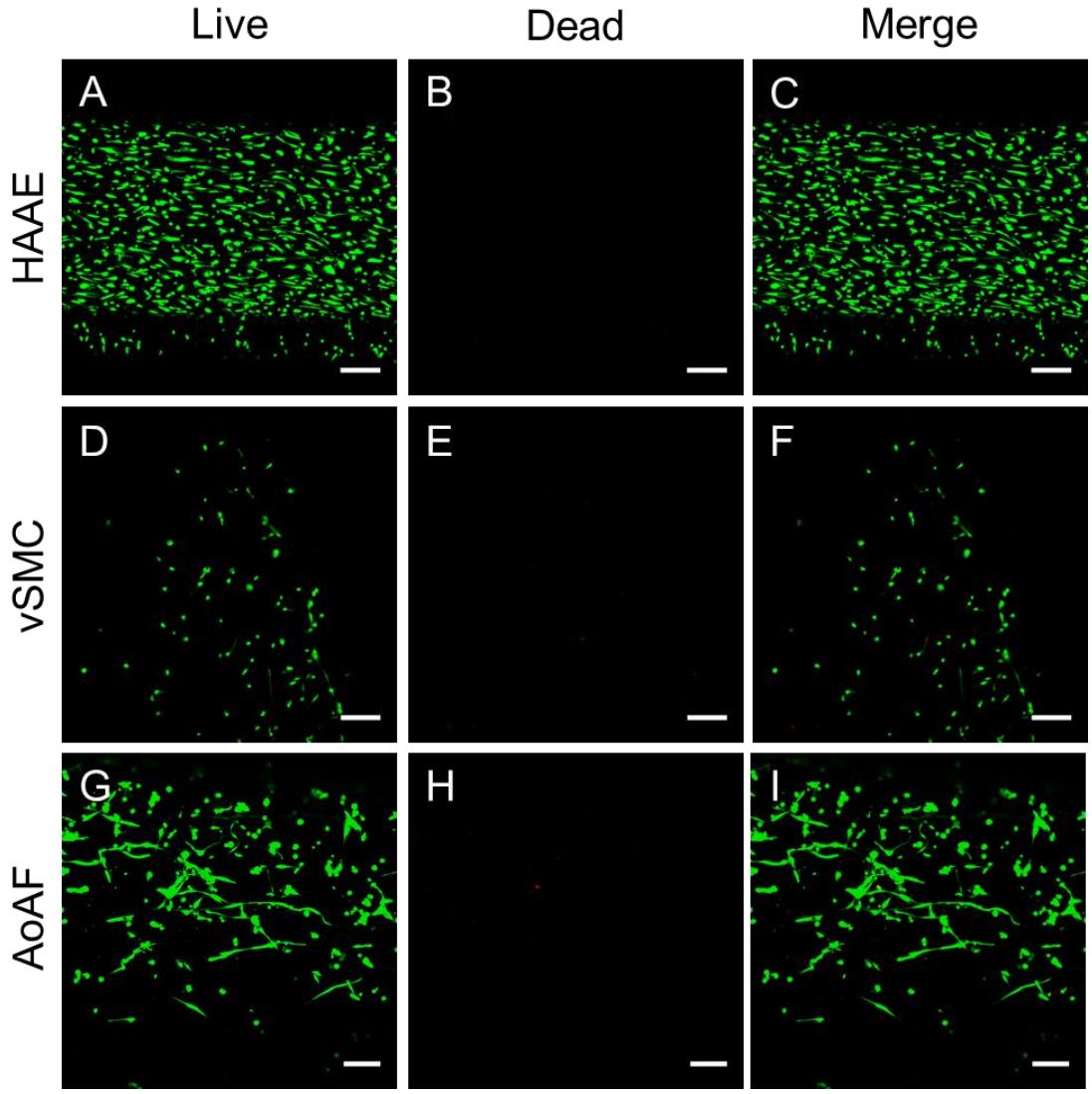

Figure 4.2 Confocal microscope images of encapsulated vascular cells within the hydrogel channels after 7 days of culture. (A-C) HAAE cells were injected into the lumen of the channel and attach to the inner surface while (D-F) vSMCs and (G-I) AoAFs are encapsulated within the hydrogel. Cells were Live/Dead stained with calcein AM (green) and ethidium homodimer (red). Scale bar = 200 μm.

4.2.11 Vascular Cell Patterning

vSMCs, AoAFs and HAAEs were stained for 30 min at 37°C with cell tracker green (10μM), red (10μM) and deep red (1μM), respectively. vSMCs and AoAFs were dispersed (2 X 10^6 cells/mL) in HA-Tz (2 wt% PBS) baths separately. vSMC bath (250 μL) was added to the well of the PDMS chamber. The initial channel wall was formed as described above for 5 min with a crosslinking solution of VPM-bisTCO (4.1 mM) and RGD-TCO (0.8 mM). The bath was removed and replaced with the AoAF bath after replenishing the crosslinker in the lumen of the channel via perfusion and incubated for 30 min while rotating the chamber clockwise. The bath was removed and replaced with fresh media. HAAEs dispersed in fresh media (8 X 10^6 cells/mL) were perfused into the channel (50 μL) and rotated overnight at 37°C. Channels were imaged after 1 day of culture using a Zeiss 710 NLO confocal microscope with a 5X objective.

4.3 Results and Discussion

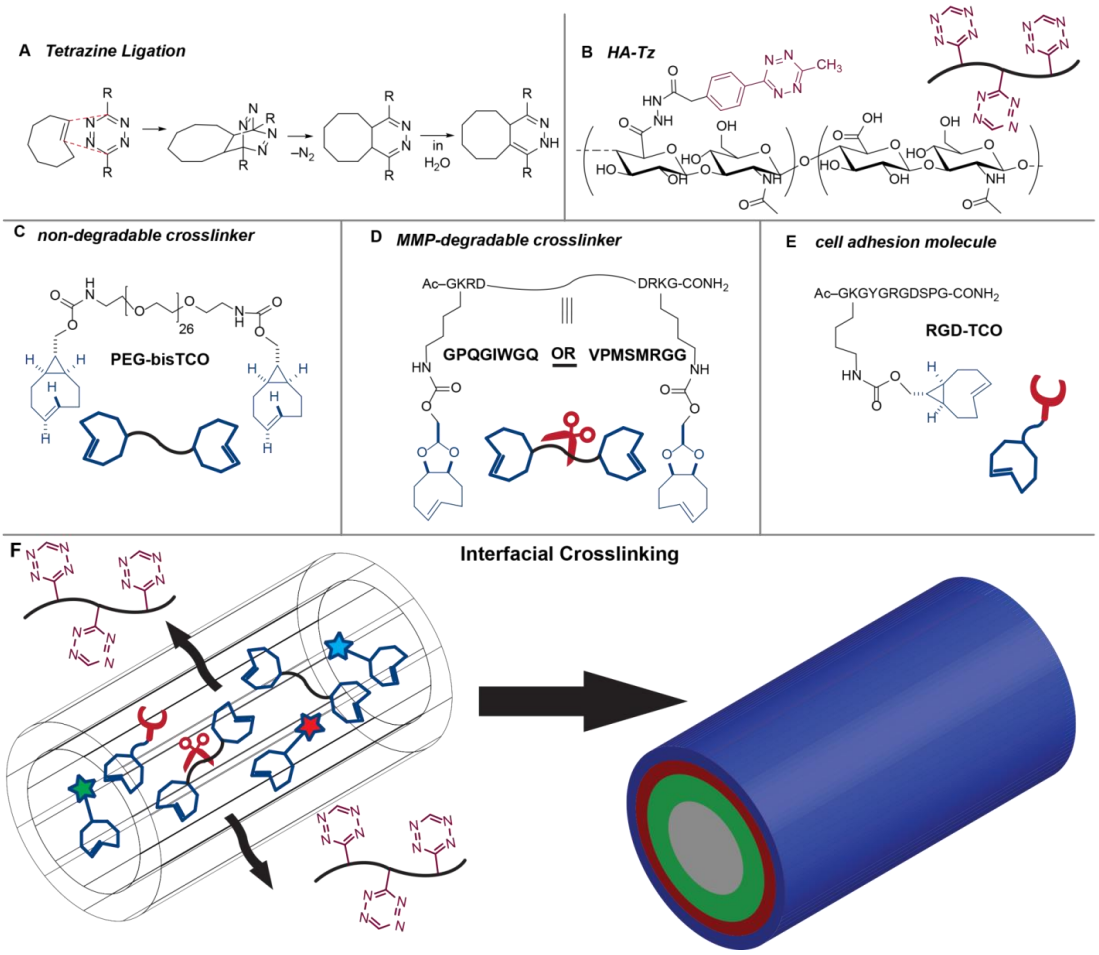

Figure 4.3 Synthetic toolbox used for hydrogel channel formation and patterning. (A) Tetrazine-TCO ligation mechanism. Hydrogel building blocks including (B) Tetrazine-modified Hyaluronic Acid (HA-Tz), bisTCO crosslinkers either (C) non-degradable (PEG-bisTCO) or (D) MMP-degradable (GIW-bisTCO and VPM-bisTCO) and (E) cell adhesive peptide conjugate (RGD-TCO). (F) Spatially patterned hydrogel channels are prepared via interfacial crosslinking by perfusion of TCO conjugated molecules into the lumen of the channel with subsequent diffusion through the channel wall to create further crosslinking at the gel-liquid interface.

Hydrogel precursors for the interfacial crosslinking were synthesized as shown in Figure 4.3. Hyaluronic acid, a non-sulfated glycosaminoglycan which is found in the extracellular matrix (ECM)[23] surrounding vascular cells, was functionalized with tetrazine (HA-Tz) via carbodiimide coupling with hydrazide functionalized tetrazine (Figure 4.1B). Quantification by UV-Vis in agreement with H^1NMR shows 18.6% tetrazine incorporation onto the HA backbone. To crosslink the HA-Tz, bifunctional TCO crosslinkers were synthesized. Poly(ethylene glycol) (PEG) diamine was conjugated with TCO (PEG-bisTCO) to serve as a non-degradable crosslinker (Figure 4.1C). Matrix metalloproteinase (MMP) sensitive peptide sequences VPMSMRGG (VPM) and GPQGIWGQ (GIW) were synthesized using solid state peptide synthesis with flanking GKRD groups. Aspartic acid and arginine groups were used to introduce charged groups to increase hydrophilicity while lysine was used for covalent conjugation of TCO to form bifunctional crosslinkers: VPM-bisTCO and GIW-bisTCO (Figure 4.3D). VPM is enzymatically degradable MMP-1, 2, 3, 7, 9 and MT1-MMP[24,25] with the cleavage site between serine and methionine (VPMS↓MRGG) while GIW can be degraded by MMP-1, 2, 3, 8 and 9[24,26] with a cleavage site between glycine and isoleucine (GPQG↓IWGQ). To introduce cell-adhesive sites into the synthetic matrix, TCO was conjugated to a peptide sequence isolated from fibronectin, GKGYGRGDSPG (RGD), to form a monofunctional linker RGD-TCO[18] (Figure 4.3E).

Covalently crosslinked hydrogel channels were fabricated via a syringe injection of bisTCO crosslinkers into a reservoir of HA-Tz while moving through a custom-made Poly(dimethylsiloxane) (PDMS) chamber in a unidirectional manner (Figure 4.1F). The rapid nature of tetrazine ligation is displayed when the HA-Tz and bisTCO molecules are introduced. Tz-$NHNH_2$ was shown to react with s-TCO and d-TCO with second order rate constants, k_2, of 6.70×10^4 $M^{-1}s^{-1}$ and 9.94×10^3 $M^{-1}s^{-1}$, respectively. At the interface where HA-Tz and bisTCO meet, an instantaneous crosslinked channel wall is generated following the path of the syringe needle. The smaller bisTCO molecules diffuse through the crosslinked wall and react with HA-Tz at the gel-liquid interface, growing the crosslinked channel wall outward radially, until completely exhausted.

To measure the mechanical properties of the hydrogel channels, the channels were allowed to crosslink for 5 min following the initial channel wall formation. To ensure a complete channel formation, ~1 mL of phosphate buffered saline (PBS) (Corning Cellgro) with 1 mL of India ink (Super Black™), used for contrast, was perfused through the channel. The surrounding HA-Tz liquid interface (outside of the channel) was maintained to help support the weight of the channel (buoyancy) and to maintain a hydrated environment. Once complete fluid communication was established and no ruptures in the channel were observed the chamber outlet was plugged. This configuration established the reference state of the hydrogel channel. To mechanically characterize the hydrogel channels, a pressure-dilation assay was conducted. A schematic of this experiment is shown in Figure 4.4A. A screw-driven

head tank was incremented upward to vary the internal pressure within the tube; each 2.54 mm step corresponded to ~25 Pa of pressure. Pressure-induced changes in channel diameter were tracked using a digital camera with a calibrated magnifier (Dino-Lite AM7915MZTL). A custom edge-detection code was written in MatLab® to identify the channel boundaries and determine the mean diameter for each tube at each pressure condition; the analysis was limited to central 30% of the channel to eliminate potential effects from the fixture boundaries as displayed in Figure 4.4B.

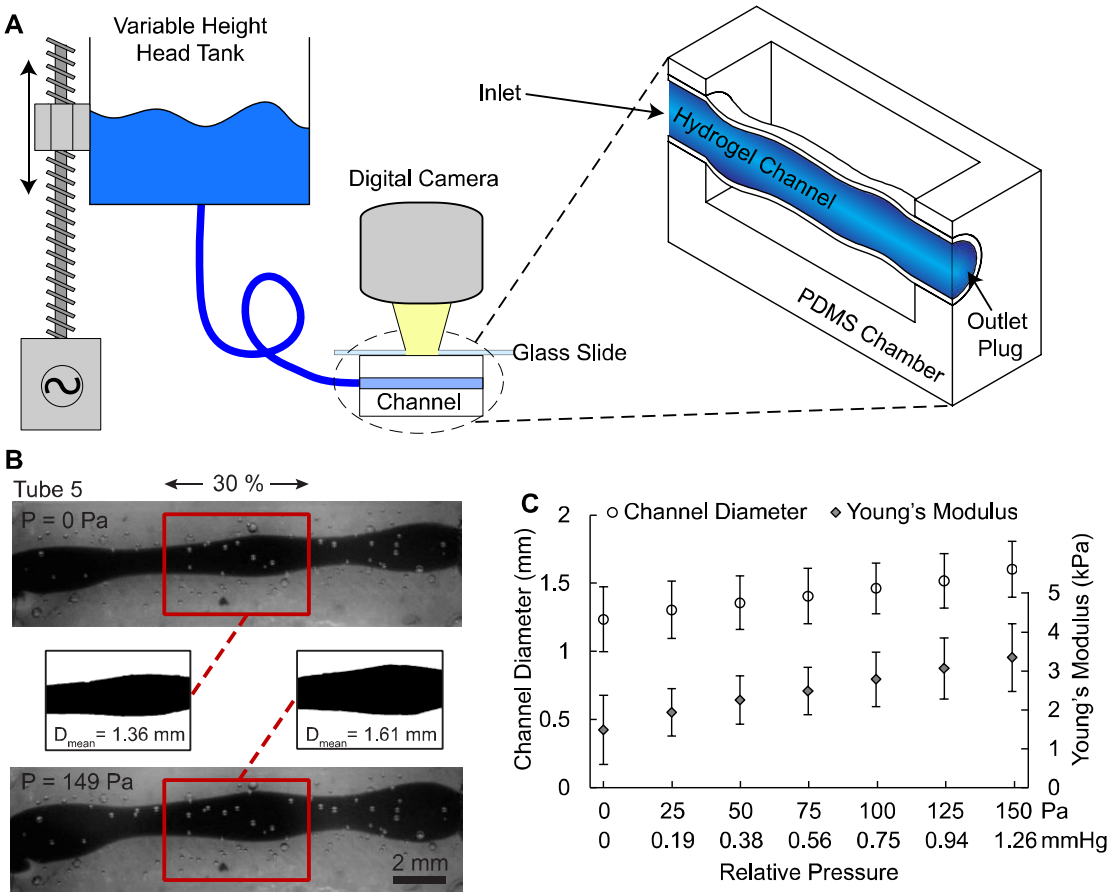

Figure 4.4 Mechanical properties of hydrogel channels. (A) Schematic for pressure-dilation experiments on hydrogel channels. The head tank is driven by a linear actuator in 2.54 mm increments. FEP tubing connects the head tank to one end of the PDMS chamber while the outlet is plugged. The chamber well is filled with HA-Tz and topped with a glass slide to prevent distortion effects from the fluid meniscus. A calibrated Dino-Lite camera is positioned over top of the channel to capture images of channel dilation during step changes in head pressure. (B) Images of hydrogel channels captured before and after applied pressure and thresholded areas of central 30% of channels used to quantify Young's modulus. (C) Average channel diameter and Young's modulus as a function of relative pressure over the range of 0-150 Pa. Young's modulus was calculated via best fit (R^2 > 0.99) of a stress-strain model for cylindrical pressure vessels with variable modulus and thickness to experimental data. The error bars represent standard deviation (n = 6).

These results were input into a large strain, thin-walled cylinder model (Poisson's ratio assumed to be 0.5)[27] to quantify Young's modulus. With a constant modulus, the model predicts increasing rates of change in diameter with pressure. The linear and, in some cases, sub-linear dependences of diameter on pressure (Figure 4.4C) suggest that the modulus increased significantly ($p < 0.05$) with strain due to polymer chain alignment. The final constitutive model assumed the modulus increased linearly with strain and produced excellent agreement ($R^2 > 0.99$) between theory and experimental results. Reported moduli represent the mean and standard deviation of the fit over the range of the measurements (n=6). The Young's modulus was found to be 1.5 ± 0.9 kPa to 3.3 ± 0.9 kPa for applied pressures of 0 to 150 Pa. While the reported modulus of native arteries is significantly higher, they have a lot of fibrous support from elastin and collagen fibers contributing to the mechanical properties.[28,29]

The interfacial diffusion-controlled crosslinking via tetrazine ligation can be utilized to form 3D spatial patterns of covalently conjugated molecules without the need for external triggers[30] or templates[31]. To demonstrate this, a hydrogel channel was formed where Clover-TCO[18] (5 μM) was incorporated into the initial bisTCO crosslinking solution. After 5 min, a bisTCO crosslinking solution containing Cy3-TCO (5 μM) was perfused into the channel and incubated for 15 min. Finally a bisTCO crosslinking solution containing Cy5-TCO (5 μM) was perfused into the channel and incubated for 45 min further. As shown in Figure 4.5A-G, the inner most layer is covalently tagged with Clover (Green, 134±14μm) followed by distinct layers

of Cy3 (Red, 75±5μm) and Cy5 (Blue, 57±3μm) with sharp boundaries, displaying the interfacial diffusion controlled nature of the crosslinking to allow for the spatial patterning of TCO conjugated molecules and proteins.

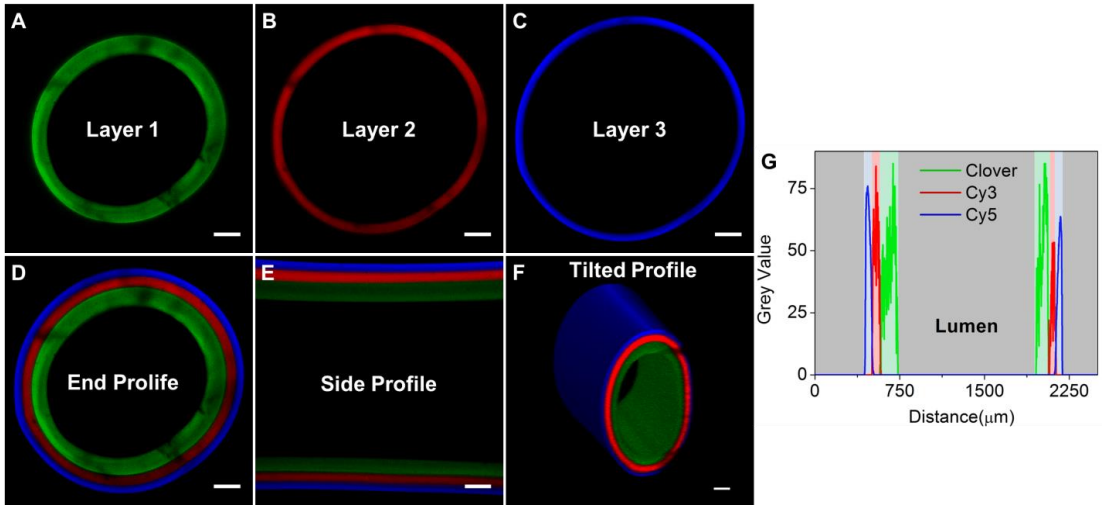

Figure 4.5 Covalent patterning of TCO conjugated fluorophores. (A) The initial wall layer is formed with a crosslinking solution containing Clover-TCO (Green) followed by solutions of (B) Cy3-TCO (red) and (C) Cy5-TCO (blue). The formed channel is presented as a (D) end profile, (E) side profile and (F) tilted profile based on confocal z-stacks. (G) The gray value of the three layers. Scale bar = 200 μm.

To further demonstrate the utility of the interfacial crosslinking in modulating the 3D microenvironment, NIH3T3 fibroblasts transfected with green fluorescent protein (GFP) were dispersed in the HA-Tz reservoir. The channel wall was initially formed with a bioinert crosslinking solution (PEG-bisTCO) along with Alexa-TCO[16] (2 μM) for 5 min. Next, a bioactive crosslinking solution (GIW-bisTCO and RGD-

TCO) was perfused into the lumen of the channel and incubated for 15 min. Finally, the initial bioinert crosslinking solution was perfused back into the lumen of the channel and incubated for 45 min. This formulation leads to the construction of a bioinert-bioactive-bioinert tri-layer structure within the hydrogel channel wall in the radial direction as depicted in Figure 4.6C. As shown in Figure 4.6A, fibroblasts encapsulated in the bioinert (blue) regions show decreased viability and remain round after 7 days of culture. The fibroblasts in the bioactive region, where cells are able to attach to their matrix through integrins and degrade it through secretion of MMPs, show higher viability and start to adopt a spindle-like morphology. After 28 days of culture (Figure 4.6B), the bioinert regions are now vacant of cells, likely due to cell migration or apoptosis while cells in the bioactive region proliferated and made cell-cell connections to form a cell-sheet. The ability to attach and break down their matrix is a vital feature of functioning cells which has shown to aide in proliferation and migration.[32,33]

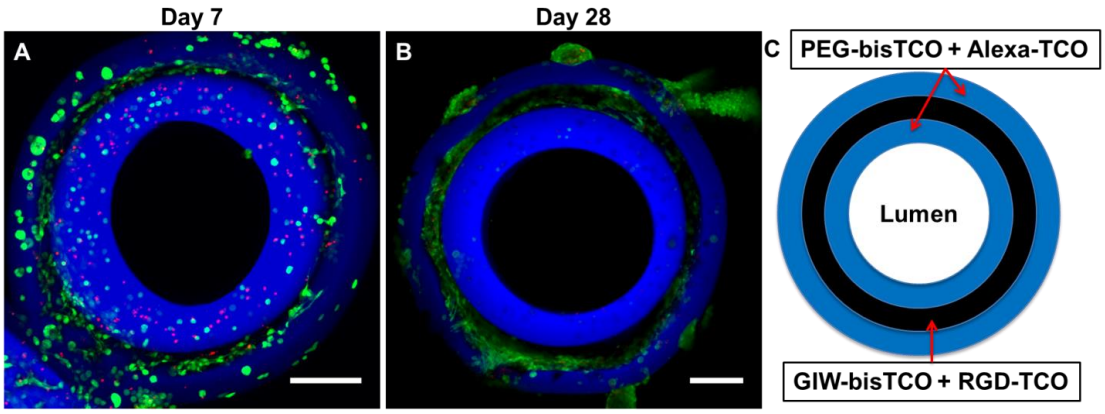

Figure 4.6 NIH3T3 fibroblast response to bioactive and blank patterened regions after (A) 7 days and (B) 28 days of culture. (C) The hydrogel channel was formed with inner and outer layers (blue) of PEG-bisTCO and Alexa-TCO while the middle (black) region is crosslinked with GIW-bisTCO and RGD-TCO. NIH3T3 were transfected with green fluorescent protein (Green) and stained with ethidium homodimer (Red). Scale bar = 200 μm.

The interfacial crosslinking platform allows for not only the spatial patterning of covalently conjugated biomolecules but also of living cells. To demonstrate this, two populations of NIH3T3 fibroblasts were labeled with either cell tracker red or cell tracker green and dispersed in separate HA-Tz reservoirs. The Red cell reservoir was first added to the chamber for the initial formation of the channel wall. After 5 min, the Red cell reservoir was removed and replaced with the Green cell reservoir. The crosslinking solution in the lumen of the channel was replenished via perfusion and the channel was incubated for 15 min. Finally the Green cell reservoir was removed and the initial Red cell reservoir was returned to the chamber well for an additional 45

min incubation period. As shown in Figure 4.7A-C, a three layer pattern of Red-Green-Red tagged fibroblasts are spatially patterned into the channel wall in the sequential order that the cell laden reservoirs were added to the chamber well in.

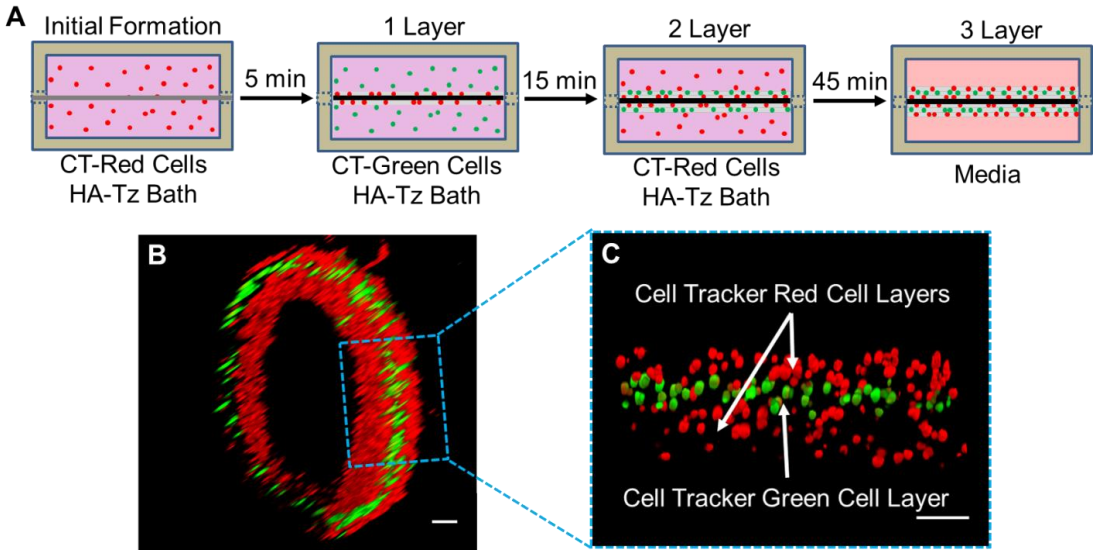

Figure 4.7 Cell Patterning. (A) NIH3T3 fibroblasts stained with Cell Tracker Red (Red) or Cell Tracker Green (Green) were patterned into the hydrogel channel. Sequentially altering of HA-Tz baths containing cell tracker red cells or green cells led to a red-green-red sandwich pattern shown as a confocal z-stack of (B) the channel and (C) the channel wall. Scale bar = 100 μm.

The anatomy of the arterial wall displays multiple layers comprised of three primary cell types in a distinct radial order. Lining the lumen are the vascular endothelial cells which serve as a barrier between blood and the arterial wall and secret cell signaling molecules such as vasodilators and vasoconstrictors.[34] Following

a thin layer of basement membrane are the vascular smooth muscle cells which control blood pressure and flow by contraction and dilation.[35] Last in the outer region are the adventitial fibroblasts which help to maintain the overall structural integrity and remodeling of the wall by depositing ECM proteins.[36] In order to fabricate a viable *in vitro* vascular model, these three cell types must be presented in this distinct radial order found *in vivo*.

The cyto-compatibility of the crosslinking chemistry and hydrogel channels were tested with three vascular cell types. Human abdominal aorta endothelial cells (HAAEs) were perfused into the lumen of the channel after 5 min of crosslinking and incubated overnight at 37°C to allow for the cells to attach to the inner channel wall of the lumen. Initially, the cells were able to attach to the bottom portion of the channel wall due to gravity but over a 7 day period, the cells were able to proliferate and migrate around the lumen to completely wrap around the wall while maintaining high viability (98%)(Figure 4.8A-D). Human aortic adventitial fibroblasts (AoAFs) and aortic vascular smooth muscle cells (vSMCs) were, separately, dispersed in HA-Tz reservoirs and subsequently encapsulated into the hydrogel channel wall during crosslinking for 5 min. vSMCs were crosslinked into the channel wall with VPM-bisTCO as it has been shown to degrade faster with SMCs.[37] Initially, the cells in both cases were round and dispersed, but a change in their morphological features to an elongated phenotype over 7 days of culture (Figure 4.8E-L) was observed while maintaining high viability of 96% and 92% for the vSMCs and AoAFs, respectively. In all three experiments, the cells demonstrated the ability to attach to the synthetic

matrix and alter their morphology (Figure 4.8D,H,L) with a spread cytoplasm along with high viability which are signs of a properly functioning cell.[38]

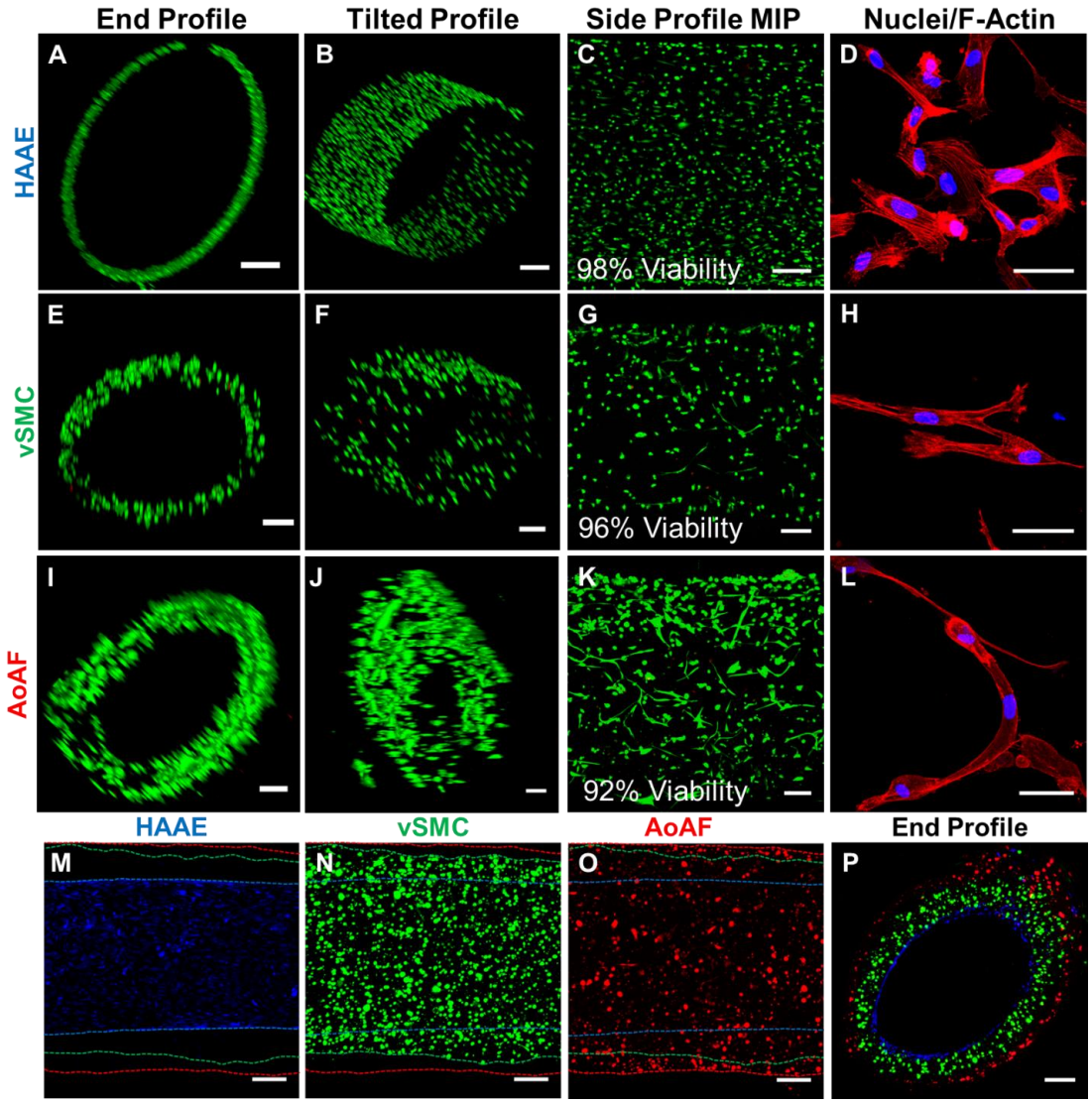

Figure 4.8 Vascular cell encapsulation and patterning. Vascular (A-D) endothelial (HAAE) were cultured on the inner lumen while (E-H) smooth muscle (vSMC) and (I-L) fibroblast (AoAF) cells were 3D encapsulated within the channel wall for 7 days. Cells were stained with (A-C,E-G,I-K) calcein AM (green) and ethidium homodimer (red) or (D,H,L) fixed and stained with DAPI (blue) and phalloidin (red). (M-P) The three cell types were stained with cell trackers and patterned into the channel with (M) the endothelial cells (blue) attached to the inner wall, (N) the smooth muscle cells (green) in the first layer of the wall and (O) the fibroblasts (red) in the outer layer of the wall. (P) The cells are shown in an end profile in their anatomical order. (A-C,E-G,I-K,M-P) Scale bar = 200 μm. (E,H,L) Scale bar = 50 μm.

Finally the HAAEs, vSMCs, and AoAFs were spatially patterned into the hydrogel channel in the anatomical order found *in vivo*(Figure 8M-P). vSMCs, tagged with cell tracker green (green), were dispersed in the HA-Tz reservoir and crosslinked into the initial channel wall for a 5 min incubation period. The vSMC reservoir was removed and replaced with a HA-Tz reservoir containing dispersed AoAFs tagged with cell tracker red (red). The lumen of the channel was replenished with more crosslinker and the channel wall was allowed to crosslink further for 30 min while rotating to prevent settling of the cells. Following, the HA-Tz reservoir was removed and replaced with fresh media. HAAEs tagged with cell tracker deep red (blue) were perfused into the lumen of the channel and allowed to attach to the inner channel wall overnight at 37°C while rotating to ensure a homogenous cell layer. The hydrogel channels were then assessed for their specific presentation of the tagged cells. As shown in Figure 4.6M-P, the cells are layered in the correct order according to the experimental setup and to their anatomical order found *in vivo*. As shown in side profile images in Figure 4.8M-O, the cells are dispersed and show an increase in diameter from the HAAEs on the channel wall(Figure 4.8M) to the vSMCs (Figure 4.6N) finally to the AoAFs on the outer layer of the channel(Figure 4.8O). This offers an elegant strategy to spatially patterning all three cell types without the need for multiple gelation steps and concentric needles[39].

4.4 Conclusions

In summary, I have demonstrated the utility of tetrazine ligation as a powerful tool for fabrication of liquid-filled hydrogel channels via interfacial diffusion-controlled crosslinking. The hydrogel channels can be spatially patterned with covalently conjugated molecules, peptides and proteins to modulate the 3D local microenvironment. The hydrogel channels can also be spatially patterned with encapsulated cells of different populations in distinct and separate layers of desired order. The ability and relative ease to spatially pattern both biochemical cues and mulitple cell populations into the hydrogel channel makes this an ideal platform for the fabrication of *in vitro* vasculature models.

4.5 Spectral Data for Chapter 4

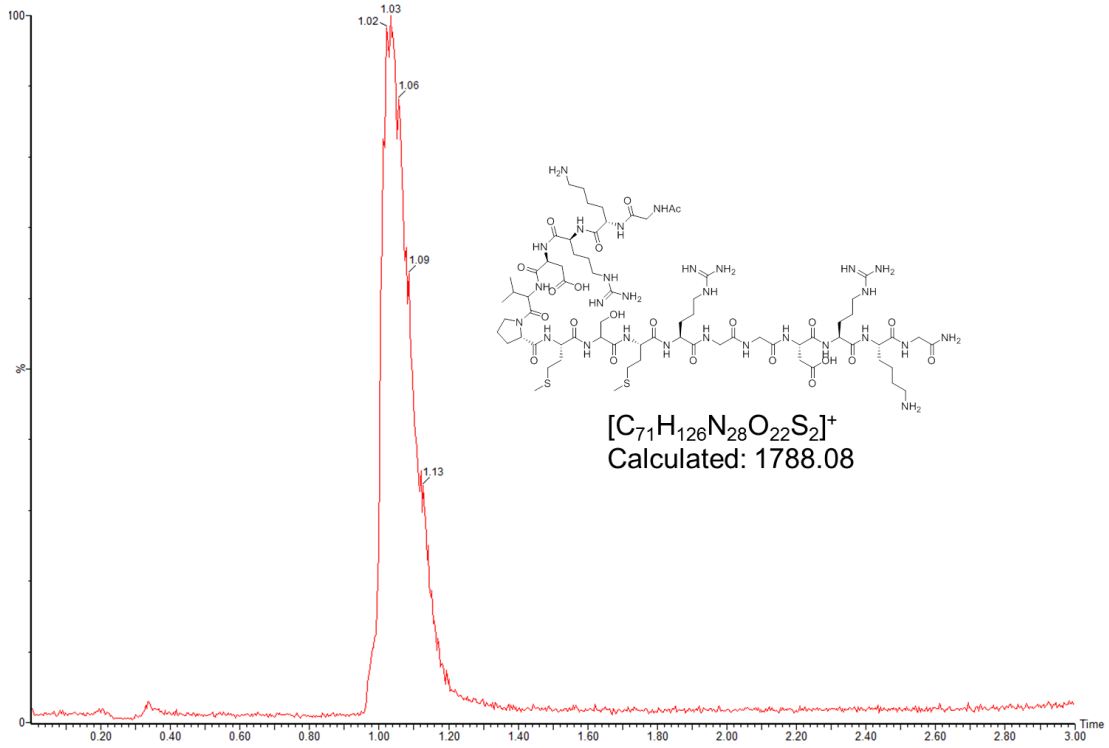

Figure 4.9 UPLC-MS spectrum of VPM peptide.

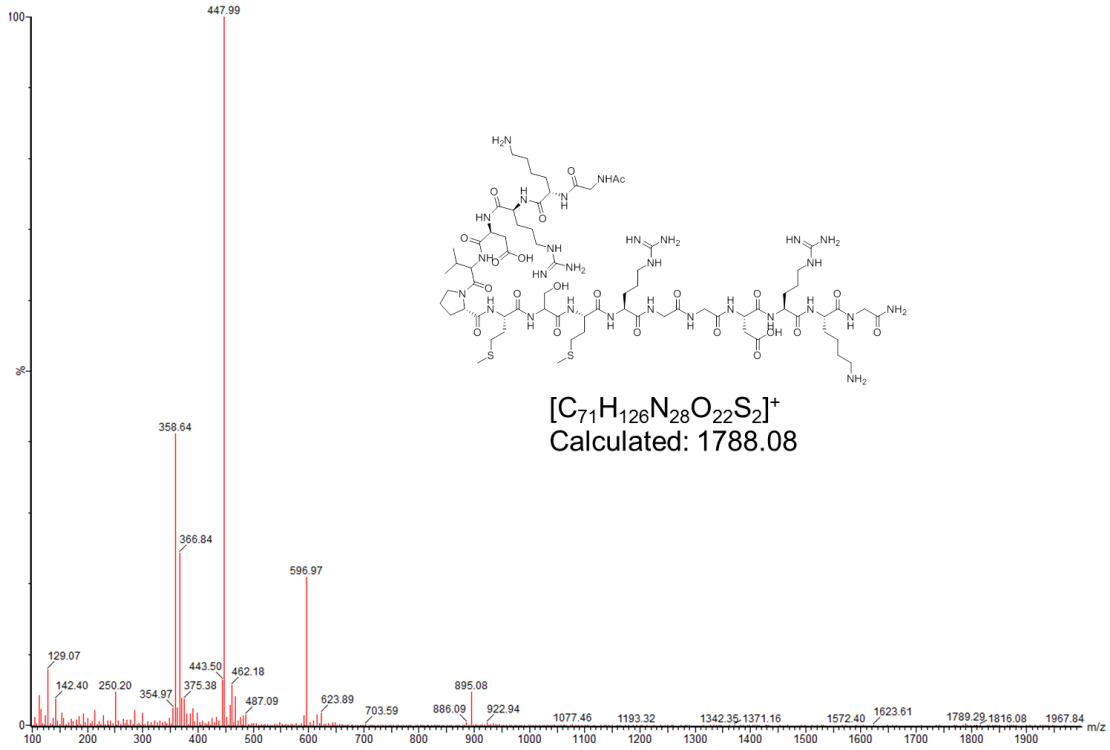

Figure 4.10 UPLC-MS spectrum of VPM peptide.

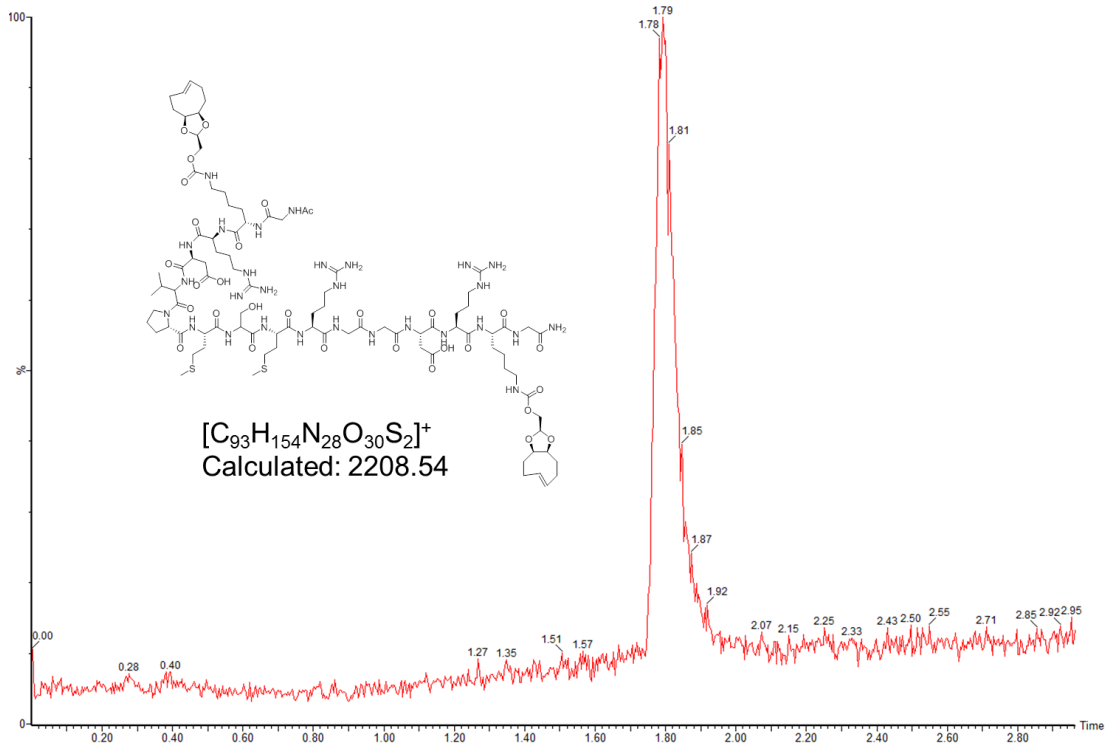

Figure 4.11 UPLC-MS spectrum of VPM-bisTCO.

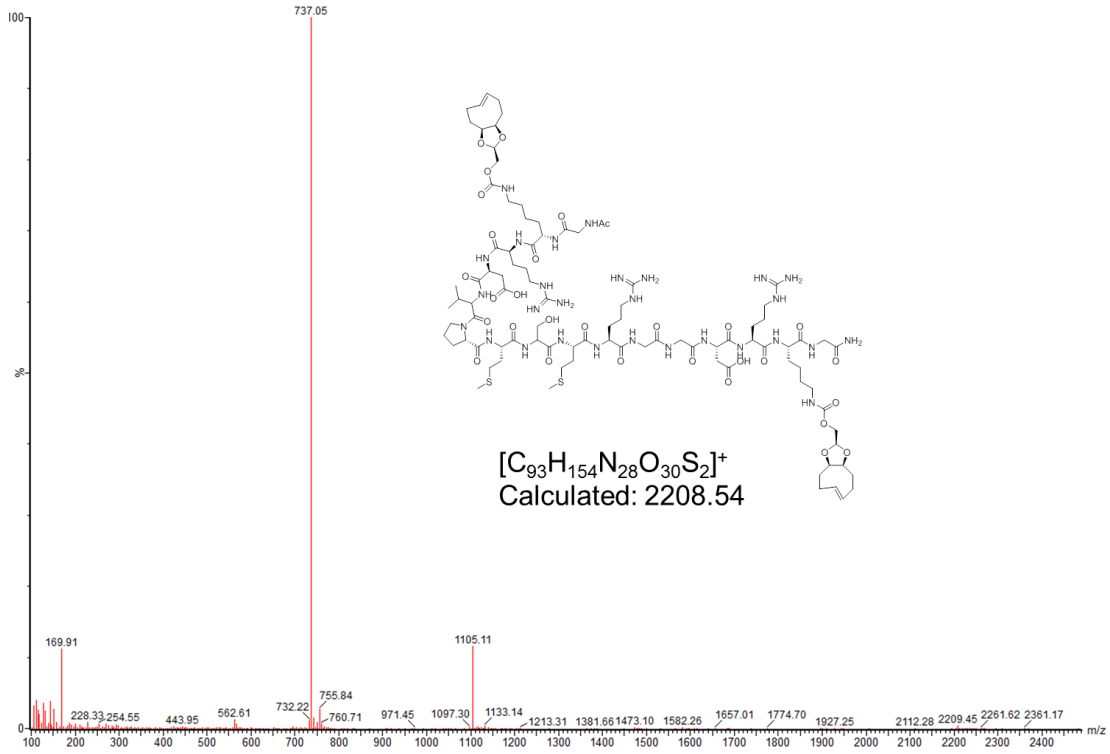

Figure 4.12 UPLC-MS spectrum of VPM-bisTCO.

REFERENCES

[1] American Heart Association. Heart Disease and Stroke Statistics, **2017**.

[2] G. M. FitzGibbon, H. P. Kafka, A. J. Leach, W. J. Keon, G. D. Hooper, J. R. Burton, J. Am. Coll. Cardiol. **1996**, 28, 616.

[3] A. Hasan, A. Paul, N. E. Vrana, X. Zhao, A. Memic, Y. S. Hwang, M. R. Dokmeci, A. Khademhosseini, Biomaterials **2014**, 35, 7308.

[4] L. L. Y. Chiu, M. Radisic, Biomaterials **2010**, 31, 226.

[5] K. Kinoshita, M. Iwase, M. Yamada, Y. Yajima, M. Seki, Biotechnol. J. **2016**, 11, 1415.

[6] K. M. Chrobak, D. R. Potter, J. Tien, Microvasc. Res. **2006**, 71, 185.

[7] M. P. Cuchiara, A. C. B. Allen, T. M. Chen, J. S. Miller, J. L. West, Biomaterials **2010**, 31, 5491.

[8] E. E. Antoine, F. P. Cornat, A. I. Barakat, J. R. Soc. Interface **2016**, 13, 20160834.

[9] N. Sadr, M. Zhu, T. Osaki, T. Kakegawa, Y. Yang, M. Moretti, J. Fukuda, A. Khademhosseini, Biomaterials **2011**, 32, 7479.

[10] H. Yoshida, M. Matsusaki, M. Akashi, Adv. Funct. Mater. **2013**, 23, 1736.

[11] J. S. Miller, K. R. Stevens, M. T. Yang, B. M. Baker, D.-H. T. Nguyen, D. M. Cohen, E. Toro, A. A. Chen, P. A. Galie, X. Yu, R. Chaturvedi, S. N. Bhatia, C. S. Chen, Nat. Mater. **2012**, 11, 768.

[12] D. B. Kolesky, K. A. Homan, M. A. Skylar-Scott, J. A. Lewis, Proc. Natl. Acad. Sci. **2016**, 113, 3179.

[13] A. P. Golden, J. Tien, Lab Chip **2007**, 7, 720.

[14] K. A. Heintz, M. E. Bregenzer, J. L. Mantle, K. H. Lee, J. L. West, J. H. Slater, Adv. Healthc. Mater. **2016**, 5, 2153.

[15] C. K. Arakawa, B. A. Badeau, Y. Zheng, C. A. DeForest, Adv. Mater. **2017**, 29, 1.

[16] H. Zhang, K. T. Dicker, X. Xu, X. Jia, J. M. Fox, ACS Macro Lett. **2014**, 3, 727.

[17] A. Darko, S. Wallace, O. Dmitrenko, M. M. Machovina, R. A. Mehl, J. W. Chin, J. M. Fox, Chem. Sci. **2014**, 5, 3770.

[18] H. Zhang, W. S. Trout, S. Liu, G. A. Andrade, D. A. Hudson, S. L. Scinto, K. T. Dicker, Y. Li, N. Lazouski, J. Rosenthal, C. Thorpe, X. Jia, J. M. Fox, J. Am. Chem. Soc. **2016**, 138, 5978.

[19] S. Liu, H. Zhang, R. A. Remy, F. Deng, M. E. Mackay, J. M. Fox, X. Jia, Adv. Mater. **2015**, 27, 2783.

[20] M. T. Taylor, M. L. Blackman, O. Dmitrenko, J. M. Fox, J. Am. Chem. Soc. **2011**, 133, 9646.

[21] H. Zhang, W. S. Trout, S. Liu, G. A. Andrade, D. A. Hudson, S. L. Scinto, K. T. Dicker, Y. Li, N. Lazouski, J. Rosenthal, C. Thorpe, X. Jia, J. M. Fox, J. Am. Chem. Soc. **2016**, 138, 5978.

[22] X. Xu, L. a Gurski, C. Zhang, D. a Harrington, M. C. Farach-Carson, X. Jia, Biomaterials **2012**, 33, 9049.

[23] K. T. Dicker, L. A. Gurski, S. Pradhan-Bhatt, R. L. Witt, M. C. Farach-Carson, X. Jia, Acta Biomater. **2014**, 10, 1558.

[24] J. Patterson, J. A. Hubbell, Biomaterials **2010**, 31, 7836.

[25] B. E. Turk, L. L. Huang, E. T. Piro, L. C. Cantley, Nat. Biotechnol. **2001**, 19, 661.

[26] H. Nagase, G. B. Fields, Biopolymers **1996**, 40, 399.

[27] N. Latifi, A. K. Miri, L. Mongeau, J. Mech. Behav. Biomed. Mater. **2014**, 39, 366.

[28] K. Hayashi, J. Biomech. … **1993**, 115, 481.

[29] A. Hasan, K. Ragaert, W. Swieszkowski, Š. Selimović, A. Paul, G. Camci-Unal, M. R. K. Mofrad, A. Khademhosseini, J. Biomech. **2014**, 47, 1949.

[30] C. A. DeForest, K. S. Anseth, Nat. Chem. **2011**, 3, 925.

[31] S. Khetan, J. A. Burdick, Biomaterials **2010**, 31, 8228.

[32] M. P. Lutolf, G. P. Raeber, A. H. Zisch, N. Tirelli, J. A. Hubbell, Adv. Mater. **2003**, 15, 888.

[33] C. R. Nuttelman, D. J. Mortisen, S. M. Henry, K. S. Anseth, J. Biomed. Mater. Res. **2001**, 57, 217.

[34] S. Chlen, S. Li, J. Shyy, Hypertension **1998**, 31, 162.

[35] J. P. Stegemann, H. Hong, R. M. Nerem, J Appl Physiol **2005**, 98, 2321.

[36] S. Sartore, A. Chiavegato, E. Faggin, R. Franch, M. Puato, S. Ausoni, P. Pauletto, Circ. Res. **2001**, 89, 1111.

[37] L. Lin, R. E. Marchant, J. Zhu, K. Kottke-Marchant, Acta Biomater. **2014**, 10, 5106.

[38] K. G. Robinson, T. Nie, A. D. Baldwin, E. C. Yang, K. L. Kiick, R. E. Akins, J. Biomed. Mater. Res. - Part A **2012**, 100 A, 1356.

[39] A. Hasan, A. Paul, A. Memic, A. Khademhosseini, Biomed. Microdevices 2**015**, 17, 1.

Chapter 5

CONCLUSIONS AND FUTURE DIRECTIONS

5.1 Conclusions and Significance

Tetrazine ligation is an ultrafast bioorthogonal reaction with second order rates exceeding 10^6 M^{-1} s^{-1}. It was previously shown to be useful for cell labeling at ultra-dilute concentrations without cytotoxicity but had not previously been applied for the fabrication of synthetic hydrogel matrices. The overall goal of this dissertation work was to fabricate complex hydrogel constructs utilizing tetrazine ligation for the development of *in vitro* engineered tissue models.

In the first part of this dissertation, tetrazine ligation was first explored for its utility in the fabrication of synthetic hydrogels. Tetrazine was conjugated to hyaluronic acid to make up the backbone of the hydrogel matrix while TCO was conjugated to PEG to make a bisTCO crosslinker. It was shown that when a droplet of HA-Tz was introduced to a bath of bisTCO, instantaneous interfacial crosslinking occurs. Over time, the smaller bisTCO molecules diffuse across the crosslinked region and react with HA-Tz at the gel-liquid interface until all tetrazine sites have been consumed. The interfacial diffusion controlled nature was utilized to show the formation of 3D ring patterns and radial gradients of fluorophores. The non-toxic nature of the tetrazine ligation and the hydrogel in general were tested with prostate cancer cells showing that the cells maintain high viability and proliferate readily. Simultaneously, tetrazine ligation was utilized to form liquid filled hydrogel channels. By inversing the order of addition, hydrogel channels were formed and the channel

wall formation was monitored by the covalent conjugation of Alexa-TCO into the channel walls. The tetrazine ligation was shown to hold a high potential for the construction of complex constructions for *in vitro* tissue models.

Subsequently, use of interfacial bioorthogonal chemistry for the preparation of spatially patterned hydrogels with distinct biochemical and biomechanical microenvironments was demonstrated. Synthesized enzymatically degradable (GIW-bisTCO) and non-degradable (PEG-bisTCO) were utilized along with mono-functional RGD-TCO for cell adhesion and PEG-TCO for modulate the stiffness. Through temporally controlled introduction these TCO conjugates during the crosslinking process, the enzymatic degradability, cell adhesivity, and mechanical properties of the synthetic microenvironment can be tuned with spatial precision. Human mesenchymal stem cells were encapsulated in hydrogels with core-shell structures and were able to respond to patterned regions. hMSCs in degradable and adhesive regions were able to degrade their matrix to adopt a spread morphology while those in the blank, non-degradable region remained round with lower viability over time. The bioorthogonal platform allows straightforward patterning of cellular microenvironments to trigger desired responses or to promote the formation of multilayer tissues.

Finally, the preparation of hydrogel channels with distinct biochemical and cell presentation was demonstrated. Hydrogel channels were fabricated with district 3D patterns by the time dependent addition of TCO conjugated fluorophores into the lumen of the channel with subsequent diffusion of the molecules through the channel wall to grow the wall thickness further. Encapsulated fibroblasts responded to regions of degradable (GIW-bisTCO) and adhesive (RGD-TCO) where the cells adopted a

spindle-like morphology and proliferated readily while cells in a blank (PEG-bisTCO) remained round. Additionally, alternating the cell laden HA-Tz bath during the channel wall formation enabled for 3D encapsulation of different cell populations within the channel wall in anatomically relevant spatial patterns. Vascular endothelial cells, smooth muscle cells and adventitial fibroblasts were patterned into the distinct radial order found *in vivo* with high viability. This novel approach for the fabrication of hydrogel channels has high potential for *in vitro* vasculature models.

The significance of this work is the development of a novel method for hydrogel patterning. Previous methods have included the use of photomasks with UV-light or two-photon with multiple reactions, enzyme mediated redox, and other lithographic approaches. These methods hold utility and advantages in precision and sophisticated designs but are not without their limitations. There are potential damaging effects of the use of UV light along with the concentration of the photoinitiator(s). There are also limitations in light penetration depth within thick hydrogels. Approaches using redox generate cytotoxic hydrogen peroxide while others require the use of laser guided systems with confocal to generate patterns which are both costly and time-consuming. My approach creates patterns in a cytocompatible way where the concentrations in the crosslinking bath are reflected in the bulk hydrogel. The patterns can be made within thick hydrogels only relying on diffusion of the TCO-conjugates with subsequent interfacial crosslinking. The platform holds potential for high throughput applications due to its relative ease of pattern generation.

5.2 Future Directions

The work described in this thesis was the utilization of tetrazine ligation for the fabrication of hydrogel biomaterials. The ability to fabricate spatially patterned

hydrogel matrices without the necessity of external triggers or template is attractive for the fabrication of *in vitro* models for studying diseased tissue. These established platforms will serve a number of future application and possible future directions are described below.

5.2.1 Incorporation of Triggerable Dihydrotetrazine (DHT)

Fabrication of the hydrogels using tetrazine ligation relies on interfacial crosslinking with the reaction between the tetrazine and TCO molecules occurring at the gel-liquid interface. Once the hydrogel is finished crosslinking, no further modification can currently be done to the hydrogels outside of remodeling done by the encapsulated cells. Recent efforts have shown the ability to pattern hydrogels after crosslinking through photolabile groups such as oNB[1] or the use of multiple reactions.[2] While my platform holds advantages of not having to use these triggers, I was not yet to show the ability to pattern hydrogels with time (4D).

One method which has started to be explored in the last few years in the Fox and Jia groups is the use of dihydrotetrazine (DHT). DHT is an unreactive intermediate in the synthesis of tetrazine. Once the DHT molecule is introduced to an oxidizer, whether it is chemical such as HRP or light induced with a photosensitizer, it becomes reactive to participate in iEDDA with dienophiles such as TCO. The Fox and Jia groups have shown its utility in the synthesis and modification of synthetic fibers[3] while the Forsythe Group has shown the ability to fabricate hydrogels[4] with norbornene functionalized PEG. Initial efforts to fabricate DHT hydrogels have been fruitless, potentially due to an unforeseen issue with singlet oxygen from the methylene blue photosensitizer.

The introduction of DHT into both the hydrogel spheres and channels would be a valuable tool for the fabrication of *in vitro* models and biomaterials. One direction would be to trigger gelation with near-IR light which would be favorable over forming hydrogels via 365 nm UV light used in thiol-ene reactions due to potential cytotoxicity. Another direction would be to pattern the DHT molecules into the hydrogel matrix. After crosslinking, the DHT groups could be oxidized to reactive tetrazines to enable further patterning of the hydrogel. By doing this, time can be used to help mimic the constant remodeling of the ECM by the cells.[5] This would also give the option to introduce signaling molecules or growth factors at the desired time point. In the case of salivary gland tissue engineering, temporal presentation of FGF10 and FGF7 to promote elongation and budding, respectively, of the salivary human stem/progenitor cells (hS/PCs) could aide in the assembly of functional tissue.[6] Another option could be to increase hydrogel stiffness through further crosslinking to study stiffening of diseased tissue.

5.2.2 Gradient Patterning

Shown in Chapter 2 as a proof of concept with Alexa-TCO, I was able to generate radial layers and gradients within the hydrogel spheres.[7] I explored patterning my hydrogels in layers further in Chapter 3 and Chapter 4 by modulating stiffness, degradability and adhesiveness but further studies on gradients within the hydrogels should still be conducted. The same parameters could be applied to the gradients of stiffness, degradability and adhesiveness. In addition, gradients of growth factors, proteins, or other signaling molecules could be used. Gradients of stiffness could be used to study durotaxis[8,9] with hMSCs which I have cultured in Chapter 3. Additionally, chemotaxis, morphogenesis, migration, wound healing, and

mechanotransduction could be studied as a result of presentation of various gradients within the hydrogel microenvironment.

The proposed direction would be similar to Chapter 2 where a syringe pump was used in continuously add the Alexa-TCO into the crosslinking solution. In the case of the stiffness gradient, mono-TCO could be continuously added into the bath to create a crosslinking density gradient with the shell being the stiffest and the core being the softest. Fluorescent imaging could be utilized to quantify the gradient but AFM should be used to quantify the radial stiffness gradient. Hydrogel prepared in a cylindrical fashion could have opposing gradients with interfacial crosslinking and diffusion occuring from either end of the cylinder. Additionally, incorporation of DHT molecules will enable gradient formation after the initial hydrogel formation. DHT-TCO could be incorporated into the crosslinking solution in a gradient manner as just described with a syringe pump. Once the DHT molecules get oxidized, the hydrogel could be placed in a bath with any TCO-conjugated molecules, peptides, proteins, or growth factors without having to rely on competing diffusion kinetics of the crosslinker.

Additionally, quantification of conjugated peptides, proteins, and molecules in the swollen equilibrium hydrogel would be of value and interest. Currently, it is assumed that the molar concentration of the molecules in the crosslinking bath is reflected in the resultant hydrogel which may not necessarily be the case. The molecular weight of the molecules used in Chapters 2-4 are all within 1.5 kDa of each other and diffusion is assumed to have equal to similar. The fluorescent conjugation and subsequent confocal imaging that I conducted has shown the qualitative patterns in the hydrogel but a more quantitative approach could be more informative. A

potential method would be to make hydrogels with varying molar percentages of RGD-TCO. Then the hydrogel could be digested and the solution could be assessed for tyrosine concentration which is part of the RGD sequence (GKGYGRGDSPG). Alternatively this could be done with fluorophore conjugated hydrogels and quantify the fluorescence with a plate reader.

5.2.3 Hydrogel Channels for In Vitro Models

The hydrogel channels initially described in Chapter 2 and further in Chapter 4 should serve as a valuable platform for *in vitro* vascular models. At their current state, they lack a few key characteristics which would help to further replicate vasculature. One is the mechanical properties. As described with the pressure dilation assay in Chapter 4, the Young's modulus of the hydrogel channels is approximately 2.5 kPa. While the vascular cells used in the study were shown to maintain high viability and show signs of morphological changes, this is significantly weaker than the arterial wall found *in vivo*. One reason for this is that many vessels found in the body have fibrous support from elastin and collagen. While the fibroblasts and smooth muscle cells will deposit some collagen elastin, respectively, it would be beneficial of the model from an engineering prospective to include fibers into the hydrogel channel during crosslinking as to not rely on the cells. One possible method is to electrospin around a needle of desired diameter.[10] The cylindrical fiber bundle would then be placed in the PDMS chamber across the inlet and outlet so that as the channel wall is formed, the fibers will be crosslinked into the hydrogel channel. If the fibers contain pendent tetrazine groups, they can additionally be covalently crosslinked into the channel. Initial studies could utilize coated PCL fibers as they are widely studied but future investigations could include elastin and collagen-like peptides incorporated into a

synthetic multi-block.[11,12] I believe this should be able to increase the modulus of the hydrogel channels to closer match that of native arteries.

The synthetic channels often have ‘waviness’ to them as reflected in the Pressure-Dilation assay in Chapter 4. This may be due to pressure differences between the HA-Tz reservoir and the injected crosslinking solution as indicated by the repeated curvature. Besides the asthetics perspective, the curvature may result in heterogeneity within the hydrogel as far as mechanical properties and encapsulated cells. This potentially could be remedied by adjusting the injection rate and the speed of the stage.

Another improvement to the current platform should be the incorporation of constant perfusion. Current perfusion in the system was done manually with a syringe or in the case of the pressure dilation, a raised head tank connected to the chamber through FEP tubing. Perfusion with a peristaltic pump would necessary for replicating *in vivo* conditions. For example, the endothelial cells are subjected to fluid shear stress which is integral for normal vessel wall function.[13] The incorporation of perfusion would also be integral to investigating various disease models affecting vasculature including atherosclerosis and intimal hyperplasia. Separately, the model could be easily tuned to investigate other areas of interest including circulating tumor cells (CTCs)[14] or blood-brain barrier (BBB)[15] models.

Finally, further cell biology should be conducted on the vascular cells with the hydrogel channels. In Chapter 4, I investigated the cells for their viability and morphology separately after seven days of culture. Further, I displayed the ability to pattern the cells into their anatomically relevant order confirmed by cell trackers after one day of culture. Culturing the three cell types together for longer culture periods

would be of interest to study their interactions, migration, ECM production, and phenotype. One study could include either long term cell trackers or transfection of fluorescent proteins within the cells in order to study their migration in regards to each other within the hydrogel. Tandem experiments could look at viability, ECM protein production, and cell-cell and cell-matrix interactions.

REFERENCES

[1] A. M. Kloxin, A. M. Kasko, C. N. Salinas, K. S. Anseth, *Science (80-.).* **2009**, *324*, 59.

[2] S. Khetan, J. A. Burdick, *Biomaterials* **2010**, *31*, 8228.

[3] H. Zhang, W. S. Trout, S. Liu, G. A. Andrade, D. A. Hudson, S. L. Scinto, K. T. Dicker, Y. Li, N. Lazouski, J. Rosenthal, C. Thorpe, X. Jia, J. M. Fox, *J. Am. Chem. Soc.* **2016**, *138*, 5978.

[4] V. X. Truong, K. M. Tsang, F. Ercole, J. S. Forsythe, *Chem. Mater.* **2017**, *29*, 3678.

[5] A. M. Hilderbrand, E. M. Ovadia, M. S. Rehmann, P. M. Kharkar, C. Guo, A. M. Kloxin, *Curr Opin Solid State Mater Sci* **2016**, *20*, 212.

[6] H. P. Makarenkova, M. P. Hoffman, A. Beenken, V. Anna, R. Meech, C. Tsau, V. N. Patel, R. A. Lang, M. Mohammadi, *Sci Signal* **2010**, *2*, 1.

[7] H. Zhang, K. T. Dicker, X. Xu, X. Jia, J. M. Fox, *ACS Macro Lett.* **2014**, *3*, 727.

[8] R. Sunyer, V. Conte, J. Escribano, A. Elosegui-Artola, A. Labernadie, L. Valon, D. Navajas, J. M. García-Aznar, J. J. Muñoz, P. Roca-Cusachs, X. T. Sunyer, *Science (80-.).* **2016**, *353*, 1157.

[9] L. G. Vincent, Y. S. Choi, B. Alonso-latorre, J. C. Álamo, A. J. Engler, *Biotechnol J.* **2014**, *8*, 472.

[10] M. B. Browning, D. Dempsey, V. Guiza, S. Becerra, J. Rivera, B. Russell, M. Höök, F. Clubb, M. Miller, T. Fossum, J. F. Dong, A. L. Bergeron, M. Hahn, E. Cosgriff-Hernandez, *Acta Biomater.* **2012**, *8*, 1010.

[11] S. E. Grieshaber, A. J. E. Farran, S. Lin-gibson, K. L. Kiick, X. Jia, **2009**, 2532.

[12] S. Liu, H. Zhang, R. A. Remy, F. Deng, M. E. Mackay, J. M. Fox, X. Jia, *Adv. Mater.* **2015**, *27*, 2783.

[13] C. F. Dewey, S. R. Bussolari, M. A. Gimbrone, P. F. Davies, *J. Biomech. Eng.* **1981**, *103*, 177.

[14] M. G. Krebs, J.-M. Hou, T. H. Ward, F. H. Blackhall, C. Dive, *Ther. Adv. Med. Oncol.* **2010**, *2*, 351.

[15] J. Bicker, G. Alves, A. Fortuna, A. Falcão, *Eur. J. Pharm. Biopharm.* **2014**, *87*, 409.

Appendix A

COPYRIGHT PERMISSION FOR REPRINT OF PUBLISHED ARTICLES

Chapter 1

1.1 Modular and Orthogonal Synthesis of Hybrid Polymers and Networks

Modular and orthogonal synthesis of hybrid polymers and networks

S. Liu, K. T. Dicker and X. Jia, *Chem. Commun.*, 2015, **51**, 5218

DOI: 10.1039/C4CC09568E

1.2 Hyaluronic Acid

Reproduced in its entirety from:

Title: Hyaluronan: A simple polysaccharide with diverse biological functions

Author: Kevin T. Dicker,Lisa A. Gurski,Swati Pradhan-Bhatt,Robert L. Witt,Mary C. Farach-Carson,Xinqiao Jia

Publication: Acta Biomaterialia

Publisher: Elsevier

Date: April 2014

Figure 1.2A-B

License Number: 4262630327145

License date: Jan 05, 2018

Licensed Content Publisher: Elsevier

Licensed Content Publication: Seminars in Cancer Biology

Licensed Content Title: Altered hyaluronan biosynthesis in cancer progression

Licensed Content Author: Naoki Itano,Koji Kimata

Licensed Content Date: Aug 1, 2008

Licensed Content Volume: 18

Licensed Content Issue: 4

Licensed Content Pages: 7

Start Page: 268

End Page: 274

Type of Use: reuse in a thesis/dissertation

Intended publisher of new work: other

Portion: figures/tables/illustrations

Number of figures/tables/illustrations: 1

Format: both print and electronic

Are you the author of this Elsevier article? No

Will you be translating? No

Original figure numbers: Figure 1

Title of your thesis/dissertation: Interfacial Bioorthogonal Crosslinking for the Fabrication of

Functional Hydrogels

Expected completion date: Jan 2018

Estimated size (number of pages): 300

Total 0.00 USD

Figure 1.3

License Number: 4262621128560

License date: Jan 05, 2018

Licensed Content Publisher: Elsevier

Licensed Content Publication: Carbohydrate Research

Licensed Content Title: Experimental approaches to hyaluronan structure

Licensed Content Author: Mary K. Cowman,Shiro Matsuoka

Licensed Content Date: Apr 11, 2005

Licensed Content Volume: 340

Licensed Content Issue: 5

Licensed Content Pages: 19

Start Page: 791

End Page: 809

Type of Use: reuse in a thesis/dissertation

Portion: figures/tables/illustrations

Number of figures/tables/illustrations: 1

Format: both print and electronic

Are you the author of this Elsevier article? No

Will you be translating? No

Original figure numbers: Figure 9

Title of your thesis/dissertation: Interfacial Bioorthogonal Crosslinking for the Fabrication of Functional Hydrogels

Expected completion date: Jan 2018

Estimated size (number of pages): 300

Total 0.00 USD

Figure 1.4A

License Number: 4262630612915

License date: Jan 05, 2018

Licensed Content Publisher: John Wiley and Sons

Licensed Content Publication: Journal of Orthopaedic Research

Licensed Content Title: Effect of link protein concentration on articular cartilage proteoglycan aggregation

Licensed Content Author: Lih-Heng Tang,Joseph A. Buckwalter,Lawrence C. Rosenberg

Licensed Content Date: Feb 18, 2005

Licensed Content Pages: 6

Type of use: Dissertation/Thesis

Requestor type: University/Academic

Format: Print and electronic

Portion: Figure/table

Number of figures/tables: 1

Original Wiley figure/table number(s): Figure 1

Will you be translating? No

Title of your thesis /dissertation: Interfacial Bioorthogonal Crosslinking for the Fabrication of

Functional Hydrogels

Expected completion date: Jan 2018

Expected size (number of pages): 300

Total 0.00 USD

Figure 1.5A

License Number: 4262621326767

License date: Jan 05, 2018

Licensed Content Publisher: Elsevier

Licensed Content Publication: The American Journal of Pathology

Licensed Content Title: Mononuclear Leukocytes Bind to Specific Hyaluronan Structures on
Colon Mucosal Smooth Muscle Cells Treated with Polyinosinic Acid: Polycytidylic Acid Inter-α-Trypsin Inhibitor Is Crucial to Structure and Function

Licensed Content Author: Carol A. de la Motte,Vincent C. Hascall,Judith Drazba,Sudip K.
Bandyopadhyay,Scott A. Strong

Licensed Content Date: Jul 1, 2003

Licensed Content Volume: 163

Licensed Content Issue: 1

Licensed Content Pages: 13

Start Page: 121

End Page: 133

Type of Use: reuse in a thesis/dissertation

Intended publisher of new work: other

Portion: figures/tables/illustrations

Number of figures/tables/illustrations: 1

Format: both print and electronic

Are you the author of this Elsevier article? No

Will you be translating? No

Original figure numbers: Figure 3

Title of your thesis/dissertation: Interfacial Bioorthogonal Crosslinking for the Fabrication of

Functional Hydrogels

Expected completion date: Jan 2018

Estimated size (number of pages): 300

Total 0.00 USD

Figure 1.5B-C

License Number: 4262630705133

License date: Jan 05, 2018

Licensed Content Publisher: Elsevier

Licensed Content Publication: Advanced Drug Delivery Reviews

Licensed Content Title: Hyaluronan-dependent pericellular matrix

Licensed Content Author: Stephen P. Evanko,Markku I. Tammi,Raija H. Tammi,Thomas N.

Wight

Licensed Content Date: Nov 10, 2007

Licensed Content Volume: 59

Licensed Content Issue: 13

Licensed Content Pages: 15

Start Page: 1351

End Page: 1365

Type of Use: reuse in a thesis/dissertation

Intended publisher of new work: other

Portion: figures/tables/illustrations

Number of figures/tables/illustrations: 1

Format: both print and electronic

Are you the author of this Elsevier article? No

Will you be translating? No

Original figure numbers: Figure 5

Title of your thesis/dissertation: Interfacial Bioorthogonal Crosslinking for the Fabrication of

Functional Hydrogels

Expected completion date: Jan 2018

Estimated size (number of pages) 300

Total 0.00 USD

Chapter 2

Reproduced in its entirety from:

Title: Interfacial Bioorthogonal Crosslinking

Author: Dicker, K.T., Zhang, H., Jia, X., Fox, J.M.

Publication: Macro Lett.

Publisher: American Chemical Society

Date: Jan 05, 2018

This ACS article is provided to You under the terms of this Standard *ACS AuthorChoice/Editors' Choice* usage agreement between You and the American

Chemical Society (“ACS”), a federally-chartered nonprofit located at 1155 16th Street NW, Washington DC 20036. Your access and use of this ACS article means that you have accepted and agreed to the Terms and Conditions of this Agreement. ACS and You are collectively referred to in this Agreement as “the Parties”).

1. SCOPE OF GRANT

ACS grants You non-exclusive and nontransferable permission to access and use this ACS article subject to the terms and conditions set forth in this Agreement.

2. PERMITTED USES

a. For non-commercial research and education purposes only, You may access, download, copy, display and redistribute articles as well as adapt, translate, text and data mine content contained in articles, subject to the following conditions:

i. The authors' moral right to the integrity of their work under the Berne Convention (Article 6bis) is not compromised.

ii. Where content in the article is identified as belonging to a third party, it is your responsibility to ensure that any reuse complies with copyright policies of the owner.

iii. Copyright notices or the display of unique Digital Object Identifiers (DOI’s), ACS or journal logos, bibliographic (e.g. authors, journal, article title, volume, issue, page numbers) or other references to ACS journal titles, web links, and any other journal-specific “branding” or notices that are included in the article or that are provided by

the ACS with instructions that such should accompany its display, should not be removed or tampered with in any way. The display of *ACS AuthorChoice* or *ACS Editors' Choice* articles on non-ACS websites must be accompanied by prominently displayed links to the definitive published versions of those articles on the ACS website.

iv. Any adaptations for non-commercial purposes must prominently link to the definitive published version on the ACS website and prominently display the statement: "This is an unofficial adaptation of an article that appeared in an ACS publication. ACS has not endorsed the content of this adaptation or the context of its use."

v. Any translations for non-commercial purposes, for which a prior translation agreement with ACS has not been established, must prominently link to the definitive published version on the ACS website and prominently display the statement: "This is an unofficial translation of an article that appeared in an ACS publication. ACS has not endorsed the content of this translation or the context of its use."

b. Each time You distribute this ACS article or an adaptation, ACS offers to the recipient a license to this ACS article on the same terms and conditions as the license granted to You under this License.

c. For permission to use ACS copyrighted articles beyond that permitted here, visit: http://pubs.acs.org/copyright/permissions.html